A BUILDING BLOCK APPROACH TOWARDS NOVEL NONLINEAR OPTICAL MATERIALS

by

Ajit Bhaskar

A dissertation submitted in partial fulfillment
of the requirements for the degree of
Doctor of Philosophy
(Macromolecular Science and Engineering)
in The University of Michigan
2007

Doctoral Committee:

Professor Theodore Goodson III, Chair
Professor Frank E. Filisko
Professor Richard E. Robertson
Professor Robert Zand

Dedication, Determination,

and Inspiration.

The three most important things needed for a PhD and these are where I got them from.

Dedication

I dedicate this dissertation to my parents for their unwavering support and encouragement.

Acknowledgements

First of all, I would like to express my sincere gratitude to my advisor Professor Goodson. Not only did he introduce me to the fascinating world of ultrafast spectroscopy but also provided me with an extremely healthy and synergistic working environment. His constant motivation and encouragement enabled me to raise everyday and look forward going to work with a smile on my face. I also consider him as a mentor and I would look up to him as a role model if I choose to become a faculty member in the future.

I would like to thank the members on my dissertation committee Professor Frank Filisko, Professor Richard Robertson and Professor Robert Zand for their valuable discussions and suggestions.

I would also like to thank Professor Goodson's group members, particularly Dr Ramakrishna Guda, Dr Oleg Varnavski, Dr Ying Wang and Dr Xingzhong Yan for patiently teaching me the details of various spectroscopic tools in our lab. I would like to thank the other postdoctoral scholars and graduate students of Professor Goodson's group who have also been an integral part of making the lab a fun place to work.

Undergraduate and high school students like Unique Luna and Adam Ross have provided me with the opportunity to mentor and impart my knowledge to them. I would like to thank them for the opportunity.

My work would not be possible without the synthetic capabilities of Professor Robert Twieg at Kent State University, Professor Michael Haley at The University of Oregon, Professor Peter Bauerle at The University of Ulm, Professor Masahiko Iyoda at Tokyo Metropolitan University and Professor Kazuya Ogawa at Nara Institute of Science and Technology. I would like to sincerely thank them for providing me with the opportunity to apply my skills and knowledge on their materials.

I would also like to thank the Macromolecular Science and Engineering program, particularly Nonna Hamilton and the Macro graduate students for making my stay in Ann Arbor an extremely pleasant and memorable one.

Last, but never least, I would like to thank my family for their invaluable support. Without them, I wouldn’t be where I am today.

Table of Contents

List of Figures

List of Tables

Abstract

A BUILDING BLOCK APPROACH TOWARDS NOVEL NONLINEAR OPTICAL MATERIALS

by

Ajit Bhaskar

Chair: Theodore Goodson III

The purpose of the present research is to develop and apply a building block approach towards the design of novel nonlinear optical (NLO) materials, capable of exhibiting enhanced Two-Photon Absorption (TPA) behavior. These materials have potential applications in biological imaging, microfabrication, sensing, photodynamic cancer therapy, optical limiting and ultrafast switching. Electronic structure, symmetry and intermolecular forces are vital for designing the right building block. The next step is to connect them to form macromolecules. However, besides covalent bonding, aggregation and self assembly of building blocks can also be utilized, which renders the strategies for materials design less reliant on chemical synthesis. The application of building block approach was illustrated using several examples, including rigid, two-dimensional architectures. These enabled the investigation of macrostructures that were synthetically inaccessible as well as demonstrated the influence of symmetry on TPA behavior. Electronic coupling between building blocks and excited state dynamics were the observed reasons for enhanced TPA. In an attempt to investigate strong coupling that would extend over the entire chromophore, novel “endless” nano-cavities were examined for their TPA behavior. Using the tools of ultrafast spectroscopy, complete delocalization was proved in these materials. Similar enhancement in giant porphyrin macrocycles, which mimic natural light harvesting systems, was observed. Another approach to harness the coupling between small building blocks in a synergistic fashion is to arrange them into branched architectures. The influence of π-character of branching units on the charge transfer character, which in turn influences the TPA behavior, was examined. Using excited state studies, not only was it observed that alkene π-bridging resulted in enhancement of TPA behavior over alkyne π-bridging, but also the mechanism for cooperative enhancement upon assembly of small chromophores into branched architecture was elucidated. Such branched materials serve as building blocks for dendrimers and a series of thiophene dendrons were investigated for enhanced TPA behavior. It was also found that such dendrons could be used for light harvesting and funneling applications. Using the knowledge gained from the investigations in branched materials, a potential application in the form of a highly sensitive and selective two-photon “turn-on” sensor for the detection of zinc ions was developed. This study could serve as a guideline for developing chromophores for imaging metal ions in biological systems using multiphoton excitation.

Chapter 1

Introduction and Background

1.1. Nonlinear Optics and Nonlinear Optical Materials

Since Maiman demonstrated the first working laser in 1960[1], the field of optical materials has undergone a metamorphosis. The interaction of matter with high intensity radiation has uncovered the fascinating world of nonlinear optical (NLO) phenomena in a wide variety of materials. The ability to change the refractive index of a material by simply changing the voltage applied across it, the ability to generate light having half the wavelength of the incident light after interaction with a material medium, the ability to switch a material's ability to transmit light reversibly by using electrical or optical stimuli, to generate wavelengths in the infrared region by spatially and temporally overlapping two beams of visible wavelengths are some of the amazing feats that can be accomplished by using nonlinear optics. This has engendered a multitude of applications in three dimensional optical data storage, microfabrication, biology, optical circuitry and signal processing among many other others. There are several categories of NLO phenomena based on the dependence of material property on the intensity of exciting radiation. This dissertation concerns itself with Two-Photon Absorption (TPA), a third order NLO phenomenon which occurs upon simultaneous absorption of two-photons by the molecule in order to be excited from its ground state to excited state.

Although the source of light for investigating NLO phenomena (lasers) has undergone constant improvement over time along with the availability of faster, more accurate and sophisticated instrumentation, it is the materials aspect that receives most attention from both fundamental and applications perspective. The search for novel materials capable of exhibiting large NLO responses is the major thrust of research in the field of nonlinear optics. In order to develop novel materials, it is of critical importance to understand the various molecular parameters that influence the NLO behavior of a material. It is the desire for understanding the structure-property relationships in NLO materials that has given birth to the field of NLO spectroscopy. As is the case with most applications, the development of materials for NLO applications began with inorganic materials. Inorganic crystals, rare earth metal salts were the subject of investigations since the first successful demonstration of nonlinear optical behavior in materials[2, 3]. However, eventually, organics carved a niche for themselves in the field of NLO materials due to their:

i) Ease of tuning chemical structure.
ii) Ease of processibility.
iii) Lower weight.
iv) Lower materials cost.

As a result, a great amount of research has focused on developing novel organic materials for NLO applications. The advent of conjugated materials, novel catalyst systems and advanced techniques in organic chemistry has facilitated the development of organic NLO materials. This dissertation concerns itself primarily with organic materials.

Organic chemistry is certainly a valuable tool for synthesizing novel materials. However, this could also place the ultimate limit on development of novel materials for TPA applications. The development of organic materials for TPA began with the investigation of small, conjugated molecules such as benzene[4], stilbene[5], xanthenes[6], fused benzene ring systems such as anthracenes[7], thiophene derivatives[8] and other commonly used dyes such as Coumarin, and its derivatives[9]. However, it was soon realized that the ultimate limit on the TPA properties using this approach would be placed by synthesis limited parameters such as strength of functional groups and the choice of π-linkers.

Hence, there seems to be a need to devise schemes in order to arrange the small chromophores in a manner to harvest the NLO behavior of individual chromophores in a synergistic fashion. It was envisioned that by arranging small molecules into long chains to form polymers, large optical nonlinearities could be obtained. As a result, several polymers were investigated for their TPA behavior. Such studies began with polydiacetylenes[10] and eventually encompassed polythiophenes[11] and polyphenylenevinylene[12] derivatives. However, this approach was met with two limitations. Firstly, like most other properties such as conjugation and carrier mobility, the NLO properties also started to show saturation behavior beyond certain number of repeat units. Additional strategies included NLO active small molecules as side chains on polymeric backbones[13]. However, this was also met with little success since synthesis became increasingly challenging and the ultimate limits in terms of TPA properties were placed by similar synthetic considerations as organic dyes. Hence, the NLO community turned its attention to oligomeric materials, a compromise between polymers and small molecules. Once again, synthetic parameters became the governing factors in terms of placing the upper limits on NLO/TPA properties.

In order to pack more chromophores into smaller space efficiently, novel multidimensional materials (quadrupoles, octupoles etc.) were developed. The idea behind adopting different dimensionalities[14] is to arrange multiple chromophores in a compact fashion. Hence, attention was directed towards branched architecture[15] using nitrogen, carbon, phosphorous, benzene rings, paracyclophane[16] rings and triazines[17] as branching centers and a wide variety of functional groups that were earlier employed for the synthesis of dipolar and quadrupolar chromophores.

However, in all of the abovementioned approaches, the ultimate limit is placed by chemical synthesis wherein the most conjugated oligomer with strongest donor and acceptor substitutions would form the functional unit with largest TPA response. The architectures are ultimately limited to linear or branched forms. There are only certain numbers of π-conjugation linkages that can be employed for obtaining conjugation. Therefore, there is a need to develop methodologies which rely on synthetically posed limits to a lesser extent and utilize other aspects material behavior such as self assembly, aggregation and novel architectures.

Hence, the **goal of my research** is to propose and investigate approaches and methodologies that extend the scope of development of novel NLO materials beyond the realm of chemical synthesis. In order to develop a macromolecule, one needs to understand and design the optimal building block. This could be a systematic approach towards developing novel NLO materials. Building block approach could also uncover the influence of less investigated parameters such as molecular symmetry and excited state dynamics, which play a key role in determining the NLO response of a material.

This could be investigated by arranging a building block in different fashions (symmetry) and this will be further demonstrated in subsequent chapters of the dissertation.

A major advantage of building approach could be the understanding of properties of macrostructures that are synthetically inaccessible. This could be due to lack of solubility, practically unfeasible synthetic schemes or prohibitive costs involved in preparing the final macrostructure. However, by breaking down the macrostructure into small building blocks, it is possible to gain insight into the NLO properties of the macrostructure via extrapolation from studying the NLO behavior of smaller sub-units. Hence, by adopting the building block approach, it is possible to project the upper limits on the NLO properties of larger molecules. In this process, several additional discoveries regarding the behavior of building blocks could be made that could further enrich the understanding of structure-property relationships for developing TPA materials.

Building blocks could also be arranged to form novel architectures, such as cyclic geometry (Chapter IV), which has not been investigated in great detail for TPA behavior. Such materials without "end-effects" present us with the possibility of completely conjugated molecular wires. Furthermore, self assembly and aggregation of such materials could provide a new avenue towards the design of TPA materials that is not limited by organic synthesis. Such approaches have been only applied to porphyrins so far[18], due to their unique chemical structures. However, in order to broaden the horizon of organic macromolecules as practical TPA materials, it is important to apply aggregation and self assembly approaches to all classes of organic materials.

The knowledge gained from building block approach is of molecular nature so its scope need not be restricted to nonlinear optics alone. Some of the concepts could be applied for development of materials for organic electronics and photonics.

Keeping these caveats in mind, my research at the University of Michigan has concentrated on investigating novel materials, which are capable of exhibiting self assembly, and conjugated aggregates for enhanced TPA behavior. Their self assembly and aggregation into a wide array of exciting macrostructures such as liquid crystals, long range ordered crystals, and dendrimers render them attractive for several applications in nonlinear optical devices such as switches, sensors, molecular machinery, biological imaging as well as organic electronics and photonics.

Thus, building block approach enables the development of novel NLO materials with strong emphasis on emphasis on understanding structure-function relationships in order to further design better materials.

1.2. Two-Photon Absorption

Just as organic materials represent a subset of a wide variety of materials, the NLO properties of a material can also be categorized depending upon the order of nonlinearity exhibited by the material. This in turn, is determined by the dependence of the material's behavior on the intensity or electric field strength of the incident radiation.

When the optical behavior of a material changes quadratically with respect to incident intensity, a nonlinear, quantum effect called Two-Photon absorption (TPA) can arise. Considering the anharmonic oscillator model for describing the displacement of charges in an organic material upon interaction with an incoming electric field, the polarizability of a material ***P (t)*** can be described as a power series in electric field strength as[19]:

$$P(t) = \chi^{(1)}E(t) + \chi^{(2)}E^2(t) + \chi^{(3)}E^3(t) + \chi^{(4)}E^4(t) + \dots \qquad (1.1)$$

Here, $\chi^{(2)}$, $\chi^{(3)}$, and $\chi^{(4)}$ are called second, third and fourth order susceptibilities respectively. A detailed derivation of fundamental equations for nonlinear optics using the concepts of quantum mechanics and Maxwell's equations is beyond the scope of this dissertation. However, it suffices to state that the wave equation in NLO media has the form[20]:

$$\nabla^2 E - \frac{n^2}{c^2}\frac{\partial^2 E}{\partial t^2} = \frac{4\pi}{c}\frac{\partial^2 P}{\partial t^2} \qquad (1.2)$$

Considering equation 1.1, cubic polarization or third order polarizability can be defined as:

$$P^{(3)}(t) = \chi^{(3)}E^3(t) \qquad (1.3)$$

Here, $\chi^{(3)}$ is the third order nonlinear optical susceptibility.

If a small signal at frequency ω_s is propagated through the medium in the presence of a strong pump signal ω_p, the frequencies chosen such that $\omega_s+\omega_p$ equals some transition frequency of the material, then the transition can take place through **simultaneous** absorption of those two photons. This refers to the phenomena of **Two-Photon Absorption (TPA)**. Hence, TPA results in the attenuation of the signal, even though the material does not absorb the signal frequency or frequencies directly. TPA is the particular NLO property that will form the focus of this dissertation. Thus, my research has concentrated on novel strategies and structure-function relationships in organic materials for enhanced Two-Photon Absorption behavior.

1.2.1. Background

The process of TPA was theoretically predicted by Maria Göppert-Mayer in 1931 in her PhD dissertation[21]. It is interesting to note that such a prediction was made nearly thirty years before the discovery of lasers. However, the first experimental evidence for TPA was provided by Kaiser and Garrett in 1961 at Bell Labs in New Jersey[22]. They investigated a $CaF_2:Eu^{2+}$ crystal. They excited this material using ruby laser (which they called an "optical maser" in their original paper) at 694.3nm and observed blue fluorescence at 425 nm. They asserted that there was no linear absorption below 22000 cm^{-1} (455 nm) and therefore the crystal was transparent at the excitation wavelength. Thus, the observed fluorescence was attributed to two-photon excitation phenomenon. They also showed quadratic dependence between observed fluorescence intensity and incident ruby laser's intensity. The crystal used was 1mm thick with a Eu^{2+} doping level of 0.1%. They recorded their fluorescence on a photographic plate, which consisted of an oversaturated spot due to ruby laser and a fluorescence spot. This was an elementary, yet powerful demonstration of **Two-Photon Excited Fluorescence** (TPEF) process.

A schematic representation of TPA is provided in Figure 1.1. In this particular example, it is assumed that the energy gap between ground state and first excited state of the molecule corresponds to the energy of a 400nm photon, which the case is observed commonly for conjugated organic chromophores. Hence, assuming that the transition is also allowed by TPA, it can be achieved by the simultaneous absorption of two 800 nm photons, if supplied with enough intensity. It is worthwhile to emphasize once again that the absorption of the two photons is a simultaneous process. There is no intermediate or virtual state involved. Hence, it is readily observed that the excitation limit has been extended from UV-Vis range to the near IR regime. Also, at longer wavelengths, scattering is reduced, which is in accordance with Rayleigh's law, which can be expressed as:

$$Scattering\,\alpha\,\frac{1}{\lambda^4} \tag{1.4}$$

Thus, by increasing the excitation wavelength by twofold, scattering can be reduced by 16 times.

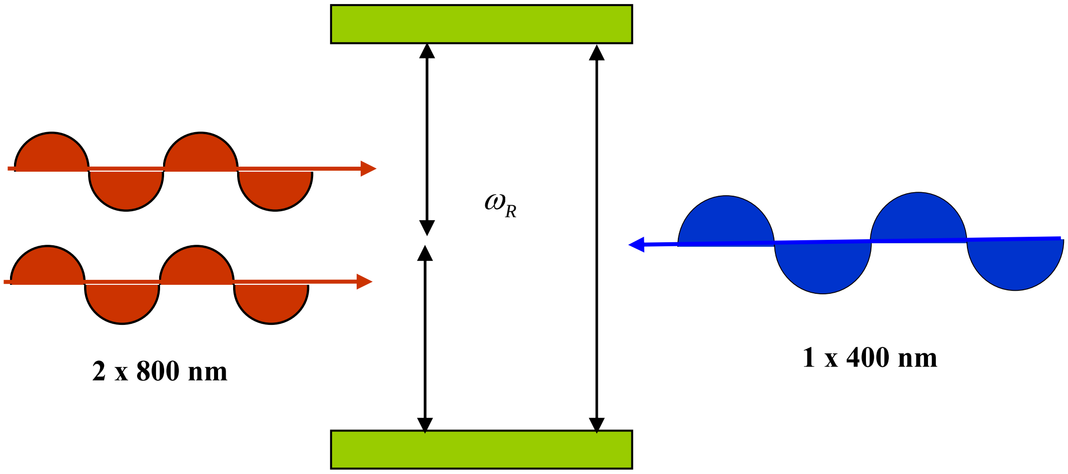

Figure 1.1. Two-Photon Absorption.

Another key feature of TPA is greater penetration depth of excitation radiation into the absorbing material. This once again arises due to use of longer wavelength for excitation which causes reduced linear absorption and less scattering. These features also result in smaller focusing volumes of the material. Thus, TPA offers certain unique advantages over conventional steady state or single photon absorption (1PA). The process shown in Figure 1.1 represents a case where both photons that excite the molecule via two-photon excitation have the same wavelength. This is known as degenerate two-photon absorption. It is also possible to perform non-degenerate two-photon absorption measurements using two photons of different wavelengths.

There are different selection rules for one and two-photon absorption[23]. If a molecule is centrosymmetric, then the transition that is allowed by one photon absorption is forbidden by TPA and vice versa. From basic symmetry considerations[24], the operator responsible for an **n**-photon transition is proportional to $x^i y^j z^k$, where x, y and z are the electron Cartesian coordinates and i, j and k are integers which must sum to n. The direct product symmetry must contain the irreducible representation of the transition operator. For centrosymmetric systems, the inversion symmetry of the Cartesian coordinates leads to familiar parity selection rules: u↔g for odd and g↔g or u↔u for even values of n.

TPA depends on the polarization of the excitation light[25-29]. Different behavior is observed for linearly and circularly polarized excitations. This is because of involvement of two different transition moments as well as different states for TPA. This is in contrast to single photon absorption which is independent of polarization of excitation source, assuming the molecules themselves are not oriented in any preferential direction.

The unique features of TPA listed above render it attractive for several applications. One of the first applications of TPA demonstrated was three dimensional optical data storage by Rentzepis[30] and coworkers in 1989. They used blocks of spiropyran (SP) dye and fulgide dye separately dispersed in PMMA. A schematic of their set-up for optical writing and reading is presented in Figure 1.2. The transmission of the 1064 nm beam by the spiropyran was probed with and without 532nm beam. In the presence of 532nm beam, TPA occurred because the SP dye was completely transparent to 532nm and 1064nm individually. As a result of TPA, a red spot was recorded. This process of probing the 1064 nm beam using a visible probe was referred to "reading". The sum frequency of 1064nm and 532nm corresponded to a 355nm beam (ultraviolet) which was absorbed by the spiropyran dye. This corresponded to the "written" state of the dye. Such two-photon induced photochromism writing process was also demonstrated using a single 640nm beam. The features that render TPA attractive for data storage are small focusing volumes, reduced scattering and greater penetration depth. This enables creation of more "bits" per unit volume.

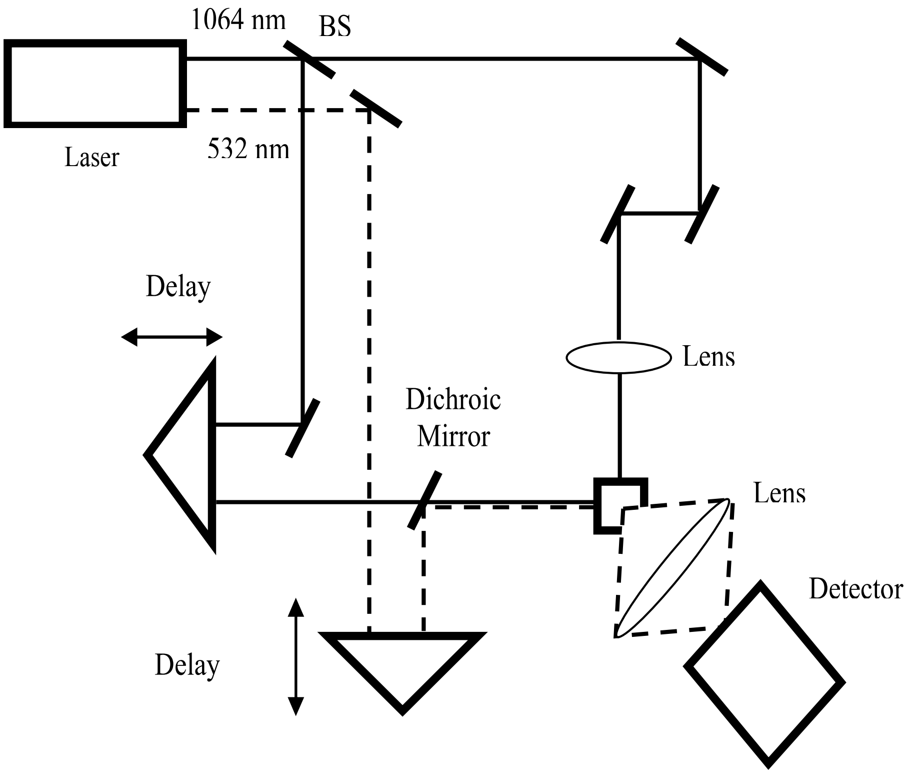

Figure 1.2. Optical reading and writing system used by Rentzepis[30].

It is interesting to note that the first application of TPA was demonstrated almost 40 years after the first TPA phenomenon was reported. This is because TPA was initially used as a spectroscopic tool for investigating states and transitions in materials that were forbidden by one-photon absorption.

Watt Webb and coworkers reported the use of two-photon excited fluorescence (TPEF) in microscopy[31-39]. Human tissues exhibit better transmission at longer wavelengths. Since TPA extends the excitation regime to near IR wavelengths, it formed the premise for this application. Combined with reduced scattering and greater penetration depth, along with capability to focus on femtoliter level volumes[40, 41], no in-focus damage of tissues under appropriate exposure conditions, TP microscopy is a powerful and popular tool used today for investigating numerous biological phenomena. Figure 1.3 illustrates the depth resolution obtained using TPEF microscopy[42]. The image to the left was acquired using single photon excitation with Argon laser as the source. The image to the right was acquired using pulsed 720nm radiation. The white circles are intended to show better depth resolution. The colored circles indicate lower degree of scattering and hence, enhanced resolution with TP excitation.

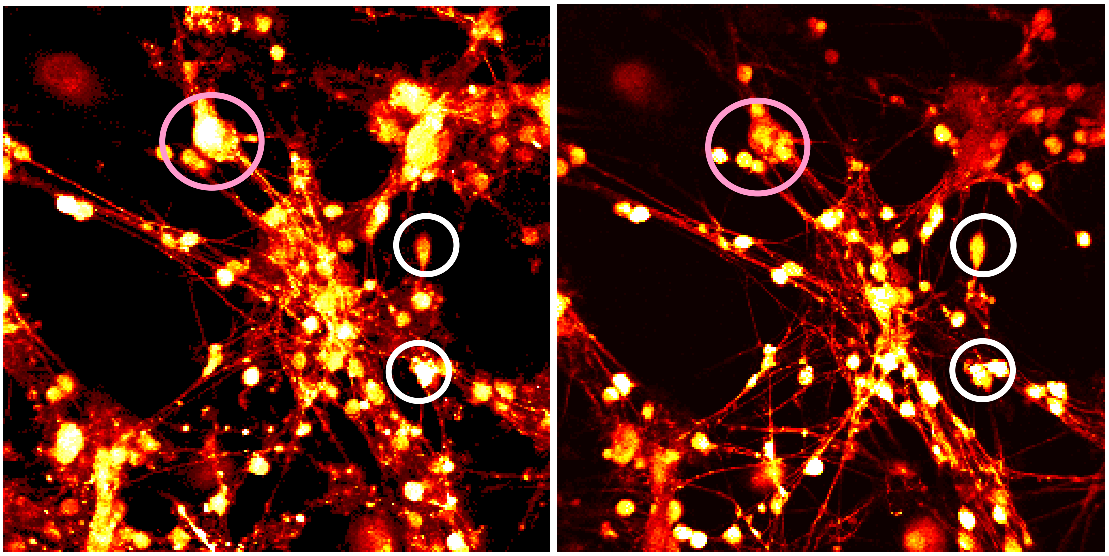

Figure 1.3. One versus Two Photon Excited fluorescence microscopy [42]. Source: http://www.bris.ac.uk/Depts/Anatomy/research/neuro/OneTwoPhoton/TwoPhoton.htm.

Another exciting application of TPA materials lies in Optical Power Limiting (OPL) [43-54]. OPL refers to the state when a large change in input signal produces only a small change in the output. This is illustrated in Figure 1.4.

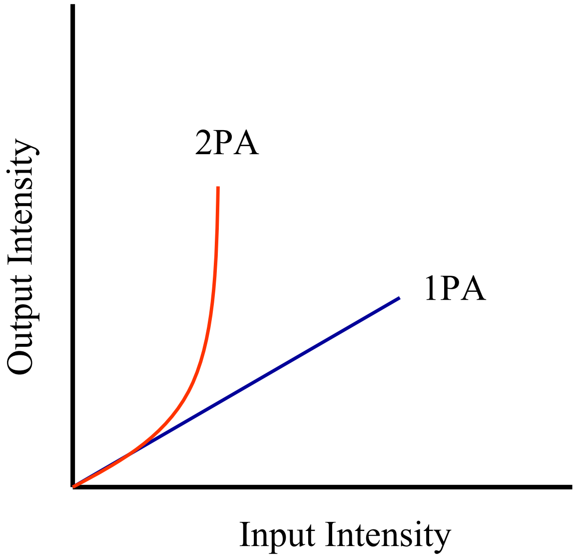

Figure 1.4. Optical power limiting.

There are two types of mechanisms that result in OPL[55]. Accumulative optical nonlinearity pertains to the situation when polarization density changes rather slowly with time, upon application of an electric field. The timescale may be comparable or even longer than the duration of excitation. Hence, accumulative nonlinearities require energy transfer which initiates nonlinear optical phenomena. Accumulative nonlinearities can be used to construct optical limiters that do not depend on the pulse duration. An example of accumulative nonlinearity is reverse saturable absorption (RSA). This is illustrated in Figure 1.5. RSA typically arises when the excited state absorption cross section of the molecule (σ_{23}) is much larger than the ground state absorption cross section (σ_{12}). If it is the other way around, then the material is said to be a saturable absorber. This means that with increasing intensity, the material eventually becomes transparent. For a material that exhibits RSA,

$$\frac{dI}{dz} = -\left[N_T\sigma_{12} + N_2(\sigma_{23} - \sigma_{12})\right]I \qquad (1.5)$$

Where N_T = total number of molecules per unit area in a slice of thickness dz, N_2 = Number of molecules in level 2 which is initially zero. Hence, equation 1.5 reduces to Beer's law. Thus, transmittance becomes

$$T = \frac{I}{I_0} = 10^{-\sigma_{12}N_T L} \qquad (1.6)$$

But at high fluence, there is ground state depletion since $\sigma_{23} >> \sigma_{12}$,

$$T = \frac{I}{I_0} = 10^{-\sigma_{23}N_T L} \qquad (1.7)$$

In this case, I still increases, but the increase is much slower since $\sigma_{23} >> \sigma_{12}$. Hence, a large ratio of σ_{23}: σ_{12} is desired for a better optical limiter.

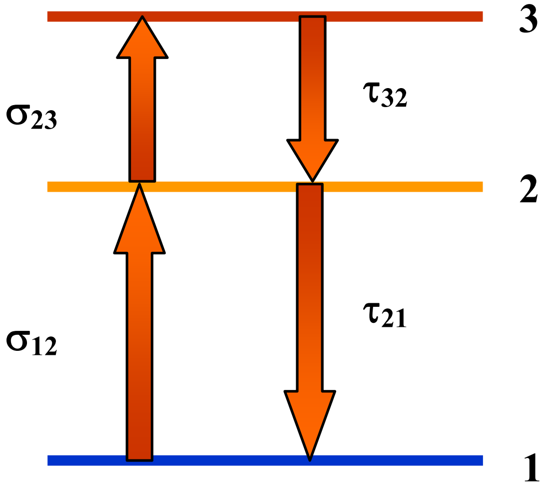

Figure 1.5. Reverse Saturable Absorption mechanism for optical power limiting[55].

Instantaneous optical nonlinearity refers to the situation when change in polarization density resulting due to application of an electric field occurs instantaneously. TPA is an example of instantaneous nonlinearity. If we consider a molecule with three distinct energy levels (Figure 1.5), for a low value of σ_{12} and very short excited state lifetime τ_{21}, state 2 effectively becomes a virtual intermediate state. So when the material absorbs a photon, it reaches the virtual state. Immediately, another photon pumps it to energy state 3. For TPA process,

$$I_L = \frac{I_0}{1 + I_0 \beta L} \tag{1.8}$$

For low β values,

$$I_L = \frac{I_0(1 - I_0 \beta L)}{1 - I_0{}^2 \beta^2 L^2}$$

Or

$$I_L = I_0(1 - I_0 \beta L) \tag{1.9}$$

Hence, as I_0 increases, I_L decreases. But if β increases, the decrease becomes sharper. Usually, β values are small so high intensities are required to realize significant TPA. In this case, the transmitted fluence can be determined as:

$$F = \frac{\tau}{\beta L} \tag{1.10}$$

Where τ is the pulse duration. It can be observed from equation 1.10 that F can be decreased by increasing β.

TPA is also used in photodynamic therapy (PDT) [56-65]. PDT is a method of treatment that involves the use of a photosensitizer in the presence of light to produce a cytotoxic effect on cancerous cells. It has been approved by FDA in U.S and has gained widespread acceptance worldwide. The growth of PDT started to accelerate after the discovery of tumor localizing properties of certain porphyrins. Dougherty[66, 67] pioneered much of the research on PDT starting in 1970s.

PDT requires three elements; a photosensitizer, light and oxygen. The photosensitizer is an efficient singlet oxygen generator, which is believed to be the cytotoxic agent. Upon excitation, the photosensitizer is excited to its singlet state which has a short lifetime. From this state, it is desirable that the photosensitizer undergoes intersystem crossing (ISC) to a long lived triplet state. The ground state of atmospheric oxygen has triplet character. Hence, triplet-triplet annihilation between the photosensitizer and oxygen occurs to generate singlet oxygen.

In currently used photosensitizers, Photofrin® is the most commonly used material. It has an absorption maximum at 400-500nm. However, tissue penetration at these visible wavelengths is minimal. Hence, there is a compromise between photosensitizer excitation efficiency and penetration depth. By utilizing TPA materials, which would exhibit TPA at ~800-1300nm, the problem associated with penetration depth could be overcome. Further, smaller focusing restricts tissue damage to a smaller area. By designing novel materials with large TPA cross sections, photoexcitation efficiency and penetration depth can be increased and this provides the thrust for research and development of novel TPA materials for PDT.

TPA also finds itself beneficial for microfabrication[68-73] (Figure 1.6). This is because unlike linear absorption, the material's absorption varies quadratically with input intensity. Hence, considering a beam with Gaussian distribution of intensity, the rate of one photon absorption of the material would fall off linearly from the center of beam incidence whereas the fall-off would be quadratic for a TPA process. Coupled with reduced scattering, smaller features could be obtained and hence, greater number of features per unit volume could be generated. Furthermore, due to better penetration depth, a particular volumetric element could be accessed more precisely using two-photon excitation. Cumpston et al have demonstrated[74] three dimensional lithographic microfabrication (3DLM) using a two-photon photopolymer resin consisting of a polymeric binder, a cross linkable acrylic monomer and a two-photon polymerization initiator. Figure 1.7 shows its structure. Photopolymerization was carried out at a threshold power of 300μW at 800 nm using a Ti: Sapphire laser operating at 76MHz and 150 fs. The fabricated structures shown in Figure 1.6 can be used as photonic band gap materials, waveguides and micromechanical electrical systems (MEMS). It was also observed that choosing the abovementioned photoinitiator resulted in more than one order of magnitude increase in the two-photon photosensitivity. Kawata and coworkers[75] have demonstrated sub-diffraction limit micromachining of a "micro-bull" using a 120pJ pulse energy Ti: Sapphire laser. Their micro-bull was of the size of a red blood cell and is shown in Figure 1.8. The accuracy of their TPA machining was 150nm which represents sub diffraction limit, considering the fact that 800nm radiation was used for this process.

Several other applications suggested for TPA include sensing[76-79], investigation of protein folding activities[80, 81], two-photon induced FRET[82], in vivo multiphoton tomography[83, 84], melanoma detection[85], cosmetic research[86] and tissue engineering[87]. A system for in vivo multiphoton imaging and tomography commercialized by JenLab[88] (DermaInspect®) is shown in Figure 1.9.

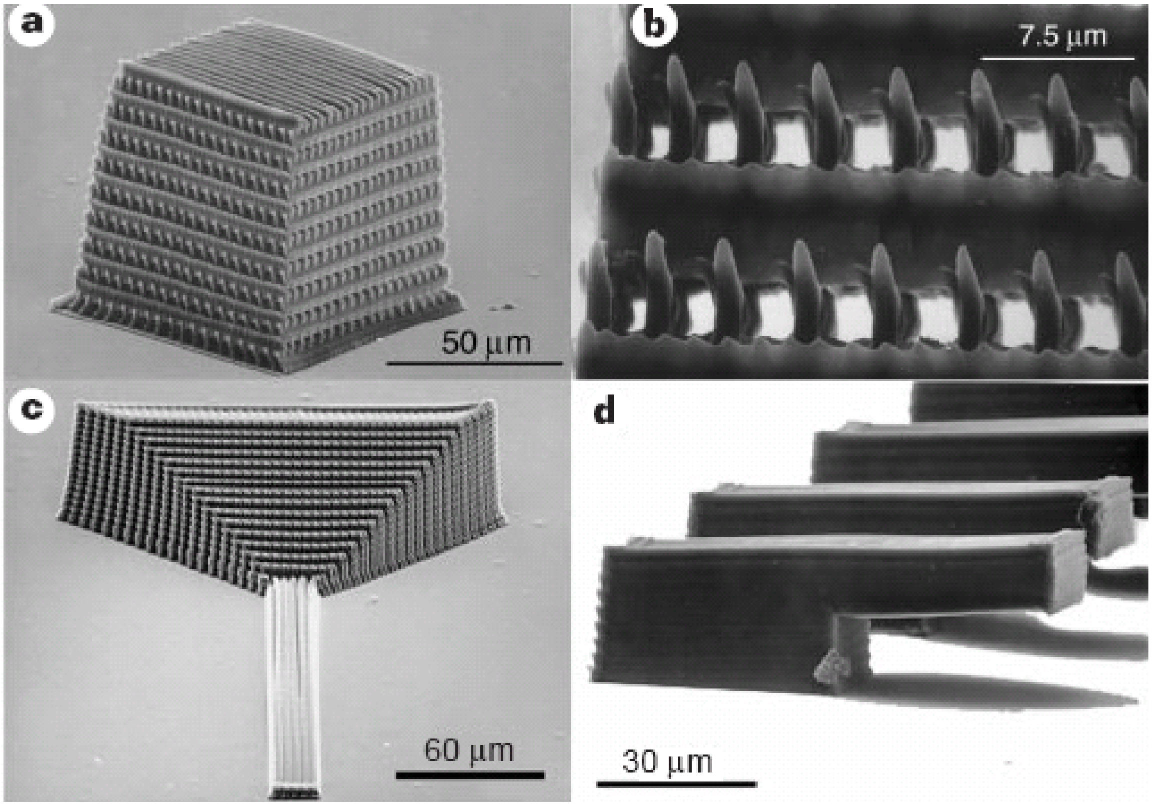

Figure 1.6. Three dimensional lithographic microfabrication using TPA initiator[74].

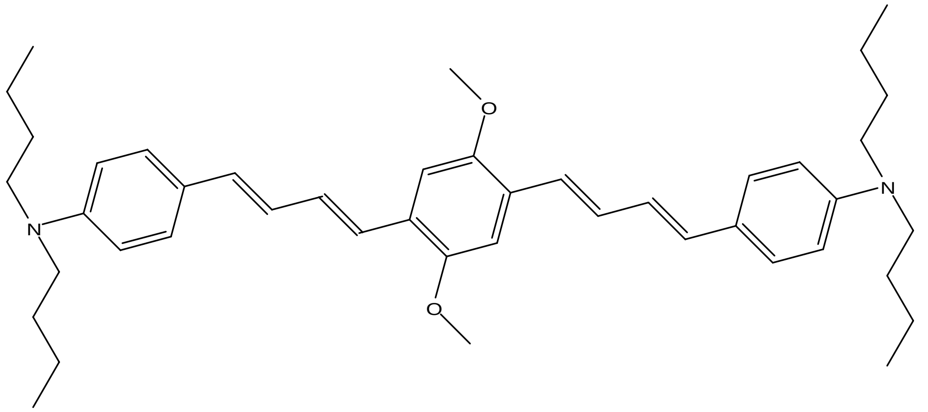

Figure 1.7. Molecular structure of the TPA initiator used for microfabrication[74].

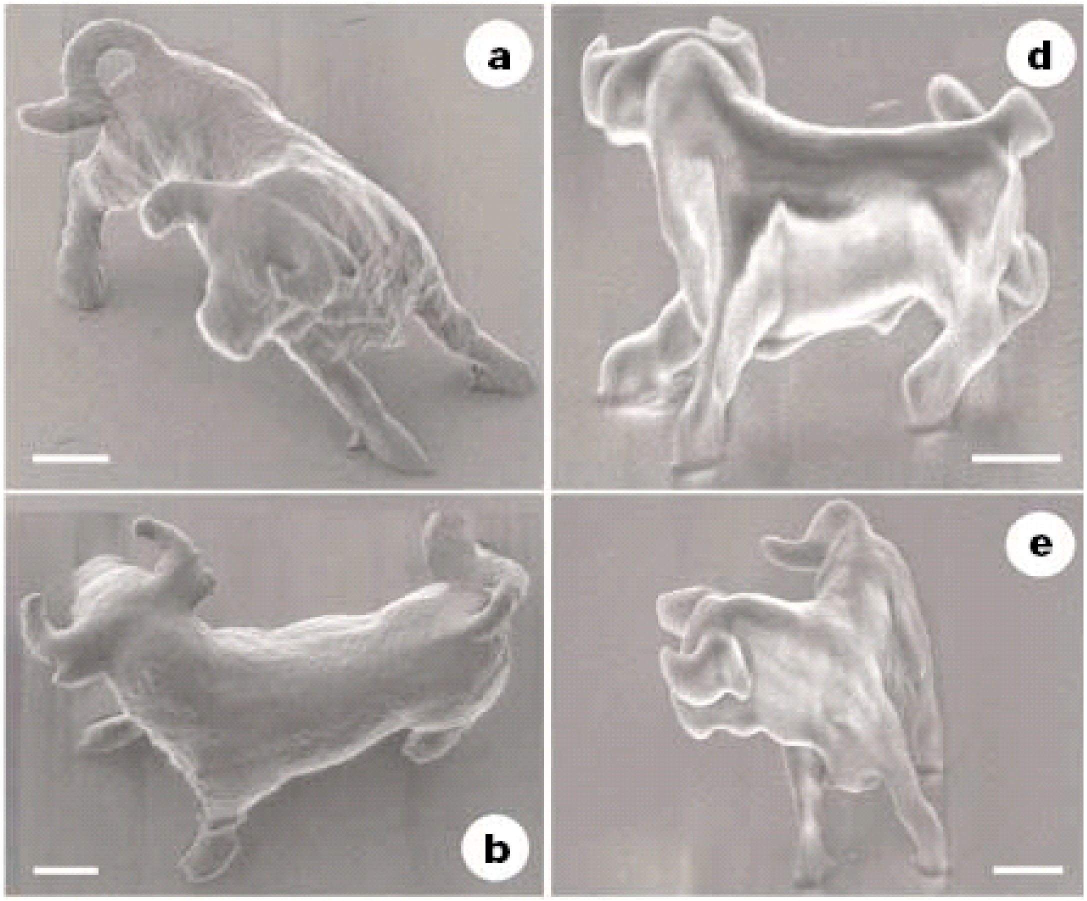

Figure 1.8. Micro-bull fabricated by Kawata and coworkers. Scale bars are 2μm[75].

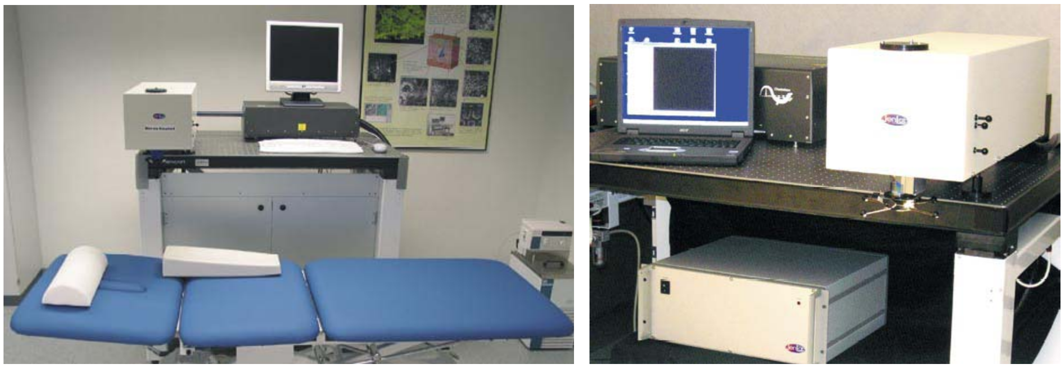

Figure 1.9. DermaInspect® system from JenLab[88]. Source: http://www.jenlab.de/prodermainspect.php.

1.2.2. Theoretical Considerations

The parameter that defines the inherent ability of a molecule to absorb two photons (of same or different wavelengths) simultaneously is called its two-photon absorption cross section (TPACS) and is denoted by the symbol δ. δ is related to the imaginary part of the third order NLO polarizability γ (and hence $\chi^{(3)}$) as[14]:

$$\delta = \frac{3}{2}\frac{\hbar\omega^2 \, \mathrm{Im}[\gamma(-\omega;\omega,\omega,-\omega)]}{\varepsilon_0 c^2} \tag{1.11}$$

This expression has been derived based on perturbation treatment of interaction between light and matter that provides expressions for molecular polarizabilities in the form of summation over all excited states of the molecules, and is called the sum-over states (SOS) formalism[96]. The SOS expression for γ can be simplified in several cases. For example, when a single low lying excited state dominates the linear optical response, then the summations over excited states that are coupled to ground state can be limited to that excited state alone and the summations over upper-lying excited states go over those few excited states that are coupled to the dominant excited state. The main chain axis component of the frequency dependent third order molecular polarizability then reduces to:

$$\gamma_{xxxx}(-\omega;\omega,\omega,-\omega) \approx \frac{1}{6h'^3} P(-\omega;\omega,\omega,-\omega)$$

$$\left[\begin{array}{l} \dfrac{M^2{}_{ge}\Delta\mu_{ge}^2}{(E_{ge}-\hbar\omega-i\Gamma_{ge})(E_{ge}-2\hbar\omega-i\Gamma_{ge})(E_{ge}-\hbar\omega-i\Gamma_{ge})} \\ + \dfrac{M_{ge}^4}{(E_{ge}-\hbar\omega-i\Gamma_{ge})(E_{ge}-\hbar\omega-i\Gamma_{ge})(E_{ge}+\hbar\omega-i\Gamma_{ge})} \\ + \sum_{e'} \dfrac{M_{ge}^2 M_{ee'}^2}{(E_{ge}-\hbar\omega-i\Gamma_{ge})(E_{ge}-2\hbar\omega-i\Gamma_{ge})(E_{ge}-\hbar\omega-i\Gamma_{ge})} \end{array}\right] \begin{array}{c} \mathbf{D} \\ \\ \mathbf{N} \\ \\ \mathbf{T} \end{array} \tag{1.12}$$

Where M_{ge} denotes transition dipole moment from ground state g to first excited state e, $\Delta\mu_{ge}$ denotes the change in dipole moment upon transition from ground to first excited state, caused by conformational changes etc. $M_{ee'}$ denotes transition dipole moment for transition from first excited state e to the TPA allowed excited state e', E denotes energy difference between the states involved in the transition and Γ is a damping factor.

The D-term of equation 1.12 is called the dipolar term since it exclusively appears in noncentrosymmetric systems. Term T involves upper (TPA allowed) excited states and is strongly dependent on the coupling of e' with e. The N-term is the negative term which is related to linear polarizability, which allows for the possibility of only one-photon resonances. Thus, this term does not make any contribution to TPA. Equation 1.12 can be further simplified by separating the peak TPA cross sections based on transitions involved. For a two-state model,

$$\delta_{2-state} \propto \frac{M_{ge}^{2}\Delta\mu_{ge}^{2}}{\frac{E^{2}_{ge}}{4}\Gamma} \tag{1.13}$$

And for a three state model,

$$\delta_{3-state} \propto \frac{M_{ge''}^{2}M_{ee'}^{2}}{(E_{ge}-E_{ge'}/2)^{2}\Gamma} \tag{1.14}$$

Hence, the key parameters affecting δ are the ground and excited state transition dipole moments, change in dipole moment term and the energy differences between the states involved. It is important to maximize the dipole moments and minimize the energy differences between different levels involved. Detailed mathematical derivations of the expressions listed above are beyond the scope of the present work and readers interested in the same are recommended to study the references listed at the end of the chapter.

Using highly rigorous application of computational tools, the SOS formalism has been utilized to estimate theoretical limits on the maximum possible TPA cross section attainable using conjugated organic chromophores. Kuzyk and coworkers have reported instructive results on such limits for doubly resonant TPA cross sections which serve as guidelines for structure-property development for TPA materials[89-91]. They have related the maximum TPA cross section under double resonance conditions to the second hyperpolarizability (and hence, $\chi^{(3)}$). They have obtained a δ_{max} value of 230, 000 GM for a single electron system. Considering a three state model, they have calculated maximum TPA cross section as a function of energy of the two-photon excited state (E_2) at three different energies of first excited state (E_1) . They observed that when E_2 = 1 eV and E_1 =

0.5 eV, the abovementioned value of 230, 000 GM was obtained. In other words, the maximum possible TPA cross section is obtained when E_1 was lowest. They have also proposed that upon varying δ_{max} as a function of E_1 for three different values of E_2, δ_{max} could be increased to 10^6 by reducing E_2 to 0.5 eV and by bringing down E_1 to ~0.25 eV. However, an energy gap of 0.25 eV would correspond to photon energy of 5μm. An organic chromophore with such low bandgap has not been reported yet. Hence, these plots serve as guidelines along which structure property relationships for certain classes of organic molecules could be optimized for maximum TPA cross sections. Their plots are presented in Figure 1.10 .

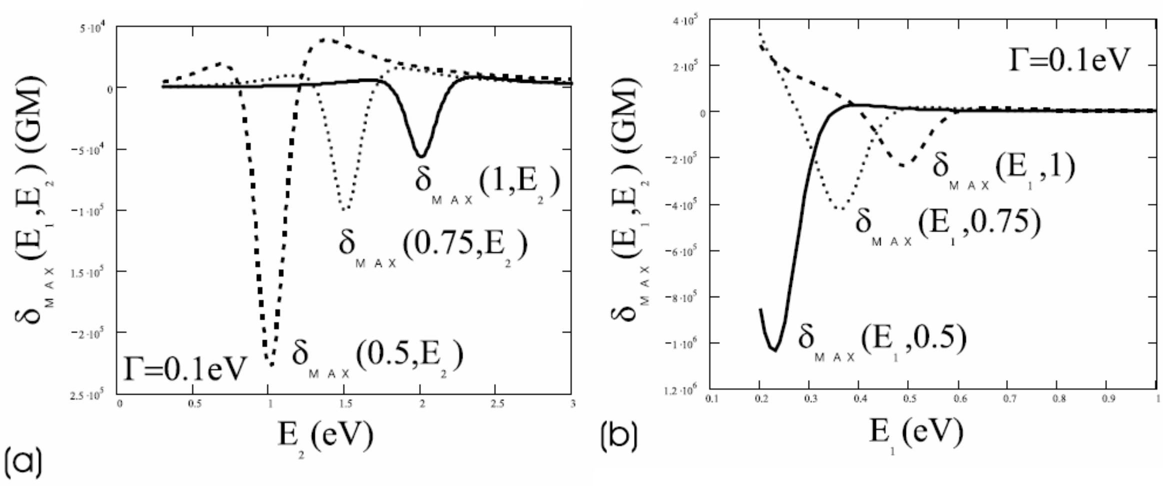

Figure 1.10. Limits on doubly resonant TPA cross section[89].

Kuzyk and coworkers have also introduced the concept of "effective electrons" that contribute towards TPA behavior, and normalized TPA cross section, which is the ratio of TPA cross section obtained to maximum in- resonance or off-resonance TPA cross section predicted from computations. As an example, two chromophores shown in Figure 1.11 are considered.

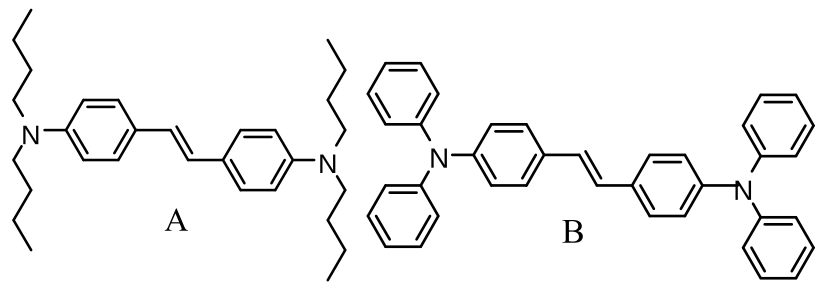

Figure 1.11. Chromophores illustrating the concept of effective electrons[90].

The number of effective electrons N_{ef} is the mean squared value over all possible chromophores. Thue, for chromophore A N_{ef} is 14, whereas for chromophore B, it is $(14^2 + 4\times6^2)^{1/2} = 18.4$. However, the value of normalized TPA cross section for B was found to be one order of magnitudelower than B. This suggested that adding four additional benzene rings was not an efficient use of pi-electrons. Hence, this study is important in terms of synthetic strategies for designing TPA materials. They key is not only to increase the number of pi-electrons, but for the additional electrons to participate in excitation process.

1.2.3. Excitations in Conjugated Aggregates

It can be deduced from the previous section that excited states play a vital role in determining the TPA properties of organic materials. Hence, it is appropriate to gain a deeper understanding into the nature of excitations and some excited state phenomena in organic molecules. Taking branched systems as an example, it was reported by Prasad and coworkers that upon investigation of a monomer and trimer composed of identical branching units, the TPA cross section of the trimer did not increase by a factor of three, but by a factor of seven[92]. This indicated cooperative enhancement and hence, coupling between individual arms of the trimer. The structures are reproduced in Figure 1.12 for convenience. In order to probe the mechanism of enhancement, our research group has carried out time-resolved ultrafast measurements on the monomer and trimer systems consisting of identical arms[93, 94]. The measurements showed a fast component in the anisotropy decay (discussed later in the dissertation) for the trimer whereas no such behavior was observed for the monomer. This result suggested that exciton delocalization contributed to energy migration in the chromophore, resulting in enhancement of NLO properties. In other words, at very short time scales, a delocalized state was present. The extent of initial delocalization also depends on the nature of branching center. Our group has performed measurements suggesting that for a given conjugated arm, a nitrogen centered chromophore results in most initial delocalization compared to carbon or phosphorous centered branched chromophores. In fact, in the carbon centered branched chromophore, Forster type energy transfer was found to be the main pathway for exciton migration in the chromophore whereas a coherent energy transfer pathway was observed in the case of nitrogen centered chromophore[15]. The values of residual anisotropy provided information on the geometry of emitting states. For example, the phosphorous centered chromophore was found to deviate farthest from planarity and had the least tendency towards coherent energy migration.

It is also possible that the branching center does not enhance conjugation. There are reports where the increase in TPA showed additive behavior with increase in number of chromophores and no cooperative enhancement. This suggests that intramolecular electronic interactions and possible contributions from homogeneous broadening and disorder play a vital role in determining the extent of enhancement of NLO properties[95].

Theoretical and experimental investigations have attempted to measure the strengths of such interactions by relating the time of depolarization at ultrafast timescales to homogeneous broadening effects and the interaction strength depending on the number of chromophores contributing to the enhancement.

In order to gain appreciation for the contribution of excited state dynamics on TPA behavior, an example is taken from the work published by Zheng et al[96]. Considering chromophores A and B (structures shown in Figure 1.13), the values relevant for three states SOS formalism are tabulated in Table 1.1. From Table 1.1, the value of [E_{ge}- $E_{ge'}/2$] for A and B are 1.07 eV and 0.99 eV respectively. Combining these with their respective ground state transition dipole moment (M_{ge}) values and substituting them in equation 1.14, TPA improvement by a factor of 2.1 cannot be explained by steady state results alone. However, considering the values of their excited state transition moments, the ratio of $M_{ee'}$ values for B and A turns out to be 2.01. Hence, without gaining insight into excited state transition dipole moments, it would not have been possible to explain the trend observed in NLO properties. There are experimental tools such as transient absorption spectroscopy that enable us to probe the excited state dynamics and will be discussed in detail in the next chapter. Hence, the design criteria for materials with large TPA cross sections for NLO applications could be very different from those for other applications. Hence, understanding the nature of excitations, migration of energy in excited states and excited state dynamics is critical for designing materials for enhanced TPA response.

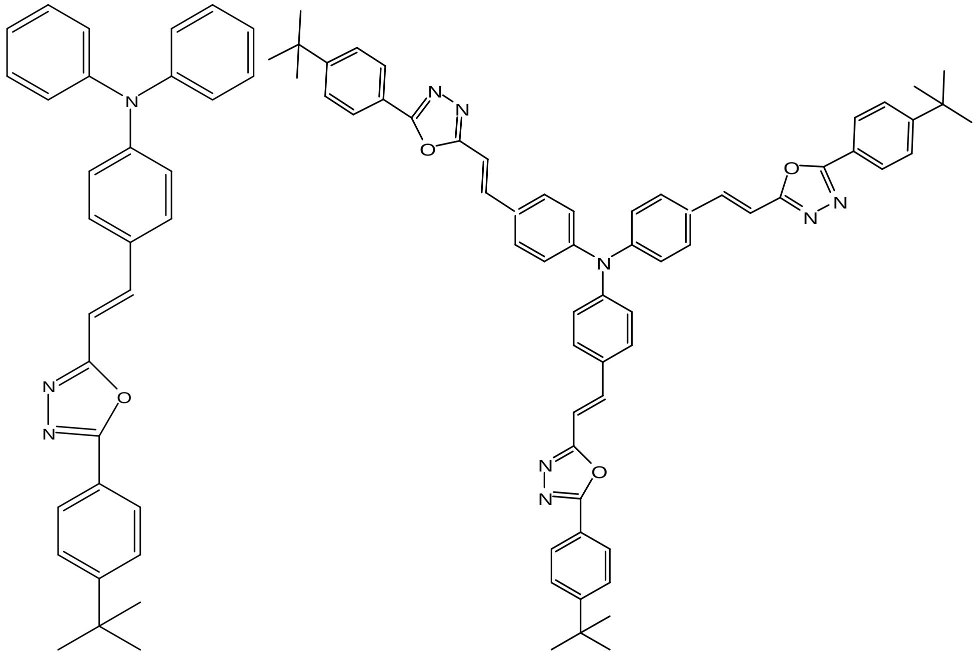

Figure 1.12. TPA chromophores investigated by Prasad and coworkers for cooperative enhancement[92].

Table 1.1. Parameters for Sum-Over-States model for chromophores A and B[96].

Molecule	E_{ge} (eV)	$E_{ge'}$ (eV)	M_{ge} (D)	$M_{ee'}$ (D)	δ (GM)
A	2.44	2.75	15.8	16.9	2467
B	2.25	2.53	15.9	24.5	5192

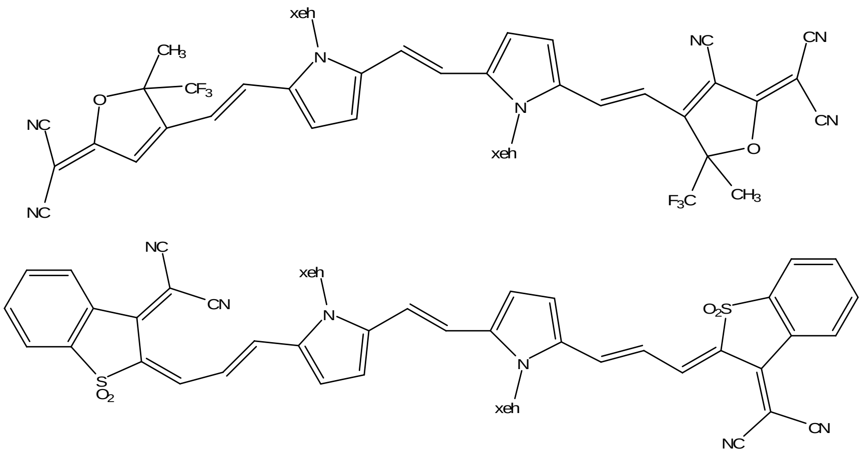

Figure 1.13. TPA chromophores investigated by Zheng et al demonstrating the importance of excited state behavior[96].

1.2.4. Structure-Function Relationships for Developing Organic Materials for TPA

This section enlists the synthetic efforts guided towards tailoring the molecular parameters that influence TPA behavior in organic materials discussed above.

1.2.4.1. Conjugation

A systematic report on structure-property relationships in conjugated organic chromophores was published by Albota et al[97]. Two chromophores illustrating the concept of increase in conjugation length are shown in Figure 1.14 . The maximum TPA cross section (δ) observed for chromophore A was 8 GM at 514 nm whereas for B it was 110 GM at 620 nm. Hence, by simply adding an additional styryl unit, not only the can δ be increased by more than one order of magnitude, but also the location of TPA maximum can be red-shifted significantly. This is attributed primarily to decrease in the energy difference term appearing in the denominators of in equations 1.13 and 1.14. Increased conjugation leads to decrease in HOMO-LUMO gap. A simplistic explanation can be provided using a particle in a box model. By increasing conjugation length, the length of the box is increased and hence, the overlap of orbital functions between ground and excited states can now occur at a lower energy.

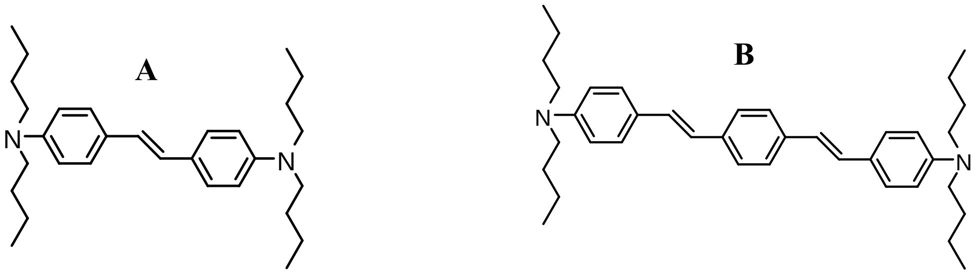

Figure 1.14. Chromophores illustrating the effect of increasing conjugation length on TPA behavior[97].

However, with additional conjugation units, it is not necessary that δ will continue to show such a dramatic increase. This is illustrated using chromophores C and D shown[97] in Figure 1.15 . Chromophore C has a δ value of 680 GM at 725 nm whereas the same for chromophore D was found to be 1270 GM at 750 nm. Hence, the trends observed in chromophores A-D with respect to conjugation length suggest that initially there is a dramatic increase in δ, but the effect becomes less as conjugation is further increased and eventually it could show saturation.

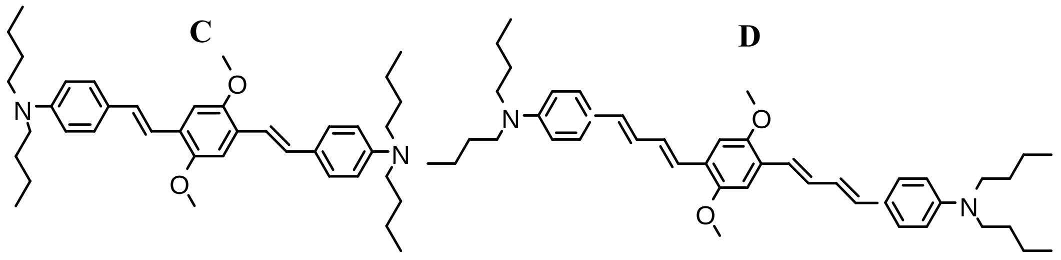

Figure 1.15. Chromophores with different conjugation lengths[97].

1.2.4.2. Donor-Acceptor Groups

The influence of addition of donor groups can be observed from chromophores E and F shown[97] in Figure 1.16 . The n-butyldiamino group in chromophore F serves as a donor because of the lone pair of electrons available in nitrogen atom. From theoretical modeling by applying sum-over-states (SOS) formalism, it was observed that the addition of donor groups caused the following effects[97]:

i) Decrease in energy term from 1.8 eV to 1.5 eV
ii) Increase in ground state transition dipole moment (M_{ge}) from 7.1 D to 8.8 D
iii) Increase in excited state transition dipole moment from 3.1 D to 7.2 D.

Based on these observations, δ should exhibit an approximately 12 fold increase. Experiments showed that δ value for chromophores E and F were 8 GM and 110 GM respectively. Considering the fact that these measurements were performed using TPEF method, which has an error of up to 20% associated with it, the results were in considerable agreement with theory. Chromophore F is called a **donor-π-donor** type chromophore since it has a π-conjugation unit sandwiched between two n-butylamino donor groups.

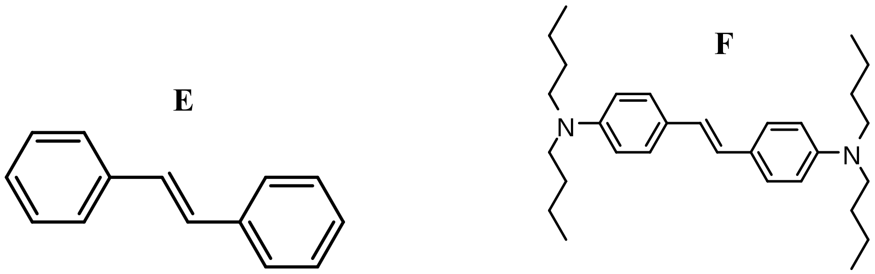

Figure 1.16. Chromophores illustrating addition of donor groups[97].

Another example[98] is shown in Figure 1.17 which contains three chromophores. Chromophore G has donor group (diphenylamino) at only one end; chromophore H has a diphenylamino group at one end and ethylsulfonyl acceptor at the other end. Chromophore I has nitro group as acceptor. Chromophore G showed δ of 28 GM at 750nm, chromophore H showed δ of 40GM at 750nm, and chromophore I showed δ of 125 GM at ~845nm. This suggests that nitro group is the strongest acceptor group, which can be proved on the basis of proton NMR studies and by investigating Hammett constant values for different functional groups.

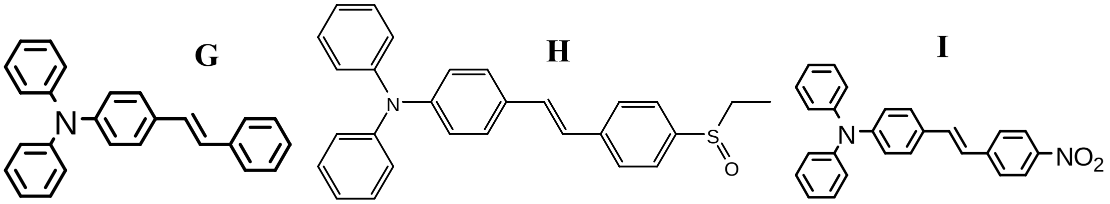

Figure 1.17. Chromophores with varying acceptor strengths[98].

Another example[99] where the donor strength is varied, while keeping the acceptor strength constant, is shown in Figure 1.18. The TPA cross section was found to improve as the donor strength was increased from dimethylamino to N-Carbazolyl, from 188 GM to 300 GM. The addition of donor/acceptor groups also present with the interesting phenomenon of solvatochromism, where the emission wavelength can be tuned by simply varying the solvent. This phenomenon is illustrated using chromophore J as an example in Figure 1.19 .

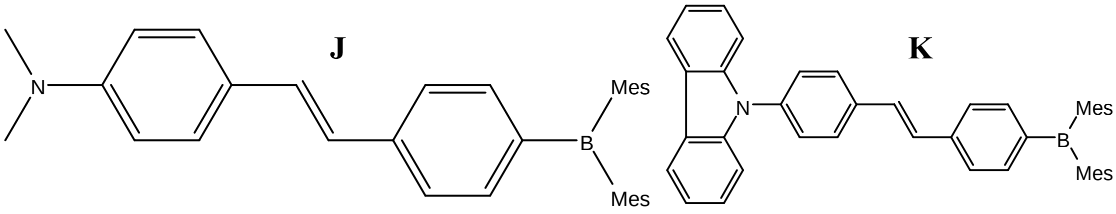

Figure 1.18. Chromophores with varying donor strengths[99].

It can be observed that as the polarity of solvent is increased from toluene (least polar) to THF to acetonitrile (most polar), the emission maximum shows bathochromic shift from 492nm to 580nm. The reason for this shift is that as solvent polarity increases, the stabilization of the conformation of the excited state of the molecule results in emission from lower energy vibrational level of the excited state to ground state. This decrease in energy of transition manifests itself as red shift in emission maximum. Hence, organic chemistry offers the flexibility to tune the properties of a given material in a variety of ways.

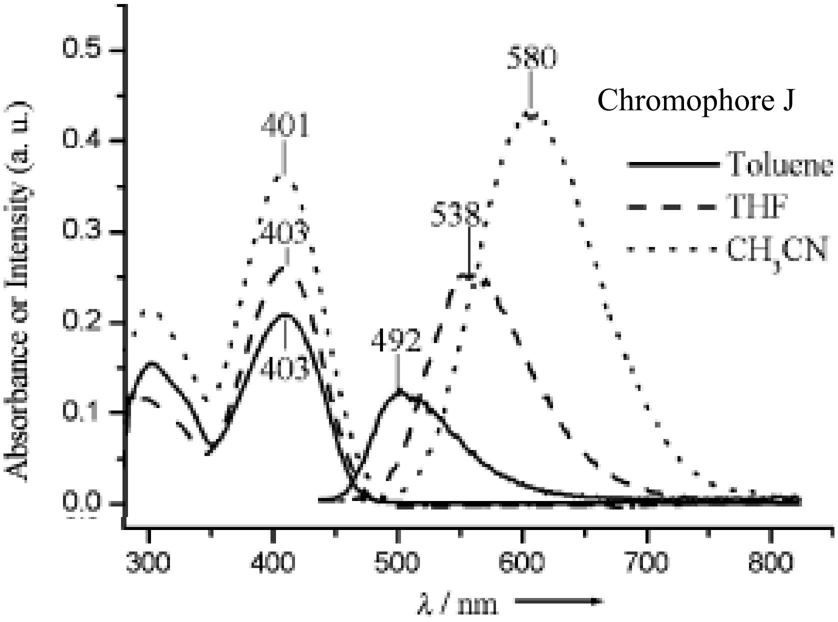

Figure 1.19. Solvatochromism exhibited by chromophore J[99].

1.2.4.3. Dimensionality

Dimensionality[14] refers to the number of “poles” in a given molecule. For example, a simple molecule consisting of a π-conjugation unit between a donor group and an acceptor group is called a dipolar molecule. Chromophores H, I, J and K are examples of dipolar molecules. A quadrupolar chromophore has contributions from two separate dipoles within the same compound. Chromophore F is an example of a quadrupole because there are two donor groups connected by a π-bridge. Hence, it is a **donor-π-donor** quadrupole with contributions from two donor-π dipolar components. A few examples[97, 100, 101] with their nomenclatures are presented in Figure 1.20.

Recently, significant attention has been focused on octupolar chromophores. A few examples[101-104] are shown in Figure 1.21 . An octupolar chromophore is a multibranched structure with three contributions from individual functional group-π dipole combinations, or "arms". Such chromophores have been designed to develop dendrimers for TPA applications. Branched architecture serves as an efficient method to pack a large number of chromophores over a small volume. As a result, the NLO properties need not scale linearly with number of individual arms.

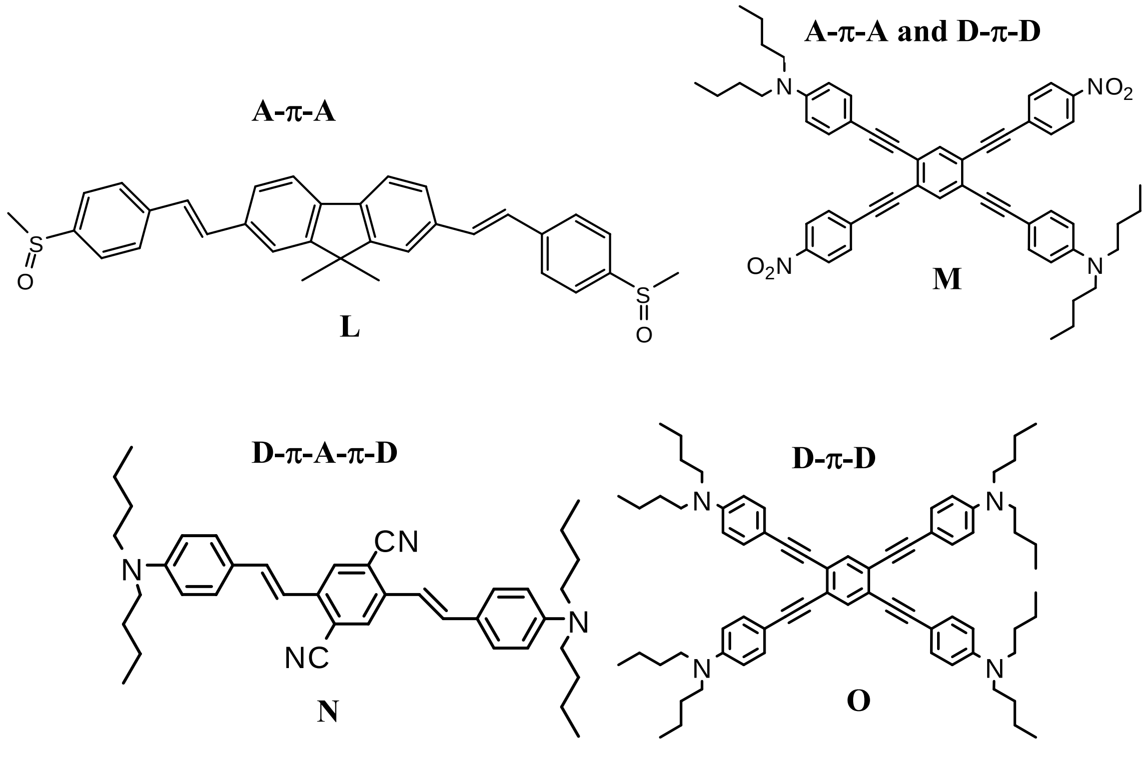

Figure 1.20. Some quadrupolar structures[97, 98, 99].

1.2.4.4. Nature of π-conjugation unit

The nature of π-bridge plays a significant role in orbital overlap and hence, conjugation of the resulting chromophore. As an example[100], three chromophores with the same central fluorene unit and n-alkyl end groups are shown in Figure 1.22 . The key difference between the chromophores is the use of phenyl, thiophene and fluorene as π-linkages. It was observed that chromophores T, U and V showed δ values of 1920 GM, 1530 GM and 2960 GM respectively. A possible explanation provided was that fluorene group increases the planarity of the molecule, which would in turn, facilitate better overlap of molecular orbitals, which could eventually lead to better delocalization.

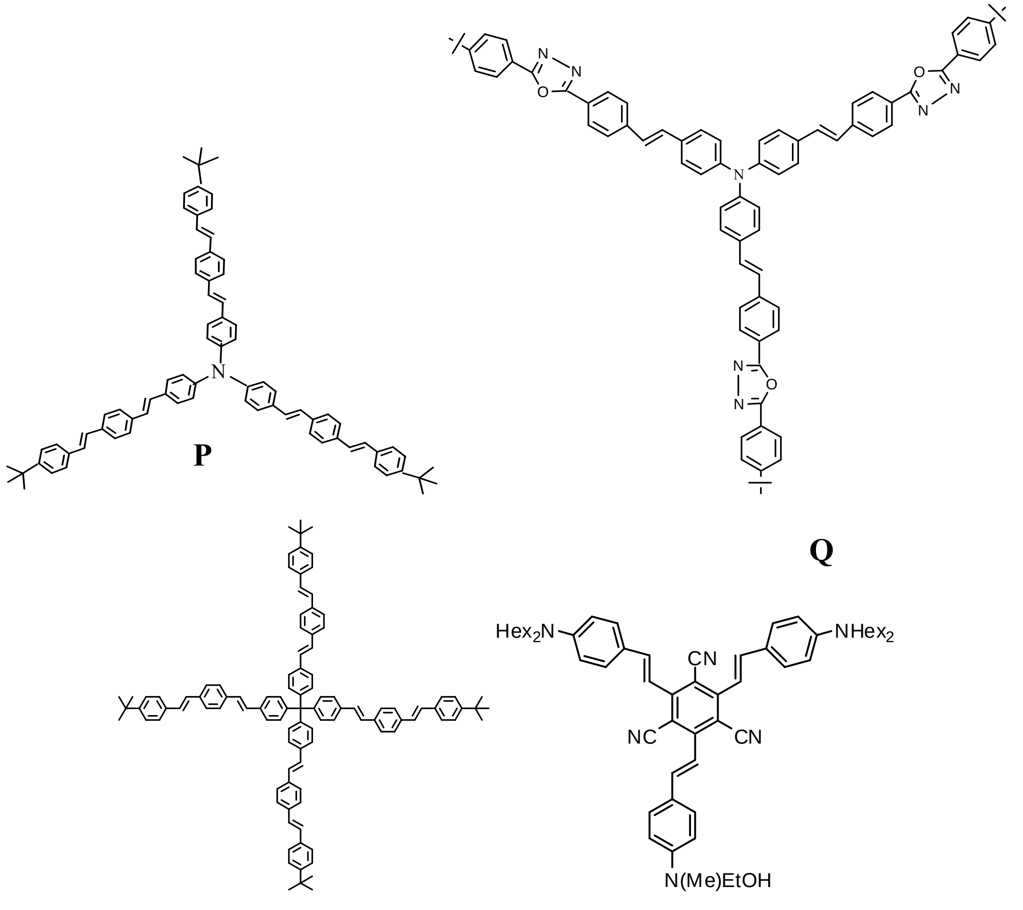

P **Q** **R** **S**

Figure 1.21. Examples of octupolar chromophores[101-104].

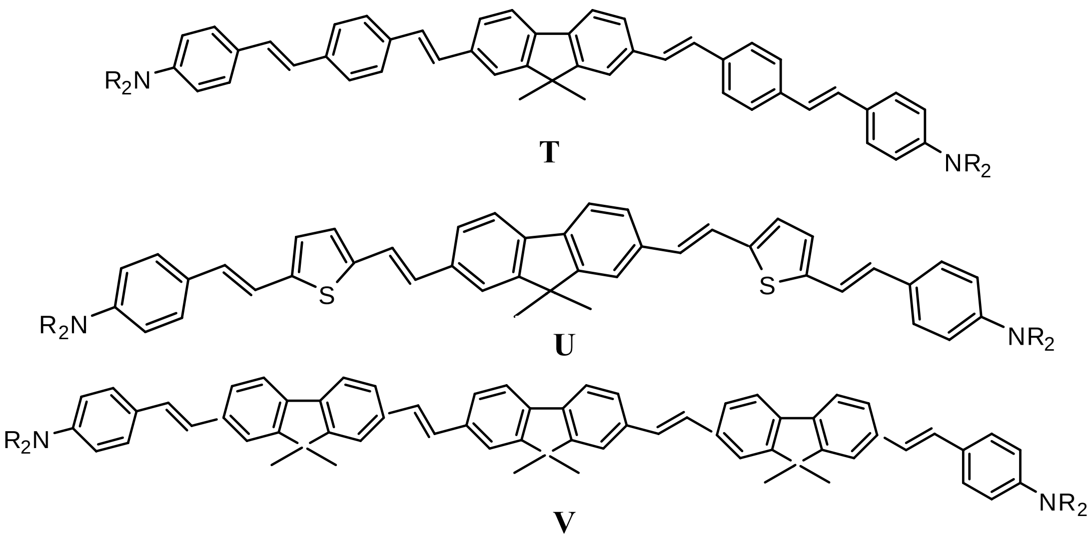

Figure 1.22. Chromophores with different π-conjugation units[100].

Several other structural parameters have been investigated for a wide variety of organic molecules. These include polarizability of central π-linkage, influence of alkyl chains for imparting solubility, substitution position of functional groups for tuning conjugation (ortho versus meta versus para) etc[105]. An exhaustive review of all those investigations is beyond the scope of this dissertation. For the sake of brevity, reference articles have been listed at appropriate places and interested readers are strongly encouraged to browse them.

1.3. Overview of Subsequent Chapters

In Chapter II, the key experimental tools for quantifying TPA behavior as well as investigating the mechanism of enhancement of TPA observed have been described, along with a brief discussion on generation of high intensity radiation for investigating NLO properties of organic materials.

In Chapter III, the building block approach is illustrated with a series of dehydrobenzoannulenes. The objective is to understand the influence of the number and arrangement (symmetry) of building blocks on the resulting TPA behavior. The results could also be helpful in projecting the limit on the TPA cross sections obtainable for large two-dimensional graphidyne networks, which are attractive from organic electronics and photonics standpoints. A triangular [18] annulene served as the basic building block for this study. Several multi annulenic systems with different number and different arrangements of the triangle were investigated for their linear and nonlinear optical behavior. The TPA cross sections were enhanced with increasing number of building blocks. The **key results** were that large TPA cross sections could be obtained without adding strong donor or acceptor groups and that the arrangement of building blocks had a significant impact on the resulting TPA behavior. This has not been demonstrated before. The trend observed in TPA behavior could not be explained on the basis of steady state measurements alone so excited state measurements were employed to elucidate the mechanism of enhancement. It was observed that symmetry breaking in the excited state and excited state transition dipole moments were influenced significantly by altering the arrangement of building blocks.

Chapter IV is a structure-function investigation in branched aggregates that serve as building blocks for conjugated organic dendrimers. The effect of nature of π-bridging unit, number of branching units, acceptor strength and the length of individual branch on the resulting TPA behavior was studied. **One of the main results** was that alkene π-bridging yielded larger TPA cross sections over alkyne π-bridging, considering TPA into the lower energy excited state. This was explained on the basis of solvent stabilization of the excited state which in turn, was related to the change in conformations in ground and excited states of the chromophores. These served as measures of change in dipole moment between ground and excited states. The mechanism of enhancement of TPA behavior upon increasing the dimensionality from monomer to a branched trimer was investigated using ultrafast pump probe spectroscopy. As the **most significant result**, the presence of an initially delocalized state followed by localization of excitation on a branch was demonstrated spectroscopically. Finally, TPA investigations were also carried out on a series of three-dimensional dendrons composed of thiophenes as building blocks. The **key findings** from this section were super linear increment of TPA cross section with increase in dendron generation and energy funneling in dendrons as a result of emission from the longest α-conjugated portion of the dendron.

In Chapter V, building blocks consisting of thiophenes, alkyne and alkene linkages were used to synthesize novel nanometer-sized cyclic cavities. Such tunable macrocycles could serve as hosts for various guest molecules. Here, the number of building blocks was increased but the overall circular geometry was preserved. The TPA behavior of the macrocycles was investigated and it was observed that TPA cross section showed large enhancement upon increase in number of building units. This was attributed to extension of delocalization over the entire macrocycle, which formed the **important finding** of this work. As another **significant contribution**, a theoretical framework for the location and coupling between excited systems was also verified using ultrafast spectroscopy.

Chapter VI is a study on porphyrins based cyclic aggregates. Such porphyrin based macromolecules represent an approach to mimic natural light harvesting molecules. The building block in this case consisted of two zinc porphyrin rings linked by a fluorene unit and two triple bonds. The building blocks were covalently connected to form giant macrocycles. However, the connection between each building block was not conjugated. As the **main contribution**, coupling between individual building blocks, even though the connecting bridges were non-conjugated, was investigated.

Chapter VII demonstrates the development of a **potential application** based on the knowledge gained from structure-property relationships detailed in chapters I-VI, particularly chapter IV. A branched chromophore was reported as the **first ever** highly selective and sensitive two-photon, turn-on zinc ion sensor. This chromophore showed quenched emission in steady state upon binding with Zn^{2+} but enhanced emission upon excitation with near infra-red laser radiation. The mechanism of sensing was elucidated by examining the ground and excited state behavior of this molecule in the presence and absence of zinc ions.

In Chapter VIII, an overall summary of the research is presented for the purpose of synopsis. The common thread between the various architectures investigated in my research is the building block approach and the motivation behind these investigations is the possibility of applications in biological imaging, sensing, ultrafast switching and artificial light harvesting systems. Studies that could be pursued as future research have also been suggested.

Summary

- TPA is a third order nonlinear optical (NLO) process.
- It finds applications in microfabrication, biological imaging, photodynamic cancer therapy and optical power limiting.
- Key molecular parameters affecting TPA behavior are conjugation, strength of donor and/or acceptor groups, dimensionality and nature of conjugating unit.
- Excited state behavior is very important and has significant influence on TPA behavior.
- Present approaches for designing materials for TPA are limited by chemical synthesis.
- The primary objective of my research is to develop a building block approach that places strong emphasis on structure-function relationships and extends the design of novel TPA materials beyond chemical synthesis by taking advantage of aggregation, self-assembly and arrangement of building blocks into novel architectures.

1.4. References

1) Thorp, J. S. *Masers and Lasers: Physics and Design*, Macmillan Publishers, 1967.
2) Franken, P. A.; Hill, A. C.; Peters, C. W.; Bond, W.; Garrett, C. G. B.; Kaiser, W. *Phys. Rev. Lett.* **1960**, *5*, 303.
3) Maiman, T. H. *Nature*, **1960**, *187*, 493.
4) Murakami, J.; Kaya, K.; Ito, M. *J. Chem. Phys.* **1980**, *72*, 3263.
5) Kleinschmidt, J.; Rentsch, S.; Tottleben, W.; Whillhelmi, B. *Chem. Phys. Lett.* **1974**, *24*, 133.
6) Rapp, W.; Gronau, B.; Iwan, N. *Chem. Phys. Lett.* **1971**, *8*, 529.
7) Kobayashi, T.; Nagakura, S. *Chem. Phys. Lett.* **1972**, *13*, 217.
8) Rentzepis, P. M.; Topp, M. R. *Org. Scintill. Liquid Scintil. Count. Proc. Intl. Conf.* **1971**, *76*, 91.
9) Parma, L.; Omenetto, N. *Chem. Phys. Lett.* **1978**, *54*, 544.
10) Chen, C. H.; McCann, M. P. Opt. Commun, **1987**, *63*, 335.
11) Sakurai, K.; Tachibana, H.; Shiga, N.; Terakura, C.; Matsumoto, M.; Tokura, Y. *Phys. Rev. B* **1997**, *56*, 9552.
12) Brazovskii, S.; Kirova, N.; Bishop, A. R.; Klimov, V.; McBranch, D.; Barashkov, N. N.; Ferraris, J. P. Opt. Mater. **1998**, *9*, 472.
13) Cha, M.; Torruellas, W. E.; Stegeman, G. I.; Horsthuis, W. H. G.; Mohlmann, G. R.; Meth, J. *Appl. Phys. Lett.* **1994**, *65*, 3648.
14) Beljonne, D.; Wensellers, W.; Zojer, E.; Shuai, Z.; Vogel, H.; Pond, S. J.; Perry, J. W.; Bredas, J.-L. *Adv. Funct. Mater.* **2002**, *12*, 631.
15) Wang, Y.; He, G. S.; Prasad, P. N.; Goodson, T. III *J. Am. Chem. Soc.* **2005**, *127*, 10128.
16) Bartholomew, G. P.; Rumi, M.; Pond, S. J. K.; Perry, J. W.; Tretiak, S.; Bazan, G. C. *J. Am. Chem. Soc.* **2004**, *126*, 11529.
17) Xu, F.; Wang, Z.; Gong, Q. *Opt. Mater.* **2007**, *29*, 723
18) Collini, E.; Ferrante, C.; Bozio,R. *J. Phys. Chem. B*, **2005**, *109*, 2.
19) Butcher, P.N.; Cotter, D. A. *The elements of Nonlinear Optics*, Cambridge University press, 1990.

20) Boyd, R. W. *Nonlinear Optics*, Academic Press Inc., 1992.

21) Goppert-Mayer, M. *Ann. Phys.* **1931**, *9*, 273.

22) Kaiser, W.; Garrett, C. G. B. *Phys. Rev. Lett.* **1961**, *7*, 229.

23) Macák, P. *Solvent and Vibrational Effects on Nonlinear Optical Properties*, Phd Dissertation, Royal institute of Technology, Stockholm, 2002.

24) Callis, P. R. *Ann. Rev. Phys. Chem.* **1997**, *48*, 271.

25) Dowley, M. W.; Eisenthal, K. B.; Peticolas, W. L. *J. Chem. Phys.***1967**, *47*, 1609.

26) Monson, P. R.; McClain, W. M. *J. Chem. Phys.* **1970**, *53*, 29.

27) Nguyen, V.-T.; Strnad, A. R.; Yafey, Y. *Phys. Rev. Lett.* **1971**, *26*, 1170.

28) Wunsch, L.; Metz, F.; Neusser, J. H.; Schlag, E. W. *J. Chem. Phys.* **1977**, *66*, 386.

29) Talukdar, B.; Chatterji, M. *Chem. Phys.* **1978**, *35*, 485.

30) Parthenopoulos, D. A.; Rentzepis, P. M. *J. App. Phys.* **1990**, *68*, 5814.

31) Denk, W.; Strickler, J. H.; Webb, W. W. *Science*, **1990**, *248*, 73.

32) Piston, D. W.; Masters, B. R.; Webb, W. W. *J. Microscopy*, **1995**, *178*, 20.

33) Xu, C.; Zipfel, W.; Shear, J. B.; Wiliams, R. W.; Webb, W. W. *Proc. Natl. Acad. Sci.* **1996**, *93*, 10763.

34) Shear, J. B.; Xu, C.; Webb, W. W. *Photochem. Photobiol.***1997**, *65*, 931.

35) Mascher-Brust, I.; Webb, W. W. *Biophys. J.* **1998,** *75*, 1669.

36) Huang, S.; Heikal, A.; A.; Webb, W. W. *Biophys. J.*, **2002**, *82*, 2811.

37) Williams, R. M.; Piston, D. W.; Webb, W. W. *FASEB J.* **1994**, *8*, 804.

38) Piston, D. W.; Kirby, M. S.; Heping, C.; Lederer, W. J.; Webb, W. W. *Appl. Opt.* **1994**, *33*, 662.

39) Xu, C.; Mertz, J.; Shear, J. B.; Webb, W. W. *Proc. SPIE,* **1996**, *2819* , 624.

40) Helchmen, F.; Denk, W. *Nat. Meth.* **2005**, *12*, 932.

41) Wang, K. H.; Majewska, A.; Schummers, J.; Farley, B.; Hu, C.; Sur, M.; Tonegawa, S. *Cell* **2006**, *126*, 389.

42) http://www.bris.ac.uk/Depts/Anatomy/research/neuro/OneTwoPhoton/TwoPhoton.htm

43) He, G. S.; Gvishi, R.; Prasad, P. N.; Reinhardt, B. A. *Opt. Commun.* **1995**, *117*, 133.

44) He, G. S.; Xu, G. C.; Prasad, P. N.; Reinhardt, B. A.; Bhatt, J. C.; Dillard, A. G. *Opt. Lett.* **1995**, *20*, 435.

45) He, G. S.; Bhawalkar, J. D.; Zhao, C.; Prasad, P. N. *Appl. Phys.. Lett.* **1995**, *67*, 2433.

46) Sahraoui, B.; Kityk, I. V.; Bielieninik, J.; Hudhomme, P.; Gorgues, A. *Opt. Mater.* **1999**, *13*, 349.

47) Charlot, M.; Izrad, N.; Mongin, O.; Reihl, D.; Blanchard-Desce, M. *Chem. Phys. Lett.* **2006**, *417*, 297.

48) Gao, Y.; Huong, N. Q.; Birman, J. L.; Potasek, M. J. *J. Appl. Phys.* **2004**, *96*, 4839.

49) Izrad, N.; Menard, C.; Reihl, D.; Doris, E.; Mioskowsi, C.; Anglaret, E. *Chem. Phys. Lett.* **2004**, *, 391*, 124.

50) Troles, J.; smektala, F.; Boudebs, G.; Monteil, A.; Bureau, B.; Lucas, J. *J. Optoelectr. Adv. Mater.* **2002**, *4*, 729.

51) Rao, N. D.; Kiran, P. P. *MCLC S&T B* **2001**, ***27***, 347.

52) Maciel, G. S.; Rakov, N.; de Araujo, C. B.; Lipovskii, A. A.; Taganstev, D. K. *Appl. Phys. Lett.* **2001**, ***79***, 584.

53) Morel, Y.; Irimina, A.; Najechalski, P.; Kervella, Y.; Olivier, S.; Baldeck, P. L.; Chantal, A. *J. Chem. Phys.* **2001**, *114*, 5391.

54) Wang, S. X.; Zhang, L. D.; Su, H.; Zhang, z. P.; Li, G. H.; Meng, G. W.; Zhang, J.; Wang, Y. W.; Fan, J. C.; Gao, T. *Phys. Lett. A* **2001**, *281*, 51.

55) Prasad, P. N.; He, G. S.; Joshi, M. P.; Swietkiewicz, J.; Manchala, G.; Lal, M.; Biswas, A.; Kim, K.-S. *MCLC S&T B* **1999**, *21*, 39.

56) Arnbjerg, J.; Banzo-Jiminez, A.; Paterson, M. J.; Nonell, S.; Borrell, J. I.; Christiansen, O.; Ogilby, P. R.

57) Karotki, A.; Khurana, M.; Lepock, J. R.; Wilson, B. C. *Proc. SPIE*, **2005**, *5969*, 1.

58) Spangler, C. W.; Starkey, J. R.; Meng, F.; Gong, A.; Drobozhiev, M.; Rebane, A.; Moss, B. *Proc. SPIE* **2005**, *5689*, 141.

59) Zhao, P. D.; Chen, P.; Tang, G. Q.; Zhang, G. L.; Chen, W. J. *Chem. Phys. Lett.* **2004**, *390*, 41.

60) Liu, J.; Zhao, Y.; Zhao, J.; Xia, A.; Lijin, J. *Proc. SPIE* **2002**, *4916*, 81.

61) Wallace, V. P.; Coleno, M. L.; Yomo, T.; Sun, C.; Tromberg, B. J. *Proc. SPIE* **2001**, *4262*, 118.

62) Koenig, K.; Riemann, I.; Fischer, P. *Proc. SPIE* **1999**, 3592, 43.

63) Fisher, W. G.; Partridge, W. P.; Dees C.; Wachter, E. A. *Photochem. Photobiol.* **1997**, *66*, 141.

64) Oh, D. H.; Stanley, R. J.; Lin, M.; Hoeffler, W. K.; Bozer, S. G.; Berns, M. W.; Bauer, E. A. *Photochem. Photobiol.* **1997**, *65*, 91.

65) Henderson, B. W.; Waldow, S. M.; Mang, T. S.; Potter, W.; Malone, P. B.; Dougherty, T. J. *Cancer Res.* **1985**, *45,* 572.

66) Nseyo, U. O.; Dougherty, T. J.; Boyle, D.; Potter, W.; Englander, L. S.; Huben, R. P.; Pontes, J. E. *J. Urol.* **1985**, *133*, 311.

67) Herrera-Ornelas, L.; Petrelli, N. J.; Mitteman, A.; Dougherty, T. J. Cancer, **1986**, *57*, 677.

68) Wei, P.; Tan, O. F.; Zhu, Y.; Duan, G. H. *Appl. Opt.* **2007**, *46*, 3694.

69) Belfield, K. D.; Ren, X.; Hagan, D. J.; Van Stryland, E. W.; Dubikovsky, V.; Miesak, E. J. *Polym. Mater. Sci. Engg.* **1999**, *81*, 79.

70) Leatherdale, C. A.; DeVoe, R. J.; *Proc. SPIE* **2003**, *5211*, 112.

71) Teh, W. H.; Durig, U.; Salis, G.; Harbers, R.; Drechsler, U.; Mahrt, R. F.; Smith, C. G.; Guntherodt, H.-J. *Appl. Phys. Lett.* **2004**, *84*, 4095.

72) Shoji, M.; Inoue, H. *Appl. Phys. Lett.* **2006**, *89*, 144101.

73) Kuebler, S. M.; mohanalingam, K.; Perry, J. W. *Proc. SPIE* **2001**, *4262*, 118.

74) Cumpston, B. H. et al, *Nature* **1999**, *398*, 51.

75) Kawata, S.; Sun, H.-B.; Tanaka, T.; Takada, K. *Nature* **2001**, *412*, 697.

76) Pond, S. J.; Tsutsumi, O.; Rumi, R.; Kwon, O.; Zojer, E.; Bredas, J.-L.; Marder, S. R.; Perry, J. W. *J. Am. Chem. Soc.* **2004**, *126*, 9291.

77) Fabbrni, G.; Riccó, R.; Menna, E.; Maggini, M.; Amendola, V.; Garbin, M.; Villano, M.; Meneghetti, M. *Phys. Chem. Chem. Phys.* **2007**, *9*, 616.

78) Righetto S.; Rondena, S.; Locatelli, D.; Roberto, D.; Tessore, F.; Ugo, R.; Quici, S.; Korystov, D.; Srdanov, V. I. *J. Mater. Chem.* **2006,** *16*, 1439.

79) Ahn, H. C.; Yang, S. K.; Kim, H. M.; Li, S.; Jeon, S.-J.; Cho, B. R. *Chem. Phys. Lett.* **2005**, *410*, 312.

80) Wang, Y.; Goodson, T. III *J. Phys. Chem. B* **2007**, *111*, 327.

81) Cotlet, M.; Goodwin, P. M.; Waldo, G. S.; Werner, J. H. *Chem. Phys. Chem.* **2006**, *7*, 250.

82) Dichtel, W. R.; Serin, J. M.; Carine, E.; Frechet, J. M. J.; Matuszewski, M.; Tang, L.-S.; Tymish, Y. O.; Prasad, P. N. *J. Am. Chem. Soc.* **2004**, *126*, 5380.

83) Schenke-Layland, K.; Riemann, I.; Damour, O.; Stock, U. A.; Konig, K. *Adv. Drug. Deliv. Rev.* **2006**, *58*, 878.

84) Konig, K.; Ehlers, A.; Stracke, F.; Riemann, I. *Skin. Pharmocol. Physiol.* **2006**, *19*, 78.

85) Riemann, I.; Schenke-Layland, K.; Ehlers, A.; Dimitrow, E.; Kaatz, M.; Elsner, P.; Matrin, S.; Konig, K. *Proc. SPIE*, **2006**, *6142*, 61420N-1.

86) Ehlers, A.; Riemann, I.; Stark, M.; Konig, K. *Microscopy Res. Tech.* **2007**, *70*, 154.

87) Lee, H.; Teng, S.; Chen, H.; Lo, W.; Yen, S.; Lin, T.; Chiou, L.; Jiang, C.; Dong, C. *Tissue Engg.* **2006**, *12*, 2835.

88) http://www.jenlab.de/prodermainspect.php

89) Kuzyk, M. G. *J. Nonlin. Opt. Phys. Mater.* **2004**, *3*, 461.

90) Moreno, J. P.; Kuzyk, M. G. *J. Chem. Phys.* **2005**, *123*, 194101.

91) Kuzyk, M. G. *Phys. Rev. Lett.* **2000**, *85*, 1218.

92) Chung, J.-S.; Kim, S.-K.; Lin, T.-C.; He, G. S.; Swatkiewicz, J.; Prasad, P. N. *J. Phys. Chem. B* **1999**, *103*, 10741.

93) Goodson, T. III *Acc. Chem. Res.* **2005**, *38*, 99.

94) Goodson, T. III; Varnavski, O.; Wang, Y. *Int. Rev. Phys. Chem.* **2004**, *23*, 109.

95) Wang, Y.; He, G. S.; Prasad, P. N.; Goodson, T. III *J. Am. Chem. Soc.* **2005**, *127*, 10128.

96) Zheng, S.; Leclercq, A.; Fu, J.; Beverina, L.; Padilha, L. A.; Zojer, E.; Schmidt, K.; Barlow, S.; Luo, J.; Jiang, S.-H.; Jen, A. K.-Y.; Yi, Y.; Shuai, Z.;

Van Stryland, E. W.; Hagan, D. J.; Bredas, J. L.; Marder, S. R. *Chem. Mater.* **2007**, *19*, 432.

97) Albota, M. *et al.* *Science* **1998**, *281*, 1653.

98) Lin, T.-C.; He, G. S.; Prasad, P. N.; Tan, L.-S. *J. Mater. Chem.* **2004**, *14*, 982.

99) Liu, Z.; Fang, Q.; Wang, D.; Cao, D.; Xue, G.; Yu, W.; Lei, H. *Chem. Eur. J.* **2003**, *9*, 574.

100) Mongin, O.; Porres, L.; Charlot, M.; Katan, C.; Blanchard-Desce, M. *Chem. Eur. J.* **2007**, *13*, 1481.

101) Slepkov, A. D.; Hegmann, F. A.; Tykwinski, R. R.; Marsden, J. A.; Spitler, E. L.; Miller, J. J.; Haley, M. M. *Opt. Lett.* **2006**, *31*, 3315.

102) Wang, Y.; He, G. S.; Prasad, P. N.; Goodson, T. III *J. Am. Chem. Soc.* **2005**, *127*, 10128.

103) Wang, Y.; Ranasinghe, M.; Goodson, T. III *J. Am. Chem. Soc.* **2003**, *125*, 9562.

104) Cho, B.-R.; Piao, M. J.; Son, K. H.; Lee, S. h.; Yoon, S. J.; Jeon, S.-J.; Cho, M. *Chem. Eur. J.* **2002**, *8*, 3907.

105) Chung, J.-S.; Kim, S.-K.; Lin, T.-C.; He, G. S.; Swatkiewicz, J.; Prasad, P. N. *J. Phys. Chem. B* **1999**, *103*, 10741.

Chapter 2

Experimental Techniques

In this chapter, experimental procedures for quantitatively measuring TPA behavior in materials and specialized spectroscopic tools for investigating excited state dynamics, fluorescence lifetimes and polarized fluorescence behavior are discussed. Commonly employed techniques such as UV-Vis spectroscopy, steady state fluorescence spectrophotometry and fluorescence quantum yield measurements are discussed in respective chapters wherever used.

2.1. Lasers: The Choice of Light Source for Studying NLO Processes

The word Laser is an acronym and it stands for **L**ight **A**mplification by **S**timulated **E**mission of **R**adiation. It is interesting to note that the first nonlinear optical phenomena reported was second harmonic generation (SHG) by Franken et al in 1961[1]. This discovery took place one year after Maiman demonstrated the first laser. Since then, lasers have developed into a multi-billion dollar industry. Hence, it is important to emphasize the need and importance of laser light sources for studying nonlinear optics. In order for the higher order (anharmonic) terms in material's oscillatory behavior to become significant, the electric field strength applied on the material should be somewhat comparable with the internal electric field that binds the electrons and ion cores together. This field[4] is typically on the order of 10^{10} V/m^2. This would correspond to an optical field whose intensity is ~ 10^{14} W/cm^2. This can be obtained using high intensity pulsed laser sources. However, the intensity required for the observation of NLO processes can be reduced significantly if there is good phase matching between the oscillations of individual dipoles so that the field radiated by each dipole interferes in a constructive fashion. Another method to reduce the intensity required to observe NLO processes by orders of magnitude is resonance enhancement, i.e. choosing the optical frequency such that it lies close to the resonant frequency of the dipoles. This not only serves to reduce the intensity required for the observation of the NLO process under question, but also provides fundamental structural information about the properties of matter that would otherwise be inaccessible through linear optics. This forms the basis of nonlinear optical spectroscopy.

As discussed above, laser light is used mainly because it can concentrate a large number of photons via pulsed operation. However, several other characteristics render lasers as a powerful tool for studying nonlinear optical phenomena.

2.1.1. Properties of Laser Light

2.1.1.1. Monochromaticity

This refers to very well defined wavelength of the laser radiation. This property arises because only an electromagnetic frequency corresponding to the gap between energy levels of the material involved in lasing can be amplified. Thus, the resonant cavity oscillates only when its frequency reaches the resonant frequency of the lasing levels.

2.1.1.2. Coherence

If we consider two points A and B on the same wavefront, then at time $t=0$, the difference between the phases is zero. If at any time $t>0$, the phase difference is still zero, then the electromagnetic wavefront is said to have perfect **spatial coherence**. In practice, however, there is partial spatial coherence, i.e. at a given time, point B lies within a narrow area with respect to point A[5].

If we consider the electric fields associated with a particular point P of a wavefront, then the wave is said to have perfect **temporal coherence** over time τ if the phase difference between the electric field values at times t and $t+\tau$ does not change. It should be noted that spatial and temporal coherence are independent of each other.

2.1.1.3. Directionality

This property is a direct consequence of the fact that only those waves that propagate parallel to the resonant cavity are amplified and sustained in the cavity.

However, in practice, laser radiation has a slight divergence, which is diffraction limited. This arises due to partial spatial coherence.

2.1.1.4. Short Time Duration

This refers to the fact that the individual pulses in a pulse train are separated by a very short period of time (picoseconds to femtoseconds). This can be achieved with a process called mode locking. The short pulse duration results in very high intensity radiation. The process of mode-locking will be described next.

2.2. Generation of Fast Pulses

Mode locking is a process by which ultrafast pulses (few femtoseconds to few picoseconds) can be generated[5]. Several frequencies reside within the resonant cavity. This is because the emission from the active medium does not correspond to one wavelength (line emission), but is spread over few wavelengths (band emission). Each wavelength residing within the cavity forms a standing wave as a result of bouncing back and forth within the cavity and corresponds to a “mode”. The extent to which different longitudinal “modes” are “locked” determines the pulse duration of the laser. Locking refers to constant phase difference between different modes. As an example, 2n+1 modes that oscillating with the same amplitude E_0 (Figure 2.1) are considered. Assuming the phases ϕ_l of the modes are locked according to the relation:

$$\phi_l - \phi_{l-1} = \phi \qquad (2.1)$$

Where ϕ is constant. The total electric field of the electromagnetic wave at a given point in the output beam can be written as[5]:

$$E(t) = \sum_{-n}^{n} {}_l E_0 \exp\{i[(\omega_0 - l\Delta\omega)t + l\phi]\} \qquad (2.2)$$

Where ω_0 is the frequency of the central mode and $\Delta\omega$ is the frequency difference.

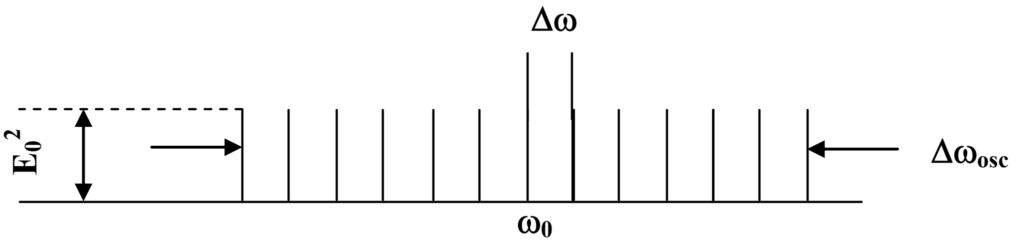

Figure 2.1. Modes in a resonant cavity with equal amplitudes[5].

Considering the phase of the central mode to be zero (for reference), equation 2.2 can be simplified as:

$$E(t) = A(t)\exp\{i\omega t\} \tag{2.3}$$

Where
$$A(t) = \sum_{-n}^{n} {}_l E_0 \exp\{il[(\omega_0 - l\Delta\omega)t + \phi]\} \tag{2.4}$$

If we now change to a new time reference t′ such that Δω t′ = Δω t + ϕ, then

$$A(t') = \sum_{-n}^{n} {}_l E_0 \exp\{il\Delta\omega)t'\} \tag{2.5}$$

Since l varies from –n to n, the summation at the right side of equation 2.5 becomes a geometric progression with a ratio equal to $\exp\{il\Delta\omega)t'\}$. Hence, this sum can be expressed as[5]:

$$A(t') = E_0 \frac{\sin[(2n+1)\Delta\omega t'/2]}{\sin[\Delta\omega t'/2]} \tag{2.6}$$

In order to understand the physical significance of this equation, the value of $A(t')^2$ (which represents the amplitude of the beam intensity) versus t′ has been plotted. In order to demonstrate the concept, arbitrary values of E_0=100, 2n+1=7, Δω=2 have been assumed. The plot is shown in Figure 2.2.

It can be clearly observed that as a result of phase locking condition, the oscillating modes produce evenly spaced pulses. The distance between maxima is ~π. Thus, two pulses are separated in time by:

$$\tau_p = 2\pi / \Delta\omega \tag{2.7}$$

However, for t′>0, the next maximum occurs at t′= (2n+1) Δωt′/2= π. Hence, the pulse duration $\Delta\tau_p = 1/\Delta\nu_{osc} = 2\pi / [(2n+1)\Delta\omega]$. Since Δω=2π/Δν= πc/L,

$$\Delta\tau_p = 2L/c \tag{2.8}$$

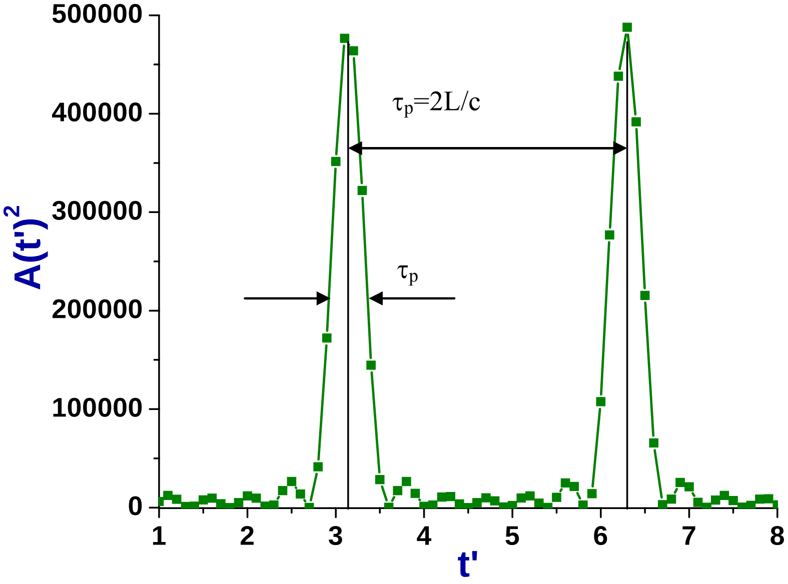

Figure 2.2. Variation of beam intensity with time for a cavity containing seven modes.

Hence, the pulse duration of the laser is the time taken to complete one round trip around the cavity. Hence, for a pulse duration of ~6.7 ps, the cavity length required is 1mm. Thus, in order to achieve a pulse duration of 30 fs (such as those obtained with modern Ti: Sapphire lasers), the cavity length required is 4.5µm. So how does one generate femtosecond pulses?

It should be noted that in the example illustrated above, an unrealistic case where all modes oscillate with the same amplitude has been considered. A set of modes defines a pulse, and in practice, the pulse has a distribution of amplitudes. An example is a Gaussian distribution of amplitudes, shown in Figure 2.3. In this case, the frequency bandwidth is defined by the full width at half maximum (FWHM). This quantity can be measured experimentally.

It is known that the Fourier transform of a Gaussian function is another Gaussian function. The general time and frequency Fourier transforms of a Gaussian pulse can be expressed as:

$$E(t) = \frac{1}{2\pi} \int_{-\infty}^{\infty} E(\omega) e^{-i\omega t} d\omega \tag{2.9}$$

And

$$E(\omega) = \frac{1}{2\pi} \int_{-\infty}^{\infty} E(t) e^{i\omega t} dt \tag{2.10}$$

Considering this, the amplitude $A(t)^2$ takes the form:

$$A(t)^2 \alpha \exp\left[-\left(\frac{2t}{\Delta \tau_p} \right)^2 \ln 2 \right] \tag{2.11}$$

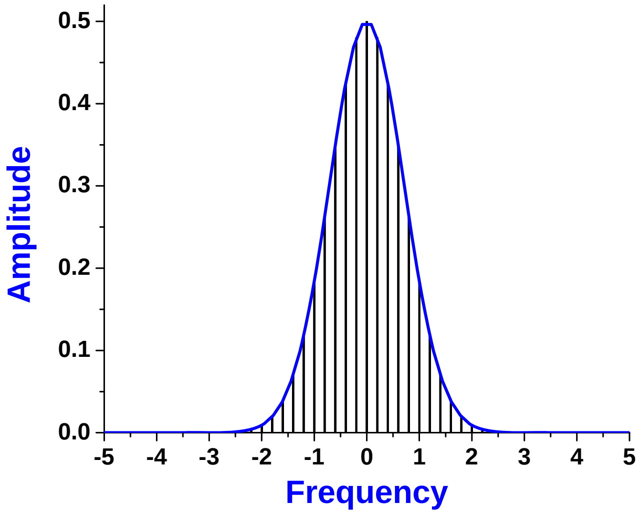

Figure 2.3. A Gaussian Pulse.

Since $\Delta \tau_p$ is related to $\Delta \nu_{osc}$, it can be realized that the electric field amplitude is proportional to the Fourier Transform of the spectral amplitude. It can be shown that for a

Gaussian pulse, $\Delta\tau_p$ (FWHM) (which can be easily measured using a spectrometer) is given by:

$$\Delta\tau_p = 0.441 / \Delta\nu_{osc} \tag{2.12}$$

In other words, $\Delta\tau_p \Delta\nu_{osc}$= constant. Such a pulse is called a Fourier Transform limited pulse or simply transform limited pulse. Further, $\Delta\nu_{osc}$ can be calculated if the bandwidth in nm is known using the relation:

$$\Delta\nu_{osc} = \frac{\Delta\lambda c}{\lambda_0^{\;2}} \tag{2.13}$$

Where λ_0 is the central wavelength at which amplitude is maximum.

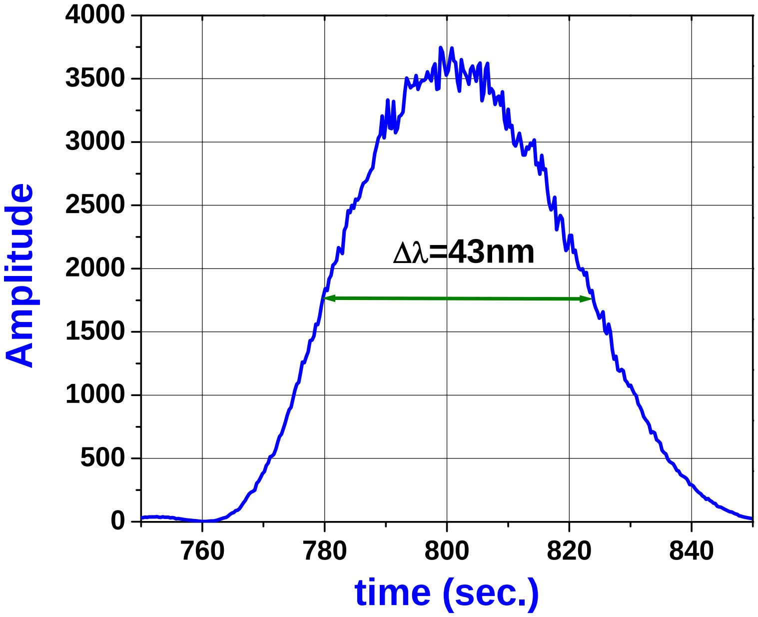

Figure 2.4. Laser spectrum acquired using Ocean Optics® Spectrometer.

It can be observed from equations 2.12 and 2.13 that a spectral bandwidth ($\Delta\lambda$) of 50 nm corresponds to a pulse duration ($\Delta\tau_p$) of 19 fs. A typical Gaussian pulse for the Kapteyn Murnane Ti: Sapphire Laser in our lab recorded using an Ocean Optics® is shown in Figure 2.4 . Mode locking is physically achieved in a laser by Kerr lens, and this principle is discussed next.

When an optical wave propagates through a medium in the presence of a d.c field, the cubic polarization ($\chi^{(3)}$) leads to a change in refractive index that exhibits quadratic variation with respect to the d.c field. This is called the quadratic electro-optic effect or Kerr effect. This phenomenon was discovered by John Kerr, a Scottish physicist.

The refractive index in the presence of a material capable of exhibiting large third order NLO response is given by:

$$n = n_0 + n_2 \times I \tag{2.14}$$

$$n_2 = \frac{12\pi^2}{n_0^2}\chi^{(3)} \tag{2.15}$$

Optical Kerr effect is generated when the electric filed is generated by light itself, instead of a d.c field. This causes the refractive index of the medium to vary quadratically with respect to local intensity of incident light. This effect is utilized in Kerr lens mode-locking (KLM), shown in Figure 2.5, which has been employed in one of the laser systems (Kapteyn Murnane or KM) used for several investigations described in this dissertation. With this mechanism, it is possible to obtain pulses as fast as ~20 femtoseconds.

KLM is based on the principle of self focusing in a material due to varying refractive index. When a beam with nonuniform intensity distribution in transverse direction propagates through a medium with positive n_2, intensity dependent self focusing of the beam takes place. The Kerr medium acts as a positive lens. The increase of focusing stops when the diameter of the beam is small enough and the linear diffraction is large enough to balance the Kerr effect. The KM laser consists of a NLO medium such as a Ti: Sapphire crystal which is pumped by 532nm continuous wave (CW) radiation. When a seed beam propagates through the crystal, Kerr lensing occurs for the high intensity (mode locked) light. In this way, CW radiation can be suppressed because losses from CW beam are high. Under normal operating conditions of the laser, the cavity consists of several longitudinal modes described earlier. Forcing all the modes to have equal phase values (mode locking), all the waves at different frequencies will constructively interfere at one point. This results in a very intense and very short pulse. Thus, the mode locking that occurs due to Kerr effect in a NLO medium as a result of the beam itself is called Kerr lens mode locking.

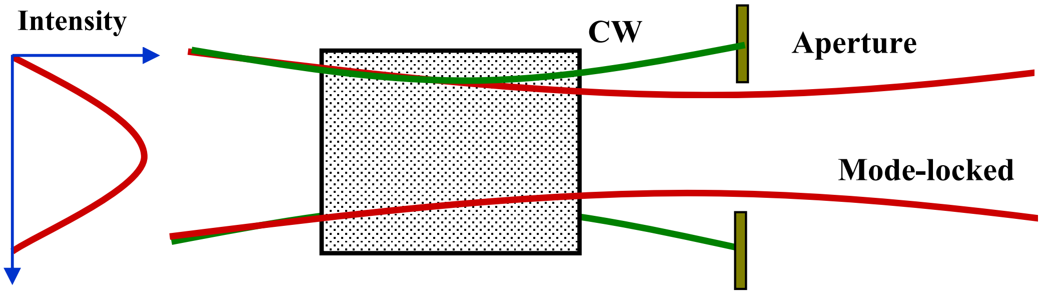

Figure 2.5. Kerr Lens mode-locking.

Besides providing high intensity of radiation, **femtosecond pulses** are also critical for certain time resolved experimentation methods such as Transient Absorption Spectroscopy and Fluorescence Upconversion, which are discussed in the following sections. Several materials investigated in this dissertation show different excited state dynamics, and the dynamics start with the "vertical" or Franck-Condon state. This state is achieved instantaneously after excitation. The only means of observation of this state is by using femtosecond pulses. In order to determine the excited state absorption spectra, it is critical that the measurements be performed prior to any excited state dynamics. Otherwise, contributions from other states will be observed. Hence, using femtosecond pulses, one can take a "snapshot" of the molecule as soon as it is excited, which enables us to calculate certain excited state characteristics. These aspects will be made clearer in the subsequent chapters which address specific concerns regarding TPA behavior of organic materials that require the investigation of excited state behavior.

2.3. Experimental Methods for Determination of TPA Cross Sections

It is important to realize that several methods exist for measuring and quantifying TPA behavior of materials. Depending on the nature of material, ease of performing the experiment and other spectroscopic considerations, one method might be preferred over the other.

2.3.1. Two-Photon Excited Fluorescence Method

Two-Photon Excited Fluorescence[6] (TPEF) method involves monitoring the fluorescence intensity as a function of incident intensity. This method is as old as the discovery of TPA itself. Kaiser and Garrett[7] reported their TPA results by monitoring the fluorescence of a $CaF_2:Eu^{2+}$ crystal as a function of excitation with a laser source. This is the method for determining the TPA cross sections of organic fluorophores throughout this dissertation. A schematic of the optical set-up used in our lab for this purpose is shown in Figure 2.6.

The laser source is either a Ti: Sapphire oscillator (Kapteyn Murnane) described earlier, which can be tuned from 760nm-830nm or an Optical Parametric Amplifier (OPA 800C, Spectra Physics, to be described later) that can be tuned from 300nm-3µm. The input intensity can be regulated using a neutral density (ND) filter designed for femtosecond pulses. Other weaker filters might heat up and develop spots on their coatings. Polarizers used for varying input intensity might result in white light generation which is found to give spurious signals. Prior to the ND filter, the beam is passed through an iris to ensure a uniform and circular beam. In case of the Ti: Sapphire oscillator, the beam is focused on the sample cell, which contains a solution of the molecule to be investigated. If OPA is used as the source, the beam is passed through another smaller pinhole prior to impinging the sample cell instead of focusing. The difference in delivering the beam to the sample cell arises due to three orders of magnitude difference in pulse energies between the oscillator and OPA. It is important to deliver the beam closer to the edge of the sample cell towards the direction of collection rather than center. This reduces the path length that the fluorescence has to travel prior to exiting the cell and being collected, thereby minimizing self absorption of fluorescence. The resulting TPEF is collected in a direction perpendicular with respect to the incident beam in order to avoid noise due to excitation light itself. The fluorescence is collected by a collecting lens (planoconvex, 1" diameter, 1" focal length) which focuses the fluorescence to the entrance of a monochromator (Cornerstone 130M, Oriel Instruments).

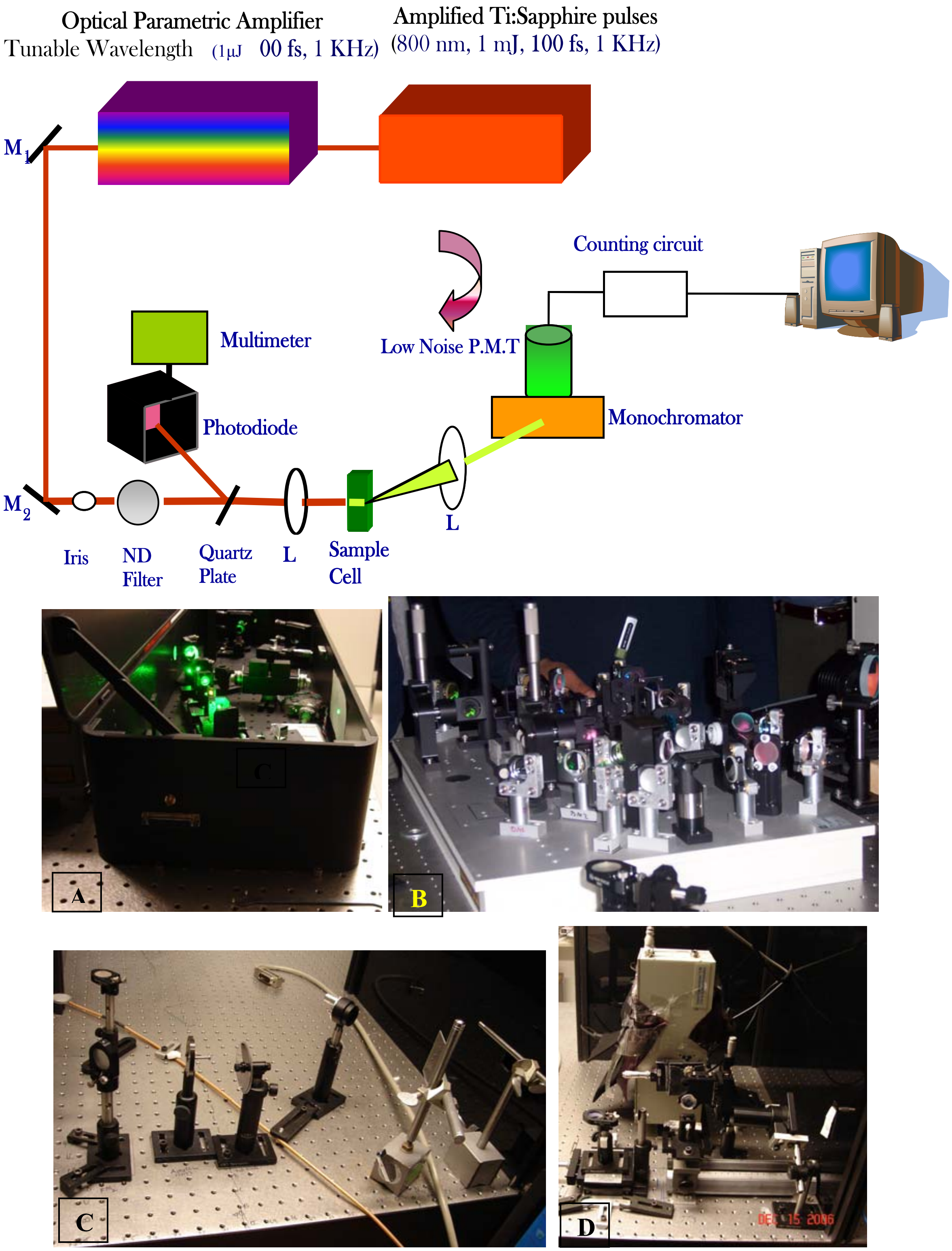

Figure 2.6. TPEF set-up used in our lab. Digital images of the set-up used in our lab are also shown. A) KM laser. B) OPA. C) Optics for guiding laser light to the sample cell, and D) focusing and collection optics.

The motion of the gratings on the monochromator is controlled by a motor. The exit slit of the monochromator is coupled with a housing containing a photomultiplier tube (PMT) (R7518P, Hamamatsu). A counting circuit (M8485 counting board, C3866 counting circuit, Hamamatsu) assembly which is interfaced with a computer converts the photocurrent from the PMT into arbitrary number of counts. In this manner, the TPEF intensity can be quantified. As incident intensity increases, the counts resulting from TPEF also increases. If a logarithmic plot with TPEF intensity as abscissa and input intensity as the ordinate is a straight line with a slope of 2, this ensures a two-photon excited process. The details of calculations involved in the computation of TPA cross section (δ) are included in chapter III. Typically, in TPEF method a reference with known TPA cross section values over a series of wavelengths is used. However, modifications of this method that eliminate the need for the reference have also been reported. Typically, Coumarin 307, Rhodamine B and Fluorescein are used as standards over 700-950 nm range, [p-bis (o-methyl-styryl) benzene] is typically used as the reference below 700nm and certain porphyrin dyes are used as standards above 1000nm. The advantages of TPEF are it is relatively easy to perform and there are no spurious effects due to excited state absorption, thermal lensing etc. that are associated with some of the other techniques. The disadvantage is that the material has to exhibit fluorescence. Hence, this method cannot be applied to certain inorganic, metallic and organometallic materials.

2.3.2. Nonlinear Transmission (NLT)

This method deals with measuring the relationship between input and output intensity after absorption by the material under investigation. A deviation from linearity indicates nonlinear absorption or transmission. A schematic diagram for the measurement of NLT[8] is shown in Figure 2.7 .

Theoretical calculations allow quantifying the relationship between input and output intensities, thereby enabling the calculation of TPA cross section or even higher order multiphoton cross sections. The transmissivity of the nonlinear medium is given by[6]:

$$T(z) = I(z)/I(0) = \frac{e^{-\alpha z}}{1+\beta z I(0)} = \frac{T_0}{1+\beta z I(0)} = T_0 T_i \qquad (2.16)$$

Here, T_0 is the linear transmissivity of the material, and it is independent of I(0).

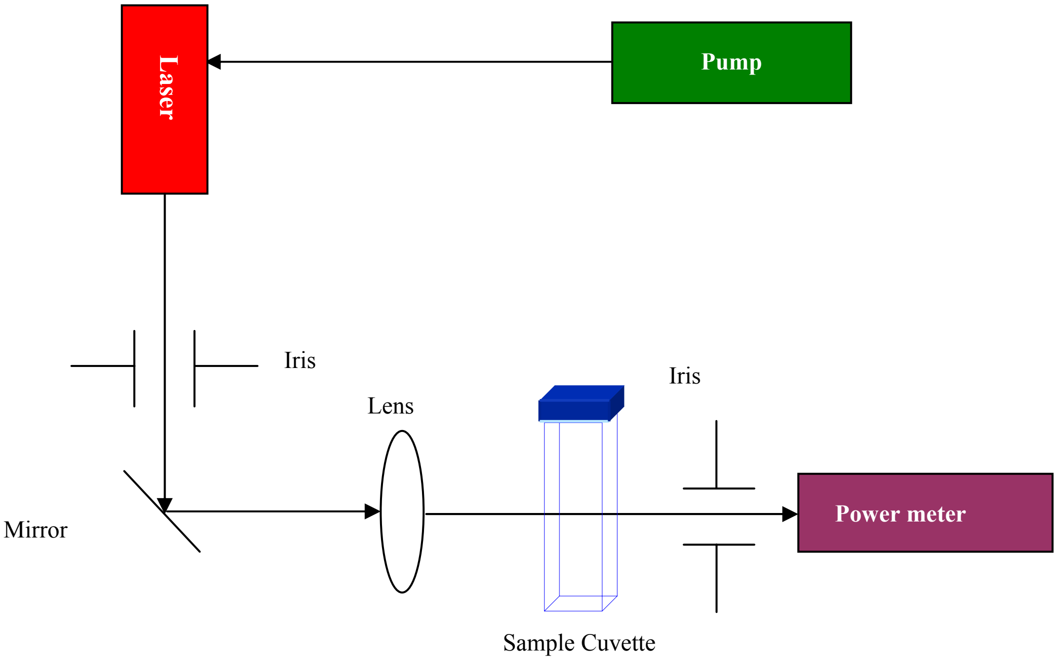

Figure 2.7. Optical set-up for nonlinear transmission measurements[8].

Thus, this method allows the experimental determination of β. For a Gaussian intensity distribution of the beam and assuming that the beam is focused near the sample, the nonlinear transmissivity T_i for a length L of the sample is given by:

$$T_i = \frac{\ln(1+\beta I_0 L)}{\beta I_0 L} \tag{2.17}$$

A shortcoming of this technique is that it cannot distinguish between sequential, stepwise absorption through real states versus direct, simultaneous absorption into one state. Also, thermal lensing is another issue associated with this technique. Furthermore, high concentration of the material is required in order to obtain high signal to noise ratio.

2.3.3. Z-Scan

The Z-scan technique, developed by Sheik-Bahae et al[9, 10], offers a useful way to probe both the non-linear refractive index and the non-linear absorption coefficient β of a sample. In the Z-scan experiment[11], a laser beam is focused to a minimum waist at the focal point along the propagation direction (z-axis) of this beam. By moving the sample along the z-axis, the light intensity in the sample is varied. When the sample is placed away from the focal point, no non-linear processes can be observed in the sample because the light intensity is too low. The light intensity within the sample is increased when the sample is moved toward the focus, producing non-linear processes. The consecutive recording of the relative power transmitted through the sample as a function of the sample position provides important information about the real part (change in refractive index) and the imaginary part (the intensity-dependent absorption coefficient) of $\chi^{(3)}$. The experimental set-up is shown in Figure 2.8. A drawback of this technique is contribution from excited state absorption, which causes the δ to appear enhanced, especially when using nanosecond pulses. Thermal lensing is another issue.

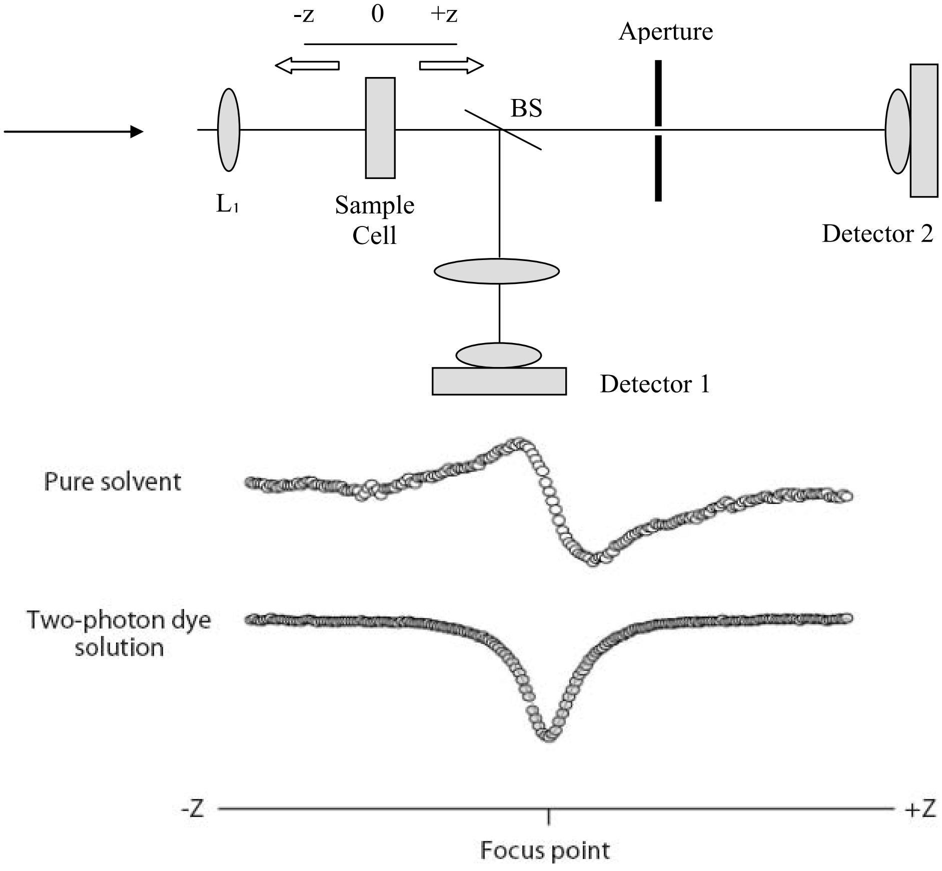

Figure 2.8. Z-scan set up and typical profile obtained from solvent and sample[11].

These are the most commonly used techniques for measuring TPA cross sections. Another technique based on laser ablation has also been reported in the literature[12]. This technique could also be extended to thin films of polymers and small organic molecules. Briefly, the laser source consists of amplified Ti: Sapphire pulses at 800nm, 150fs and 1 kHz. The output of the laser is delivered to a galvanometer scanner which is digitally controlled. A variable ND filter is used to change the input intensity and a high scanning speed of 43mm/sec. is used to scan the samples. A telecentric lens is employed to focus the beam on the film surface. The final diameter of the laser beam upon contact with the film is ~6mm. Based on intensity required to initiate ablation of the film at different concentrations of the dye, its TPA cross section is calculated.

2.3.4. Non-Degenerate Pump Probe Method[13]

In this technique, an amplified femtosecond laser system pumps two widely tunable optical parametric amplifiers (OPAs). A strong (high irradiance) pump beam from OPA1 induces the nonlinearity in the sample and a weak probe beam from OPA2 monitors that nonlinearity. To be able to measure a wide spectral range of the 2PA spectrum, the probe beam used is a very broadband white-light continuum (WLC) pulse (400 -1700 nm) produced by focusing 1-2 μJ into a 2.5 mm thick piece of calcium fluoride. The two pulses, pump and probe, are overlapped in both space and time on the sample under investigation. As a result, one photon from the pump and one photon from the probe (within the broadband WLC) are simultaneously absorbed. By monitoring the transmission of the broadband WLC probe using a dual fiber input spectrometer that is coupled to a dual diode array, it is possible to ascertain the strength of the 2PA versus wavelength or equivalently the 2PA spectrum.

The pump wavelength is set to 1200 nm when acquiring the nonlinear absorption spectra to avoid any degenerate 2PA of the pump itself. This is done for the purpose of avoiding any spurious excited state absorption following 2PA of the pump beam itself. The non-degenerate will exhibit larger 2PA cross-sections than those found by degenerate excitation due to pre-resonance enhancement effects[14]. The magnitude of this enhancement is determined by the photon energies of the pump and probe and the transition energies of the one- and two-photon allowed states. Using equation (2) in reference 14, the transition energies of the lowest lying one-photon allowed states as determined from the linear absorption spectra, and the energies of the higher lying two-photon allowed states extracted from the nonlinear absorption spectra, an enhancement factor due to non-degenerate excitation is determined. Although this factor does show some dispersion over a range of wavelengths, the effect is small and the factor is found to be approximately 2.0. Therefore, non-degenerate excitation will exhibit a two-fold increase in the strength of 2PA compared to degenerate excitation. This should be taken into account while drawing comparisons from various techniques.

2.4. Techniques for Investigating Excited State and Fluorescence Dynamics

2.4.1. Fluorescence Lifetime Measurements

Time correlated single photon counting (TCSPC) is a technique used to determine fluorescence lifetimes of a fluorescent organic chromophore. The technique involves the excitation of the sample with pulses from a laser and the detection system monitors the time difference between the excitation pulse and the first fluorescence photon from the sample. The prerequisite for this measurement is that only one photon is observed for a large number of excitation pulses. In other words, an extremely low count rate must be ensured such that the system operates in single photon counting mode. In such a situation, the statistics follow Poisson distribution and a true time-resolved emission profile is obtained.

The optical signal generates an electrical START pulse, which is then routed into a photodiode to START the input of time to amplitude converter (TAC) to initialize the charging operation. Excitation by the optical pulse gives rise to emission of photons. These photons are then detected by a photomultiplier tube (PMT) at right angle to the direction of excitation to generate an electrical STOP pulse. The STOP pulse is also routed to the TAC. On receiving the STOP signal, TAC stops its charging operation and generates an electrical output, having an amplitude proportional to the time difference (Δt) between the START and STOP pulses reaching the TAC. The TAC output pulse is then fed to the input of a multi channel analyzer (MCA) through an analogue to digital converter (ADC). The ADC generates a numerical value corresponding to the TAC output pulse and thus selects an appropriate channel of the MCA and the count is added to the channel. The above cycle (from excitation to data storage) is repeated for a large number of times and the end result is a result histogram of the counts versus the number of channels on the MCA is generated. This represents the fluorescence decay profile.

Only when the collection rate of emission photons by the STOP pulse is very low, as illustrated by statistical treatment [15, 16], true emission decay is represented. The emission decay thus observed has to be de-convoluted with the instrument response to get the actual lifetime. The instrument response function (IRF) is measured using a scatterer in place of the sample. Typically, the chromophore solution is replaced with pure solvent for this purpose. The width of IRF function depends on the excitation source and detection systems used. All the measurements in case of laser excitation are performed by keeping the excitation polarizer at vertical position and the emission polarizer at magic angle (54.7°) with respect to the excitation polarizer. The fluorescence collected at magic angle with respect to the excitation polarization is free from any anisotropy components and represents the actual total fluorescence intensity decay. Appropriate cut-off filters are placed before the focusing lens to remove any scattered excitation light entering the monochromator from the sample cell. The obtained decay curves are fit to either a single exponential or multi exponential functions as described by Equation 2.18. Iterative reconvolution method is used to determine the pre-exponential factors and lifetimes. Non-linear least-squares method is used for obtaining the abovementioned parameters. Levenberg-Marquardt algorithm (also called Marquardt method)[17, 18] is adopted for the non-linear analysis.

$$I(t)=\sum_{i=1}^{n}\alpha_i e^{-t/\tau_i} \tag{2.18}$$

where τ_i and α_i are the emission lifetimes and pre-exponential factor of the ith component, respectively of the sample. The quality of the fit was judged by the reduced χ^2 value, which should be close to 1 and the random distribution of weighted residuals.

For the set-up used in our lab (Figure 2.9), the laser used is the Kapteyn Murnane Ti: Sapphire oscillator. The 800 nm output is frequency doubled using a BBO crystal. The resulting second harmonic signal at 400 nm is passed through a cut-off filter in order to remove 800nm fundamental beam. A beam splitter directs a small portion of the beam into a photodiode which serves as the “start pulse”. The waveplate **P** ensures horizontal polarization of excitation beam. The 400nm radiation is focused on the sample cell using a planoconvex lens. The resulting fluorescence photons are collected in a perpendicular direction with respect to excitation in order to avoid noise due to 400nm radiation. A collection lens directs the beam into the entrance of a monochromator in order to separate fluorescence from excitation. The fluorescence is then detected by the “stop” PMT, which is connected to a photon counting module that controls the multichannel analyzer (MCA) and other electronic modules of the experiment. Using software (Fluorofit®), the decay profile obtained can be fit with exponentials and hence the fluorescence lifetime of the chromophore can be obtained.

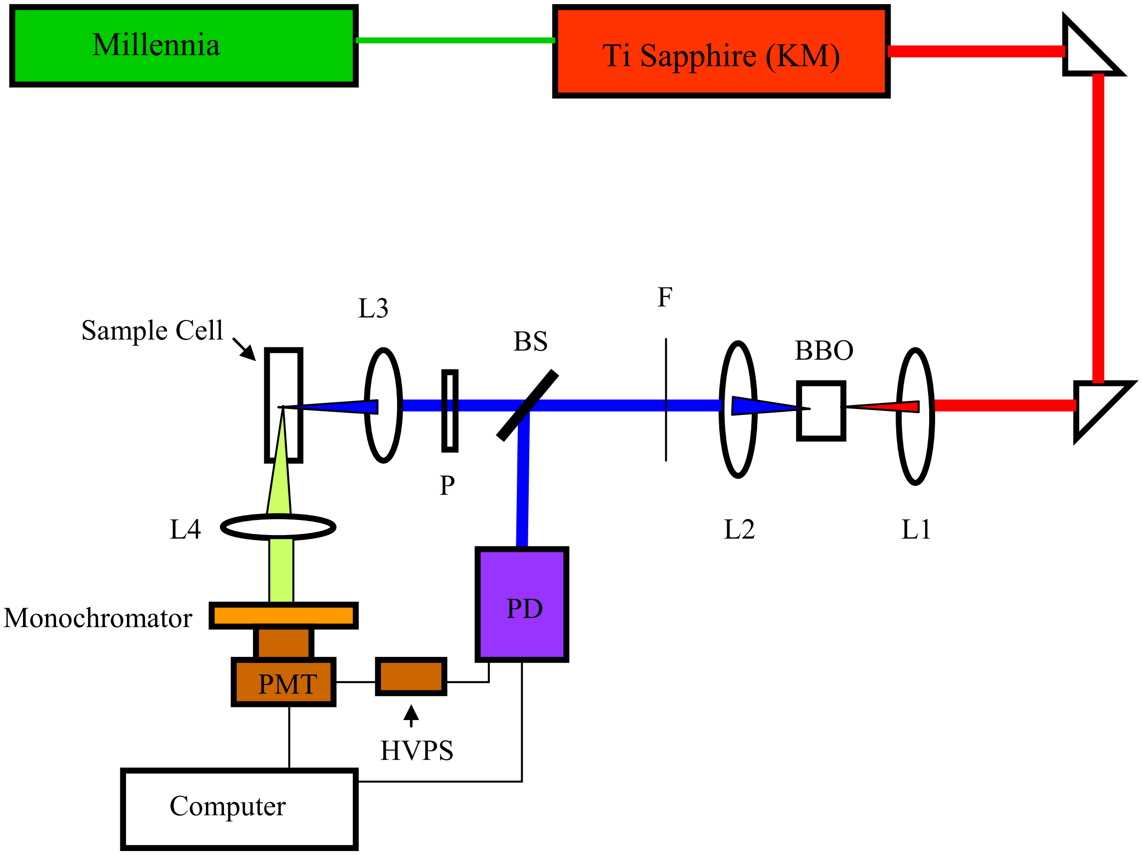

Figure 2.9. Time correlated single photon counting (TCSPC) set-up used in our lab.

2.4.2. Ultrafast Transient Absorption Spectroscopy

Transient Absorption[19] (TA) is a pump probe technique for investigating the excited state behavior of molecules. Essentially, it consists of exciting (pumping) the molecule via single photon excitation at a wavelength lower than the absorption maximum of the material. After excitation, the molecule is subjected to interaction with a tightly focused white light continuum (WLC) probe. By monitoring

a) Which wavelength(s) of the WLC continuum (probe) does the molecule interact with and

b) How does this interaction change with time,

It is possible to monitor the excited state dynamics of the molecule. This is achieved by monitoring the change in absorbance of the probe beam before and after the application of the pump beam. This is performed at each wavelength of the probe beam as a function of time. Hence, one obtains data that can be represented in three dimensions, namely changes in absorbance, wavelength and time. A schematic illustrating the principle of TA spectroscopy is shown in Figure 2.10.

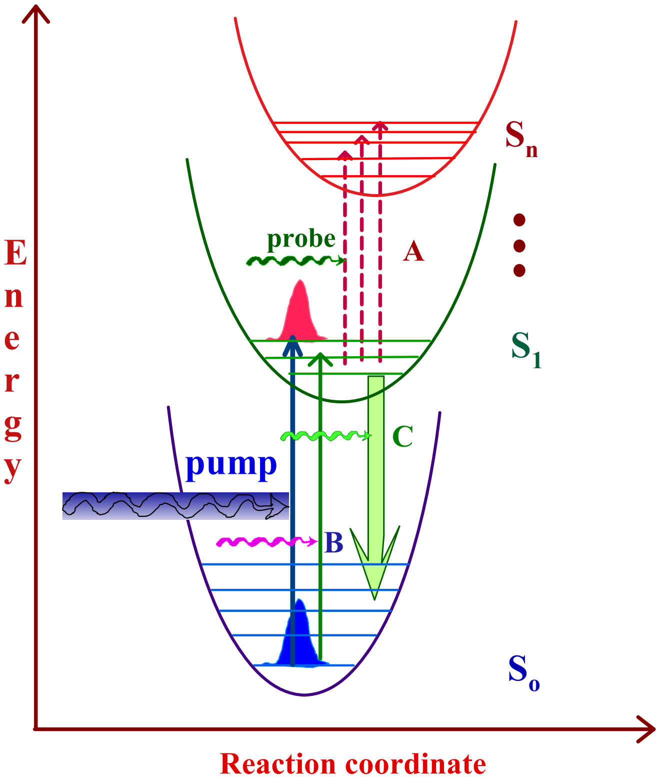

Figure 2.10. Principle behind transient absorption spectroscopy.

Assuming the material under investigation does not absorb any probe wavelength in the absence of pump beam, the absorbance is zero. Assuming that upon application of pump beam, the molecule absorbs 20 combined photons at various wavelengths from the probe beam out of 100 photons (the numbers are arbitrary for the sake of discussion), the change in absorbance is positive. Clearly, the photons absorbed by the molecule are utilized to promote it from its first excited state to higher excited states. Thus, a positive change in absorbance (ΔA) constitutes excited state absorption (ESA).

Next, a case where the molecule shows some absorption at some of the probe wavelengths prior to pumping is considered. Assuming that the molecule absorbs 50 probe photons prior to pumping, this corresponds to steady state absorption from ground state to first excited state. Upon application of pump, the ground state population will be depleted. As a result, fewer probe photons will be absorbed. In this case, the change in absorbance ΔA is negative. This scenario corresponds to bleaching.

As a final scenario, a case when there is no absorption of probe prior to pumping is considered. Upon pumping, the molecule reaches its first excited state. It is possible that the interaction of the excited state results in stimulated emission. Hence, the probe photons are not being absorbed, but “emitted” by the molecule. Thus, stimulated emission is another example of a signal caused by negative ΔA.

These three cases represent the most frequently encountered signals in transient absorption measurements. By monitoring the kinetics of these signals, the excited state dynamics of a molecule can be resolved. It is possible to monitor singlet→triplet transitions, bleach recovery of the ground state, vibrational cooling, thermalization and several other important transitions using transient absorption spectroscopy. It is important to state that the material need not be fluorescent in order to be investigated using TA measurements. A sample three dimensional plot obtained from the software showing the change in absorbance at various wavelengths as a function of time is shown in Figure 2.11 . The results were obtained from a tri-branched system (discussed in Chapter IV). Also shown in Figure 2.11 are the kinetics at two selected wavelengths; 630 nm and 520 nm. The signal at 630 nm decays with time and corresponds to decay of initial excited state population. The signal at 520 nm shows concomitant growth with time and is a new state (discussed in Chapter IV). The entire process takes place between 0 fs to 3 ps.

Hence, using TA measurements, one can monitor the evolution of new states over ultrafast timescales.

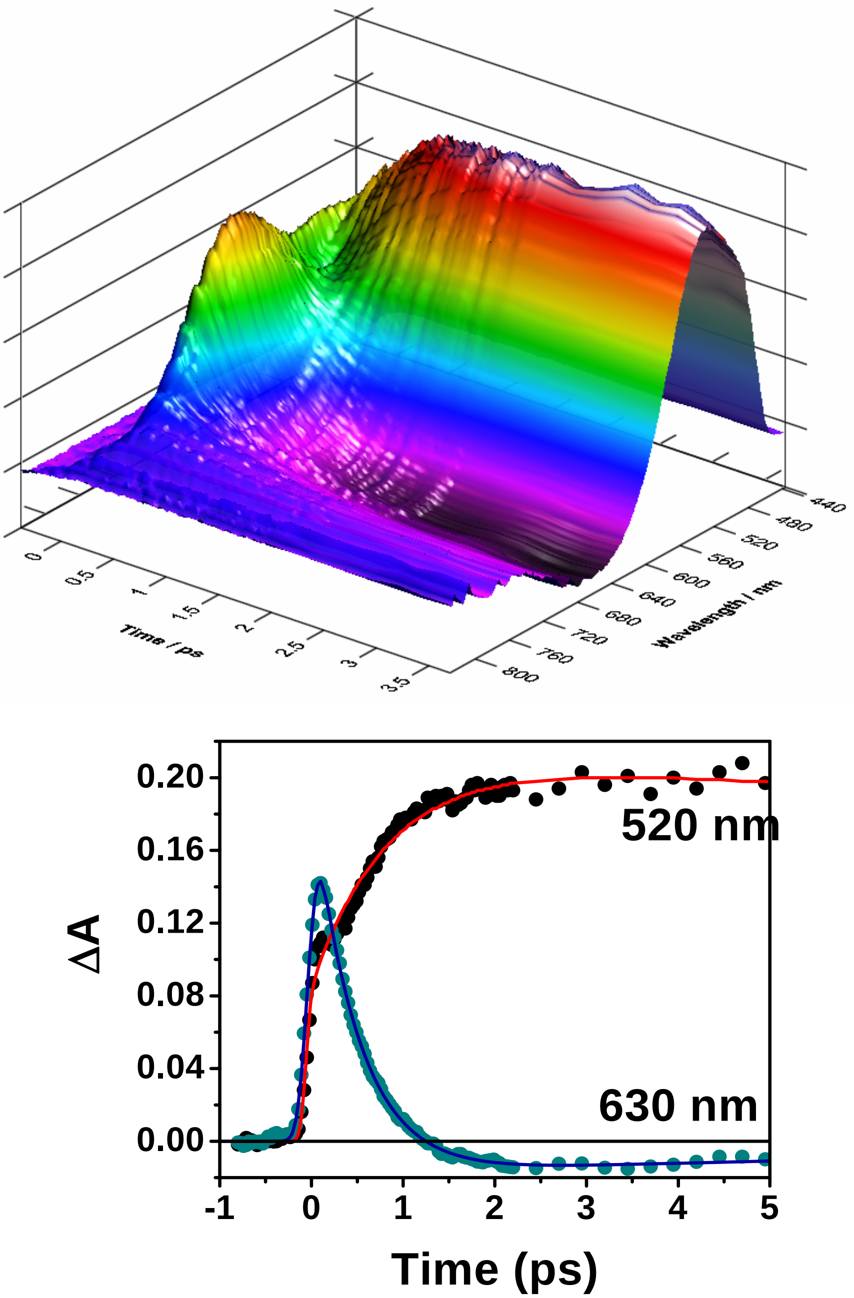

Figure 2.11. Sample results from transient absorption measurements.

In our lab, the light source for TA measurements is an Optical Parametric Amplifier (OPA-800C, Spectra Physics). A 532 nm continuous wave (CW) laser (Millennia, Spectra-Physics) pumps a Ti: Sapphire system (Tsunami, Spectra Physics) to generate seed pulses at 800nm, ~20 fs and ~93MHz. The pulse energy is on the order of nanoJoules. The seed pulses are amplified inside a regenerative amplifier (Spitfire Pro, Spectra Physics) in three stages. The first stage is pulse stretching. Here, using a retroreflecting mirror assembly, the longer (redder) spectral end of the pulse is made to travel faster than the shorter end (bluer). This results in a negative Group Velocity Dispersion (GVD) and hence, the pulse is stretched temporally.

The next stage is regenerative amplification. This refers to the recirculation and subsequent amplification of low energy seed pulses. This is an effective method for producing pulses with high peak power. Using a Pockels Cell (PC), good quality pulses from the stretcher are selected for amplification. The seed pulse is focused onto a Ti: Sapphire crystal, which is pumped by a pulsed 532 nm Nd: YLF laser (Empower, Spectra Physics). After a single pass through the crystal, the pulse energy of the seed is amplified by a factor of 3 to 4, but there is plenty of gain left in the amplifier for more passes because the gain obtained from one pass in not sufficient to eliminate the population inversion of the gain medium (Ti: Sapphire crystal). Typically, a pulse is passed about 20 times before the pulse energy level is high enough to eliminate the population inversion. The high energy per pulse is achieved by reducing the frequency from MHZ to kHz, which enables concentration of the energy into fewer pulses. The stage at which the amplified pulses are ready for the next step (pulse compression) is determined by another Pockels Cell.

The final step is pulse compression. The purpose of this step is to reduce the pulse duration back to ~100 fs. Compression is essentially the “reverse” of a pulse stretching. Hence, using retroreflectors, the shorter (bluer) end of the pulse is made to travel faster than the longer end (redder). This results in a positive Group Velocity Dispersion (GVD) and hence, the pulse is compressed temporally. The resulting output from the amplifier is at 800nm, 1 kHz, and ~100 fs. The average power is ca. 1W. The pulse energy is on the order of microJoules. Such high energy pulses are necessary to pump the Optical Parametric Amplifier (OPA) assembly.

The OPA derives its gain from a nonlinear frequency conversion process, which could be either an upconversion or downconversion process. The amplified pulses from Spitfire are split using a beamsplitter (BS) so that ~2mW power is directed for white light generation using a sapphire plate. The remainder is further divided into two unequal portions using another beamsplitter. One of them (15%) overlaps with the white light spatially and temporally at a BBO crystal. The temporal overlap is controlled by a delay line. This is called pre-amplification and is confirmed by small amount of Optical Parametric Generation (OPG) which manifests itself as a green glow on a white business card observed after the BBO crystal at which the 800nm and the white light beams overlap. The resulting output from the crystal consists of a signal and an idler beam. The signal is removed using dichroic mirrors and the returning idler beam overlaps spatially and temporally with remaining 85% of the original 800 nm beam in a process called power amplification. The resulting signal and idler beams have opposite polarizations because a Type II BBO crystal is employed for amplification. This renders the separation of signal from idler (or vice versa) easy using a simple polarizer. Residual 800 nm beam is removed using a dichroic mirror. Typically, the signal beam can be tuned from 1 μm – 1.625 μm by rotating the BBO crystal at the appropriate angle. The idler can be tuned from 4.263 μm – 1.615 μm. By using second and fourth harmonics of the signal and idler beams, it is possible to obtain wavelengths from 300 nm – 4 μm. This enables the investigation of linear and nonlinear optical properties over a broad range of wavelengths. The second and fourth harmonics are generated by using additional BBO crystals. The desired output from the OPA constitutes the pump beam.

A small portion of the output from Spitfire is deflected using a beamsplitter. Approximately ~5% of the output is guided into the transient absorption spectrometer assembly using two mirrors. The beam is delayed with a computer controlled motion controller and is then focused into a 2 mm sapphire plate to generate white light continuum and this constitutes the probe beam. The white light is then overlapped with the pump beam in a 2 mm quartz cuvette containing the sample and the change in absorbance of the probe light is collected by a CCD detector (Ocean optics®). Data acquisition is controlled by the software from Ultrafast Systems Inc. Typical power of probe beam is ~ 10 μJ/cm^2 while that of pump beam is ~1000 μJ/cm^2. Magic angle polarization is maintained between the pump and probe using a wave plate in order to avoid any contributions from anisotropy due to polarization of the incoming radiations. Pulse duration is obtained from the non-resonant fitting of the solvent response, similar to that described for TCSPC technique. Typical value is ~120 fs. The sample is stirred with a rotating magnetic stirrer. A schematic of the set-up used in our lab is shown in Figure 2.12.

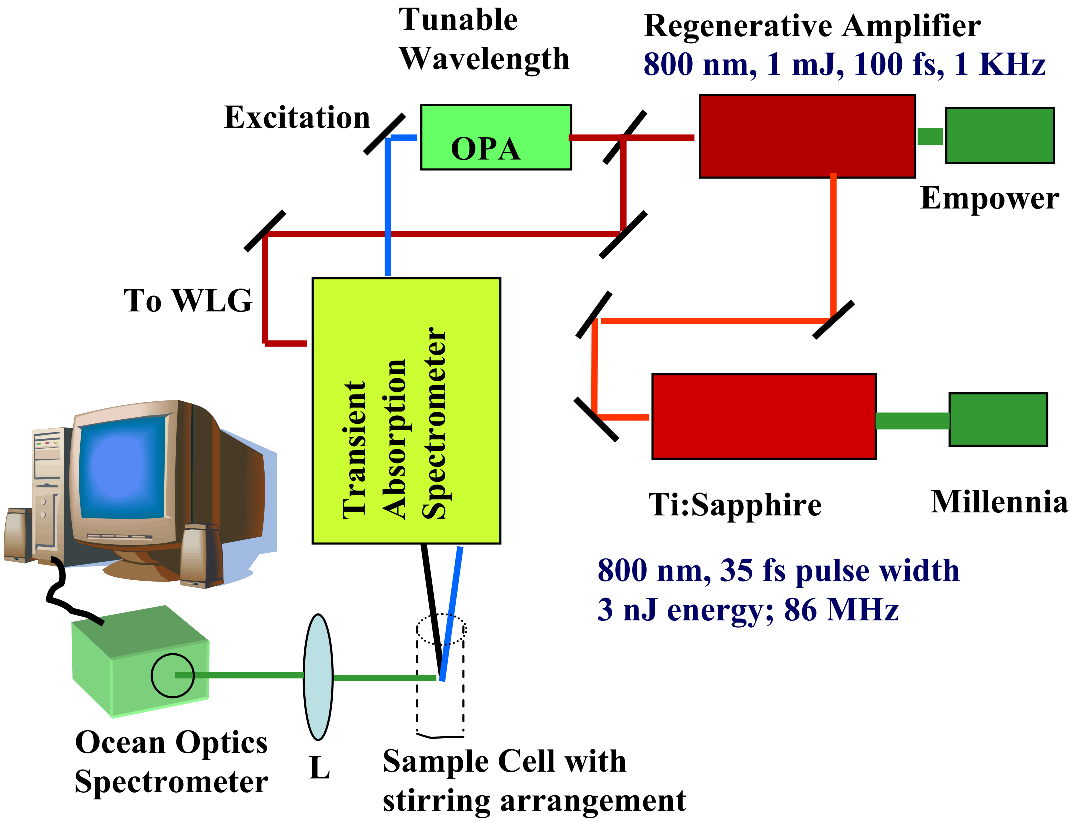

Figure 2.12. Transient absorption spectrometer used in our lab.

2.4.3. Fluorescence Upconversion

Time-resolved polarized fluorescence can be studied using femtosecond up-conversion[20-22] technique. The sample solution is excited with a frequency-doubled light from a mode-locked Ti-sapphire laser (Tsunami, Spectra Physics). This produces pulses of approximately 100fs duration in the wavelength range of 380-430nm. The polarization of the excitation beam for the anisotropy measurements is controlled with a Berek compensator. The resulting incident beam falls on the sample which is contained in a circular sample cell with an optical path length of 1mm and held in a rotating holder to avoid possible photo-degradation and other accumulative effects. The horizontally polarized fluorescence component emitted from the sample is up-converted in a nonlinear crystal of β-barium borate using a pump beam at ~800nm that is first passed through a variable delay line. This serves as an optical gate and enables the fluorescence to be resolved temporally with a time resolution of ~200fs (pump-excitation 400/800nm cross correlation function had a FWHM of 230 fs). Spectral resolution is achieved by dispersing the up-converted light in a monochromator and detecting it by using a photomultiplier tube (Hamamatsu R1527P). It is important to note that we can observe the fluorescence dynamics on the time scale covering almost 4 decades (200fs-1ns) in one scan. The excitation average power is typically kept below 3 milliwatts. This corresponds to excitation pulse energy well below 0.1 nJ. In this excitation intensity regime the fluorescence dynamics is found to be independent of the excitation intensity for all investigated samples.

Besides the second harmonic of the Ti-Sapphire-laser, the system is also able to work with excitation using third harmonic (tunable around 266nm) and that from fundamental beam directly (two-photon excitation mode). In order to produce the third harmonic light, the second harmonic and the fundamental beams are combined in an additional BBO crystal which is able to generate the sum frequency beam around 266nm with intensities up to 15mW. For two-photon (fundamental) excitation mode, the second harmonic unit is disabled by either turning the BBO crystal by the appropriate amount or by simply removing it. The beam splitter which splits out the excitation beam is replaced with one that reflects 50% of the fundamental beam for excitation. The filter rejecting visible light is installed in excitation channel to make sure that the fundamental light is the only source of excitation. The fluorescence upconversion/detection part of the system remains unchanged which allows us to accurately compare the fluorescence profiles at particular detection wavelength under one- and two photon excitation. A schematic of the set-up used in our lab is shown in Figure 2.13. When employing isotropic fluorescence and fluorescence anisotropy to monitor exciton migration, it is important to keep in mind that different phases of energy transfer may not be observed experimentally to the same extent. Downhill energy transfer will be detected by both population dynamics and spectral migration as well as by orientation dynamics as a decay of anisotropy.

In contrast, isoenergetic energy transfer does not lead to a substantial overall red-shift of emission, but anisotropy decay will still be observed. This is nicely illustrated by comparing anisotropy decay and spectral migration kinetics with red excitation in polymers; spectral migration is complete in a few ps, while anisotropy continues to evolve beyond 100ps. Anisotropy decay measurements may also have a limitation when applied to an isotropic sample; if energy transfer is very efficient, the orientation of the dipole moments can be rapidly randomized and the anisotropy will drop to zero.

Even if energy transfer still proceeds, it cannot be monitored by anisotropy measurements anymore. Thus, care should be taken to characterize energy transfer by anisotropy decay if the anisotropy approaches zero. Therefore, in highly oriented systems such as polymer films, anisotropy is mainly reflecting the first few steps of energy transfer, whereas energy continues to migrate along and between polymer chains for a much longer time.

Hence, in an isotropic system, both spectral migration and anisotropy dynamics reflect downhill EET; both observables are most sensitive to the early parts of the energy transfer. Isoenergetic EET in an isotropic system cannot be observed by spectral migration and should be monitored by anisotropy decay dynamics.

Anisotropy can be obtained from fluorescence behavior obtained from parallel and perpendicular polarizations of excitation light. Anisotropy is then given by:

$$A = \frac{I_{\Pi} - I_{\perp}}{I_{\Pi} + 2I_{\perp}} \qquad (2.19)$$

The decay of anisotropy with time provides information on energy migration. Also, the value of residual anisotropy provides information on the geometry of the final emitting state. For a planar geometry, the value of residual anisotropy is 0.1. As mentioned in Chapter 1, a fast decay component in anisotropy decay corresponds to coherent energy migration whereas presence of slower component suggests contribution from hopping or Forster energy transfer.

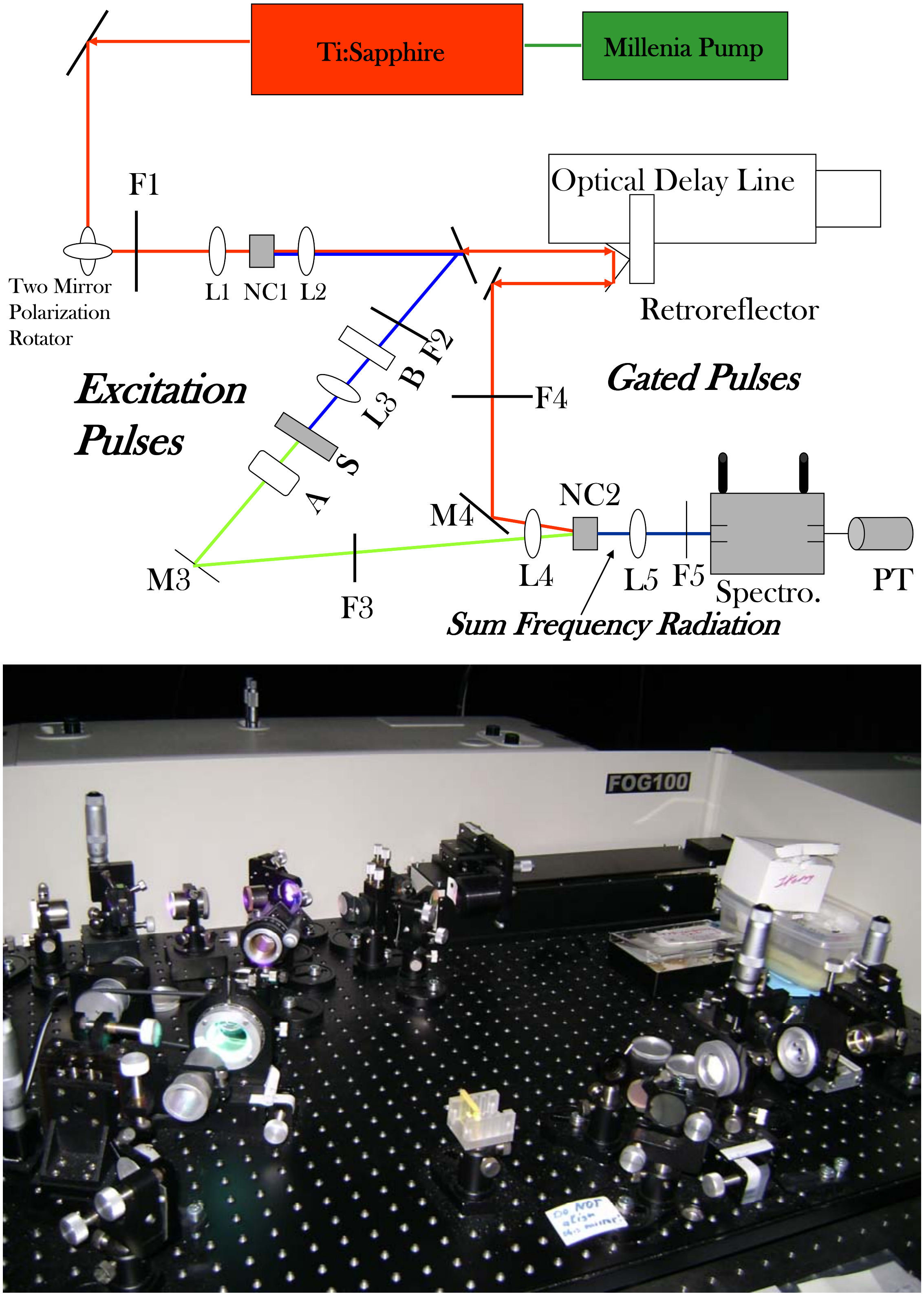

Figure 2.13. Femtosecond fluorescence upconversion set-up used in our lab. Digital image of the set-up is also presented.

Summary

- In order to observe nonlinear optical (NLO) phenomena such as two-photon absorption (TPA), high intensity of electric field is required, for which laser radiation is the ideal choice.
- Mode-locking is the process by means of which high intensity pulses are generated.
- A quantitative measure of TPA behavior is the TPA cross section and it can be measured using the two-photon excited fluorescence (TPEF) method, nonilear transmission (NLT) and the Z-scan methods.
- In order to investigate excited state behavior, transient absorption measurements are very useful.
- Ultrafast upconversion is an attractive tool for investigating excitation migration dynamics.
- The use of femtosecond pulses enables us to investigate phenomena immediately after photoexcitation which could be critical in determining excitation dynamics as well as accessing the immediate excited state of the chromophore.

2.5. Reference

1) Franken, P. A.; Hill, A. C.; Peters, C. W.; Bond, W.; Garrett, C. G. B.; Kaiser, W. *Phys. Rev. Lett.* **1960**, *5*, 303.

2) Butcher, P.N.; Cotter, D. A. *The elements of Nonlinear Optics*, Cambridge University press, 1990.

3) Boyd, R. W. *Nonlinear Optics*, Academic Press Inc., 1992.

4) Munn, R. W.; Ironside, C. N. *Principles and Applications of Nonlinear Optical Materials*, CRC press, 1993.

5) Svelto, O.; Hanna, D. C. *Principles of Lasers*, Plenum Press, 1989.

6) Xu, C.; Webb, W. W. *J. Opt. Soc. Am. B.* **1996**, *13*, 481.

7) Kaiser, W.; Garrett, C. G. B. *Phys. Rev. Lett.* **1961**, *7*, 229.

8) Townsend, P. D.; Jackel, J. L.; Baker, G. L.; Shelburne, J. A., III; Etemad, S. *Appl. Phys. Lett.* **1989**, *55*, 1821.

9) Sheik-Bahae, M.; Said, A. A.; Van Stryland, E. W. *Opt. Lett.* **1989**, *14*, 955.

10) Sheik-Bahae, M.; Said, A. A.; Wei, T. H.; Hagan, D. J.; Van Stryland, E. W. *IEEE J. Quantum Electron.* **1990**, *26*, 760.

11) Lin, T.-C.; Chung, S.-J.; Kim, K.-S.; Wang, X.; He, G. S.; Swatkiewicz, J.; Pudavar, H.; Prasad, P. N. *Adv. Polym. Sci.* **2003**,*161*, 157.

12) Nam, J. R.; Kim, C. H.; Jeoung, S. C.; Lim, K. S.; Kim, H. M.; Jeon, S.-J.; Cho, B. R. *Chem. Phys. Lett.* **2006**, *427*, 210.

13) Yamaguchi, S.; Tahara, T. *Chem. Phys. Lett.* **2004**, *390*, 136.

14) Hales, J. M.; Hagan, D. J.; Van Stryland, E. W.; Schafer, K. J.; Morales, A. R.; Belfield, K. D.; Pacher, P.; Kwon, O.; Zojer, E.; Bredas, J. L. *J. Chem. Phys.*, **2004**, *121*, 3152.

15) O'Connor, D. V.; and Phillips, D. *Time Correlated Single Photon Counting*, Academic Press, New York, **1984**.

16) Demas, J. N. *Excited State Life Time Measurements* Academic Press, New York, **1983.**

17) Bevington, P. R. *Date Reduction and Error Analysis for the Physical Sciences*, McGraw Hill, New York, **1969**.

18) Marquardt, D. W. *Journal of the Society for Industrial and Applied Mathematics*, **1963**, *11*, 431.

19) Oshako, Y.; Thorne, J. R. G.; Phillips, C. M.; Hochstrasser, R.; Zeigler, J. *J. Chem. Phys.* **1989**, *93*, 4408.

20) Ranasinghe, M. I.; Varnavaski, O. P.; Pawlas, J.; Hauck, S. I.; Lowie, J et al *J. Am. Chem. Soc.* **2002**, *124*, 6520.

21) Varnavski, O.; Yan, X.; Mongin, O.; Blanchard-Desce, M.; Goodson, T. III. *J. Phys. Chem. C* **2007**, *111*, 149.

22) Goodson, T., III. *Ann. Rev. Phys. Chem.* **2005**, *56*, 581.

Chapter 3

Rigid, Symmetric, Two-Dimensional Graphidyne Networks

3.1. Introduction

Graphidyne is considered as a potentially important allotrope of carbon. It is essentially an extended, planar network consisting of diphenylacetylene arms[1, 2]. Its structure is shown in Figure 3.1. Since graphidyne is strain free, it is not expected to rearrange back to graphite. Besides its structure, another unique feature of graphidyne is the presence of holes (ca. 2.5 Å) in the planar sheets. This enables insertion of dopant atoms through intra-sheet intercalation, a feature not available to graphite[3].

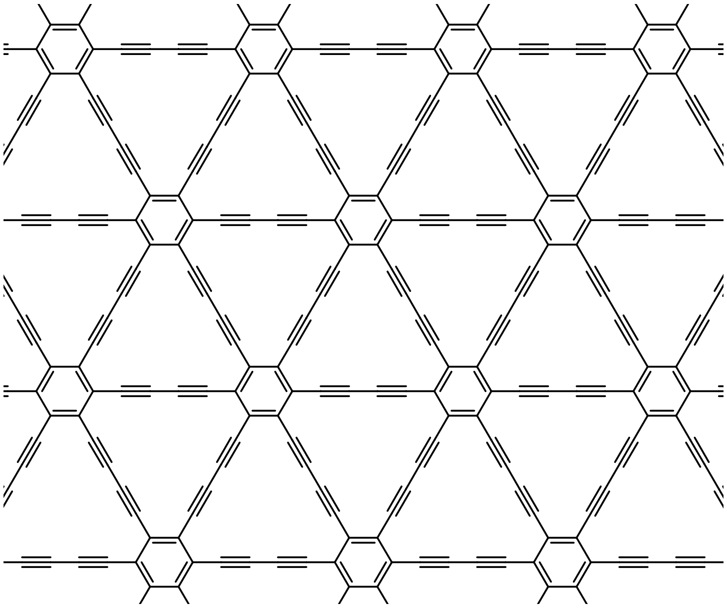

Figure 3.1. Chemical structure of graphidyne network.

The extended π-conjugation in these systems could give rise to interesting material properties such as electrical conductivity[4-8]. From NLO perspective, such extended conjugation should give rise to large hyperpolarizabilities, giving rise to potentially interesting TPA behavior[9-14]. However, the synthesis of such a large network is extremely challenging. Even if the synthesis of such a network is achieved, its solubility in common organic solvents would be quite poor. Hence, the investigation of linear and nonlinear optical properties of graphidyne network as a whole does not seem to be plausible. However, an alternative approach to understand the NLO behavior of graphidyne network could be via application of the building block approach. The dodecahydrotribenzo[18]annulene **1** (Triangle, Figure 3.2) could be considered as a building block for the abovementioned graphidyne network. By examining the NLO properties of a variety of substructures, each composed of **1**, it is possible to study the NLO behavior as a function of:

a) The number of building blocks
b) Arrangement of building blocks that yield different symmetries

A series of such structures[15] is presented in Figure 3.2. Molecules **3** (Bowtie) and **4** (Boomerang) are each composed of two triangular building blocks. However, the Bowtie has D_{2h} symmetry whereas the Boomerang shows C_{2v} symmetry. Hence, by changing the arrangement of building blocks, different symmetries can be obtained. It is of interest to investigate the influence of symmetry on TPA behavior, since symmetry has a significant effect on the nature of ground and excited states[16, 17]. Similarly, molecule **5** (Half-wheel) and molecule **6** (Radiation symbol) can be regarded as substructures of graphidyne network composed of three building blocks. In half-wheel, the three triangles are fused into one another, resulting in C_{2v} symmetry, whereas the radiation symbol possesses D_{3h} symmetry. The purpose of n-decyl groups in these materials is to merely improve the solubility in organic solvents. The donor strengths of these groups are too small to cause any significant effect on the NLO properties. The importance of investigating the NLO behavior of molecule **2** (linear) can be realized by considering the structures of molecules **3-6** which contain the linear arm. Hence, in order to distinguish the contribution of extended conjugation from a linear arm from the triangular building block, it is important to include molecule **2** in this study.

Another intriguing feature of such rigid annulenes is that they are capable of forming self assembled structures such as nanobelts[18-19], nanofibers[20-22] and nanoribbons[23]. These features render such rigid annulenes attractive for nonlinear optical device fabrication. Furthermore, some annulenes have also been proposed to function as molecular muscles[24]. Hence, a methodology based on studying building blocks extends the scope for development of NLO materials beyond synthetic stipulations such as strength of donor-acceptor groups etc. to arranging the same unit in different symmetries and taking advantage of additional features such as self-assembly.

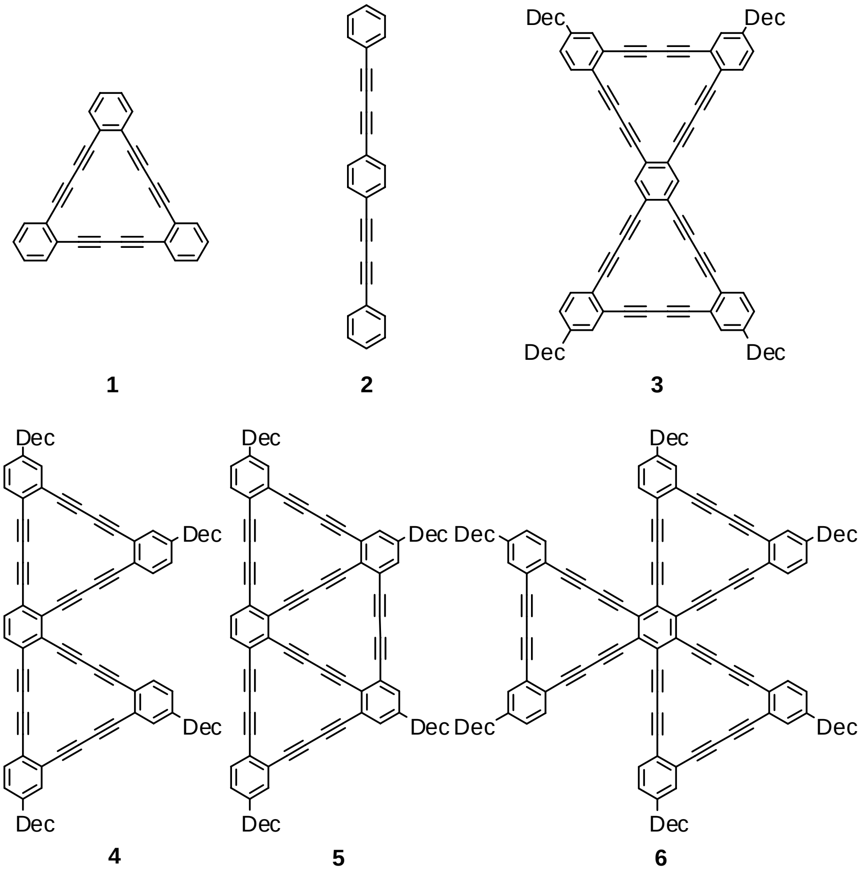

Figure 3.2. Structures of annulenes investigated in this study.

3.2. Experimental

Professor Michael Haley has performed the sythesis of the materials and the synthetic procedures have been reported by him elsewhere[3, 15]. Essentially, Sonogashira cross coupling reactions were employed using Pd[P(o-Tol)$_3$]$_2$ and CuI as the catalyst system. All annulenes were used as received without any further purification. They were dissolved in dichloromethane (Acros Organics, spectrophotometric grade). The concentrations were of the order of 10^{-6}M-10^{-5} M. The concentrations of the annulenes could be calculated conveniently since the molar extinction coefficients for all the abovementioned annulenes in dichloromethane were known[3, 15]. These solutions were used for two photon absorption (TPA) cross section measurements.

3.2.1. Optical Absorption and Emission Measurements

The absorption spectra of the molecules were measured using an Agilent (Model # 8341) spectrophotometer. They are presented in Figure 3.3. Their emission spectra were acquired using a Shimadzu RF-1501spectrofluorimeter and are shown in Figure 3.4.

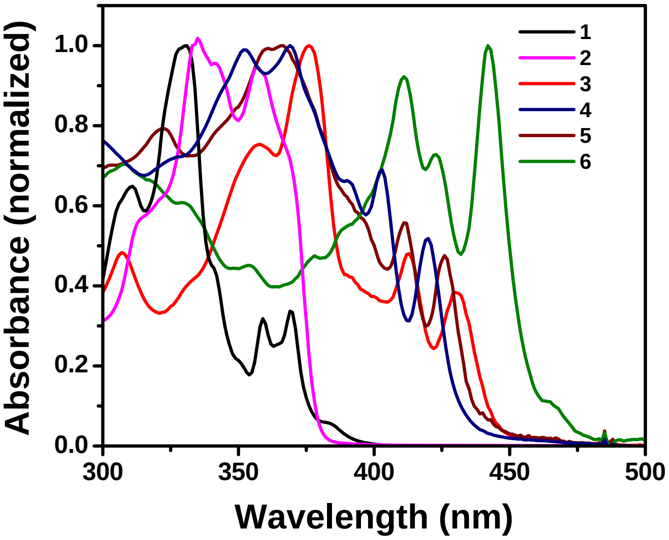

Figure 3.3. Absorption spectra of the annulenes in dichloromethane.

3.2.2. Fluorescence Quantum Yield Measurements

The quantum yields of the annulenes were measured using a known procedure[25]. This involved matching the optical density of the annulene with a dye whose quantum yield is known at the excitation wavelength. Then their emission spectra were recorded.

Quantum yields for molecules **2** through **6** were determined using Coumarin 307 as the standard. For molecules **1** and **2**, Bis-MSB [p-bis(o-methylstyryl) benzene] was used as the reference in order to provide a better match between their absorption and emission maxima. The solutions were purged with argon for 2 minutes prior to measuring their emission spectra. This precludes any spurious effects due to oxidation. Then, the following relation was used to determine the quantum yields:

$$\phi_F = (\phi_F)_S \frac{\int J(\bar{\nu})d\bar{\nu}}{\int J_S(\bar{\nu})d\bar{\nu}} \frac{(J_a)_S}{J_a} \frac{n^2}{n_S^{2\,2}} \tag{3.1}$$

Where,

$(\phi_F)_S$ = Quantum yield of the standard

$\int J(\bar{\nu})d\bar{\nu}$ = Area under the fluorescence emission curve for the sample

$\int J_S(\bar{\nu})d\bar{\nu}$ = Area under the fluorescence emission curve for the standard.

$(J_a)_S$ = Absorbance of the standard

J_a = Absorbance of the sample

n = Refractive index of the solvent used for the sample.

n_s = Refractive index of the solvent used for the standard.

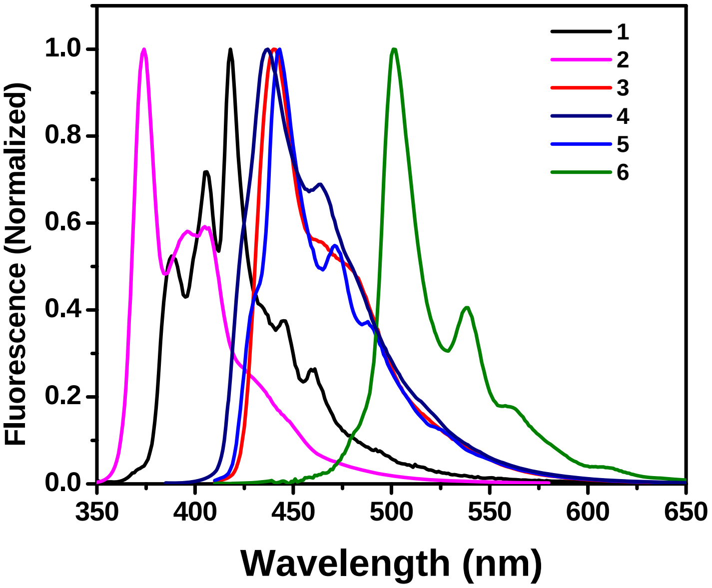

Figure 3.4. Emission spectra of annulenes.

These measurements may have some error due to sensitivity of the fluorescence spectrophotometer and other environmental conditions. Detailed calculations for the determination of quantum yield are illustrated using **3** as an example in Section 3.3.

3.2.3. Two Photon Absorption Cross Section Measurements

The TPA cross sections (δ) of the annulenes were measured using the Two-Photon Excited Fluorescence (TPEF) method[26]. A typical experimental procedure consisted of calibrating a power meter with the digital multimeter for the excitation wavelength of interest. Then the standard is placed inside the sample cell holder. For each value of input intensity, the TPEF counts are recorded. Ten values for input power and ten values for TPEF counts are recorded, averaged and stored in an electronic format. "Dark counts" were also recorded by blocking the laser beam. Any counts under these conditions are a combination of dark noise from the PMT itself and residual light leaking from the surroundings. Hence, while performing calculations (detailed later in this chapter); the dark counts are subtracted from the TPEF counts to yield corrected TPEF counts. These corrected counts are used for further data analysis.

3.2.4. Transient Absorption Measurements

Femtosecond transient absorption investigations have been carried out using ultrafast pump-probe spectrometer detecting in the visible region. The pump beams used in the present investigation, i.e. 375, 430 nm, were obtained from the fourth harmonic of the signal and idler beams respectively. They were focused onto the sample cuvette. The probe beam was delayed with a computer controlled motion controller and then focused into a 2 mm sapphire plate to generate white light continuum. The white light was then overlapped with the pump beam in a 2 mm quartz cuvette containing the sample and the change in absorbance for the signal was collected by a CCD detector (Ocean optics). Data acquisition was controlled by the software from Ultrafast Systems Inc. Typical power of probe beam was ~ 10 $\mu J/cm^2$ while that of pump beam was around 1000 $\mu J/cm^2$. Magic angle polarization was maintained between the pump and probe using a wave plate. Pulse duration was obtained from the non-resonant fitting of the solvent response, which was around 120 fs. The sample was stirred by a rotating magnetic stirrer and little degradation of the sample was observed during the experiments.

3.3. Results and Discussion

3.3.1. Optical Absorption and Steady State Fluorescence Measurements

The steady state properties of molecules **1-6** are presented in Table 2.1. A look into the absorption spectra shown in Figure 3.1 reveals interesting features. Characteristic two peaks in the low energy region are observed for all the molecules except for **2**. The presence of two lower energy peaks in molecules **1**, **3, 4**, **5** and **6** are explained through an exciton model and are ascribed to near neighbor interactions between the linear diphenylbutadiyne (DPB) arms that constitute the triangle. A detailed theoretical investigation involving some of the annulenes studied in this chapter has been published earlier[30] which further elaborated on the exciton model suggested above. In molecules **3, 4** and **5,** the lower energy peaks show a bathochromic shift with respect to **1**, but their relative intensities are less than the higher energy peaks. However, in case of **6**, not only does the lower energy peak show a red shift, but it also exhibits maximum intensity. Interesting vibrational progressions have been observed for molecules **1**, **4**, **5** and **6** possessing two different frequencies. As we progress from molecule **1**, **3-6**, the frequencies tend to gain intensity from one another, corroborating effective electronic coupling between the diphenylbutadiyne (DPB) units and the dodecadehydro[18]annulene core[30]. The results also suggest that in molecule **6**, the coupling between individual building units is the strongest. Comparing building blocks **1** and **2**, it is interesting to observe that **2** does not show the characteristic vibronic signature observed in **1**. This suggests that even though both **1** and **2** are composed of the same diphenylbutadiyne arm, the coupling between individual DPB arms is better in **1**. This is in accordance with the theoretical treatment[30] of molecular orbitals for **1** and **2**.

Comparing molecules with similar number of building blocks such as **3** and **4**, it is clearly observed that the arrangement of building units causes a significant difference in absorption spectra. Molecule **3** shows a pronounced red shift in its absorption spectrum compared to **4**. This applies to both features; the higher energy peak as well as the lower energy vibronic features. It is interesting to note that molecule **3** has a higher order of symmetry (D_{2h}) than molecule **4** (C_{2v}). Similarly, molecule **6**, which has a higher order of symmetry (D_{3h}) than molecule **5** (C_{2v}) shows a bathochromic shift in its absorption features. Explore the influence of trends observed in absorption behavior on TPA characteristics could reveal some interesting trends.

Examination of the emission spectra also reveals certain intriguing features. Molecules with higher order of symmetry show a red-shift in their emission maxima when compared with their counterparts composed of similar number of building blocks. This effect is especially pronounced for molecule **6** which shows a 61 nm red-shift with respect to **5**. However, this could be due to increased number of DPB arms (chromophore density). This is typically related to increase in conjugation length which is expected to produce a bathochromic shift in emission spectra[31-34]. This could also explain the large difference in absorption spectra between **5** and **6**, along with the electronic coupling considerations discussed above. Quantum yield results summarized in Table 3.1 indicate that molecule **3** shows the largest value of 0.45. There is no particular trend between order of symmetry and quantum yield. Molecules **1**, **2**, and **6** show lower quantum yields than **3**, **4**, and **5**. This suggests that there could be breaking of symmetry once the molecule is excited which could give rise to additional nonradiative pathways. Such a hypothesis can be tested using transient absorption measurements which will be discussed later in this chapter.

A sample calculation for determining the quantum yield is shown for Bowtie (molecule **3**). Coumarin 307 dissolved in methanol (quantum yield = 0.53) was used as the reference. The excitation wavelength used was 385 nm. The optical densities of the reference and Bowtie's solution in dichloromethane were matched at 385 nm. The corresponding absorption spectra are shown in Figure 3.5. The emission spectra of the solutions are presented in Figure 3.6. Here, the ordinate is wavenumbers in cm^{-1}, as required by equation 3.1.

$$\phi_F = (\phi_F)_S \; \frac{\int J(\bar{\nu})d\bar{\nu}}{\int J_S(\bar{\nu})d\bar{\nu}} \frac{(J_a)_S}{J_a} \frac{n^2}{n_S^{2\,2}} \tag{3.1}$$

where,

$(\phi_F)_S$ = 0.53

$\int J(\bar{\nu})d\bar{\nu}$ = 2.484×10^{10} cm^{-1}

$\int J_S(\bar{\nu})d\bar{\nu} = 2.534\times10^{10}\ \text{cm}^{-1}$

$(J_a)_S = 0.026$

$J_a = 0.033$

$n = 1.424$

$n_s = 1.33$

Substituting these values into equation 3.1, $\phi = 0.45$.

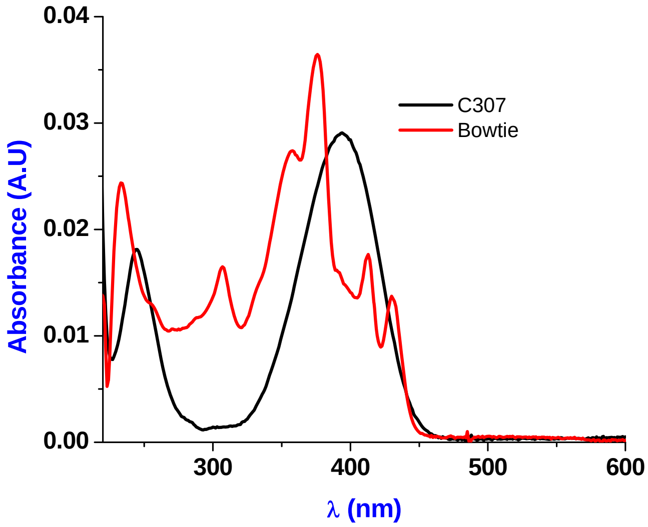

Figure 3.5. Absorption spectra of Coumarin 307 and **3** for quantum yield measurements.

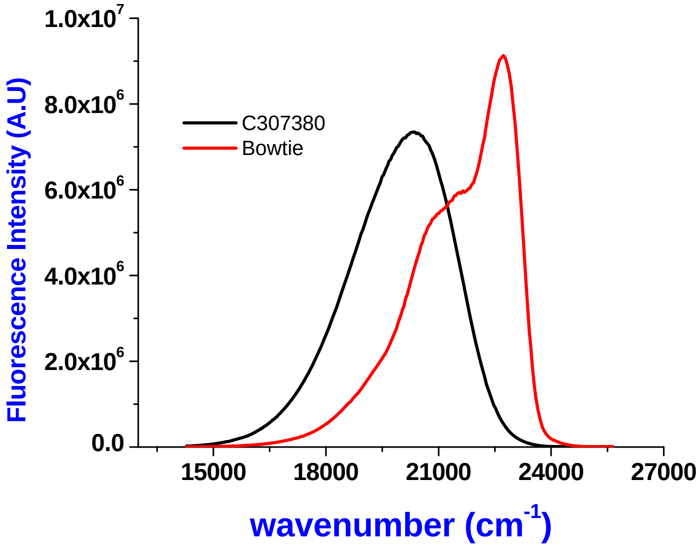

Figure 3.6. Emission spectra for quantum yield determination of **3**.

Table 3.1. Steady state properties of molecules 1-6.

Molecule (Symmetry)	**λ_{abs} (nm)**	**λ_{em} (nm)**	**η**
1 (C_{3h})	**332**, 359, 369	389	0.18
2 ($D_{\infty h}$)	334, **358**	**374**	0.08
3 (D_{2h})	**376**, 413, 430	**438**	0.45
4 (C_{2v})	**370**, 404, 421	**438**	0.29
5 (C_{2v})	**366**, 411, 426	**439**	0.32
6 (D_{3h})	411, 423, **442**	**500**	0.12

3.3.2. TPA Cross Section Measurements

The mathematical relationship that relates the intensity dependent TPEF signal to the TPA cross section of the molecule is shown in equation 3.2 below[26].

$$F(t) = \boxed{\frac{1}{2}\eta\delta c n}\boxed{\frac{g_p}{\pi\lambda f\tau}}\boxed{\phi}\langle P(t)\rangle^2 \tag{3.2}$$

Where,

F(t) = TPEF photons collected per unit time (photons/sec.)
η = Fluorescence quantum yield (dimensionless)
δ = TPA Cross section (cm^4-sec./(photon-molecule))
c = concentration of the molecule (molecules/cm^3)
n = refractive index of the solvent (dimensionless)
g_p = shape factor (dimensionless) = 0.664 for Gaussian pulses.
λ = wavelength (cm) (800 nm for the purpose of demonstration)
f = frequency of laser source (pulses/sec) = 75×10^6 pulses/sec. (for KM laser)
τ = pulse duration (sec.) (=35×10^{-15} sec. for KM laser at 800 nm)

φ = collection efficiency (dimensionless)
$<P(t)>$ = Input Intensity (photons/ cm^2-sec.)

The terms in equation 3.2 grouped within yellow box are the parameters that are related to the sample solution. The terms grouped in orange are laser parameters and the terms grouped in green are related to the optical set-up. The purpose of using the standard is to determine the collection efficiency. This refers to the efficacy with which photons at the emission maximum are collected from the focusing volume of the solution. Ideally, the emission maximum of the standard and the sample should be identical because the photomultiplier tube's sensitivity changes with wavelength. However, a rather small library of standards with known TPA cross sections is available[26, 35]. Coumarin 307 (emission maximum at 501 nm) was used as the standard from 705 nm – 840 nm. Fluorescein (emission maximum at 521 nm) was used as the standard from 840 nm onwards. For wavelengths below 705 nm, bis-MSB or p-bis(o-methyl-styryl) benzene (emission maximum at 415 nm) was used as the standard[36, 37]. None of the standards have their emission maxima identical to that of molecule **3** (438 nm). Hence, this introduces some error in TPA cross section measurements. A stepwise procedure for the determination of TPA cross section δ is outlined below.

3.3.2.1. Calculation of Input Intensity

The variable $<P(t)>$ is an intensity term so it is essential to convert the input power in mW as measured by the power-meter into a photon flux or input intensity in photons/ cm^2-sec. In order to determine the intensity of the incoming beam, it is necessary to know the diameter of the laser beam that incident at the cuvette. This can be calculated by considering a case of diffraction limited focusing by a lens. This is illustrated in Scheme 3.1.

Scheme 3.1. Determination of spot size using diffraction limited focusing.

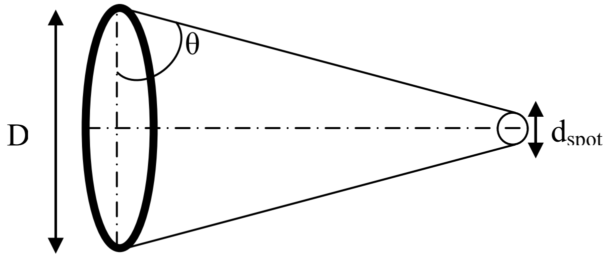

$$\theta = 1.22\frac{\lambda}{D} \tag{3.3}$$

θ = focusing angle

D = diameter of the laser beam as it enters the focusing lens

λ = wavelength (cm) = 800 × 10^{-7} cm

In this case, D is the size of the iris shown in Scheme 3.1. This is known to be 0.275 cm.

Hence, θ = 3.5491 × 10^{-4}

Diameter of the beam at the spot of focusing $d_{spot} = 2f\theta$

f = focal length of the lens = 11cm

Hence, d_{spot} = 1.24 ×10^{-2} cm

Hence, area of the focused spot $A_{spot} = \pi\frac{d_{spot}^2}{4}$ = 1.22 ×10^{-4} cm^2

Hence, intensity corresponding to 1mW of average power $\overline{W} = \frac{10^{-3}}{A_{spot}}$

Hence, $\overline{W}$ = 2.52 ×10^6 Watts/sec-cm^2 = 2.52 ×10^6 J/sec-cm^2

Energy of one 800 nm photon $E = \frac{hc}{\lambda}$

h = Planck's constant = 6.626 × 10^{-34} J-sec.

c = velocity of light = 3 ×10^{10} cm/sec.

Thus, E = 2.485 $\times 10^{-19}$ J/photon. Hence, the factor by which average power needs to be multiplied to convert 1mW average power into intensity in photon/cm^2-sec. = $\frac{\overline{W}}{E}$. This equals 1.014 $\times 10^{25}$ photon/ cm^2-sec.

3.3.2.2. Calculation of Collection Efficiency (ϕ)

Since $\eta\delta$ for Coumarin 307 at 800 nm is known[26], we can use this information to compute the collection efficiency ϕ of the system.

For Coumarin 307,

$\eta\delta$ at 800 nm = 14 GM = 14 $\times$ 10^{-50} cm^4-sec./(photon-molecule)

n = 1.33 (methanol is used as solvent)

c = 10^{-4} M = 10^{-4} moles/lt. = 10^{-7} moles/cm^3 = $10^{-7} \times 6.023 \times 10^{-23} = 6.023 \times 10^{16}$ molecules/cm^3.

λ = 800 nm = 800 $\times$ 10^{-7} cm

f = 75 $\times$ 10^6 pulses/sec.

τ = 35 $\times$ 10^{-15} sec.

g_p = 0.664

Taking logarithms on both sides of equation 3.2, we have:

$$\log(F(t)) = 2\log\langle P(t)\rangle + \log\left(\frac{1}{2}\eta\delta c n \frac{g_p}{\pi\lambda f\tau}\phi\right) \qquad (3.4)$$

Hence, a logarithmic plot of fluorescence intensity versus input intensity should be a straight line with a slope of 2. This confirms a two-photon excitation process. The intercept provides information on the collection efficiency since other parameters are known for Coumarin 307. The raw data obtained for Coumarin 307 from the set-up along with the logarithmic plot between TPEF intensity and input intensity are shown in Table 3.2 and Figure 3.7 respectively. The first two columns are the raw counts and digital multimeter readings obtained from the measurements. The voltmeter-power meter calibration curve at 800 nm is shown in Figure 3.8 . Using the equation obtained, the multimeter reading can be substituted for “x” to calculate the input power in mW, which is presented in column #3. It should be noted that there is an intercept to this equation which is an artifact since zero power should correspond to zero mV on the multimeter. This artifact can be attributed to residual light leaking from the surroundings. Hence, on some occasions a precise slope of 2 may not be obtained. In this case, minor changes to this slope can be made to improve the slope close to 2. However, it is important to use identical equations for the standard and the sample. The next column shows the input intensity in photons/cm^2-sec. using the conversion factor determined above. Corrected counts are obtained by subtracting 3438 counts from every entry in the first column since this was the number of dark counts obtained upon blocking the beam. Ideally, this number should be zero. Similar to the intercept scenario with the calibration curve, 10% change in dark counts could be necessary to improve the slope close to 2. It is necessary to keep the slopes of both standard and sample as close to each other for accurate comparison. The intercept and slope are sources of error among measurements but these can be rectified fairly easily. These errors are less serious than fundamental issues such as excited state absorption and thermal lensing associated with other techniques used for TPA cross section measurement such as nonlinear transmission and Z-scan. The next two columns in Table 3.2 are logarithms of input intensity and corrected counts respectively.

Comparing the equation obtained for Coumarin 307 shown in Figure 3.7 with equation 3.4,

$$-48.1033 = \log\left(\frac{1}{2}\eta\delta cn\frac{g_p}{\pi\lambda f\tau}\phi\right) = \log\left(\frac{1}{2}\eta\delta cn\frac{g_p}{\pi\lambda f\tau}\right) + \log(\phi) \tag{3.5}$$

Substituting the values of $\eta\delta$, c, n, g_p, f, λ and τ,

$-48.1033 = -23.248 + \log(\phi)$

$\therefore \phi = 1.395 \times 10^{-25}$.

Table 3.2. Data obtained for Coumarin 307 at 800 nm.

Counts	Multimeter Reading (mV)	Input Power P (mW)	Input Intensity (I)	Corrected counts cc	log (I)	log(cc)
423351	713.70	15.20	8.43504E+26	419912	26.93	5.62
373296	663.00	14.21	7.88472E+26	369858	26.90	5.57
299822	587.80	12.72	7.05953E+26	296384	26.85	5.47
259275	543.30	11.83	6.5662E+26	255836	26.82	5.41
223875	499.20	10.85	6.02234E+26	220436	26.78	5.34
177873	438.30	9.64	5.34811E+26	174434	26.73	5.24
149918	398.70	8.83	4.90087E+26	146480	26.69	5.17
124572	361.10	8.05	4.46976E+26	121134	26.65	5.08
94897	310.00	6.98	3.87381E+26	91459	26.59	4.96
70686	262.90	5.97	3.31425E+26	67247	26.52	4.83
56583	232.70	5.32	2.95028E+26	53145	26.47	4.73
39844	191.03	4.40	2.44143E+26	36406	26.39	4.56
25946	148.53	3.45	1.9145E+26	22508	26.28	4.35
19925	126.63	2.95	1.63984E+26	16487	26.21	4.22
15112	105.90	2.48	1.3779E+26	11674	26.14	4.07
9954	78.36	1.85	1.02696E+26	6516	26.01	3.81
6945	57.62	1.37	7.60442E+25	3506	25.88	3.54
5177	40.25	0.97	5.35764E+25	1739	25.73	3.24
4304	28.40	0.69	3.81718E+25	866	25.58	2.94
3438	0.03					

3.3.2.3. Calculation of TPA Cross Section of the Molecule

As an example, calculations for molecule **3** at 800 nm are shown. The numerical data is presented in Table 3.3. The plot showing TPEF intensity dependence is shown in Figure 3.9. Comparing the equation obtained for molecule **3** with equation 3.4, we have

$$-48.1033 = \log\left(\frac{1}{2}\eta\delta cn\frac{g_p}{\pi\lambda f\tau}\phi\right) = \log\left(\frac{1}{2}\eta cn\frac{g_p}{\pi\lambda f\tau}\phi\right) + \log(\delta) \qquad (3.6)$$

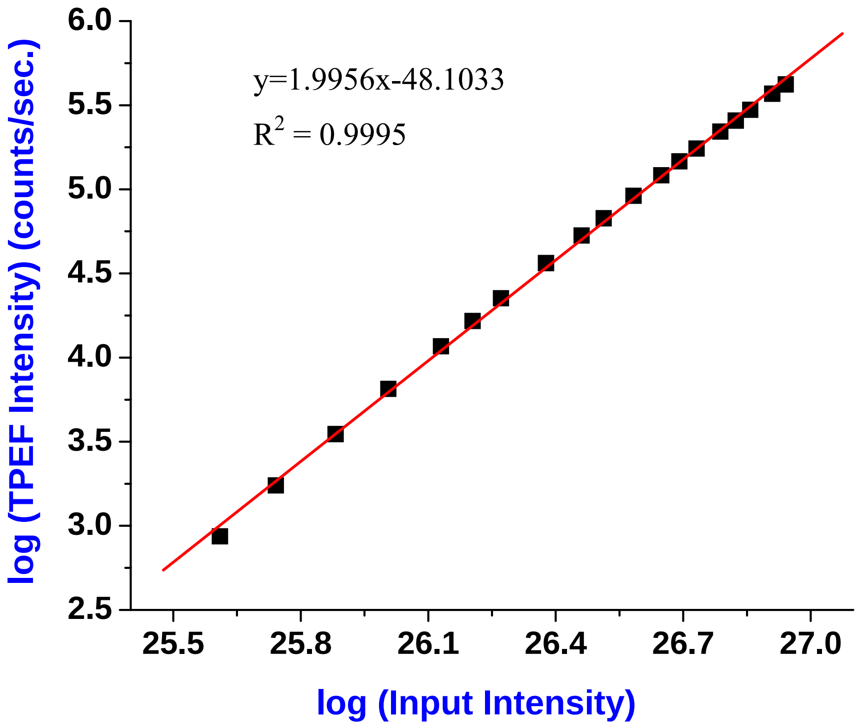

Figure 3.7. Logarithmic plot showing quadratic dependence between TPEF intensity and input intensity for Coumarin 307.

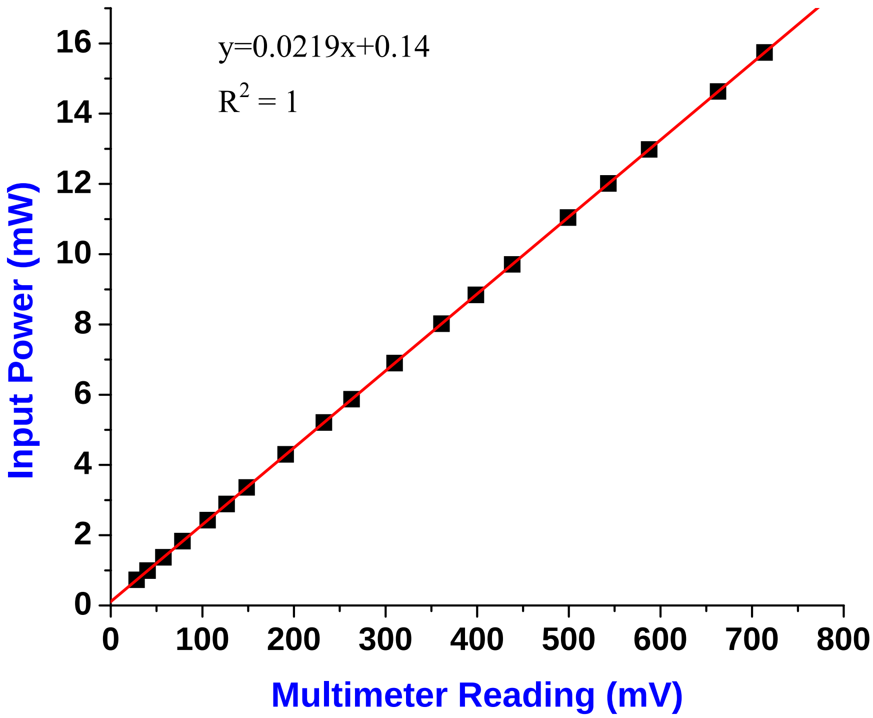

Figure 3.8. Calibration curve for converting multimeter reading into input power.

Table 3.3. Data obtained for molecule 3 (Bowtie) at 800 nm.

Counts	**Multimeter Reading (mV)**	**Input Power P (mW)**	**Input Intensity (I)**	**Corrected counts cc**	**log (I)**	**log(cc)**
643990.3	705.5	15.56	8.63623E+26	640506.3	26.94	5.81
412065.8	551	12.18	6.75856E+26	408581.8	26.83	5.61
303448.1	463.4	10.26	5.69394E+26	299964.1	26.76	5.48
231919.7	400.7	8.89	4.93193E+26	228435.7	26.69	5.36
188103.4	358.7	7.97	4.4215E+26	184619.4	26.65	5.27
144145.2	309.6	6.89	3.82478E+26	140661.2	26.58	5.15
95353.3	246.9	5.52	3.06277E+26	91869.3	26.49	4.96
72068.2	212.4	4.76	2.64349E+26	68584.2	26.42	4.84
47993.4	169.68	3.83	2.12431E+26	44509.4	26.33	4.65
35726.8	143.68	3.26	1.80832E+26	32242.8	26.26	4.51
25385.2	117.73	2.69	1.49295E+26	21901.2	26.17	4.34
17748.8	94.3	2.18	1.2082E+26	14264.8	26.08	4.15
11919.5	72.27	1.69	9.40464E+25	8435.5	25.97	3.93
7482.4	49.07	1.19	6.5851E+25	3998.4	25.82	3.60
5857.7	38.56	0.96	5.3078E+25	2373.7	25.72	3.38
3483.2	0.03					

For molecule **3**,

η = 0.45 as obtained from quantum yield measurements

The concentration was determined by measuring the absorption spectrum of the dichloromethane solution prior to TPEF measurements. The corresponding plot is shown in Figure 3.10 . The molar extinction coefficient for this molecule in dichloromethane is known[15]. Using this information, the concentration can be calculated using the relation:

$$c = \frac{A}{\varepsilon \times l} \tag{3.7}$$

Where c = concentration in mol/l.

A = Absorbance at given wavelength

ε = Molar extinction coefficient at the given wavelength ($M^{-1}cm^{-1}$)

Taking absorption maximum at 358 nm as an example, ε_{358} = 133000 $M^{-1}cm^{-1}$, A = 1.716. l = path length of the cuvette = 0.4 cm

Hence, c = 3.175 $\times 10^{-5}$M = 1.529$\times 10^{16}$ molecules/cm^3

The values of ϕ, n, g_p, f, λ and τ are known (refractive index for dichloromethane is 1.424). Substituting these values in Equation 3.6,

$$-47.91 = -0.065 + \log(\delta)$$

Hence, δ = 1.429 $\times 10^{-48}$ cm^4-sec./(photon-molecule)

1 Goppert-Mayer or 1 GM = 10^{-50} cm^4-sec. / (photon-molecule)

Hence, δ = 142.9 GM.

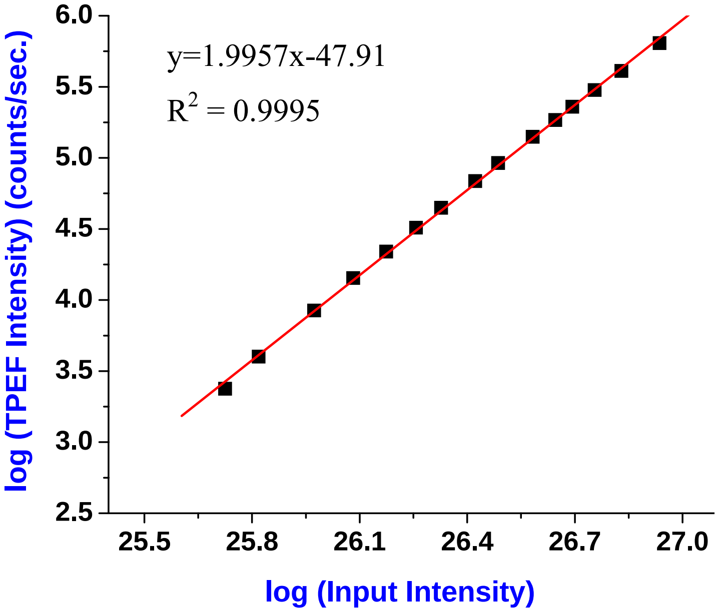

Figure 3.9. Logarithmic plot showing quadratic dependence between TPEF intensity and input intensity for molecule **3**.

In this manner, the TPA cross section δ is calculated for all the molecules at all wavelengths. However, this procedure can be simplified. By plotting the results for both Coumarin 307 and Bowtie on the same graph, one should obtain two parallel lines displaced by a certain amount along the y-axis. By drawing vertical lines and noting the intercepts for the reference and the sample, one could calculate the TPA cross section for bowtie. This procedure could be applied at two to three different regions so that an average value of TPA cross section could be obtained. This method obviates the need for converting input power into input intensity since the factor of conversion involved is the same for both Coumarin 307 and Bowtie. This makes the calculation more convenient. In this manner, the TPA cross section spectra for all molecules are obtained. It must be noted that due to errors associated with matching the slopes, dark counts and artifacts in multimeter calibration, smaller library of available standards with known δ values over a range of wavelengths, the error associated with measurement of δ could be as high as 20%. Also, it is implicitly assumed that the one and two-photon excited fluorescence quantum yields are same, even though the location of TPA cross section maximum could be different from its corresponding steady state equivalent wavelength. The TPA cross section spectra for molecules **1**-**6** are presented in Figure 3.11. The TPA cross sections are plotted as a function of wavelength. TPA cross sections below 550 nm for some of the annulenes yielded slopes of 1.6-1.9. This suggests contribution from linear (steady state) absorption which is typically arises due to tail of the absorption spectrum at longer wavelengths. The nonlinear optical properties are also summarized in Table 3.4 .

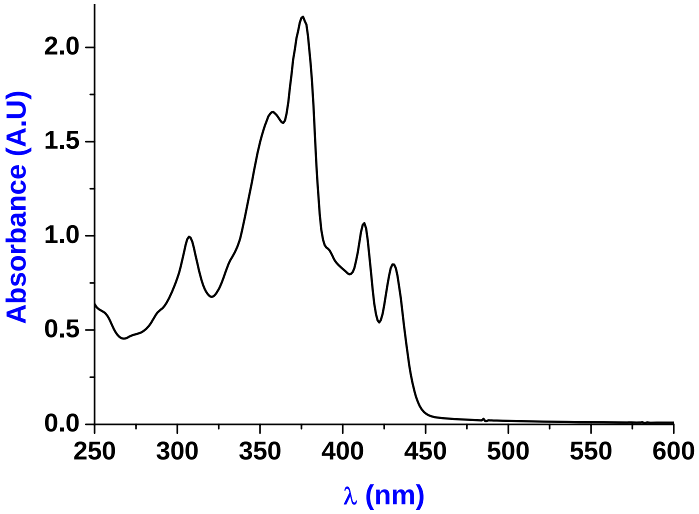

Figure 3.10. Absorption spectrum of molecule 3 used for TPEF measurements.

Several interesting observations can be made from Figure 3.11. First and foremost, the δ_{max} values for molecules **1** and **2** are very low; namely 17 GM and 11.5

GM respectively (listed in Table 3.4). However, considering molecule **4** (Boomerang), which consists of two triangular building blocks, δ_{max} shows greater than 30 fold improvement to 393 GM. By rearranging the same building blocks to form a bowtie (molecule **4**), δ_{max} can be increased by over 60 fold to 700 GM. This suggests the following:

a) It is possible to build novel materials with large δ values using building blocks that have very small TPA cross sections.

b) There is a nonlinear increase in δ as the number of building blocks is increased.

c) There seems to be excellent communication or coupling between individual building blocks in the larger macrostructures consisting of multiple building blocks.

d) The arrangement of building blocks has a profound effect on δ_{max}.

e) Structures with higher order of symmetry were found to have larger δ_{max} values.

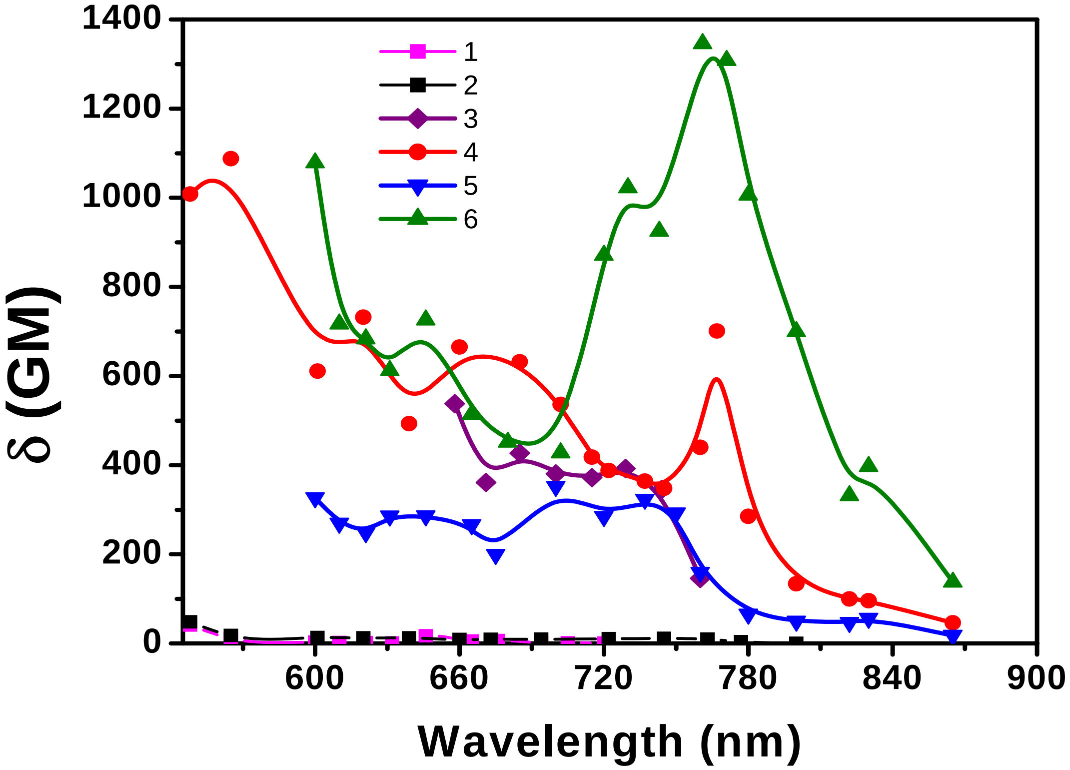

Figure 3.11. TPA cross sections for molecules 1-6.

The influence of arrangement of building blocks is further accentuated by comparing molecules **5** and **6**. In this case, the δ_{max} for radiation symbol **6** shows nearly three fold improvement over δ_{max} for half-wheel (**5**). Also, among all the molecules investigated, **6** shows the largest TPA cross section value of ca. 1400 GM. The δ_{max} values reported here are quite high, especially considering the fact that these materials do not have any strong donor or acceptor groups. Hence, the TPA cross section values reported can be further improved by adding donor and acceptor groups. In an attempt to illustrate this, molecule **7**, whose structure is shown in Figure 3.12 was investigated for its TPA cross section[37, 38] and it was determined to be 650 GM at 760 nm using TPEF experiments in our lab. This represents a nearly 50 fold improvement over the parent building block **1**. The maximum value of δ for molecule **7** could be much higher than this. In this manner, the TPA cross sections of molecules **3**-**6** could be improved significantly.

Table 3.4. Nonlinear optical properties of molecules 1-6.

Molecule (Symmetry)	**δ_{max}(GM)**	**Number of π-e$^-$**	**δ'(per π-e$^-$)**
1 (C_{3h})	11.5	30	0.4
2 ($D_{\infty h}$)	17	26	0.65
3 (D_{2h})	701	54	13
4 (C_{2v})	393	54	7.3
5 (C_{2v})	353	58	6.1
6 (D_{3h})	1346	78	17.3

It can be observed from the structures of molecules **1**-**6** that as we progress from molecules **1** to **3** and then to **6**, there is an increase in number of diphenylbutadiyne chromophores. This increase in chromophore density is expected to increase TPA cross section. In order to emphasize that the trends observed in δ_{max} are not merely due to increase in chromophore density, we calculated the number of π-electrons in each molecule and divided δ_{max} by the total number of π-electrons to yield δ′, which is δ_{max} per π-electron. This is a more representative measure of the inherent TPA cross section of the molecule. The number of π-electrons is calculated by considering a triple bond to have 4 π-electrons and a double bond to have 2 π-electrons.

So, for molecule 1, which has 6 triple bonds and 3 double bonds, the total number of π-electrons is 30. Dividing its δmax value of 11.5 GM by 30, its δ′ was found to be 0.4 GM. The δ′ values for molecules 1-6 are reported in Table 3.4 . It can be clearly observed that δ′ shows significant increase upon increasing the number of triangular building units from molecule **1** to molecule **3** (Bowtie). In fact, the increase is more than one order of magnitude. Similarly, molecule **6** (Radiation symbol) shows nearly 40 fold improvement in δ′ over the parent building block. If there were no enhancement, the values for δ' should have been the same for all molecules, suggesting additive behavior in TPA cross section as a result of increase in chromophore density. However, that is not the case observed here. Therefore, the TPA results suggest strong coupling between individual diphenylbutadiyne arms that comprise molecules **3** and **6**. The same can be inferred about molecules **2**, **4** and **5**.

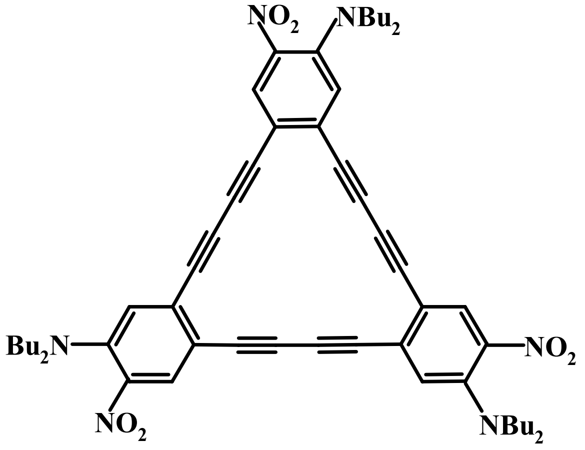

Figure 3.12. Structure of donor-acceptor substituted triangle **7**.

The question that still remains unanswered at this point is the effect of arrangement of building block (triangle) on δ and δ′. Considering molecules **5** and **6**, it is interesting to ask why δ_{max} shows more than threefold increase when three triangles are arranged in different fashions. In order to address this, we first resort to a three states model that delineates key molecular parameters that influence the TPA cross section δ. A simplified equation is shown below[36].

$$\delta \quad \propto \quad \sum_{e'} \frac{M_{ge}^2 M_{ee'}^2}{[E_{ge} - E_{ge'}/2]^2 \Gamma} \tag{3.8}$$

Where M_{ij} is the transition dipole moment from state i to j and E_{ij} is the energy difference between states i and j. Γ is the damping factor.

In order to calculate [E_{ge} – ($E_{ge'}$/2)], it is necessary to know the one and two photon absorption maxima. These can be obtained from their one and TPA cross section spectra respectively. The results for molecules **1-6** are presented in Table 3.5. For molecule **5**, E_{ge} corresponds to the energy of a 426 nm photon, which equals 2.91 eV. Similarly, $E_{ge'}$ corresponds to the energy of a 357 nm photon, which equals 3.48 eV. Hence, [E_{ge} – ($E_{ge'}$/2)] equals 1.18. The same for molecule **6** is 1.18 as well. This demonstrates that the denominator of equation 3.8 is virtually identical for molecules **5** and **6**. So the energy difference term does not explain the greater than threefold improvement in δ. The values for [E_{ge} – ($E_{ge'}$/2)] for molecules **1-6** are also presented in Table 3.5. The ground state transition dipole moment M_{ge} is considered next. M_{ge} can be calculated using the following equation:

$$M_{ge}^2 = \frac{1500 \ln(10) \hbar c n}{2\pi^2 N_A} \int \frac{\varepsilon(\bar{\nu})}{\bar{\nu}} d\bar{\nu} \tag{3.9}$$

Where,

n = refractive index of the solvent,

N_A = Avogadro number,

ε = Molar Extinction coefficient (obtained from absorption spectra).

$\bar{\nu}$ = wavenumber in cm^{-1}.

The integral $\int \frac{\varepsilon(\bar{\nu})}{\bar{\nu}} d\bar{\nu}$ refers to the area under the curve of a plot with $\frac{\varepsilon(\bar{\nu})}{\bar{\nu}}$ as the abscissa and $\bar{\nu}$ as the ordinate. Such a plot for molecule **3** is shown in Figure 3.13. The area under this plot is calculated to be 33410 $M^{-1}cm^{-1}$. From equation 3.9,

n = 1.424

$N_A = 6.023 \times 10^{23}$ molecules/mole

$\hbar = 1.054 \times 10^{-27}$ erg-sec.

c = 3×10^{10} cm/sec.

Substituting these values in equation 3.9, M_{ge} = 19.9×10^{-19} e.s.u = 19.9 Debye.

Similarly, M_{ge} for other molecules can be calculated. The M_{ge} values for molecules **1**-**6** are shown in Table 3.5.

Table 3.5. Location of one and TPA maxima for molecules **1-6.**

Molecule (Symmetry)	**λ_{abs} (nm)**	**λ_{TPA}^{max} (nm)**	***M_{ge}(D)***	***[E_{ge}-$E_{ge'}$/2]***
1 (C_{3h})	**332**, 359, 369	372	11.8	1.69
2 ($D_{\infty h}$)	334, **358**	322	11.7	1.55
3 (D_{2h})	**376**, 413, 430	383	19.5	1.27
4 (C_{2v})	**370**, 404, 421	365	18.9	1.25
5 (C_{2v})	**366**, 411, 426	357	18.3	1.18
6 (D_{3h})	411, 423, **442**	381	17.6	1.17

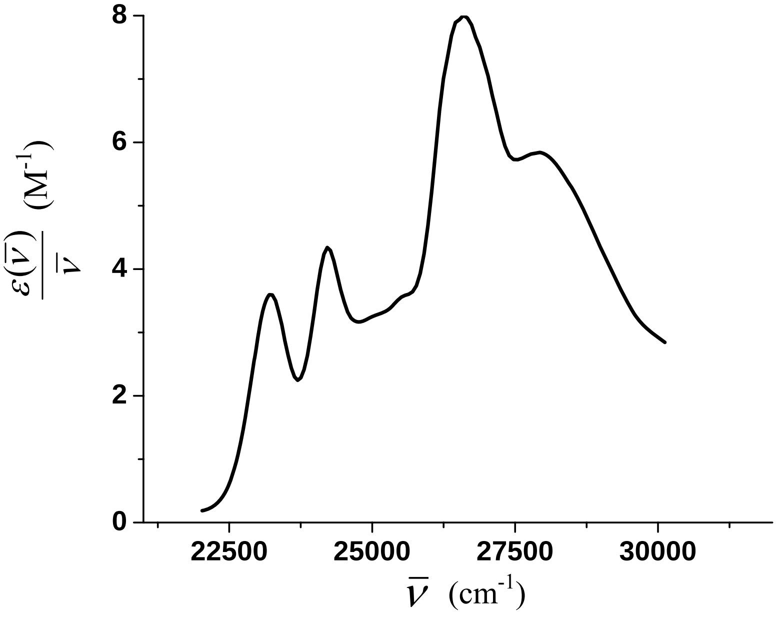

Figure 3.13. Plot for determining ground state transition dipole moment for **3**.

From Table 3.5, it can be observed that M_{ge} for **5** is greater than **6**. Thus, based on steady state results alone, it appears that the TPA cross section for molecule **5** should be greater than that of **6**. However, this is in contrast with the trends observed in TPA behavior where molecule **6** shows greater than threefold increase in δ_{max} over **5**. It is thus suggested that the oscillator strength of this particular transition is not the only determining factor which is dictating the increase in the δ of the annulenes studied here. Hence, it becomes critical to determine the excited state transition dipole moments ($M_{ee'}$) for these molecules. In order to achieve this, the excited state absorption spectra should be measured. For this purpose, transient absorption measurements were employed and the results obtained from the same will be discussed next.

3.3.3. Ultrafast Transient Absorption Measurements

Measurements of the excited state extinction coefficients for all the investigated chromophores have been carried out under actinometric (same incident photon flux) conditions using perylene as the standard with known singlet state extinction coefficient (13,000 $M^{-1}cm^{-1}$ at 710 nm) [40]. This corresponds to a particular value of optical density in the excited state under the experimental conditions. Thus, if excited state absorption spectra are measured for the molecules under investigation, based on the optical density of the annulenes, their excited state coefficients could be determined. The results for molecules **1**, **3-6** are shown in Figure 3.14. The plots shown represent a "snapshot" of the excited state of the molecules 150 fs after excitation. Equation 3.9 can be modified to determine their excited state transition dipole moments as:

$$M_{ee'}^{2} = \frac{1500\ln(10)\hbar cn}{2\pi^{2}N_{A}}\int\frac{\varepsilon(\overline{\nu})}{\overline{\nu}}d\overline{\nu} \qquad (3.10)$$

The numerical values for molecules **1**, **3-6** are listed in Table 3.6. M_{ge} values are also shown for comparison. It is evident from the results that $M_{ee'}$ for **6** is significantly higher than **5**. This explains the enhancement of TPA cross section observed for molecule **6** over **5**.

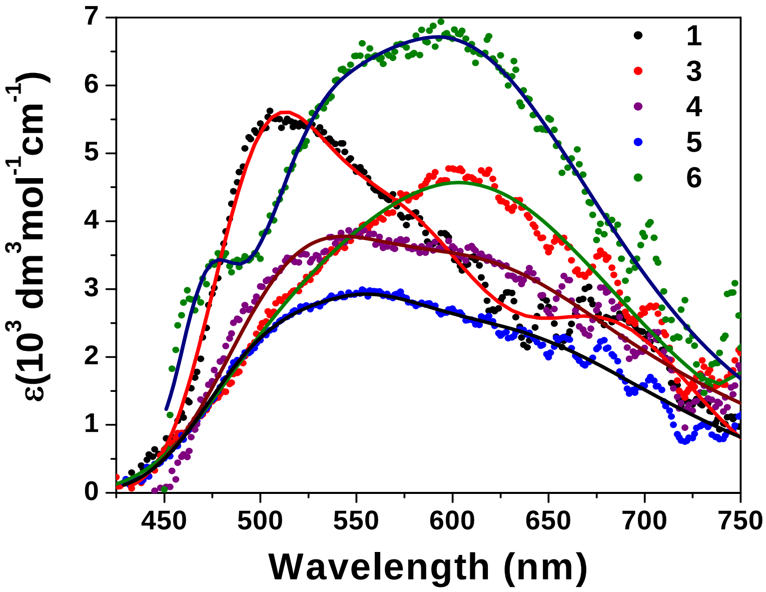

Figure 3.14. Excited state extinction coefficients for molecules **1, 3-6.**

Table 3.6. Excited state transition dipole moments for molecules **1, 3-6.**

Molecule (Symmetry)	M_{ge} **(D)**	$M_{ee'}$ **(D)**
1 (C_{3h})	11.8	4.7
3 (D_{2h})	19.3	4.5
4 (C_{2v})	18.9	4.3
5 (C_{2v})	18.3	3.7
6 (D_{3h})	17.6	6.0

Transient absorption measurements can also monitor the dynamics of excited states. By observing the changes in interaction of the excited state with the white light continuum as a function of time, it is possible to monitor excited state dynamics. This is illustrated with molecule **3** as an example. Figure 3.15 shows the transient absorption spectra of molecule **3** at different time delays from 150 fs to 30 ps after excitation at 425 nm. The spectrum at each time delay consists of a broad excited state absorption (ESA) in the range of 450 to 750 nm with a maximum around 610 nm. It can be noted from Figure

3.15 that the ESA features remain the same from 150 fs to 30 ps. This suggests that the symmetry of molecule **3** does not break, since no new states are observed. This explains the higher quantum yield of molecule **3** since the transition from the excited state to new state (if formed) would have to occur via nonradiative pathway. Kinetic decay trace of bowtie in DCM probed at 540 nm is shown in Figure 3.16. The decay trace has been fitted with a single lifetime of 2.5 ns which corresponds to the fluorescence lifetime of molecule **3**.

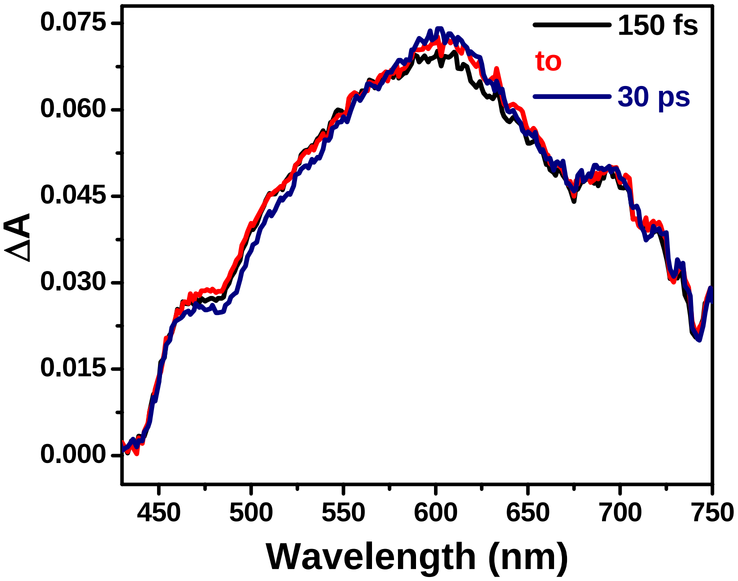

Figure 3.15. Transient absorption spectra of molecule **3** at different time delays from 150 fs to 30 ps.

Excited state absorption measurements carried out for chromophore **4** are shown in Figure 3.17. The spectrum at each time delay consisted of ESA with a maximum around 600 nm. As the time delay increases from 150 fs to 1.2 ps, ultrafast deactivation of immediate ESA has been observed with a growth of ESA in the blue wavelength region of 500 nm. Symmetry distortion in the excited state might be the reason behind ultrafast deactivation. As a result, a new intermediate symmetry state evolves which should influence the excited state transition dipole moment $M_{ee'}$. However, from excited state extinction coefficient measurements shown in Figure 3.14, it is clearly seen that the $M_{ee'}$ values for Bowtie and Boomerang are nearly identical. Thus, it can be inferred that this intermediate state does not enhance on $M_{ee'}$ in case of molecule **4**.

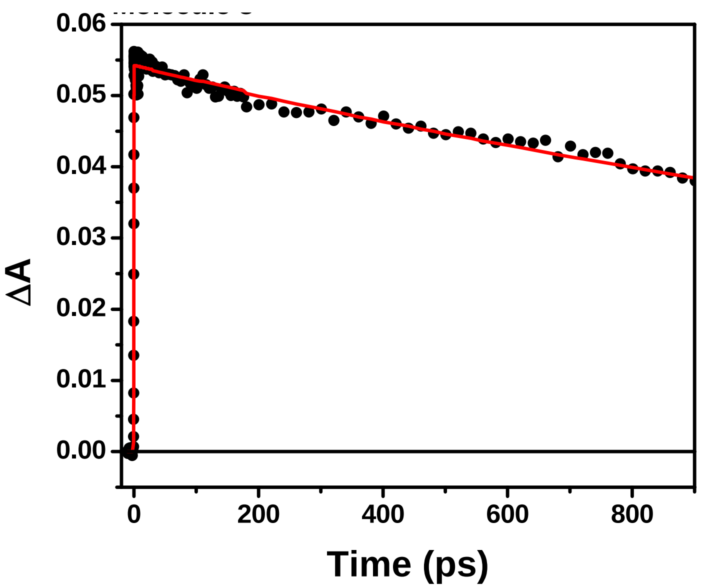

Figure 3.16. Kinetic decay trace of molecule **3** at 540 nm.

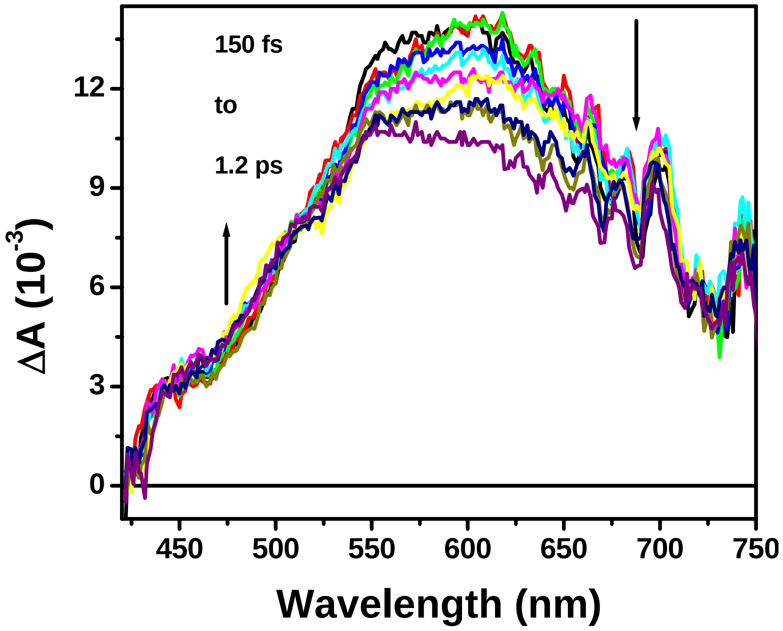

Figure 3.17. Transient absorption spectra at different time delays from 150 fs to 1.2 ps for molecule **4**.

Transient absorption results for annulene **5** are presented in Figure 3.18. There are two characteristic ESA features, one centered at 580 nm which shows decay with increasing time delay. The other feature at 465 nm shows growth. This, like Boomerang (annulene **4**), shows symmetry distortion. However, the value of $M_{ee'}$ for annulene **5** is lower than both **3** and **4**. This result indicates that the evolution of the intermediate has a somewhat deleterious effect on $M_{ee'}$.

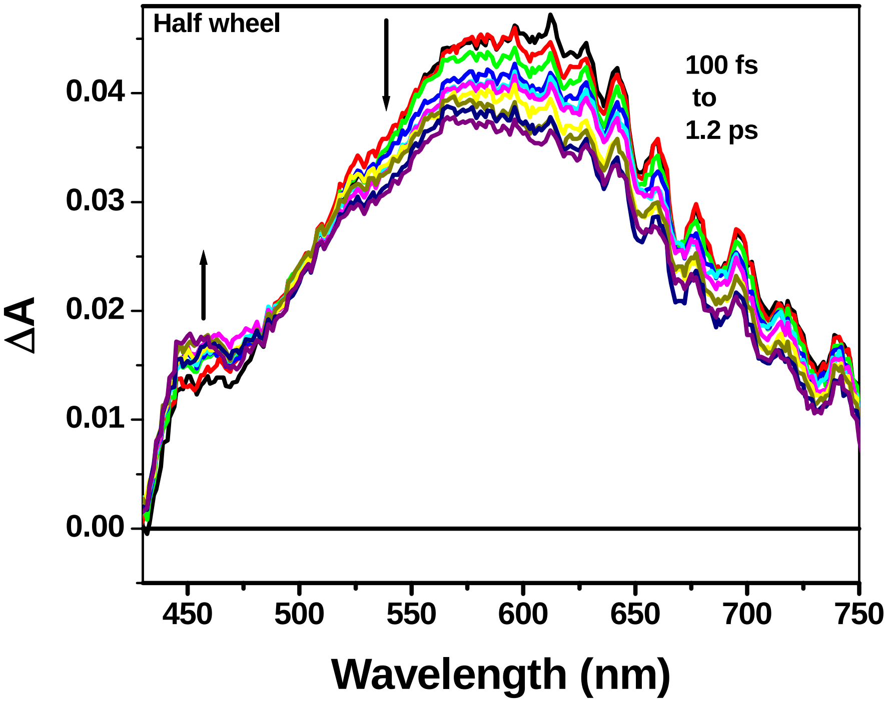

Figure 3.18. Transient absorption spectra of molecule **5** at different time delays from 100 fs to 1.2 ps.

The data from Table 3.4 shows that Radiation symbol (molecule **6**) has the largest TPA cross-section among all the investigated annulene networks. Transient absorption measurements have been carried out on Radiation symbol to understand the mechanism behind the increased TPA cross-section. Figure 3.19 shows the transient absorption spectra of radiation symbol at different time delays from 200 fs to 20 ps. Similar to linear molecule 2, the transient absorption features at initial time delay is quite different than those observed at later time delays. At an initial time delay of 200 fs, the ESA has a maximum around 540 nm while at later time delays the ESA has distinctly different absorption features with maxima centered on 480 and 530 nm. Global fit analysis shown in Figure 3.20 yielded three important time constants, one around 450 fs, another around 4.2 ps and a long lifetime component. These results suggest that the excited state dynamics of the radiation symbol is not simple and it consists of a non-radiative pathway to form an immediate excited state and the long lived component corresponds to the emitting state. The results are in accordance with the observed large Stokes shift and low quantum yield for **6**.

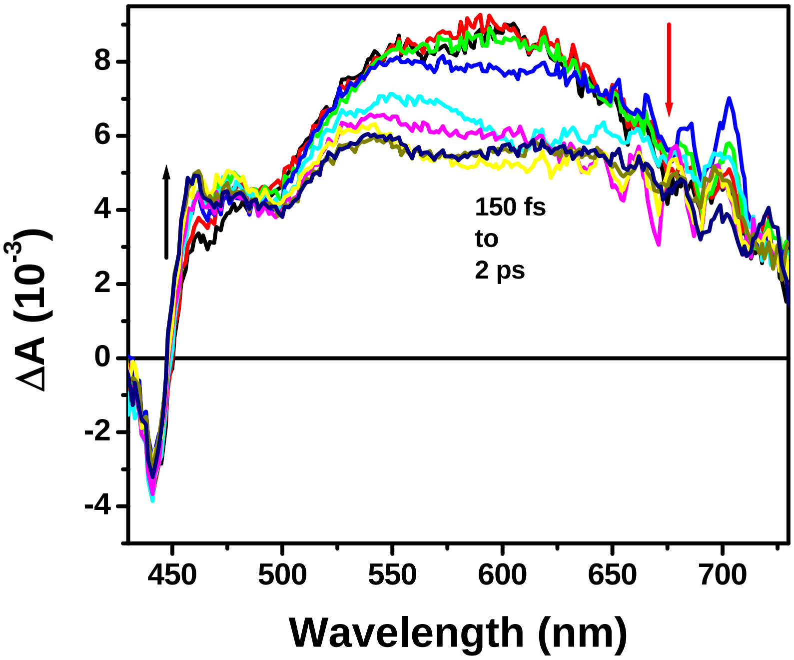

Figure 3.19. Transient absorption spectra at different time delay for Radiation symbol (annulene **6**).

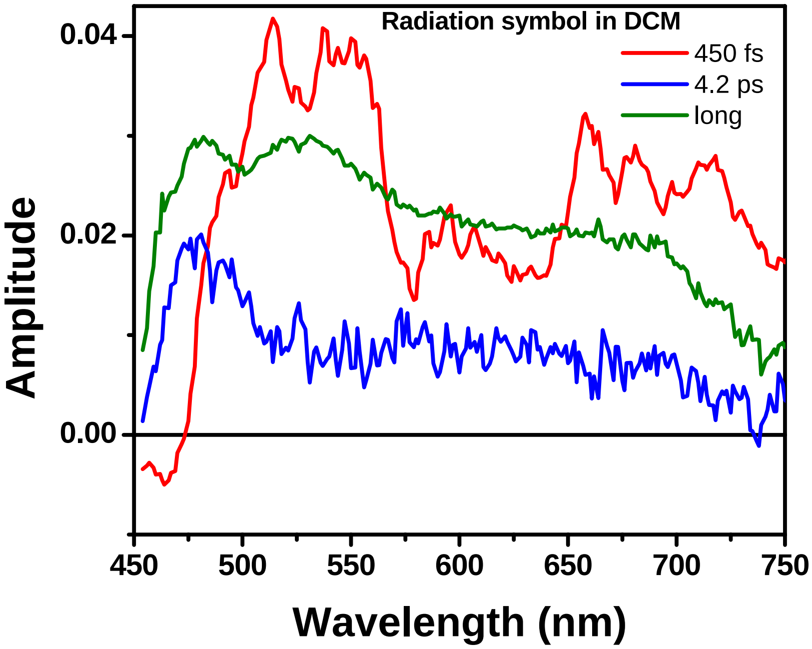

Figure 3.20. Species associated spectra of molecule **6.**

It is interesting to note that for all molecules that exhibit symmetry distortion, the lower energy ESA feature shows decay and the higher energy ESA feature shows growth. This indicates that with respect to ground state, the energy of the new state formed is lower than that of its parent state which decays. This is illustrated in Scheme 3.2.

Considering equation 3.8, this should reduce the value of $E_{ge'}$. However, only molecule **6** shows increased TPA cross section. Hence, it appears that the enhancement of $M_{ee'}$ rests on the degree of allowedness of the transition from ground state to the intermediate excited state. From excited state extinction coefficient measurements, it is evident that annulene **6** has the largest $M_{ee'}$ among all annulenes investigated. Hence, it appears that in this case, symmetry distortion enhances $M_{ee'}$ by increasing the degree of allowedness of the transition from g to e′. This is contrary to what has been observed with molecules **4** and **5**. Another interesting observation upon comparison between molecules **4**, **5**, and **6** is that annulene **6** has the highest order of symmetry. Hence, a molecule with lower symmetry could result in the formation of an intermediate excited state, but the transition dipole moment into that state may not be as strong as it would be for a molecule with higher order of symmetry. In other words, symmetry distortion might enhance $M_{ee'}$ only if the molecule has higher order of symmetry. Hence, transient absorption measurements are able to provide some explanation for the mechanism of enhancement of TPA cross section in the annulenes investigated in this study.

Scheme 3.2. Excited state absorptions from initial and intermediate excited states.

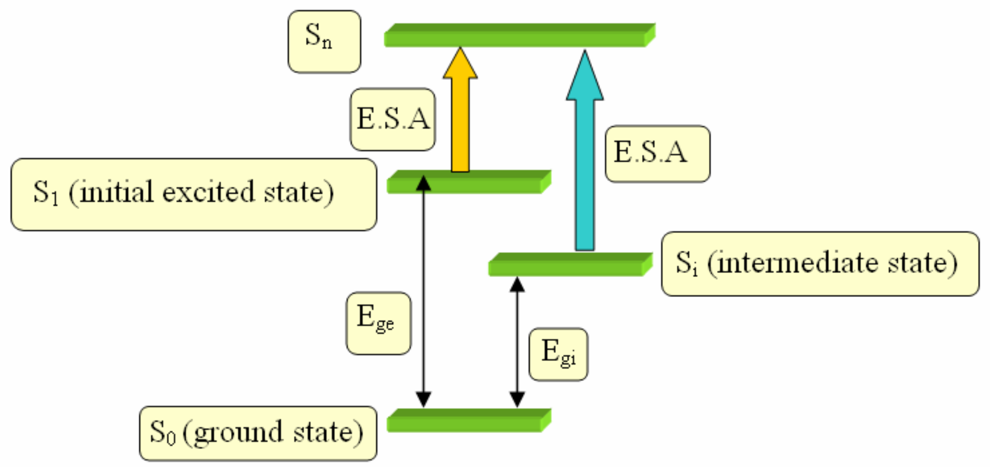

3.4. Conclusions

This study serves as an illustration of the building block approach. It also demonstrates one of the advantages of this approach in its ability to understand and project the nonlinear optical behavior of a large structure that is synthetically inaccessible, by breaking it down into smaller constituents. In the present study, the parent dodecahydrotribenzo[18]annulene served as the building block. It was demonstrated for the first time that besides that increasing the number of building blocks to increase the TPA cross sections, one could also change the arrangement of building blocks (and hence the symmetry) to improve TPA properties. TPEF measurements were used to quantify the TPA behavior of six model annulene networks. The trends observed in TPA cross section δ could not be explained by steady state measurements alone. Characterization of the excited state using transient absorption spectroscopy yielded excited state transition dipole moments ($M_{ee'}$) which explained the trends observed in δ. Transient measurements also proved beneficial in elucidating the mechanism of enhancement of TPA cross sections. A higher order of symmetry yields larger TPA cross section by virtue of symmetry breaking in the excited state.

Summary

- The building block approach enables us to investigate the nonlinear optical (NLO) properties of structures that are synthetically inaccessible.
- Arrangement of building blocks (symmetry) has a profound effect on the two-photon absorption (TPA) properties.
- It is possible to obtain large TPA cross sections using building blocks having small TPA cross sections, without having to resort to charge transfer approach.
- Steady state measurements were unable to explain the trends observed in TPA behavior.
- Transient absorption measurements enabled us to study the excited state properties, which elucidated the mechanism of enhancement of TPA cross sections in the annulene networks studied in this chapter.
- Since excited state studies involved examination of Franck-Condon state, the only means of accessing such information is by using femtosecond pulses.

3.5. References

1) Baughman, R. H. et al *J. Chem. Phys*. **1987**, *87*, 6687.
2) Narita, N.; Nagagi, S.; Suzuki, S.; Nakao, K. *Phys. Rev. B* **1998**, *58*, 11009.
3) Wan, B. W.; Brand, S. C.; Pak J. J.; Haley, M. M. *Chem. Eur. J* **2000**, *6*, 2044.
4) Tetsuo, M.; Narita, S.; Klein, D. J. *Chem. Phys. Lett.* **2005**, *402*, 554.
5) Tsai, F.-C.; Chang, C.-C.; Liu, C.-L.; Chen, W.; Jenekhe, S. A. *Macromolecules* **2005**, *38*, 1958.
6) Byrne, P. D.; Mueller, P.; Swager, T. M. *Langmuir* **2006**, *22*, 10596.
7) Carrasco, P. M.; Grande, H. J.; Milagros, C.; Alberdi, J. M.; Areizaga, J.; Pomposo, J. A. *Synthetic Met.* **2006**, *156*, 420.
8) Harima, Y.; Kim, D.-H.; Tsutitori, Y.; Jiang, X.; Patil, R.; Oyama, Y.; Ohshita, J.; Kunai, A. *Chem. Phys. Lett.* **2006**, *420*, 387.
9) Zhao, M.; Cui, Y.; Samoc, M.; Prasad, P. N.; Unroe, M. R.; Reinhardt, B. A. *J. Chem. Phys.* **1991**, *95*, 3991.
10) Thienpont, H.; Rikken, G. L. J. A.; Meijer, E. W.; ten Hoeve, W.; Wynberg, H. *Phys. Rev. Lett.* **1990**, *65*, 2141.
11) Matsuzaki, Y.; Nogami, A.; Tsuda, A.; Osuka, A.; Tanaka, K. *J. Phys. Chem. A* **2006**, *110*, 4888.
12) Eisler, S.; Slepkov, A. D.; Elliott, E.; Luu, T.; McDonald, R.; Hegmann, F. A.; Tykwinski, R. R. *J. Am. Chem. Soc.* **2005**, *127*, 2666.
13) Gubler, U.; Concilio, S.; Bosshard, C.; Biaggio, I.; Gunter, P.; Martin, R. E.; Edelmann, M. J.; Wytko, J. A.; Deidrich, F. I. *Appl. Phys. Lett.* **2002**, *81*, 2322.
14) Huijts, R. A.; Hesselink, G. L. J. *Chem. Phys. Lett.* **1989**, *156*, 209.
15) Wan, B. W.; Haley, M. M. *J. Org. Chem.* **2001**, *66*, 3893.
16) Hoshi, T.; Kobayashi, M.; Tanizaki, Y. *J. Am. Chem. Soc.* **1986**, *108*, 3867.
17) Hirata, Y.; Okada, T.; Mataga, N.; Nomoto, T. *J. Phys. Chem.* **1992**, *96*, 6559.
18) Grimsdale, A. C.; Mullen, K. *Angew, Chem. Intl. Ed.* **2005**, *44*, 5592.
19) Che, Y.; Datar, A.; Yang, X.; Naddo, T.; Zhao, J.; Zang, L. *J. Am. Chem. Soc.* **2007**, *129*, 6354.

20) Balakrishnan, K.; Datar, A.; Oitker, R,; Chen, H.; Zuo, J.; Zang, L. *J. Am. Chem. Soc.* **2005**, *127*, 10496.

21) Naddo, T.; Che, Y.; Zhang, W.; Balakrishnan, K.; Yang, X.; Yen, M.; Zhao, J.; Moore, J. S.; Zang, L. *J. Am. Chem. Soc.* **2007**, *129*, 6978.

22) Balakrishnan, K.; Datar, A.;Zhang, W.; Yang, X.; Naddo, T.; Huang, J.; Zuo, J.; Yen, M.; Moore, J. S.; Zang, L. *J. Am. Chem. Soc.* **2006**, *128*, 6576.

23) Zhang, X.; Zhang, X.; Zou, K.; Lee, C.-S.; Lee, S.-T. **2007**, *129*, 3527.

24) Marsella, M. J.; Piao, G.; Tham, F. S. *Synthesis*, **2002**, *9*, 1133.

25) Maciejewski, A.; Steer, R. P. *J. Photochem.* **1986**, *35*, 59.

26) Xu, C.; Webb, W. W. *J. Opt. Soc. Am. B.* **1996**, *13*, 481.

27) Sharma, P.; Vatsa, R. K.; Maity, D. K.; Kulshreshtha, S. K.; *Rapid Commun. Mass. Spectrom.* **2004**, *18*, 2383.

28) Bibler, N. E.; *J. Phys. Chem.* **1971**, *16*, 2436.

29) Katsumura, Y.; Buehler, R. E. *Radiat. Phys. Chem.* **1989**, *34*, 543.

30) Anand, S.; Varnavski, O.; Marsden, J. A.; Haley, M. M.; Schlegel, B. H.; Goodson, T. III *J. Phys. Chem. A* **2006**, *105*, 1305.

31) Rodriguez, J. G.; Tejedor, J. L. *J. Org. Chem.* **2002**, *67*, 7631.

32) Zheng, L.-S.; Lin, N.; Reid, S.; Wang, B. *Tetrahedron* **2007**, *63*, 5427.

33) Li, j.; Sun, M.; Bo, Z. *J. Polym. Sci. A* **2007**, *45*, 1084.

34) Shimizu, H.; Fujimoto, K.; Furusyo, M.; Maeda, H.; Nanai, Y.; Mizuno, K.; Inouye, M. *J. Org. Chem.* **2007**, *72*, 1530.

35) Xu, C.; Williams, R. M.; Zipfel, W.; Webb, W. W. *Bioimaging* **1996**, *4*, 198.

36) Beljonne, D.; Wensellers, W.; Zojer, E.; Shuai, Z.; Vogel, H.; Pond, S. J.; Perry, J. W.; Bredas, J.-L. *Adv. Funct. Mater.* **2002**, *12*, 631.

37) Kennedy, S. M.; Lytle, F. E. *Anal. Chem.* **1986**, *58*, 2643.

38) Sarkar, A.; Pak, J. J.; Rayfield, G. W.; Haley, M. M. *J. Mater. Chem.* **2001**, *11*, 2943.

39) Zhou, X.; Ren, A.-M.; Feng, J.-K.; Liu, J.-X. *Can. J. Chem.* **2004**, *82*, 1172.

40) Ramakrishna, G.; Singh, A. K.; Palit, D. K.; Ghosh, H. N. *J. Phys. Chem. B* **2004**, *108*, 12489.

Chapter 4

Investigation of Two-Photon Absorption Properties in Branched Architectures

4.1. Overview

This chapter deals with the investigation of nonlinear optical (NLO) properties of small chromophores arranged in branched architecture. The common link between chapter III and this chapter is the application of building block concept. The small branched chromophores studied in this chapter serve as building blocks for dendrimers. The first section of this chapter addresses fundamental structure-function relationships among branched chromophores such as branch length, nature of conjugation within a branch and strength of acceptor group at the periphery of the branch in an attempt to design the optimal building block for developing dendrimeric macromolecules tailored towards specific NLO applications.

The next section of this chapter addresses the fundamental reasons behind cooperative enhancement observed upon increasing the dimensionality of a molecule from a linear dipole to a tri-branched octupole. Cooperative enhancement refers to superlinear increase in two-photon absorption (TPA) behavior with increase in number of branches. A trimer, tris-4, 4', 4''-(4-nitrophenyl-ethynyl)triphenylamine (T-NPTPA) and its monomeric counterpart 4-N, N-dimethylamino-4'-nitrotolane (DMNAT) have been investigated to address the mechanisms behind cooperative enhancement.

The chapter concludes with the investigation of thiophene based dendrons for their NLO behavior. Such branched macro-architectures are considered as three-dimensional space filling pbjects and have the potential to serve as light harvesting and funneling systems. This completes the investigation of branched architecture from small building blocks to large dendrons.

4.2. Structure-Property Relationships in Novel Alkene and Alkyne Branched Chromophores

4.2.1. Background

The development of conjugated organic molecules with large two-photon absorption (2PA) cross-sections[1] is of broad interest to many areas of research. Much of the interest is driven by potential applications in 3D microfabrication[2-5], photodynamic therapy[6], two-photon microscopy[7-10], optical power limitting[11-12], and optical data storage[13-15]. In order to realize these applications, novel molecules with large 2PA cross sections in the visible, near infrared and telecommunication wavelengths are desired. Several design approaches have been reported for the synthesis of organic molecules with large 2PA cross-sections. Molecules with dipolar and quadrupolar character have been the focus of development[16-28]. Numerous dipolar chromophores have been synthesized with varying donor-π-acceptor configurations, as well as different π-bridging centers, and different donor-acceptor strengths in order to probe the structure and 2PA property relationships[1, 20, 22].

Recent investigations indicate that increasing the dimensionality of donor-π-acceptor molecules is a good approach as certain branched systems exhibit enhanced 2PA cross-sections over their linear counterparts[29, 30]. This is believed to be a consequence of cooperative interaction among the individual arms[30]. The interest in multiple branched systems for 2PA also stems from the fact that relatively large 2PA cross-sections may primarily be realized from low lying excited states. Consequently, considerable research has been carried out towards the design and synthesis of multiple branched chromophores. Several configurations such as donor-π-acceptor, donor-π-donor and acceptor-π-acceptor chromophores with different branching centers, tri and tetra branched structures have been synthesized and studied[29-50].

Mechanistic investigations aimed at understanding the factors that influence the magnitude of 2PA cross-section in multiple branched systems suggest that it is a complex interplay between intra-arm coupling, electronic delocalization, and extent of intramolecular charge transfer[37-44]. Belijonne et al[29] have suggested that within the exciton picture, the 2PA cross-section in octupolar molecules should scale by a factor of three in comparison to their dipolar counterparts by virtue of increased charge transfer among three arms. Cho et al[50] have theoretically shown that in branched molecules, the 2PA cross-section increases as the strength of donor-acceptor increases. Among several branching centers investigated in octupolar systems, triphenylamine systems were found to show better enhancement of 2PA cross-sections with increased branching[29-32]. Prasad and co-workers[30] have shown a seven fold enhancement of 2PA cross-section for trimer (PRL series) over its monomeric counterpart in a triphenylamine cored branched molecule. Macak et al[49] suggested that electronic coupling is nominal between the arms and vibronic coupling between the arms is significant in enhancing the 2PA of PRL series of dyes that they investigated. Mechanistic studies on the same series of dye molecules suggested that effective electronic delocalization[44] and increased amount of intramolecular charge transfer were possible reasons behind the enhanced 2PA cross-section. Also, several triphenylamine cored branched molecules have been synthesized with varying donor-acceptor strengths, substituents, and conjugation lengths in an attempt to study enhanced TPA behavior[30-33].

Though larger donor-acceptor strength is important for higher 2PA cross-section, the nature and length of π-linker does play a crucial role in increasing the 2PA cross-section and nonlinear optical (NLO) properties. It has been shown in dipolar chromophores that richer π-electron systems improve the intramolecular charge transfer character and therefore enhance the NLO properties[51]. Several π-bridging chromophores have been considered for improving the 2PA cross-section. Among them, alkene π-bridging is most widely studied and it has been suggested that in many of the linear systems, alkene-π-bridging is better over alkyne π-bridging[52-53]. However, due to several reasons pertaining to intra-arm electronic coupling, charge delocalization and charge transfer, the consequences of π-bridging on NLO and 2PA properties in branched systems may be different from the linear quadrupolar molecules[54-56]. It has been theoretically predicted from ab-initio calculations that the 2PA cross-sections of alkyne π-bridging containing quadrupolar molecules are not significantly different from their alkene π-bridging analogues[56, 57]. However, a systematic experimental study of 2PA in branched trimers with different π-bridging and the underlying mechanisms has not been reported.

In order to understand the effect of π-bridging, acceptor strength and conjugation length on 2PA cross-sections of multi-branched chromophores, a new set of triphenylamine cored branched molecules with pyridine as acceptors (molecules **A** to **D**, structures shown in Figure 4.1) have been investigated for their NLO behavior. Two-photon absorption cross-sections of these molecules have been measured by two-photon excited fluorescence and non-degenerate pump-probe techniques. Comparisons of 2PA cross-sections were also made with *N*, *N*, *N*-tris[4-{2-(4-{5-[4-(*tert*-butyl)phenyl]-1,3,4-oxadiazol-2-yl}phenyl)-1-ethenyl}phenyl]amine (**PRL-701**) and tris[4-(3', 5'-di-tert-butyldistyryl benzenyl) phenyl] amine (**N(DSB)$_3$**). The nature of π-bridging was varied from alkene (**A** and **C**) to alkynes (**B** and **D**). The conjugation length within individual branch was varied (**A** to **B**, **C** to **D**) and acceptor strength at the end of each branch (**B**, PRL-701 and N(DSB)$_3$) was also varied. Steady-state and time-resolved spectroscopic techniques have been employed to probe the mechanism of enhancement of 2PA. The observed 2PA cross-sections were correlated with the extent of intramolecular charge transfer, which was probed by femtosecond transient absorption spectroscopy. The results of 2PA measurements have shown that alkene-π-bridged chromophores have superior 2PA properties over the alkyne-π-bridged counterparts in the lower energy band. The observed trends were successfully correlated with the results from transient absorption spectroscopy. Further, increase in acceptor group strength and increase in conjugation length within a branch were also found to increase 2PA cross-sections.

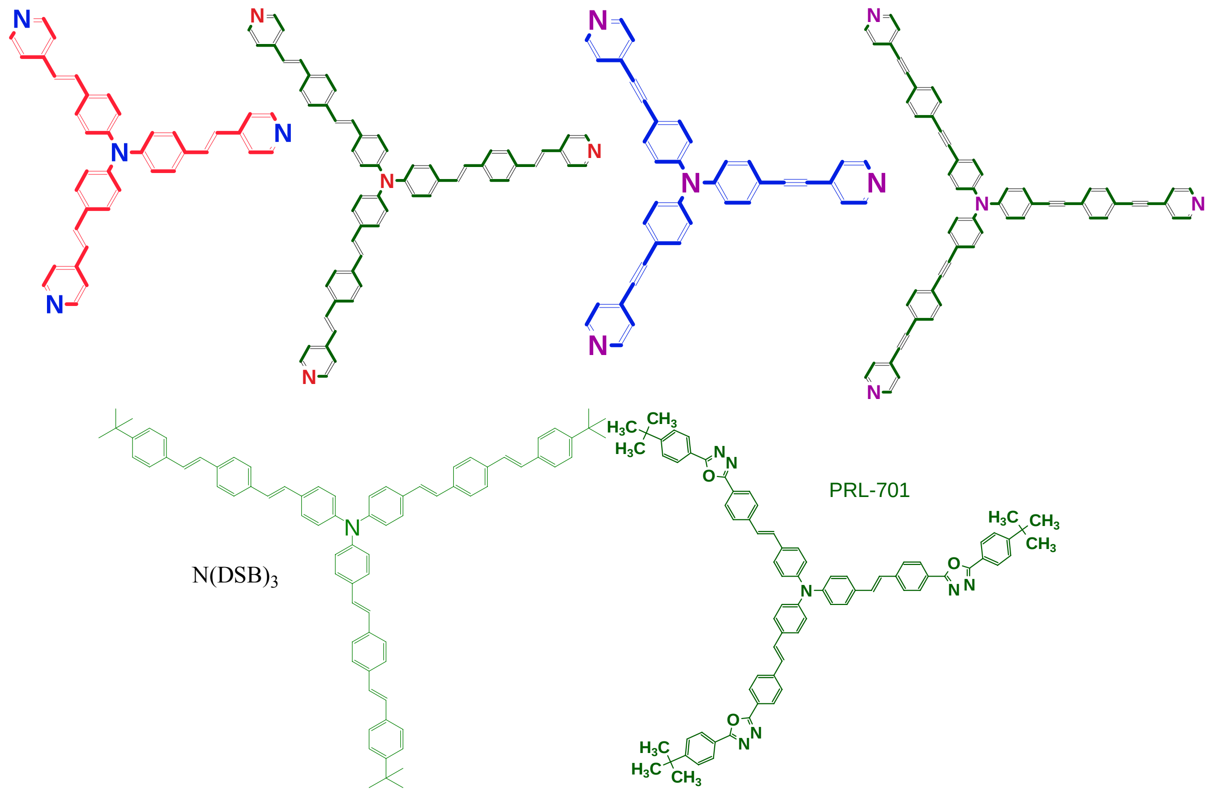

Figure 4.1. Chemical structures of branched chromophores studied.

4.2.2. Experimental Details

4.2.2.1. Synthesis of Chromophores

Professor Robert Twieg at Kent State University has synthesized chromophores A-D and was generous enough to provide us with these materials for spectroscopic characterization. Chromophores N(DSB)$_3$ was synthesized by Dr Ying Wang in our group and PRL-701 was obtained from Professor Paras Prasad's laboratory.

4.2.2.2. Steady State Measurements

All compounds were used as received without any further purification. They were dissolved in tetrahydrofuran (THF) (Sigma-Aldrich, spectrophotometric grade). The absorption spectra of the molecules were measured using an Agilent (Model # 8341) spectrophotometer. In order to measure molar extinction coefficients, the original stock solutions were diluted to 10^{-6} M. The emission spectra were acquired using a Shimadzu

RF-1501 instrument. The quantum yields of the molecules were measured using a known procedure[58]. Coumarin 307 was used as the standard. The absorbance was limited to equal to or less than 0.03. The solutions were purged with argon for 3 minutes prior to measuring their emission spectra. The following relation was used to calculate the quantum yields:

$$\phi_F = (\phi_F)_S \frac{\int J(\bar{\nu})d\bar{\nu}}{\int J_S(\bar{\nu})d\bar{\nu}} \frac{(J_a)_S}{J_a} \frac{n^2}{n_s^2} \tag{4.1}$$

These measurements may have some error due to sensitivity of the fluorescence spectrophotometer and other environmental conditions.

4.2.2.3. Two-Photon Excited Fluorescence Measurements

In order to measure the two photon absorption cross sections, we followed the two photon excited fluorescence (TPEF) method[59]. A 10^{-4} M Coumarin 307 solution in methanol was used as the reference. The laser used for these measurements was a Kapteyn Murnane (KM) mode-locked Ti: Sapphire laser. The bandwidth at 800 nm was 47 nm, and the pulse duration was ~30 fs. The input power from the laser was varied by using a polarizer. An iris was placed prior to the polarizer in order to ensure a circular beam. The beam from the polarizer was focused on the sample cell (quartz cuvette, 0.5cm path length) using a lens with a focal length of 11.5 cm. The fluorescence was collected in a direction perpendicular to the incident beam. A 1″ focal length planoconvex lens was used to direct the collected fluorescence into a monochromator. The output from the monochromator was coupled to a PMT. The photons were converted into counts by a photon counting unit. A logarithmic plot between collected fluorescence photons and input intensity gave a slope of two, ensuring a quadratic dependence between the same. The intercept enabled us to calculate the two photon absorption cross sections.

4.2.2.4. Non-Degenerate Two-Photon Absorption Measurements

In addition to the degenerate 2PA cross-sections taken at discrete wavelengths described above, the full non-degenerate 2PA spectra of the molecules were also obtained[60]. The femtosecond laser system employed was a CPA-2001 (CLARK-MXR) amplified Ti: Sapphire system operating at 775 nm with ~0.9 mJ/pulse, 140 fs pulses at a 1 kHz repetition rate. This laser in turn pumped two widely tunable optical parametric amplifiers (TOPAS, Light Conversion Ltd.). In this experiment, a strong (high irradiance) pump beam from TOPAS1 induced the nonlinearity in the sample and a weak probe beam from TOPAS2 monitored that nonlinearity. To be able to measure a wide spectral range of the 2PA spectrum, the probe beam used was a very broadband white-light continuum (WLC) pulse (400 -1700 nm) produced by focusing 1-2 μJ into a 2.5 mm thick piece of calcium fluoride. The two pulses, pump and probe, were overlapped in both space and time on the sample under investigation. In this non-degenerate experiment one photon from the pump and one photon from probe (within the broadband WLC) were simultaneously absorbed. By monitoring the transmission of the broadband WLC probe using a dual fiber input spectrometer (Spectro150, Acton) that was coupled to a dual diode array (Princeton Instruments DPDA 2048), we could ascertain the strength of the 2PA versus wavelength or equivalently the 2PA spectrum.

The pump wavelength was set to 1200 nm when acquiring the nonlinear absorption spectra to avoid any degenerate 2PA of the pump itself. This was done for the purpose of avoiding any spurious excited state absorption following 2PA of the pump beam itself. The non-degenerate will exhibit larger 2PA cross-sections than those found by degenerate excitation due to pre-resonance enhancement effects[61]. The magnitude of this enhancement is determined by the photon energies of the pump and probe and the transition energies of the one- and two-photon allowed states. Using equation (2) in reference 61, the transition energies of the lowest lying one-photon allowed states as determined from the linear absorption spectra, and the energies of the higher lying two-photon allowed states extracted from the nonlinear absorption spectra, an enhancement factor due to non-degenerate excitation was determined. Although this factor did show some dispersion over the region of interest (i.e. 380 – 450 nm), the effect is small and the factor was found to be approximately 2.0 over this range. Therefore, non-degenerate excitation will exhibit a two times increase in the strength of 2PA compared to degenerate excitation. The values of the non-degenerate cross-sections, discussed later, have been scaled by this factor for a more direct comparison with the values of the degenerate 2PA cross-sections.

4.2.2.5. Fluorescence Lifetime Measurements

Time correlated single photon counting (TCSPC) measurements were performed in order to determine the lifetimes of the branched structures investigated. For the set-up used in our lab (Figure 4.2), the laser used was the same as for TPEF measurements (Kapteyn-Murnane Ti: Sapphire oscillator). The 800 nm output was frequency doubled using a BBO crystal. The resulting second harmonic signal was passed through a cut-off filter in order to remove 800nm fundamental beam. A beam splitter directed a small portion of the beam into a phtotodiode which served as the "starting" of optical signal. The waveplate **P** ensured horizontal polarization of excitation beam. The 400nm radiation was focused on the sample cell using a lens. The resulting fluorescence photons were collected in a direction perpendicular with respect to excitation in order to avoid noise due to 400nm radiation. A collection lens collimated the beam into the entrance of a monochromator in order to separate fluorescence from excitation. The fluorescence was then detected by the "stop" PMT, which was connected to a photon counting module that controlled the multichannel analyzer (MCA) and other electronic modules of the experiment. Using software (Fluorofit®), the decay profile obtained could be fitted with exponentials and hence the fluorescence lifetime of the chromophore could be obtained.

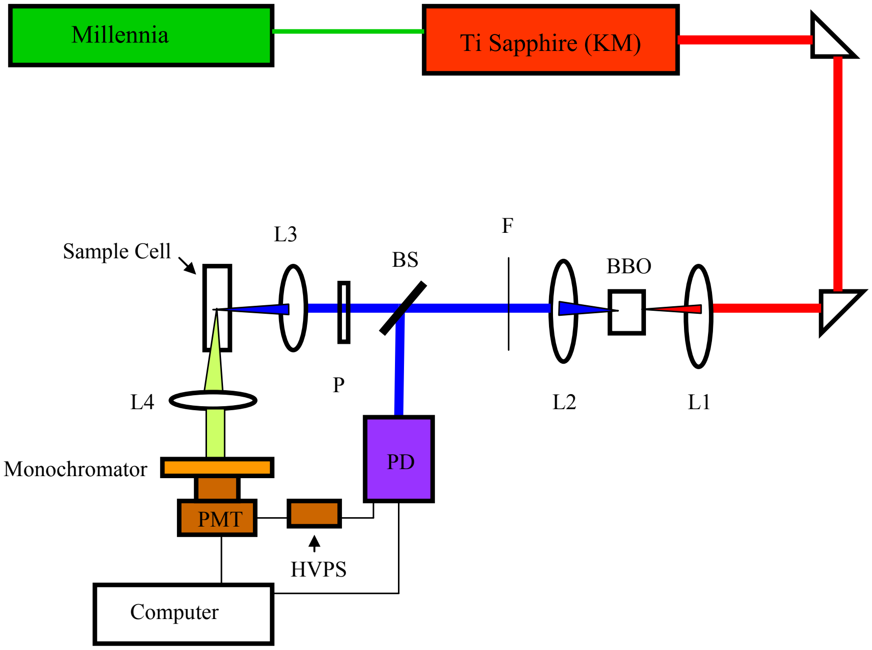

Figure 4.2. Time correlated single photon counting (TCSPC) set-up used in our lab.

4.2.2.6. Ultrafast Transient Absorption Measurements

Femtosecond transient absorption investigations have been carried out using ultrafast pump-probe spectrometer detecting in the visible region. Briefly, 1 mJ, 100 fs pulses at 800 nm with a repetition rate of 1 kHz were obtained from Nd:YLF(Empower) pumped Ti:Sapphire regenerative amplifier (Spitfire, Spectra physics) with the seed pulses from Millennia pumped Ti:Sapphire oscillator (Tsunami, Spectra physics). The output of laser beam was split to generate pump and probe beam pulses with a beam splitter (85% and 15%). The pump beam was produced by an optical parametric amplifier (OPA-800). The pump beam used in the present investigation, i.e., 420 nm, was obtained from the fourth harmonic of the idler beam and was focused onto the sample cuvette. The probe beam was delayed with a computer controlled motion controller and then focused into a 2 mm sapphire plate to generate white light continuum. The white light was then overlapped with the pump beam in a 2 mm quartz cuvette containing the sample and the change in absorbance for the signal was collected by a CCD detector (Ocean optics). Data acquisition was controlled using the software from Ultrafast systems inc. Typical power of probe beam is < 0.1 μJ while the pump beam is around ~0.5 to 1 μJ per pulse. Magic angle polarization was maintained between the pump and probe using a wave plate. The pulse duration was obtained from fitting of the solvent response, which was ~130 fs. The sample was stirred by a rotating magnetic stirrer.

4.2.3. Results and Discussion

4.2.3.1. Optical Absorption and Steady State Fluorescence Measurements

The linear and nonlinear optical properties of all the branched systems are summarized in Table 4.1. The optical absorption and emission characteristics of all compounds in THF are shown in Figure 4.3. One notes the expected shift in the absorption maximum to longer wavelengths upon comparing from **A** to **B** and from **C** to **D** due to increase in conjugation length. Also, the absorption maxima of alkyne π-bridged compounds are blue shifted relative to their alkene counterparts. This could be due to the fact that in the alkene chromophores, all the carbon atoms on the branches are sp^2 hybridized. However, in the case of the alkyne chromophores, the carbon atoms are both sp and sp^2 hybridized. This could result in poorer π-orbital overlap and mismatch in energies of the π orbitals[66-67]. It should also be noted from Table 4.1 that as the acceptor strength increases (from tert-butyl benzene to dioxazole to pyridine) the Stokes shift increases (4206 cm^{-1} for the alkene system **B** is higher compared to two previously reported nitrogen centered chromophores ($N(DSB)_3$ and PRL-701)[44] where the pyridine group is replaced by *t*-butyl and oxadiazole groups respectively). The increase in Stokes shift can be attributed to increase in charge transfer character of the respective chromophores. For the molecules with same acceptors, alkene π-bridged chromophores were found to have higher Stokes shift than alkyne π-bridged chromophores.

Table 4.1. Summary of linear and nonlinear optical properties of the chromophores.

Molecule	**λ_{abs}(nm)**	**λ_{em}(nm)**	**δ (GM)**	**η**	**τ_r (ns)**	**M_{ge} (D)**
A	406	479	[a]370 (187)	0.23	10	3.3
B	426	519	[a]1037 (812)	0.26	8	3.9
C	377	428	[b]91 (102)	0.58	2.7	5.6
D	391	455	[a]280 (283)	0.55	2.7	5.8
$N(DSB)_3$	419	484	[a]270	0.48	3	5.9
PRL-701	422	502	[a]491	0.51	2.9	5.5

[a]800 nm excitation, [b]770 nm excitation. Values in parentheses are from non-degenerate pump probe measurements; λ_{abs}, λ_{em} are absorption and emission maxima respectively; δ is 2PA cross-section, η is the fluorescence quantum yield; τ_r is the radiative lifetime and μ is the emission transition dipole moment calculated from Strickler-Berg formula[68].

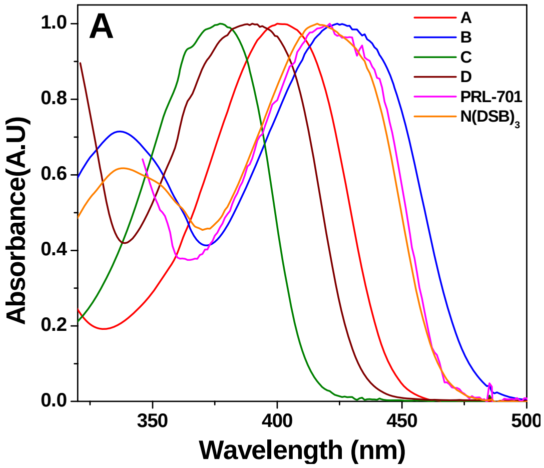

Figure 4.3. A) Absorption spectra and B) Fluorescence spectra of the investigated branched molecules.

Fluorescence quantum yield and fluorescence lifetimes (using time-correlated single photon counting) have been determined for all the molecules. The alkyne π-bridged chromophores showed approximately twice the quantum yield than their alkene counterparts (Table 4.1). From lifetimes of the excited states, radiative lifetimes and emission transition dipole moments (μ) have been determined and are provided in Table 4.1. It can be noted that the alkene π-bridged chromophores **A** and **B** have lower μ than their alkyne counterparts **C** and **D**. It is also noteworthy that conjugation length does not have a significant impact on the radiative lifetimes of these chromophores. Based on the optical absorption measurements (extinction coefficients and area under the absorption curves), the absorption transition dipole moments (M_{ge}) have also been calculated. An increase in the conjugation length is found to increase the M_{ge}. The acceptor strength does not seem to play a major role in determining M_{ge}, while it does have a significant impact on the observed Stokes shift. Based on the transition dipole moments calculated from steady-state measurements, it appears that the alkyne π-bridged branched chromophores would have greater 2PA cross sections than their alkene analogues. On the other hand, the trend observed from Stokes shift measurements show that the alkene-π-bridged chromophores would have higher 2PA cross-sections than the alkyne counterparts. This suggests that steady-state measurements alone cannot explain the trends observed in branched chromophore systems, and time-resolved techniques should be employed to elucidate the observed trends in TPA behavior, which will be discussed next.

4.2.3.2. Two-Photon Absorption Cross Section Measurements

Two-photon absorption cross-section measurements have been carried out using two-photon excited fluorescence (TPEF) as well as non-degenerate 2PA method. Figure 4.4 shows the 2PA cross-section spectrum for chromophores **A** through **D**, the cross-sections (δ) are plotted versus transition energy expressed in wavelength. As a comparison, the 2PA cross-section maxima over 770-800 nm (at the maximum of lowest energy absorption band) for the molecules are listed in Table 4.1 as well (shown in parentheses are the non-degenerate 2PA cross-sections at those wavelengths). It is worth reiterating that non-degenerate measurements show larger 2PA that TPEF results at equivalent wavelengths for degenerate excitation. For this reason the values in Table 4.1 have been reduced by an appropriate scaling factor to make a more direct comparison with the degenerate 2PA cross-sections[61].

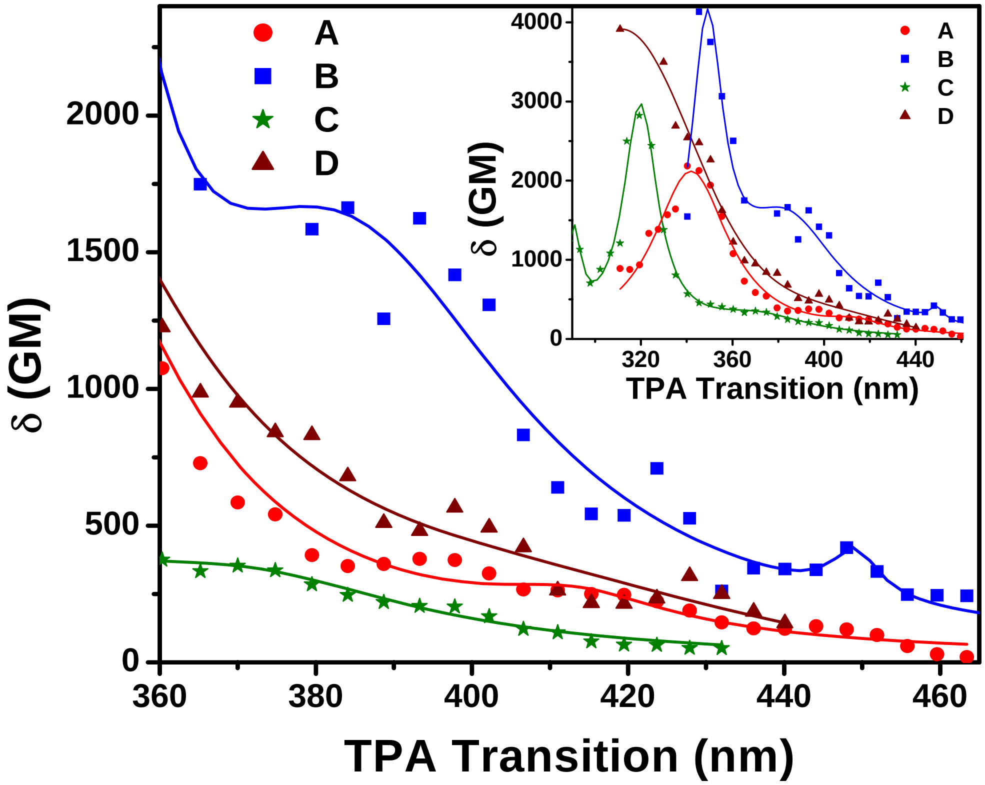

Figure 4.4. Non-degenerate 2PA spectra of the molecules in the low energy absorption band. Inset shows the entire spectrum. The lines are shown as guides for the eye.

There are several comparisons that can be made regarding the 2PA properties observed in these systems. First, a comparison between the linear and nonlinear absorption spectra reveals that all the molecules exhibit substantial 2PA into the lowest energy absorption band (i.e. 380 – 450 nm) and can be attributed to relaxed symmetry restrictions in these systems. There also exists a stronger, higher energy two-photon allowed state which lies in between the two one-photon bands (inset of Figure 4.4), which has been attributed to strong electronic coupling between the branches. Furthermore, the trends observed for both the degenerate and non-degenerate 2PA cross-sections in Table 4.1 are quite similar. The two alkene containing systems (**A** and **B**) differ only by an increase in the conjugation length of the individual arm by one vinyl unit. In the lowest energy absorption band, one observes a three-fold increase in 2PA cross section for **B** in comparison to **A**. The same trends can be noted for compounds **C** and **D** which contain alkynes. This effect of increasing conjugation length on 2PA cross-section has been well documented in the literature[69, 70]. Increase in conjugation reduces the detuning term (the energy difference between the ground and first excited state and the ground and TPA state) in the sum-over-states expression[29] and also increases the transition dipole moment. As a result of these two contributions, the 2PA cross section increases significantly. Comparing chromophores **B** and **D**, which contain similar chromophore density, it is clearly seen that the 2PA of the alkene branched system **B** is approximately 3.7 times higher than its alkyne counterpart **D**. Similarly, the ratio of 2PA cross-section between **A** and **C** is 4. A direct comparison between molecular systems can be made by normalizing the cross-sections listed in Table 4.1 to their respective molecular weights. Still, the alkene chromophores show a 4-fold increase in 2PA cross section when compared to the corresponding alkynes at the low energy peak.

The influence of acceptor strength is also seen from the results presented in Table 4.1. As the acceptor unit is changed from t-butyl benzene to oxadiazole in $N(DSB)_3$ to PRL-701 respectively, a substantial increase in 2PA cross-section is observed. This effect is more pronounced when a stronger acceptor, namely pyridine, is introduced in molecule **B**. The argument that acceptor strength increases from t-butyl benzene to pyridine can be verified from their Hammett constants[71]. Chromophore **B** has four times higher δ than $N(DSB)_3$. These observations can be attributed to increased acceptor strength that imparts higher amount of charge transfer character. It has been shown theoretically by Cho et al[49] that the 2PA cross-section increases with increase in donor or acceptor strength. The measurements presented here show that the extent of charge transfer character is important in increasing the 2PA cross-section.

A surprising trend is observed when considering the high energy two photon absorption band shown in the inset of Figure 4.4. When compare **A** and **B** are compared, there is an increase in the 2PA cross-section by a factor of 2 and about 1.5 when **C** and **D** are compared, suggesting the effect of conjugation length. As the conjugation length is increased, the absorption transition dipole moment also increases (Table 4.1) and the detuning factor decreases, thereby increasing the 2PA cross-section. It is interesting to see the trend observed in 2PA cross-section to high energy states for alkene and alkyne π-bridging branched chromophores. When **A** and **C** are compared, the alkyne π-bridged chromophore **C**'s cross-section is ~1.4 times higher than its corresponding alkene analogue (**A**). As mentioned above, the expected trend in transition moments suggests that the TPA in the alkene systems is larger. This is contrary to what the steady-state results indicate. However, ultrafast time-resolved measurements, which provide information on excited state characteristics, are able to probe these differences. It is to be noted here that when 2PA cross-section to higher energy states are concerned, it involves the knowledge of excited state transition dipole moments (from sum over states formalism). Estimates of excited state transition dipole moments can be obtained from ultrafast transient absorption measurements, and the results obtained from the same will be discussed next.

4.2.3.3. Transient Absorption Measurements

Among all the investigated trimers, trimer **B** showed largest 2PA cross-section in comparison to other chromophores. By changing the bridging unit from alkyne to alkene there is a substantial increase in 2PA cross-section. The 2PA cross section also increases with increase in acceptor strength. Thus, it is evident that the charge transfer character of the molecules plays an important role in 2PA behavior. Steady-state measurements by virtue of absorption, emission transition dipole moments and Stokes shifts were unable to provide a conclusive explanation for the observed differences in 2PA cross-section of alkene and alkyne π-bridging molecules. Thus, we evaluated the extent of charge transfer in the excited state as well as excited state transition dipole moments by ultrafast pump-probe measurements. In order to illustrate the importance of extent of intramolecular charge transfer (ICT) in the excited state immediately after photo-excitation on the 2PA cross-sections, ultrafast transient absorption measurements on molecules **A** thru **D** were carried out. Shown in Figure 4.5 A are the transient absorption spectra at different time delays (from 150 fs to 26 ps) for trimer **B** in THF. At 150 fs, bleach in the region of 450 to 540 nm and a positive transient at λ>540 nm are observed. The bleach centered at ~470 nm can be ascribed to the stimulated emission from the ICT state of trimer. The positive absorption is attributed to the excited state absorption (ESA) arising from the ICT state.

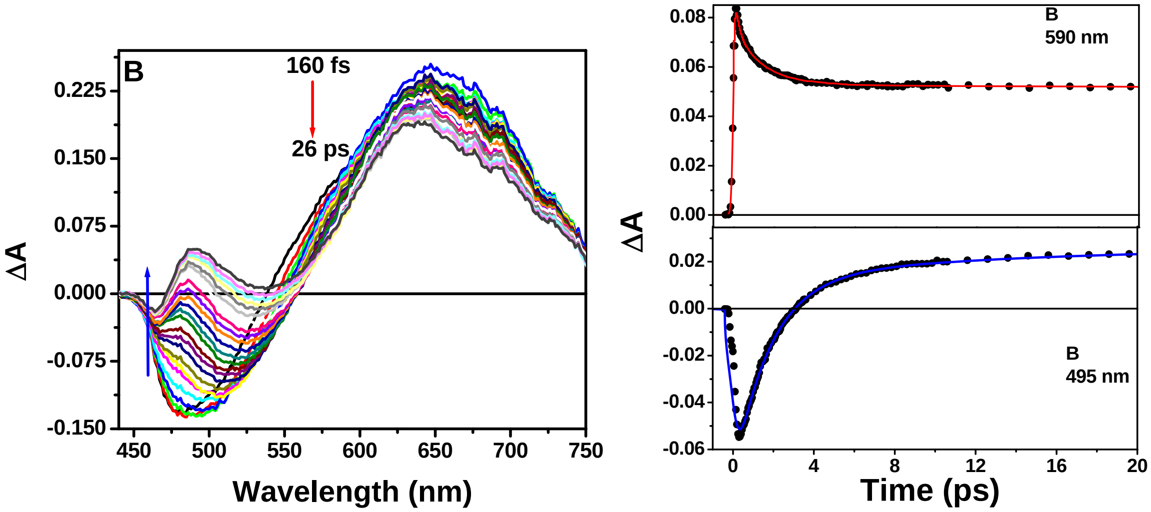

Figure 4.5. A) Transient absorption spectra for **B** in THF at different time delays. B) Kinetics at 590 nm and 495 nm.

The observation of stimulated emission and ESA from ICT state at a time delay of 150 fs suggests that the internal conversion from the initially populated C_3 symmetry state to charge localized ICT state happens much faster than 100 fs which indicates that the Franck-Condon (FC) state and the ICT state are intimately linked by the same reaction coordinate. However, as the time delay is increased to 26 ps, a new transient starts to grow in the region of 460 to 540 nm with a decay of ESA of the ICT state. Population of this transient was found to increase with increasing polarity of the solvent and strength of donor/acceptor. Thus, this ESA was ascribed to that of the solvent and conformationally stabilized ICT state (ICT' state). It is to be noted here that ICT′ state is non-emissive and can be ascribed to a twisted intramolecular charge transfer state. The kinetic traces shown in Figure 4.5B show that the decay of ICT state matches with the growth of ICT' state and that they constitute a predecessor-successor pair. Global fit analysis of all the decay traces has yielded two time constants of 2.8 ps and >1 ns. The time constant of 2.8 ps has been ascribed to the time scale of internal conversion from ICT state to ICT' state whereas >1 ns time constant is ascribed to the excited state lifetime.

Transient absorption measurements have also been carried out on trimer **D** dissolved in THF and the corresponding transient absorption spectra are shown in Figure 4.6A. At the initial time delay, bleach in the region of 450 to 500 nm and a positive absorption greater than 500 nm with a maximum around 560 nm is observed. The bleach has been ascribed to stimulated emission from the ICT and the positive absorption to ESA of ICT state. Ultrafast charge localization from FC state to ICT state has been observed here as well, suggesting that the FC and ICT states are linked by the same reaction coordinate.

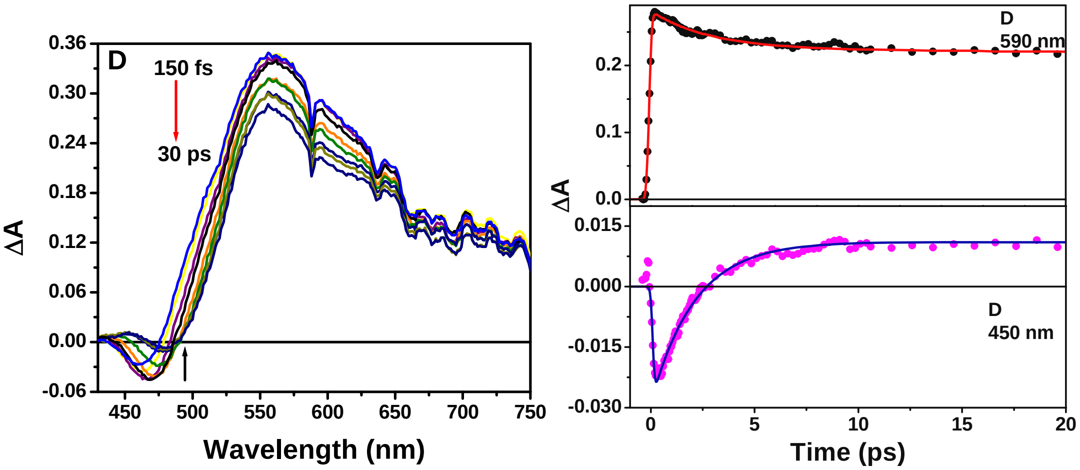

Figure 4.6. A) Transient absorption spectra of **D** in THF at different time delays. B) Kinetics of the transients at 590 nm and 450 nm.

Similar to what was observed for trimer **B**, formation of a new transient is observed as the time delay is increased to 30 ps although the amplitude of the observed new transient is small. Evolutions of the transients are better viewed by following the kinetic decay traces at 450 nm and 590 nm as shown in Figure 4.6B. Kinetics at 450 nm shows the presence of the new transient state and its growth matches well with the decay of ESA at 590 nm. This new transient can once again be attributed to the ESA of ICT' state. Global fit analysis has yielded two time constants of 2.1 ps and >1 ns similar to what has been observed in case of **B**. However, it is interesting to note that the population of this ICT' state is different for **D** and **B**; it is higher in case of **B** over **D** in the same solvent. As mentioned above that the population of ICT' state depends on the polarity of the solvent and strength of acceptor. Thus, it can be used as an indicator of the amount of charge transfer in the excited state of the trimers. Figure 4.7 shows the comparison of the population of ICT' to ICT state for **B** and **D** in THF at a time delay of 30 ps. Under similar solvent polarity (THF), the population of ICT' state can be directly ascribed to the degree of charge transfer character. It can be observed from Figure 4.7 that the amplitudes of ICT' states for the alkene branched system **B** is much higher in comparison to alkyne branched system **D** in the same solvent. This result suggests that the amount of charge transfer in case of B is larger than D. As the 2PA cross-section mainly concerns with the FC state, the amount of charge transfer concerning the FC state has a significant impact on 2PA cross section.

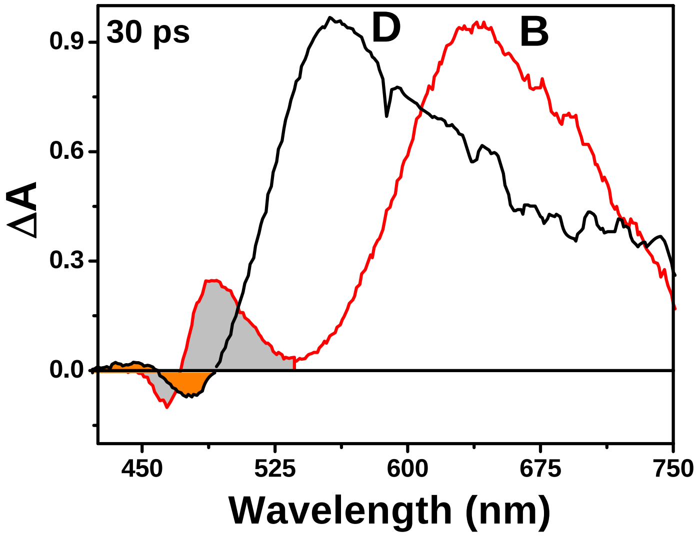

Figure 4.7. Comparison of the ICT' states for trimers **D** and **B**. It can be observed that the population of ICT′ for **B** is higher than **D**.

The FC and ICT states are intimately linked by the same reaction coordinate by virtue of ultrafast charge localization from FC to ICT state. Hence, one can extrapolate the extent of charge transfer observed in ICT state to the FC state[72, 73]. The results thus confirm that the extent of charge transfer in the alkene-branched system **B** is higher than **D** and thereby it displays higher 2PA cross-section. The result of a larger δ for **B** in comparison to **D** was somewhat surprising as one also notes the increase in quantum yield and calculated transition dipole moments for the alkyne system **D**. However, the magnitude of δ in alkyne π-system **D** is significantly smaller than that observed for the alkene $\pi-$system **B** and this mainly involves the issue of the increased CT character and stronger delocalization. This conclusion is obtained from time-resolved transient absorption measurements as the steady-state measurements favor a larger cross-section for **D** instead of **B**.

Another important aspect that has been observed in 2PA cross-section measurements is that as the acceptor strength is increased, the 2PA cross-section also increases. This can be mainly ascribed to the CT of both ground and excited states. It is well known that greater acceptor strength results in greater degree of charge transfer in a donor-acceptor type system and thereby larger nonlinear optical properties. It has been demonstrated earlier in this section that the extent of CT in the excited state can be monitored by femtosecond pump-probe spectroscopy. Similar transient absorption measurements have been carried out to understand the effect of acceptor strength on 2PA cross-section. Shown in Figure 4.8 are the transient absorption spectra of PRL-701 and $N(DSB)_3$ in acetonitrile (3D representation of the ESA spectra) in which PRL-701 has shown larger 2PA cross-section by virtue of larger acceptor strength. Upon comparing $N(DSB)_3$ and PRL-701, with PRL-701 having the stronger acceptor in oxadiazole molecule, it is clearly seen that the ratio of ICT':ICT population is greater for PRL-701, suggesting that the amount of CT in case of PRL-701 is higher than $N(DSB)_3$.

Also, estimates of excited state extinction coefficients have been made for the chromophores **B** and **D** under actinometric conditions using ultrafast transient absorption spectroscopy. It has been observed from our transient measurements that the excited state extinction coefficient of chromophore **B** is ~2.5 times larger than that of **D**. Using excited extinction coefficients and the area under the curves of ESA spectra, we have determined the excited state transition dipole moments. It was found that the values for the same was ~1.5 times higher for alkyne branched chromophore **D** in comparison to alkene branched chromophore **B**. Higher excited state transition dipole moment contributes mainly to the 2PA into the higher energy two-photon absorption bands.

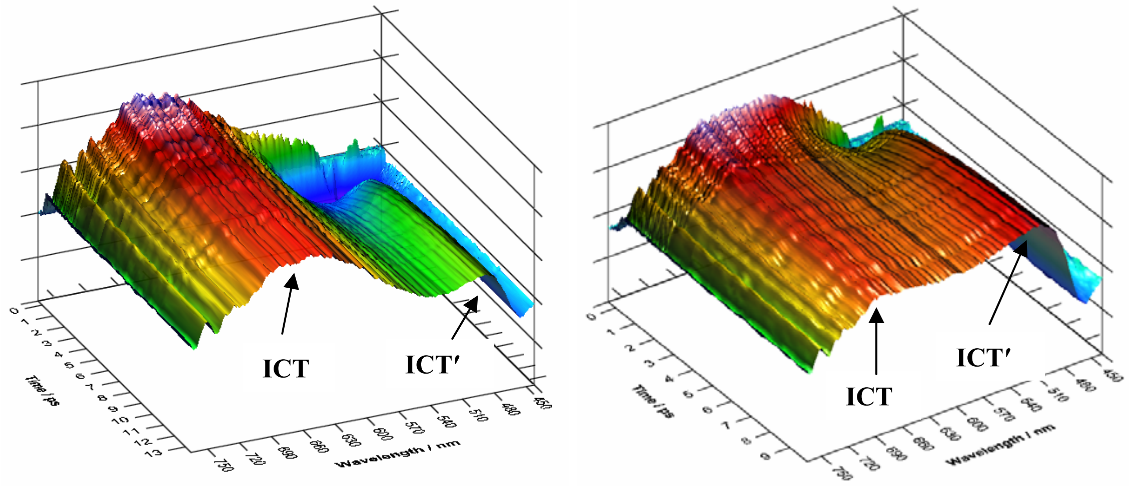

Figure 4.8. Comparison of the ICT′ states' populations for molecules N(DSB)$_3$ and PRL-701 in acetonitrile. It can be observed that ICT′: ICT is greater for PRL-701.

4.2.4. Factors Influencing TPA Cross Sections and Rationale

As mentioned in the introductory section, several parameters influence the effective 2PA cross-sections of molecules. Within the framework of sum-over states model[29], the TPA cross-section into lowest energy absorption band for non centro-symmetric molecules can be expressed as

$$\delta_{2-state} \propto \frac{M_{ge}^{2}\Delta\mu_{ge}^{2}}{\Gamma} \qquad (4.2)$$

And for 2PA into high lying states which are not dipole coupled to ground state can be written as:

$$\delta_{3-state} \propto \frac{M_{ge'}^{2}M_{ee'}^{2}}{(E_{ge}-E_{ge'}/2)^{2}\Gamma} \qquad (4.3)$$

Here, M_{ge}, $M_{ge'}$ are transition dipole moments from ground state to excited states e and e' respectively. E_{ge}, $E_{ge'}$ are the corresponding transition energies from ground state to e and e' states respectively. Γ is the damping factor. Equation 4.2 is the dipolar term while equation 4.3 is the two-photon term in the complete sum-over states model. Under this model, the 2PA cross-section to the low-lying excited state of chromophores containing charge transfer states is mainly controlled by three important parameters: the excitation energy, oscillator strength and change in dipole moment related to low-lying CT state[29]. For the higher energy 2PA states, along with these parameters it is also controlled by the excited state transition dipole moment. Present 2PA cross-section measurements of triphenylamine cored branched molecules have displayed some interesting magnitudes of 2PA cross-section with respect to the nature of substituents.

4.2.4.1. Effect of Conjugation Length

The two alkene π-bridge containing systems (**A** and **B**) differ by an increase in the conjugation length of the branch and concurrently one observes ~ three-fold increase in 2PA cross section for **B** in comparison to **A**. The same trend can be noted for compounds **C** and **D,** both containing alkyne π-bridges. It can be observed from Table 4.1 that as the conjugation length is increased, there is a clear red shift in the optical absorption and emission spectra for both alkene and alkyne linked molecules. The Stokes shift also increases with increase in conjugation length, indicating an increase in effective conjugation length. All these parameters result in increase of the oscillator strength of absorption band[70, 71] and the transition dipole moment of the absorption. Also, the shift of absorption to longer wavelengths with increase in conjugation decreases the detuning energy present in the two-photon term, (equation 4.3) thereby enhancing the 2PA cross-section.

4.2.4.2. Acceptor Strength

With increasing acceptor strength from $N(DSB)_3$ to PRL-701 to **B**, there is enhancement in two-photon absorption cross-section. Unlike quadrupolar molecules, where the one-photon allowed states are not two-photon allowed, in multi-branched chromophores, the low lying states are both one and two-photon allowed. In such a situation, one-photon photophysics and excited state deactivation can be correlated with the observed two-photon absorption cross-sections. Although the enhancement of 2PA cross-sections through substitution with electron-withdrawing and electron donating groups is well established both experimentally and theoretically, the electronic origin of the enhancement is not yet fully understood[29]. In the present investigation, through our transient absorption measurements, we have shown that as the acceptor strength is increased, the extent of charge transfer in the FC state increases This will result in a net change in the dipole moment and significantly contribute to the D-term in two-photon absorption cross-section and thereby increasing the 2PA cross-section with increase in acceptor strength. However, this argument cannot be explained solely on the basis of steady-state measurements.

4.2.4.3. Nature of π-bridging Unit

It has been shown in literature that in donor-π-acceptor molecules, lowest energy ICT state is influenced not only by the donor/acceptor strength but also by the π-bridge and substituents[74]. In the present investigation, a direct comparison between molecular systems can be made by normalizing the cross-sections listed in Table 4.1 to their respective number of π-electrons. In this case, alkene π-bridging containing molecules **A** and **B** exhibit larger normalized 2PA values (by 4.4 and 4.0 times, respectively) than their alkyne π-bridged counterparts of **C** and **D**. One also notes from Table 4.1 that within the two respective systems (alkene and alkyne) there is no significant change in the transition dipole moment. Transient absorption measurements carried out for alkene and alkyne π-bridged chromophores of **B** and **D** have shown higher population of ICT' state for **B** over **D** which indicate that the extent of charge transfer in ICT state of **B** is greater than **D**. It has also been observed that there is ultrafast charge localization from the FC to ICT states indicating that the two states are intimately connected by same reaction coordinate. Thus, the amount of CT in ICT state is correlated to FC state, which indicates that the extent of charge transfer is higher for alkene π-bridged chromophores over alkyne π-bridged chromophores. This result will contribute significantly to the net change in dipole moment of the molecule and to the dipole term of 2PA (equation 4.3, 2PA into one photon allowed CT state). This explains the higher cross-section observed for alkene π-bridged chromophores over alkyne π-bridged chromophores for the low energy peak.

However, 2PA into high energy 2PA states involves the summation of equation 4.3 and equation 4.4. From transient absorption spectroscopy, two important results are obtained with regard to alkene and alkyne π-bridged chromophores. The extent of charge transfer which contributes mainly to 2PA into low lying 2PA band is higher for alkene-π-bridged chromophores than alkyne analogues while the estimates of excited state transition dipole moments favor the alkyne π-bridged chromophore over their alkene counterparts. As these two terms have opposing trends, the summation of these terms give almost equal 2PA cross-section into higher energy 2PA bands for both **B** and **D**. This stresses very strongly the use of combined techniques (TPEF, non-degenerate pump-probe, ultrafast transient absorption spectroscopy) to investigate the details of the differences in observed 2PA cross-sections. Actually, this can be regarded as a novel approach in which different 2PA techniques as well as steady-state and time-resolved measurements are all used to unravel the mechanism of the 2PA cross-section enhancement. The extent of charge transfer in the excited state has been clearly evaluated and one finds that this approach is more in depth than the measurements of the cross-sections alone.

4.3. Ultrafast Excited State Relaxation Dynamics of a Branched Donor-π-Acceptor Chromophore: Evidence of Charge Delocalized State

4.3.1. Background

Among several geometries investigated for better NLO and TPA properties, branched organic chromophores with donor-π-acceptor configuration have gained a great deal of interest recently[33-38]. This is largely due to their enhanced TPA and NLO properties with respect to their monomeric counterparts. Several experimental and theoretical investigations have been carried out to gain a mechanistic understanding of structure-property relationships relating to TPA behavior. It has been shown experimentally that the strength of donor and acceptor groups, conjugation length, geometry and nature of ground and excited states have a significant impact on TPA cross-section[27, 29, 50, 52, 75-77]. Information on all these parameters can be availed if there is a proper and systematic understanding of the nature of ground and excited states. Time-resolved measurements by virtue of one-photon photophysics and excited state dynamics provide us the abovementioned information in real time.

Another important aspect relating to the TPA properties of these multi-branched chromophores the extent to which optical excitation is delocalized[35-43]. If it is delocalized over the entire molecular assembly, it is possible to monitor the same using time-resolved spectroscopic techniques. However, such optical excitations tend to get localized or trapped in certain locations of the molecular assembly within the time scale of optical excitation[42] or much faster than the lifetime of the excited state[77]. Symmetry breaking upon photo-excitation in molecules with 2-fold or 3-fold symmetry leading to polar excited states has been extensively studied[78-80] to understand the fundamental aspects of charge delocalization. De Schryver and co-workers[78, 79] have studied the nature of excited state of C_3-symmetry amino-substituted triphenyl benzene derivatives with the aid of transient absorption, time-resolved fluorescence and time-resolved microwave conductivity measurements. They found that the bath-equilibrated polar excited state was localized on one branch[79]. However, limited time-resolved reports are available in literature, which are aimed at understanding the excited state deactivation of branched systems except by our group[21-27] and others[45, 81]. It has been shown theoretically that there is an initial charge delocalized state accompanied by charge stabilization on one arm of the chromophore with a lowering of symmetry for certain triphenyl amine centered molecules[37]. Extensive investigations towards understanding of the mechanism behind the enhancement of NLO properties on several branched chromophores[38-43] have been carried out by our group. Ultrafast transient absorption, fluorescence upcoversion and photon-echo spectroscopy results on the PRL series of dye molecules have shown that along with the delocalized charge, extent of charge separation in the excited state indeed plays a vital role in governing the TPA cross-sections[44]. Our earlier time-resolved measurements on the nitro trimer series of dye molecules[40, 42] have indicated the presence of a C_3-symmetry state with charge delocalization immediately after optical excitation. It would be interesting to realize such a C_3-symmetry state spectroscopically, and to monitor the eventual localization of excitation into a single arm. This is the motivation behind present work.

In the present section, presence of charge delocalized C_3-symmetry state of a trimer has been confirmed and investigated by transient absorption spectroscopy in real time. Pump-probe measurements have been carried out on the trimer, tris-4, 4', 4''-(4-nitrophenyl-ethynyl) triphenylamine (T-NPTPA) and the monomer 4-N, N-dimethylamino-4'-nitrotolane (DMNAT). Their structures are shown in Figure 4.9. Transient absorption measurements on the trimer in different solvents have conclusively shown the presence of a delocalized state after optical excitation.

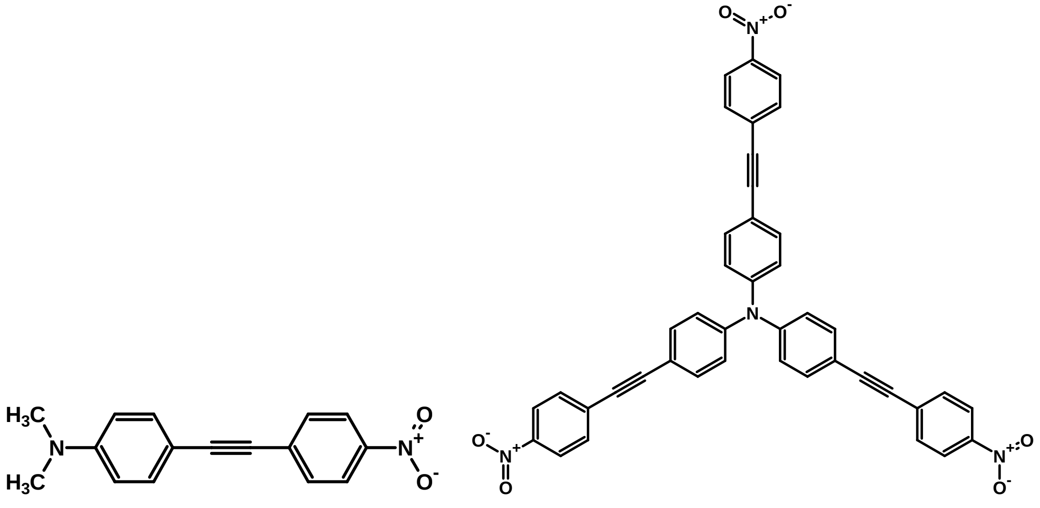

DMNAT **T-NPTPA**

Figure 4.9. Molecular structures of the monomer and trimer branched structures.

4.3.2. Experimental

4.3.2.1. Materials

The monomer, DMNAT and trimer T-NPTPA were obtained as a gift from Professor Robert Twieg, who has also reported their syntheses[40]. Toluene (Tol), tetrahydrofuran (THF), acetonitrile (ACN) and dimethyl sulfoxide (DMSO) from Aldrich (spectroscopic grade) were used as solvents. They were used as received without further purification.

4.3.2.2. Methods

Optical absorption measurements were carried out with an Agilent 8432 UV-Vis absorption spectrometer. Steady-state fluorescence measurements were carried out with a Spex Fluorimeter. Femtosecond transient absorption investigations were carried out using an ultrafast pump-probe spectrometer detecting in the visible region. This system contained 1 mJ, 100 fs pulses at 800 nm with a repetition rate of 1 KHz that were obtained from Nd:YLF(Evolution) pumped Ti:Sapphire regenerative amplifier (Spectra physics spitfire) with the input from Millennia pumped Ti:Sapphire oscillator (Spectra physics, Tsunami). The output of laser beam was split to generate pump and probe beam pulses with a beam splitter (85% and 15%). The pump beam was produced by an optical parametric amplifier (OPA-800C, Spectra Physics). The pump beam used in the present investigation, i.e. 420 nm, was obtained from the fourth harmonic of the idler beam and was focused onto the sample cuvette. The probe beam was delayed with a computer controlled motion controller and then focused into a 2 mm sapphire plate to generate white light continuum. The white light was then overlapped with the pump beam in a 2 mm quartz cuvette containing the sample and the change in absorbance for the signal was collected by a CCD detector (Ocean optics). Data acquisition was controlled by the software from Ultrafast systems inc. Typical power of probe beam was < 0.1 μJ while that of the pump beam was ~1 to 2 μJ per pulse. Magic angle polarization was maintained between the pump and probe using a wave plate. Pulse duration was obtained from the non-resonant fitting of the solvent response, which was approximately 120 fs. The sample was stirred by a rotating magnetic stirrer and little degradation of the sample was observed during the experiments.

In order to measure the two photon absorption cross sections, two photon excited fluorescence (TPEF) method was employed. A 10^{-4} M Coumarin 307 solution in methanol was used as the reference. The laser used for the study was a Kapteyn Murnane (KM) mode-locked Ti:Sapphire oscillator. The fluorescence was collected in a direction perpendicular to the incident beam. A logarithmic plot between collected fluorescence photons and input intensity yielded a slope of two, ensuring a quadratic dependence between the same. The intercept enabled us to calculate the two photon absorption cross sections.

4.3.3. Results and Discussion

4.3.3.1. Photophysical Properties of Monomer and Trimer

Figure 4.10 A and B show the optical absorption and emission spectra of the monomer and the trimer in toluene and THF respectively. It can be noted from Figure 4.10 A and B that the ground state absorption spectra of monomer and trimer look similar in toluene and THF with minor differences. The trimer shows two distinct absorption peaks at ~422 and 318 nm with a shoulder at 374 nm, while the monomer shows two main peaks at 423 nm and 302 nm. The low energy absorption bands for both the monomer and trimer can be ascribed to charge transfer processes while the high energy absorption bands arise from $\pi \rightarrow \pi^*$ transition. The absorption spectrum did not show any major changes with respect to solvent polarity. Similar solvent dependence on optical absorption features are observed for other donor-acceptor dipolar and octupolar molecules[37, 81, 82] and can be explained on the basis of a coupled valence bond state model[82]. Though the absorption behavior is similar for monomer and trimer in toluene, the emission spectra are quite different.

It can be observed from Figure 4.10A that the emission maxima of monomer in toluene is shifted ca. 50 nm to longer wavelength, while the emission maxima of monomer and trimer in THF (Figure 4.10B) are similar except that the emission quantum yield of monomer in THF is much lower than that of trimer. These results present us with an interesting scenario in regards to the polarity of emitting states in monomer and trimer. The results show that the emitting state of trimer is less polar in toluene than that of the monomer while it has similar polarity as monomer in THF. The less polar emitting state of the trimer could be due to the charge delocalized C_3-symmetry state and the more polar emitting state could arise from localized charge transfer state which might have been formed by lowering the symmetry of initial excited state. Similar solvatochromism has been reported for this trimer in our previous measurements[40]. From steady-state electronic absorption and emission measurements, the absorption and emission transition dipole moments of the monomer and trimer have been estimated the using generalized formulae reported in literature[83, 84]. Respective absorption and emission transition dipole moments are provided in Table 4.2 . As expected, the molar extinction coefficient of trimer is three times higher than the monomer and the absorption and emission dipole moments of trimer are also higher than those for the monomer. The fact that the emission dipole moments of monomer and trimer are different indicates the emitting state of trimer is quite different than monomer. Also, the proximity between emission and absorption transition dipole moments for individual molecules suggests that the emitting state of trimer is delocalized over entire molecule. However, considering the fluorescence in a medium polarity solvent (THF), the maxima are found to be similar for both monomer and trimer, suggesting that the emission states are same for both molecules. Thus, further time-resolved experiments are required in order to explain the observed differences between the emitting states of trimer in toluene and THF.

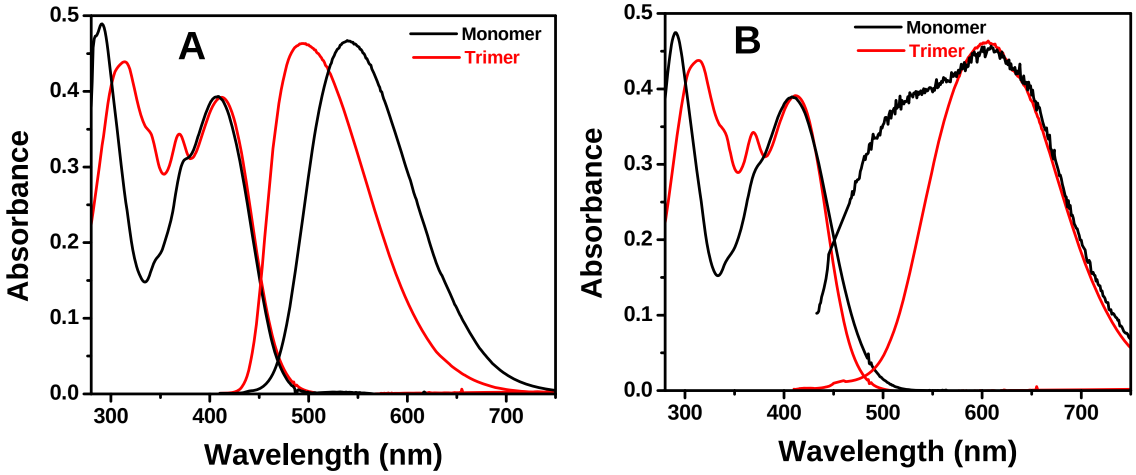

Figure 4.10. A) Absorption and emission spectra of monomer and trimer in Toluene. B) Absorption and emission spectra of monomer and trimer in THF.

Table 4.2. Absorption and emission transition dipole moments of investigated chromophores in toluene.

Compound	ε (cm^2 mol^{-1})	τ_r (ns)	M_{ge} (D)	M_{eg} (D)	δ_{TPA}(GM)
Trimer	51391	2.8	8.54	6.45	575
Monomer	18875	8	5.02	4.33	130

ε = molar extinction coefficient, τ_r = radiative life time (ratio of fluorescence life time and fluorescence quantum yield), M_{ge} and M_{eg} are absorption and emission transition dipole moments respectively. δ_{TPA} is the two-photon absorption cross-section obtained at 800 nm.

4.3.3.2. Two-Photon Excited Fluorescence Measurements

In previous publications[30, 40], it was shown using degenerate four-wave mixing measurements of monomer and trimer in solution that the third order nonlinearity is comparable to that of other highly conjugated systems reported. Also, nonlinear transmission measurements with a nanosecond laser from our group have shown that the nonlinear absorption coefficient of the trimer is significantly higher than that of the monomer. To corroborate the earlier NLO property measurements from degenerate four wave mixing and nonlinear transmission, two-photon excited fluorescence (TPEF) measurements have been carried out using femtosecond pulses to measure the TPA cross-sections of the monomer and the trimer in toluene. The measurements were carried out at 785, 800, 815 and 830 nm. The results from TPEF measurements are shown in Figure 4.11. The maximum TPA cross-section obtained in this range is presented in Table 4.2 . The maximum TPA cross-section was 575 GM for the trimer and 130 GM for the monomer, both maxima occurring at 800 nm.

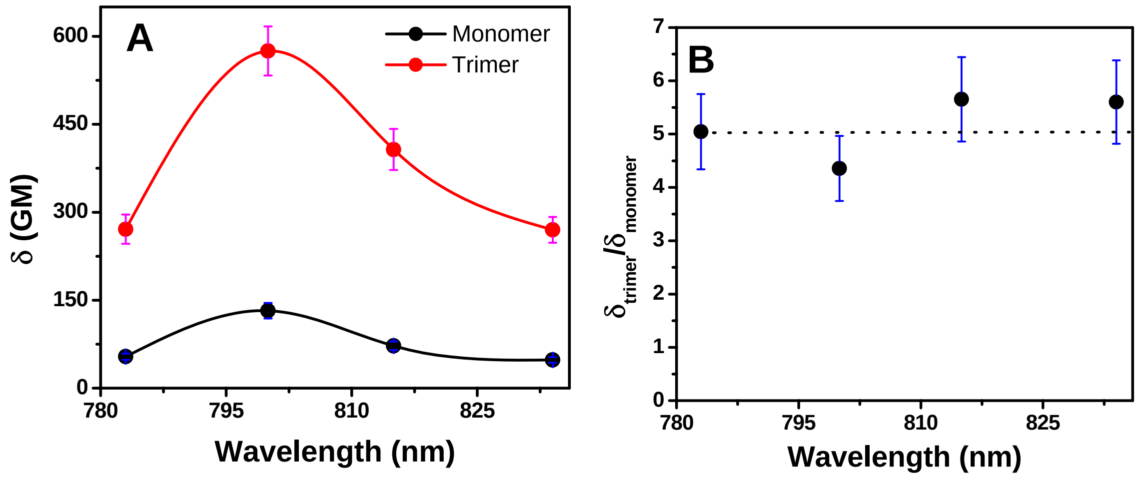

Figure 4.11. A) TPA cross-section versus wavelength for monomer and trimer in toluene and (B) the ratio of TPA cross-sections of trimer: monomer.

It can be noted from Table 4.2 that δ of trimer is at least four times higher than the monomer at different wavelengths, which is in accordance with the earlier nonlinear transmission measurements. Similar enhancement has been observed for several other triphenylamine cored branched molecules[30, 77]. Even the cross-section per π-electron for trimer is calculated to be 1.5 times higher than that of monomer. The mechanism behind the enhancement of TPA cross-section to this low energy one photon allowed state can be availed by probing the excited state dynamics of the chromophores.

4.3.3.3. Femtosecond Transient Absorption Measurements

Transient absorption measurements of monomer and trimer in different solvents have been carried out after excitation at 420 nm. Figure 4.12A shows the transient absorption spectra at different time delays for the trimer in toluene. At a time delay of 200 fs, the transient absorption spectrum consisted of two main excited state absorption (ESA) bands with maxima around 530 nm and 660 nm respectively. At 5 ps, both features shift to lower wavelengths to ~ 510 and 650 nm respectively. At ~30 ps, the shift of transient absorption is complete with an ESA band with maxima at ~490 and 640 nm. Global fit analysis using single value decomposition (SVD) of the spectrum has been carried out and the ESA features are fitted with two time constants, namely 4.8 ps, and a component longer than 1 ns (Figure 4.12B). The observed fast component of 4.8 ps is attributed to either vibrational relaxation of the excited state or solvation of the excited state by the solvent. As the solvation time of toluene (2.4 ps)[85] is quite different than the fast component observed in the present measurements, the observed features can be attributed to vibrational relaxation of the excited state[86, 87]. The excited state decaying with a time constant of >1 ns is ascribed to singlet state decay as this value matched well with the fluorescence lifetime obtained from time-correlated single photon counting measurements.

The monomer shows entirely different transient absorption features in toluene. Shown in Figure 4.12C are the transient absorption spectra at different time delays for the monomer in toluene. As the time delay is increased from 100 fs to 500 fs, ESA with a maximum at 540 nm shows a small blue shift to a maximum around 520 nm and a growth of stimulated emission is observed at around 580 nm. Global fit analysis has been carried for the transient absorption spectrum at different time delays and corresponding transient absorption features are fitted with time constants of 1.8 ps and > 1 ns (Figure 4.12D). The time constant of 1.8 ps (time taken to give the stimulated emission at around 580 nm) is similar to the solvation time of toluene[85]. Thus, it can be suggested that stabilization from the ESA of Franck-Condon (FC) state occurs to yield an intramolecular charge transfer

(ICT) state. It is interesting to note that the emission from ICT state is seen even in a nonpolar solvent such as toluene.

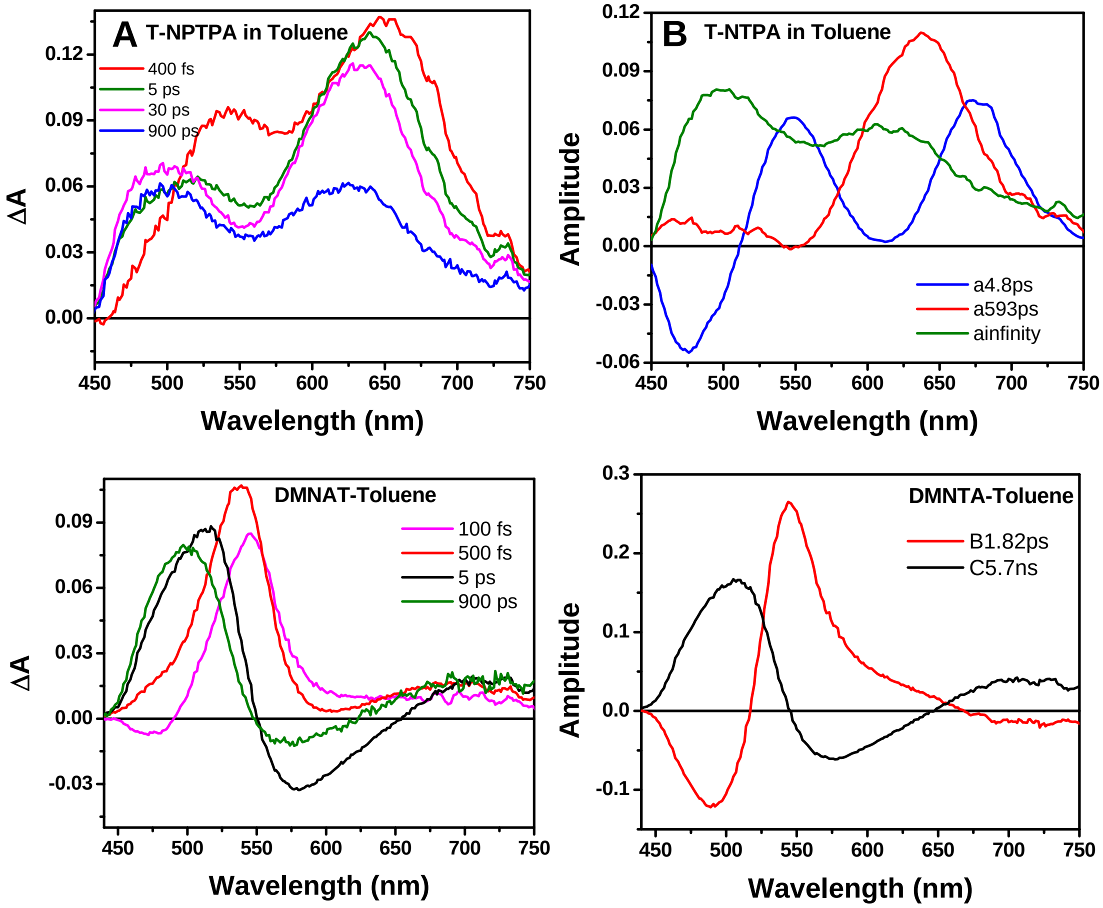

Figure 4.12. Femtosecond transient absorption spectra of trimer in toluene at different time delay (A) and the species associated spectrum (B). Transient absorption spectrum of monomer in Toluene at different time delays (C) and corresponding species associated spectra (D).

The transient absorption results of monomer and trimer in toluene suggest that the emitting states are entirely different for the two systems and are supported by steady-state fluorescence measurements. The results suggest that the emission from trimer results from a state which is less influenced by solvent polarity and most likely arises from a delocalized state (C_3-symmetry) as indicated by its higher radiative emission transition dipole moment. The observation of C_3-symmetry state for trimer in present transient absorption measurements are well supported by the ultrafast fluorescence anisotropy and

3-pulse photon echo measurements carried out on these chromophores[39, 40]. The fact that there is no indication of ICT state in case of trimer points to a barrier between the FC and ICT state.

Steady-state measurements have indicated that the emission from trimer in medium polarity solvent of THF is similar to monomer. In such a scenario, it is interesting to investigate if the nonpolar C_3-symmetry state can be observed even in a medium polarity solvent. Thus transient measurements were carried out on monomer and trimer in THF. Figure 4.13A and B show the transient absorption spectra of trimer in THF at two different time delay regions of 100 to 400 fs and 450 fs to 3.6 ps respectively. At 100 fs, the transient absorption spectrum consists of two ESA bands with maxima around 520 nm and 650 nm. It is worth noting that the initial transient absorption spectrum is similar to that observed in toluene. The two absorption bands decay to give rise to a transient absorption feature at 500 nm and the stimulated emission starts to appear around 1 ps (Figure 4.13B). Figure 4.13B shows that the transient thus formed continues to evolve to give rise to the ESA band at 580 nm and stimulated emission at 650 nm with a clear isosbestic point at 580 nm. Global fit analysis showed that the initially formed excited state decays to give another state with stimulated emission with a time constant of 600 fs (close to the solvation time of THF[88]) and the emission decays with a lifetime of ~300 ps. As pointed out earlier the initially observed excited state is similar to the transient absorption observed in toluene suggesting that upon photo-excitation of trimer a nonpolar excited state (delocalized C_3-symmetry state, FC state) is formed from which an ICT state is formed. The slow rate of internal conversion from FC state to ICT state enables us to spectroscopically view the C_3-symmetry state even in THF.

It has been observed from steady state fluorescence measurements that the emission spectrum is similar for monomer and trimer in THF and it has also been suggested that this emission is arising from identical states in both molecules. Most probably this emission is from the ICT state, where the charge is localized in one arm of the branch as the emission is similar to that of the monomer. Transient absorption measurements of monomer in THF have been carried out and are shown in Figure 4.14. It can be observed from Figure 4.14 that the state responsible for stimulated emission is growing with a time constant of 280 fs. It is interesting to note that the transient absorption spectrum responsible for emission in monomer (Figure 4.14B) is similar to trimer (Figure 4.13B). The state thus formed decays back rapidly to give rise to a non-emissive state, with ESA maximum at 650 nm and a time constant of 2.2 ps. The final state decays to ground state with a lifetime of 35 ps. Observed additional involvement of a non-emissive state, which is assigned to twisted intramolecular charge transfer (TICT) state[89] due to twisting of NO_2 group explains the low fluorescence quantum yield observed for this molecule.

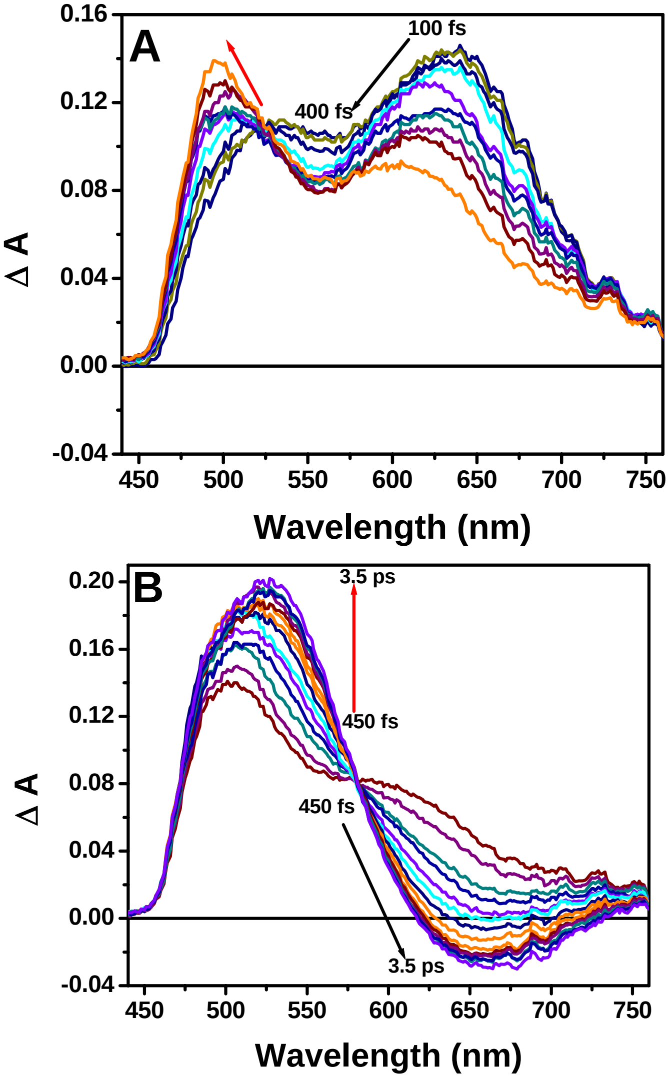

Figure 4.13. Transient absorption data for the trimer T-NPTPA in THF. (A) 100 fs to 400 fs, (B) 450 fs to 3.6 ps.

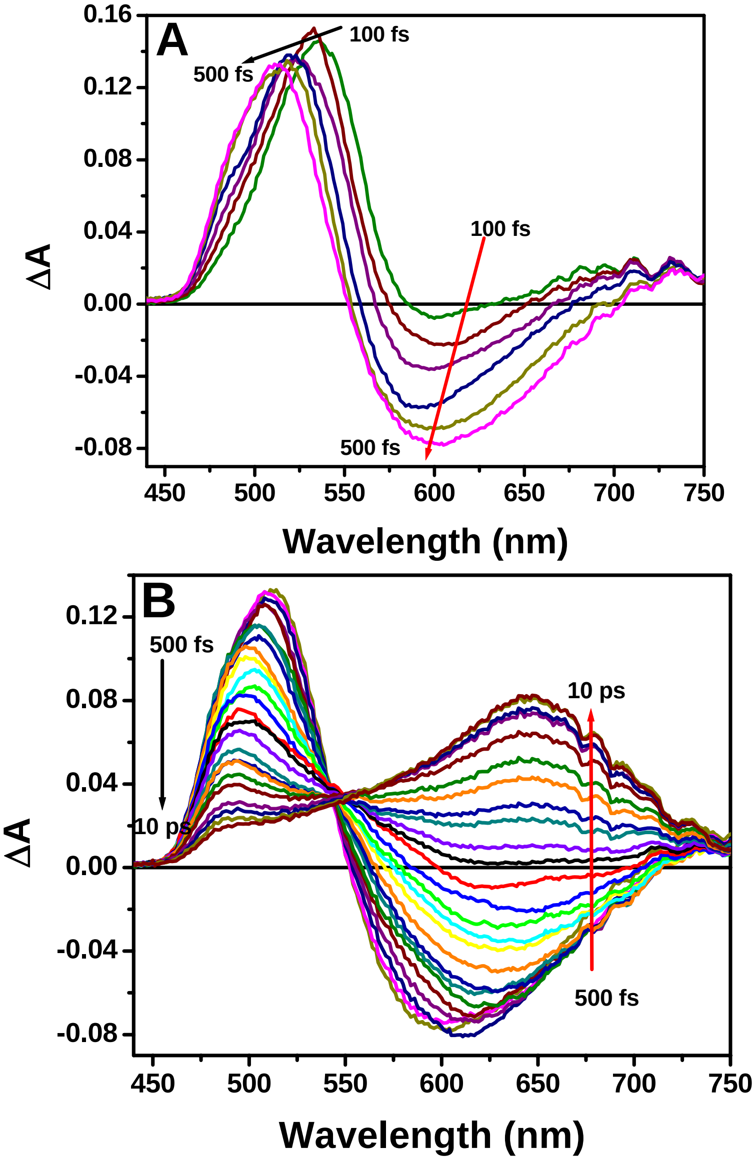

Figure 4.14. Transient absorption data for the monomer in THF. (A) 100 fs to 600 fs. (B) 600 fs to 10 ps.

It is evident from the transient measurements in THF that the emission arises from similar states in both monomer and trimer while there is an additional involvement of non-emissive state in case of monomer which is absent in trimer.

4.3.3.4. Mechanism of Excited State Deactivation

Steady-state and transient absorption measurements of monomer and trimer in two-solvents discussed above were successful to a good extent in understanding the excited state deactivation of the chromophores. For further insight and complete excited state deactivation of the chromophores, transient absorption measurements for both monomer and trimer have been carried out in more polar solvents such as acetonitrile and dimethylsulfoxide (DMSO). Transient lifetimes obtained for the monomer and trimer in different solvents from the global fitting analysis of their respective transient absorption spectra are provided in Table 4.3.

Table 4.3. Summary of solvent dependent excited state lifetimes obtained from global fit analysis.

Solvent	Monomer	Trimer
Toluene	1.82 ps, >1 ns	4.8 ps, >1 ns
THF	280 fs, 2.2 ps, 35 ps	600 fs, 300 ps
Acetonitrile	270 fs, 2 ps	120 fs, 2.5 ps
Dimethyl sulfoxide	140 fs, 530 fs, 5.5 ps	80 fs, 1.5 ps, 7.8 ps

It has been shown that transient absorption measurements carried out on trimer in toluene showed emission from an initial charge delocalized state with C_3-symmetry. The locally excited state observed in trimer can be considered as C_3-symmetry state since the emission transition dipole moment observed from this state is significantly higher than that of monomer. The excited state dynamics of trimer in toluene can be described as follows: Upon photo-excitation of the trimer, the molecule excites vertically to its Franck-Condon (FC) state which is a C_3-symmetry (Scheme 4.2) state with charge delocalized throughout the molecule. However, intramolecular dephasing takes place very rapidly which is clearly observed in the time-resolved anisotropy measurements. This suggests effective intramolecular electronic coupling[40, 42]. The state thus formed vibrationally relaxes and decays with a lifetime of >1 ns. In case of monomer, the optical excitation takes the molecule to a FC state which relaxes to an intramolecular charge transfer (ICT) state that gives rise to emission. The ICT state thus formed decays back to ground state with a lifetime of >1 ns.

Scheme 4.1. A cartoon diagram showing the photophysical processes of monomer and trimer in different solvents. LE indicates the locally excited state is the C3-symmetry state in case of trimer; ICT is intramolecular charge transfer state. ICT' state is a conformationally relaxed intramolecular charge transfer state.

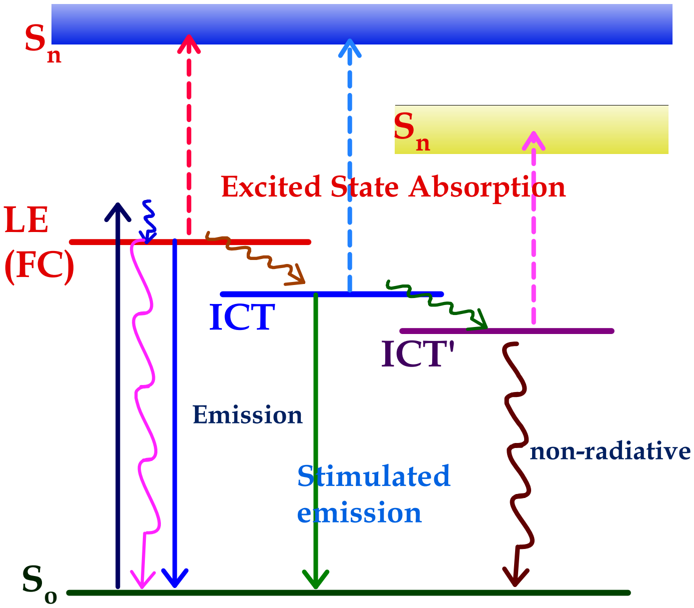

In a medium polarity solvent such as THF, the emission from the monomer and trimer arise from the same state. Transient absorption measurements for trimer in THF have unambiguously shown that there is an initial ESA which is similar to that of toluene. From this initial state, a state with a stimulated emission in the longer wavelength region is formed which decays back to ground state with a lifetime of 300 ps. Thus the optical excitation of trimer in THF excites the molecule to a charge delocalized state (LE state) which lowers its symmetry to give rise to ICT state (similar to what is observed for the monomer) with a time constant of 600 fs. Hence, spectroscopic evidence of initial charge delocalized state has been observed even in THF. The time scale of internal conversion of locally excited C_3-symmtery state to ICT (600 fs) is relatively longer and hence we are able to successfully observe the charge delocalized state.

While the transient measurements for monomer in THF have shown that along with the ICT state there is also a presence of a dark state (most probably due to twisted intramolecular charge transfer, TICT state) but no such state has been observed for trimer. However, in very high polarity solvents such as dimethyl sulfoxide and acetonitrile the presence of dark state has been observed even for trimer. It can be observed from Table 4.3 that the dynamics in highly polar solvents for both monomer and trimer involve very fast decay pathways back to ground state. The dynamics also involve very fast relaxation to a non-radiative ICT' state for both monomer and trimer, most likely arising from the TICT state with twisting of NO_2 groups[89, 90]. Although the dark state in the excited state deactivation of trimer is observed in high polarity solvents, yet the initial transient absorption spectrum is observed to be similar to toluene and THF. This suggests that the FC state is similar in all solvents and has a C_3-symmetry. Overall excited state dynamics of the monomer and trimer in different solvents can be summarized using Scheme 1. Steady-state measurements for trimer merely indicates a less polar emissive state in toluene, while transient measurements unambiguously suggest that the delocalized C_3-symmetry state is the FC state for the trimer in all solvents.

4.3.3.5. Correlation of Nonlinear Optical Properties and Excited State Dynamics

Observed TPA cross-sections of monomer and trimer are in accordance with the fact that the donor-π-acceptor molecules with increased dimensionality possess high NLO and TPA properties over their linear counterparts. The extent of electronic coupling between the individual branches possessing charge transfer, effective electronic delocalization, enhanced intramolecular charge transfer and the complex interplay of all these parameters are regarded as plausible mechanisms behind TPA enhancement with increase in dimensionality. Femtosecond time-resolved measurements have been employed to probe the mechanism behind the observed enhancement by comparing the excited state dynamics of the monomer and the trimer.

The important result of the present ultrafast transient measurements is the spectroscopic evidence of a charge delocalized C_3-symmetry state (FC state) for the trimer molecule. The slow time-scale of internal conversion from FC state to charge stabilized ICT state enabled us to observe the C_3-symmetry state of the trimer. In order to address the consequence of the slow rate of internal conversion from FC state to ICT state on TPA cross-section, we resort to a sum-over-states (SOS) formalism. In the realm of SOS formalism, the TPA cross-section (δ) into lowest energy absorption band for non centro-symmetric molecules can be expressed as[29]

$$\delta_{2-state} \propto \frac{M_{ge}^{2}\Delta\mu_{ge}^{2}}{\Gamma} \tag{4.3}$$

Here, M_{ge} is the transition dipole moment from ground to excited state and $\Delta\mu_{ge}$ is the change in dipole moment from ground to excited state. Γ is the damping factor. $\Delta\mu_{ge}$, the change in dipole moment mainly depends on the charge correlation differences of ground and excited states. The observed fact that there is a barrier between FC and ICT state indicates that they are not coupled with each other intimately and as the FC state is less polar, the magnitude of $\Delta\mu_{ge}$ will be less and this term will not contribute significantly to TPA cross-sections and only M_{ge} will influence the TPA cross-section. The delocalized nature of the FC state of trimer observed from combined time-resolved measurements and higher absorption transition moments of trimer over monomer clearly establish the proposition. However, if the rate of internal conversion between FC and ICT states is fast, it suggests that the FC and ICT states are intimately connected and the change in dipole moment term contributes significantly to TPA cross-section as has been observed for other triphenyl amine branched chromophores[72].

4.4. Oligothiophene Dendrimers as Novel Materials for Nonlinear Optical Applications

4.4.1. Introduction

Organic materials possessing excellent optical and electrical properties have been the focus of intense research for several years since they have potential applications in photovoltaic devices[89, 90], light harvesting[91-93] and organic electronics[94]. This is because of their ease of synthesis and ability to fine tune their physical properties to meet the needs of technological applications. Among several methodologies for better functional organic materials, a building block approach based on the dendritic architecture with hierarchy of branched organic structures has been suggested to be an efficient design criterion for new artificial light harvesting and solar energy conversion devices[95-102]. Energy funneling from the peripheral chromophores of the dendrimer to the core[95] has been observed and this has stimulated research in this field. Additionally, the enthusiasm in the field of organic dendrimers is also motivated by its possible applications in organic light emitting diodes (OLEDs)[103-106] and nonlinear optical devices [35, 107-111]. Among several organic chromophores utilized to synthesize dendritic structures, thiophenes or oligothiophenes find a unique place as they have been well investigated for their versatile chemistry[112-116], applications in OLEDs[117-119], field effect transistors[120, 121] and organic photovoltaic and light harvesting devices[122-126] such as solar cells. For example, organic solar cells based on P3HT (poly-3-hexylthiophene) polymer/fullerene derivatives are one of the best available organic solar cells with an efficiency of 4-5%[127].

Although several oligomers and polymers of thiophene have been synthesized[128-133] and investigated extensively, not until recently has an all thiophene dendrimer been synthesized[134-138]. Bauerle and co-workers[138] have synthesized space filling 3D-functionalized oligothiophene dendrimers for their application in light harvesting, solar energy conversion and optoelectronics. Efficient excitation delocalization and excitation energy transfer are needed for organic materials to mimic natural light harvesting systems. Time-resolved measurements on these dendrimers as a function of generation could evaluate the extent of excitation delocalization and energy transfer processes which are needed to evaluate their capabilities in optical applications.

In addition, strong intra-chromophore interactions, efficient energy transfer and migration through the structural design of dendritic architecture and formation of delocalized excited states render them with enhanced NLO properties (especially two-photon absorption (TPA) cross-section) in comparison to their linear counterparts[37, 38, 41, 107-108, 111]. TPA behavior of organic branched chromophores has been a subject under spotlight for a decade[1, 29, 30, 42-44, 72] or so since it has shown promising applications in several fields discussed earlier. Several π-conjugated phenyl cored[37], nitrogen centered[35] dendritic chromophores have been synthesized recently and their TPA cross-sections were measured which have shown cooperative enhancement with increase in dendrimer generation. In this context, TPA cross-sections of thiophenes and their derivatives have also been investigated[139, 140]. Since all-thiophene dendrons and dendrimers have the ability to form space filling solid state objects[139], it will be interesting to utilize these thiophene dendrimers as potential two-photon absorbing materials in solution and solid-state in addition to their potential as artificial light harvesting systems.

The dynamics of photo-induced processes in such dendrons could provide some insight into their optical applications. Excited state dynamics of oligothiophenes and polythiophenes[141-156] has been investigated in the literature for understanding the fundamental mechanism behind their applications in light harvesting, solar energy conversion and organic electronics. Several measurements on singlet and triplet states of thiophenes were carried out using femtosecond pump-probe spectroscopy[141-154] and the nature of singlet states was studied using time-resolved fluorescence[155, 156]. Westenhoff et al[153, 154] have reported the anomalous excitation energy transfer through torsional relaxation in the polythiophene derivative of poly[3-(2,5-dioctylphenyl)thiophene] (PDOPT). Kobayashi and co-workers[155, 156] have reported chain length dependent stationary and time-resolved fluorescence spectra of α-oligothiophenes and shown that hydrodynamic slip model successfully explains the reorientation dynamics. Amidst several time-resolved experiments on oligothiophenes and polythiophenes, no experimental or theoretical investigation is available on the excited state dynamics of all-thiophene dendrimers and their generation dependence to prove their potential as light harvesting mimics.

In the present section, the TPA properties and excited state dynamics of a thiophene dendrimer system up to the third generation (G_0 to G_3) have been investigated. TPA cross-section sections have shown super-linear increase of cross-section per unit thiophene with increase in dendrimer generation. Femtosecond time-resolved measurements have shown that the excitation is delocalized over a large portion of the dendrimer and is responsible for the observed enhancement in TPA cross-sections and efficient light harvesting. Our results also have shown the phenomenon of excitation energy migration to the longest emitting state over ultrafast time scale, mimicking the energy funnel system employd by nature. Additionally, generation dependent torsional relaxation in the emitting state has been observed which tends to assist in planarizing the molecule.

4.4.2. Experimental

4.4.2.1. Materials

Professor Peter Bauerle at the University of Ulm, Germany has synthesized the dendrons. The general synthetic procedures have been reported by him elsewhere[139]. Their structures are shown in Figure 4.15. All the measurements were carried out in tetrahydrofuran (THF) (Aldrich) unless stated otherwise.

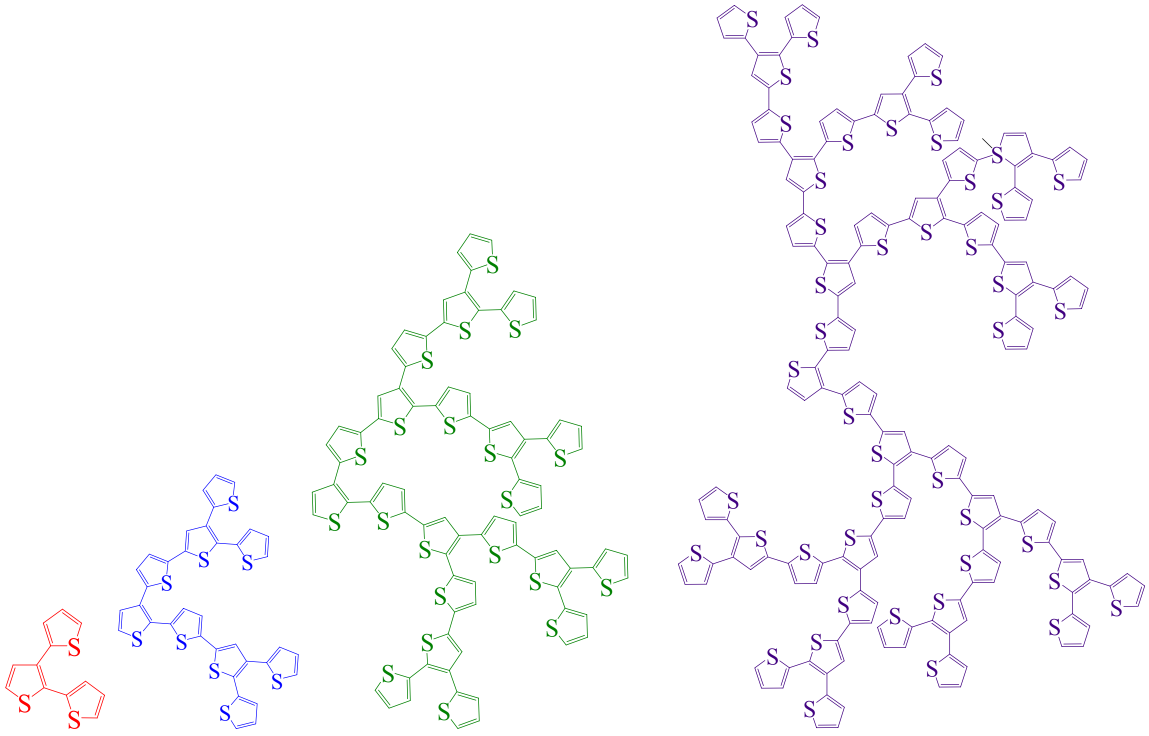

3T (G_0) **9T (G_1)** **21T (G_2)** **45T (G_3)**

Figure 4.15. Molecular structures of the investigated 3D oligothiophene dendrimers.

4.4.2.2. Steady State Measurements

Optical absorption measurements were carried out using an Agilent UV/Vis absorption spectrometer. Steady-state fluorescence measurements were carried out using a Jobin Yvon Spex Fluoromax-2 spectrofluorometer. The quantum yields of the molecules were measured using a known procedure and Coumarin 307 was used as the standard.

4.4.2.3. Two-Photon Excited Fluorescence (TPEF) Measurements

To measure the two-photon absorption cross-sections (δ), two-photon excited fluorescence (TPEF) method was employed. A 10^{-4} M Coumarin 307 solution in methanol was used as the reference over a wavelength range of 700-800 nm. In order to measure the TPA cross-sections for wavelengths less than 700 nm, p-bis (o-methyl styryl) benzene (MSB) dissolved in cyclohexane was used as the reference. A mode-locked Ti: Sapphire oscillator (Kapteyn Murnane (KM)) was used for determining the δ over 760-820nm. For the remaining wavelengths (630-760 nm and 820-900 nm), an optical parametric amplifier (OPA-800C, Spectra physics) was employed. The seed used was a mode locked Ti: Sapphire laser (Tsunami, Spectra Physics). This was amplified using a regenerative amplifier (Spitfire, Spectra Physics) which in turn was pumped by an Nd: YLF laser (Empower, Spectra Physics). The amplified pulses were obtained at 1 kHz, 800 nm and ~100 fs which was used for pumping the OPA.

4.4.2.4. Fluorescence Lifetime Measurements

Time Correlated Single Photon Counting (TCSPC) was used to determine the fluorescence lifetimes of the thiophene dendrimers used in this study. The laser used was the KM system described earlier. The second harmonic from the 800 nm output was used for these measurements.

4.4.2.5. Femtosecond Transient Absorption Measurements

Transient absorption was used to investigate the excited state dynamics of the thiophene dendrimers at different excitation wavelengths. Briefly, the pump beam was produced by the OPA-800C described above. The pump beams used in the present investigation were obtained from the fourth harmonic of signal and idler beams and were focused onto the sample cuvette. The probe beam was delayed with a computer controlled motion controller and then focused into a 2 mm sapphire plate to generate white light continuum. The white light was then overlapped with the pump beam in a 2 mm quartz cuvette containing the sample and the change in absorbance for the signal was collected by a CCD detector (Ocean optics). Data acquisition was controlled by the software from Ultrafast systems inc. Typical energy of the probe beam was < 0.1 μJ while that of the pump was around ~0.1 to 0.4 μJ per pulse. Magic angle polarization was maintained between the pump and probe using a wave plate. The pulse duration was obtained by fitting the solvent response, which was ~130 fs. The sample was stirred with a rotating magnetic stirrer and no photo-degradation of the sample was observed during experiments.

4.4.3. Results and Discussion

4.4.3.1. Linear Optical Properties

The ground state absorption and fluorescence spectra of the increasing generation of dendrimers (G_0 to G_3) dissolved in THF are shown in Figure 4.16. The absorption spectrum of the smallest dendron (G_0) shows two features at ~ 270 and 310 nm while G_1 has a maximum around 378 nm. The absorption maximum was observed to exhibit bathochromic shift with increasing dendrimer generation (Table 4.4). An interesting aspect pertaining to the absorption spectra is that for the higher generations of dendrimers, not only is there a red shift of the absorption maximum but also a broadening of the absorption spectrum to longer wavelength regions[51]. This is ascribed to the fact that the higher generation of dendrimers consists of several linear α-oliogthiophene branching units whose absorption spectra shift to longer wavelengths with increasing chain length[131]. In a simpler arithmetic calculation of the number of α-oligothiophenes in each dendrimer yields following trend:

$$G_0 = 3T = (\alpha\text{-}2T + \alpha - T),$$

$$G_1 = 9T = (\alpha\ \text{-}4T + \alpha\text{-}3T + 2\ \alpha\text{-}T),$$

$$G_2 = 21T = (\alpha\text{-}6T + \alpha\text{-}5T + 2\ \alpha\text{-}3T + 4\ \alpha\text{-}T), \text{ and}$$

$$G_3 = 45T = (\alpha - 8T + \alpha\text{-}7T + 2\ \alpha - 5T + 4\ \alpha\text{-}3T + 8\ \alpha\text{-}T).$$

This scheme is based on counting contiguous linear segments of alpha-substituted thiophenes. The increase in the length of continuous alpha-substituted segments with increasing dendron generation is clearly manifested in the increase in extinction coefficients as well as the red shift and broadening of absorption spectra.

A very interesting trend is observed upon inspection of fluorescence spectra with increasing dendrimer generation as well. The emission spectra exhibit a bathochromic shift as the generation is increased (Figure 4.16 and Table 4.4) but there is no broadening of the emission spectra and the emission maximum has good correlation with highest linear oligothiophene branching unit in each dendrimer, such as α-4T for G_1, α-8T for G_3 reported in literature[131]. It appears that the fluorescence is arising from the longest α-conjugated unit and is invariant to the excitation wavelength. This behavior indicates intramolecular excitation energy transfer from shorter chromophores to the longest chromophore, which then emits energy.

From the optical absorption measurements, it is observed that the absorption spectrum is a linear combination of the absorption spectra of several linear α-oligothiophene units and different excitation wavelengths can excite preferentially different linear oligothiophenes which constitute the dendrimer. However, the fluorescence spectra of the dendrimers suggest the possibility of intramolecular excitation energy transfer to longest oligothiophene in respective dendrimer. Time-resolved measurements have been carried out to understand the actual mechanism of excitation (whether it is localized or delocalized) and to probe the phenomenon of intramolecular excitation energy transfer and are discussed next.

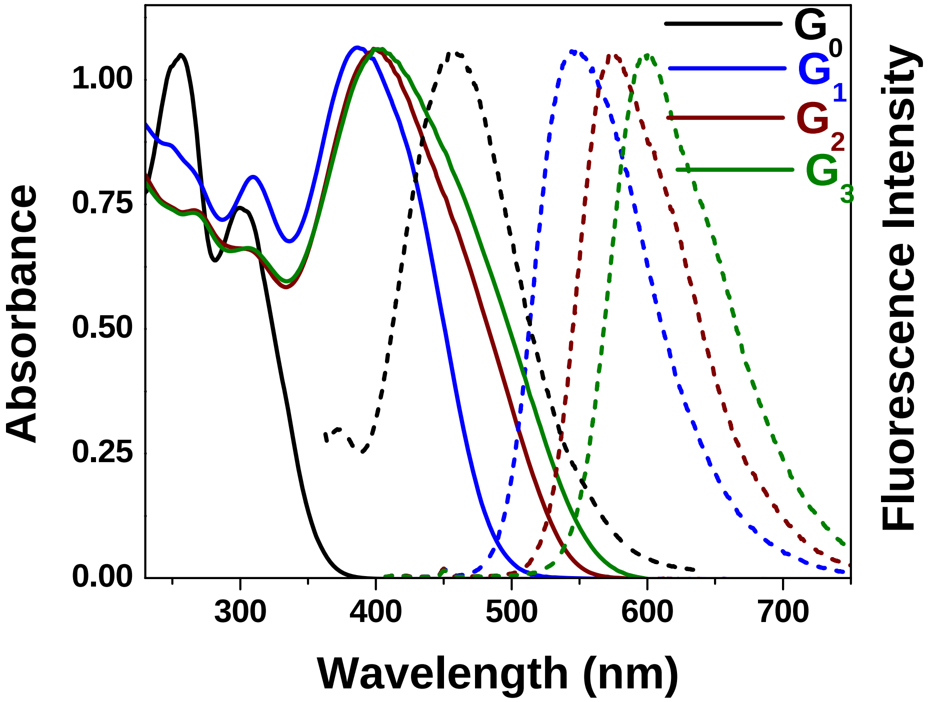

Figure 4.16. Optical absorption (solid lines) and fluorescence spectra (dashed) of different generation of thiophene dendrimers.

Table 4.4. Linear optical properties of thiophene dendrimers.

Compound	**λ_{abs} (nm)**	**λ_{em} (nm)**	**Φ_f**	**τ_f (ps)**	**M (D)**
G_0	302	440	0.02	-	4.9
G_1	371	517	0.09	790	9.6
G_2	382	542	0.05	500	14.8
G_3	385	565	0.06	690	19.2

Φ_f is the emission quantum yield, τ_f is the fluorescence lifetime obtained from time-correlated single photon counting, and M is the absorption transition dipole moment in Debye.

4.4.3.2. Two-Photon Absorption

Having investigated the one photon absorption measurements and found that the absorption can be a linear combination of several α-oligothiophene units, it is of interest to examine the nonlinear optical properties such as TPA cross-section as a function of dendrimer generation. To achieve this, TPA cross-section measurements have been carried out using two-photon excited fluorescence (TPEF) method. Shown in Figure 4.17 are the TPA excitation spectra for G_1 to G_3. The data for G_0 is not shown since it spans in the wavelength region of 550 to 640 nm and has very low TPA cross-section of less than 8 GM. Peak cross-section values for the dendrimers increase from 8 GM for G_0 to 1150 GM for G_3 respectively. The variation of peak TPA cross section with total number of thiophene rings in the dendrimer is shown in Figure 4.18. In order to accentuate that the increase in TPA is not merely due to increase in chromophore density, but is also aided by coupling between thiophene units, a plot of TPA cross-section per unit thiophene is calculated and plotted as a function of dendrimer generation in Figure 4.19. It is observed that the TPA cross-section has enhanced with increase in dendrimer generation. If there were no super-linear increase in TPA cross-section with dendrimer generation, a straight line parallel to cross-section of one thiophene should have been observed (Figure 4.19) for the plot of TPA cross-section per unit thiophene versus dendrimer generation. However, the plot deviates and shows a super-linear behavior. This phenomenon is reminiscent of what has been observed in the case of cooperative enhancement of TPA cross-section with increasing dimensionality in branched chromophores[30], as well as increase of TPA cross-sections in nitrogen centered dendrimers[111]. Time-resolved spectroscopic techniques can probe the mechanism behind such an enhancement in TPA cross-section and this has been demonstrated in our earlier investigations (Chapter II, Sections 3.1 and 3.2).

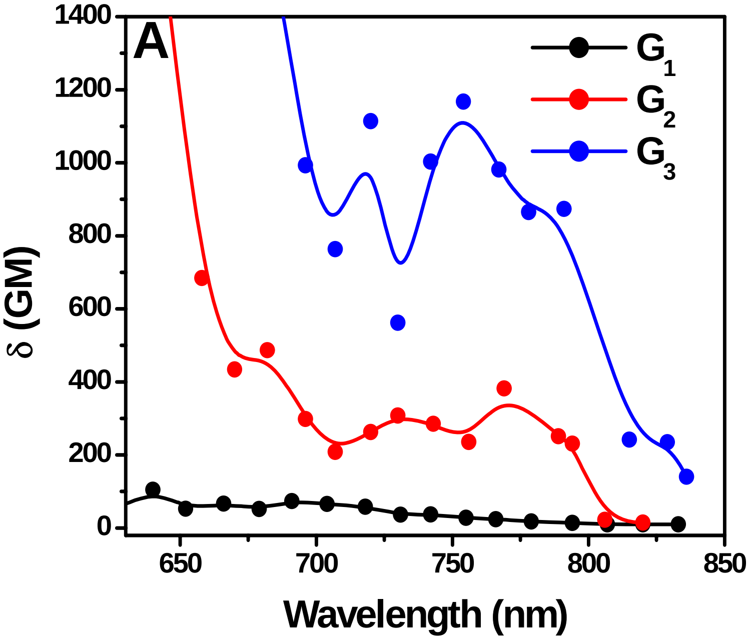

Figure 4.17. Two-photon excitation spectra of thiophene dendrons.

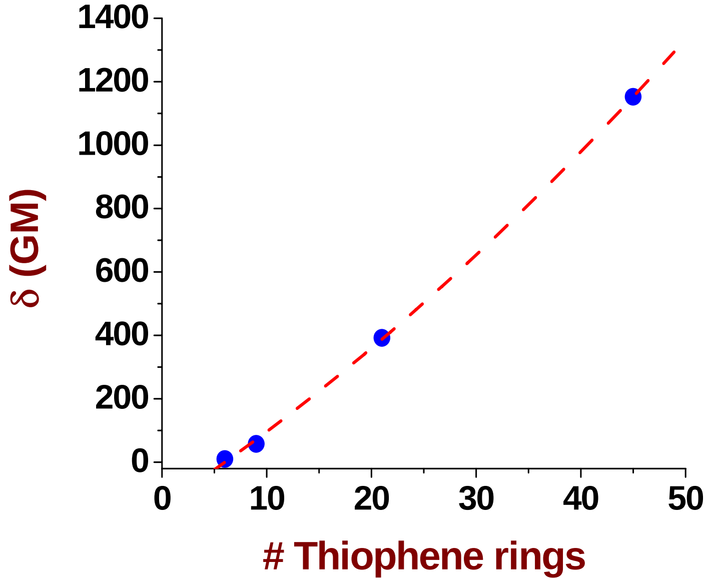

Figure 4.18. Peak TPA cross- section versus number of thiophene rings in each dendrimer. A quadratic fit is shown as a guide for the eye.

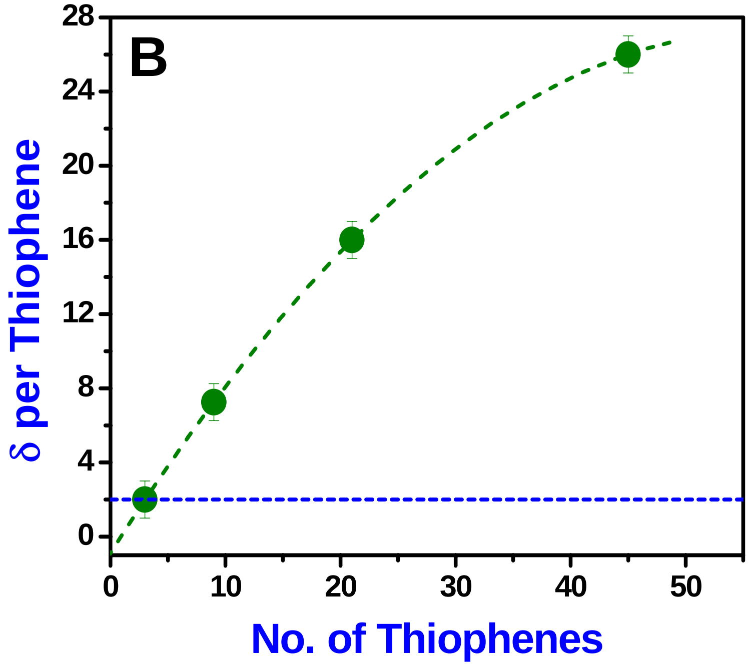

Figure 4.19. Plot of TPA cross-section per thiophene versus number of thiophene rings.

4.4.3.3. Transient Absorption Measurements

To understand the mechanism behind the enhanced TPA cross-sections with increasing dendrimer generation as well as to explore the fundamental excitation and energy transfer processes in these 3D oligothiophene dendrimers, femtosecond transient absorption measurements have been carried out. Several investigations on dynamics of excited states of oligothiophenes and polythiophenes have been reported in the literature via transient absorption and time-resolved fluorescence techniques[80-95]. Lanzani et al[81] have measured the excited state dynamics of α-4T with and without substituents using femtosecond pump-probe spectroscopy. It was shown that there were two main components of the relaxation of the excited state other than the singlet state decay. A fast component of around 700 fs was ascribed to vibrational relaxation which was present in both unsubstituted and substituted α-4T while the torsional relaxation component of 4 ps was observed only in substituted α-4T suggesting that it needed additional planarization[81]. In the present investigation, G_0 showed a vibrational relaxation component with a time constant of 860 fs and no torsional component. This is expected since G_0 is unsubstituted.

Figure 4.20 shows the transient absorption spectra at initial time delays from 100 fs to1.7 ps for G_2 in THF after excitation at 425 nm. It can be observed from Figure 4.20 that at 100 fs (immediately after photo-excitation); the transient absorption spectrum consists of a bleach with maximum around 480 nm, an ESA with maximum around 640 nm, and a shoulder at 540 nm. Bleach at 480 nm is due to the depletion of the ground state while the ESA with a maximum at 640 and 540 nm is ascribed to the singlet-singlet absorption of the Franck-Condon (FC) state of G_2.

In an effort to understand whether the excitation is delocalized or localized, measurements were carried out at different excitation wavelengths to either side of the absorption spectrum (blue and red) so that the possibility of preferential excitation of certain segments of the dendrimer could be monitored, since segments of different conjugation lengths would absorb at different wavelengths. Shown in Figure 4.21 are the transient absorption spectra of G_2 in THF immediately after photo-excitation at different wavelengths from 360 nm to 425 nm. It can be observed that the excited state absorption spectra of FC state of the dendrimer is invariant to the excitation wavelength, confirming the presence of a delocalized excited state.

Furthermore, this ESA of delocalized state decays very fast and concurrent bleach with a maximum around 560 nm starts to grow at the same time scale (Figure 4.20). This bleach is ascribed to that of the stimulated emission arising from the longer oligothiophene present in the G_2 i.e. α-conjugated 6T. From a mechanistic standpoint, similar features are also observed for G_1 and G_3 immediately after photo-excitation, including the presence of delocalized states which proceeded to give the stimulated emission from the longest thiophene in their respective dendrimer in similar time scales. The results are summarized in Table 4.5. As an example, the transients for G_3 are shown in Figure 4.22. It can be observed that the ultrafast time constant is similar for all generations, and further experiments, not described here for the sake of brevity, confirmed that the transients were fairly independent of excitation wavelength, further corroborating the presence of a delocalized state and precluding the attribution of the ultrafast time constant to vibrational relaxation processes.

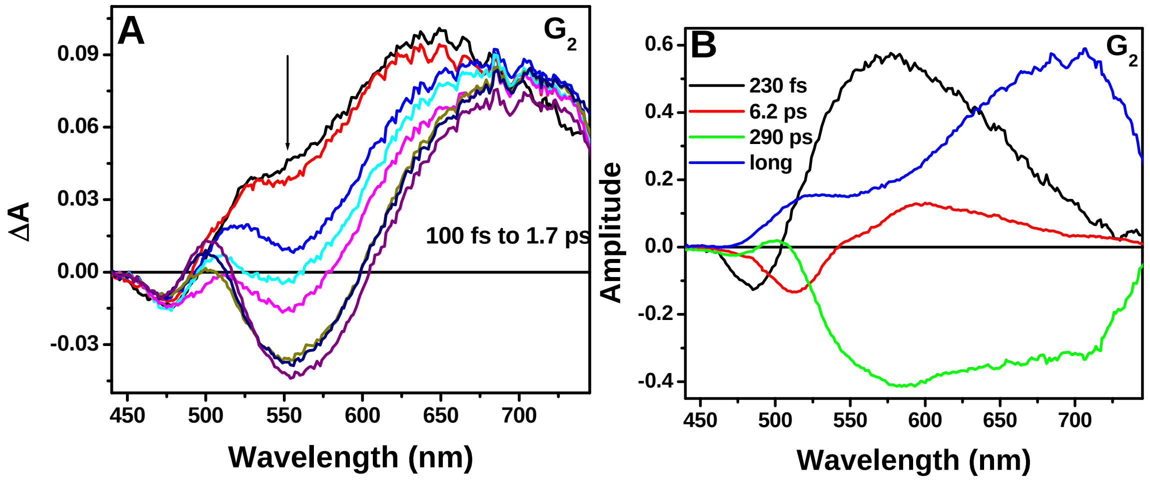

Figure 4.20. A) Transient absorption spectra of G2 in THF from 100 fs to 1.7 ps. B) Transient spectra of principle coefficients of G2 in THF after single value decomposition and global fit analysis.

The time scale for the growth of bleach is around 230 fs for G_2 and it has been ascribed to ultrafast excitation energy transfer from the collective excitation of thiophenes in dendrimer to the longest α-conjugated segment α-6T. Such ultrafast phenomenon has also been observed in phenyl-acetylene cored dendrimers[157]. This confirms the hypothesis of the dendrimer collecting the excitation as a whole (delocalization) followed by subsequent funneling to the longest α-conjugated thiophene segment. Thus, all thiophene dendrimers discussed in this section can be potentially used as light harvesting systems.

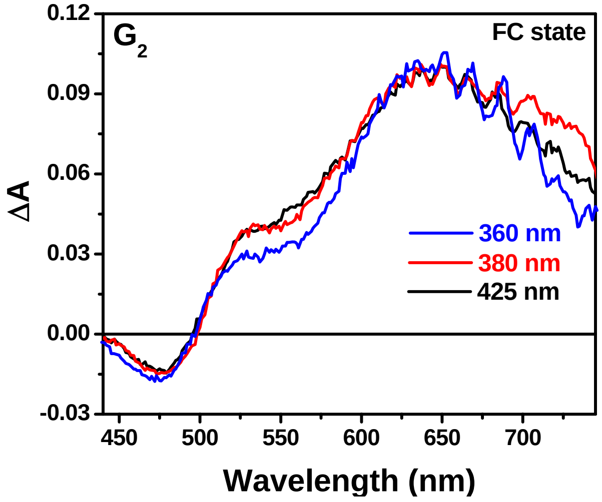

Figure 4.21. Normalized transient absorption spectra of FC state of G2 in THF after excitation at 360 nm, 380 nm and 425 nm.

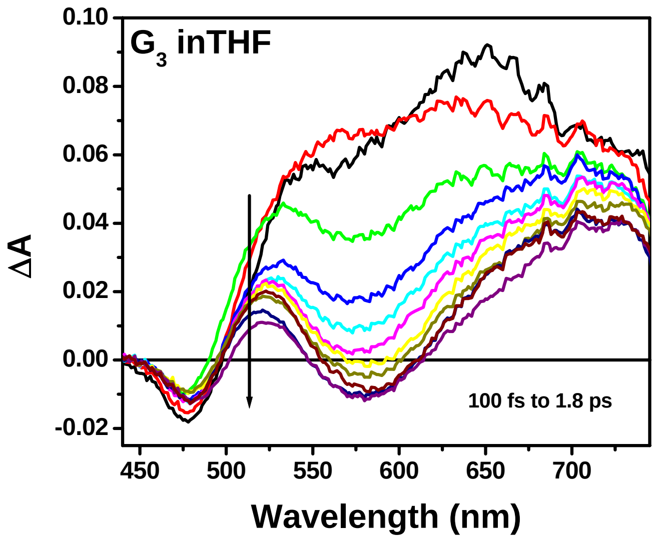

Figure 4.22. Transient absorption spectra of G3 in THF.

The presence of a delocalized state demonstrates strong electronic coupling between individual thiophene rings which manifests itself as enhancement of ground state transition moment M_{ge} which is observed from Table 4.4. Hence, enhancement of TPA cross section is observed with increasing dendrimer generation.

Table 4.5. Excitation wavelength dependent lifetimes of the dendrimers.

Sample	360 nm	380 nm	425 nm
G_0	τ_1 = 860 fs, τ_2 = --, τ_3 = 330 ps, long	------------	------------
G_1	τ_1 = 250 fs, τ_2 = 3.5 ps, τ_3 = 560 ps, long	τ_1 = 260 fs, τ_2 = 3.5, ps τ_3 = 480 ps, long	τ_1 = 220 fs, τ_2 = 2.5 ps, τ_3 = 330 ps, long
G_2	τ_1 = 230 fs, τ_2 = 4.5 ps, τ_3 = 410 ps, long	τ_1 = 250 fs, τ_2 = 4.9 ps, τ_3 = 280 ps, long	τ_1 = 230 fs, τ_2 = 6.2 ps, τ_3 = 290 ps, long
G_3	τ_1 = 280 fs, τ_2 = 10.7 ps, τ_3 = 410 ps, long	τ_1 = 290 fs, τ_2 = 9.1 ps t3 = 350 ps, long	τ_1 = 300 fs, τ_2 = 12.2 ps, τ_3 = 420 ps, long

4.5. Conclusions

In this chapter, conjugated organic chromophores arranged in branched architecture have been investigated for nonlinear optical properties. The chapter began with a systematic structure-property relationship study using nitrogen cored tri-branched molecules as model systems. Interesting trends were observed in steady state as well as TPA behavior. The alkene chromophores of same branch length showed larger TPA cross sections than their alkyne counterparts. Using time-resolved spectroscopy, this observation was attributed to greater population of solvent stabilized intramolecular charge transfer state in alkene chromophores, which translated into increased charge transfer character of the Franck-Condon state.

The next section addressed the fundamental reasons behind the cooperative enhancement observed upon increase in dimensionality of a chromophore from a dipole (monomer) to an octupole (tri-branched). Firstly, the enhancement was confirmed by TPA cross section measurements. Steady state measurements showed interesting photophysics in emission behavior. The emitting state appeared to be different in nature for the trimer. This was confirmed using time-resolved transient absorption measurements. Transient measurements proved the presence of a delocalized C_3-symmetry state in trimer. Presence of a barrier between C_3-symmetry state and ICT state in trimer enabled us to spectroscopically view the charge-delocalized state. This refers to the observation that with increasing solvent polarity, there is a transfer from C_3-symmetry state (less polar) to intramolecular charge transfer state (more polar) for the trimer. The presence of delocalized state translates into electronic coupling between the arms of the trimer and hence, enhanced TPA cross section.

Finally, in order to demonstrate that small branched molecules serve as building blocks for larger dendrimers, we investigated several all-thiophene dendrons with potential applications as light harvesting systems. From the optical absorption measurements, it was observed that the absorption spectrum was a linear combination of the absorption spectra of several linear oligothiophene units. However, the fluorescence spectra of the dendrimers suggest the possibility of intramolecular excitation energy transfer to longest α-conjugated oligothiophene thiophene in the respective dendrimer. TPA cross section measurements showed increasing δ per thiophene unit values with increasing dendrimer generation, suggesting strong electronic coupling and delocalization. Time-resolved measurements proved this, along with ultrafast energy funneling of the excitation to the largest α-conjugated oligothiophene segment.

Summary

- Building block approach was applied to branched architecture.
- Alkene π-linkers were found to yield better two-photon absorption (TPA) cross sections that alkyne π-linkers.
- Steady state measurements were not sufficient to explain the observed TPA enhancement..
- Transient absorption measurements revealed the presence of solvent stabilized intramolecular charge transfer state which is related to change in dipole moment. This in turn has a profound impact on the TPA cross section.
- The mechanism of enhancement of TPA cross section upon increasing the dimensionality from dipole (monomer) to octupole (tri-branched) was investigated using transient absorption spectroscopy.
- Transient measurements revealed the presence of an initially charge delocalized state in the trimer whereas such a state was absent in case o monomer.
- Such initial delocalization followed by eventual localization of excitation of charge on a single branch results in large change in dipole moment as well as transition dipole moment, leading to enhanced TPA behavior.
- Dendron-type macromolecules composed of thiophene units were investigated for their TPA behavior.
- Super-linear increase in TPA cross section was observed with increasing dendron generation.
- Using transient absorption measurements, ultrafast funneling of energy to longest α-conjugated thiophene segment was deemed to be the reason for enhancement of TPA behavior.

4.6. References

1. (a) Cumpston, B. H. *et al. Nature* **1999**, *398*, 51. (b) Albota, M. *et al. Science* **1998**, *281*, 1653.
2. Zhou, W.; Kuebler, S. M.; Braun, K. L.; Yu, T.; Cammack, J. K.; Ober, C. K.; Perry, J. W.; Marder, S. R. *Science* **2002**, *296*, 1106.
3. Kawata, S.; Sun, H.-B.; Tanaka, T.; Takada, K. *Nature* **2001**, *412*, 697.
4. Sun, H.-B.; Mizeikis, V.; Xu, Y.; Juodkazis, S.; Ye, J.-Y.; Matsuo, S.; Misawa, H. *Appl. Phys. Lett*. **2001**, *79*, 1.
5. Maruo, S.; Nakamura, O.; Kawata, S. *Opt. Lett.* **1997**, *22*, 132.
6. Denk, W.; Strickler, J. H.; Webb, W. W. *Science* **1990**, *248*, 73.
7. Bhawalkar, J. D.; Kumar, N. D.; Zhao, C. F.; Prasad, P. N. *J. Clin. Laser Med. Surg.* **1997**, *15*, 201.
8. He, G. S.; Markowicz, P. P.; Line, P.-C. Prasad, P. N. *Nature* **1999**, *415*, 767.
9. Xu, C.; Zipfel, W.; Shear, J. B.; Williams, R. M.; Webb, W. W. *Proc. Natl. Acad. Sci. U.S.A.* **1996**, *93*, 10763.
10. Larson, D. R.; Zipfel, W. R.; Williams, R. M.; Clark, S. W.; Bruchez, M. P.; Wise, F. W.; Webb, W. W. *Science* **2003**, *300*, 1434.
11. He, G. S.; Xu, G. C.; Prasad, P. N.; Reinhardt, B. A.; Bhatt, J. C.; McKellar, R.; Dillard, A. G. *Opt. Lett.* **1995**, *20*, 435.
12. Ehrlich, J. E.; Wu, X. L.; Lee, I.-Y. S.; Hu, Z.-Y.; Ro¨ckel, H.; Marder, S. R.; Perry, J. W. *Opt. Lett.* **1997**, *22*, 1843
13. Parthenopoulos, D. A.; Rentzepis, P. M. *Science* **1989**, *245*, 843.
14. Strickler, J. H.; Webb, W. W. *Opt. Lett.* **1991**, *16*, 1780.
15. Belfield, K. D.; Schafer, K. J. *Chem. Mater.* **2002**, *14*, 3656.
16. Marder, S. R.; Beratan, D. N.; Cheng, L. T. *Science* **1991**, *252*, 103.
17. Kanis, D. R.; Ratner, M. A.; Marks, T. J. *Chem. Rev.* **1994**, *94*, 195.

18. Bre´das, J.-L.; Cornil, K.; Meyers, F.; Beljonne, D. In *Handbook of Conducting Polymers*; Skotheim, T. A., Elsenbaumer, R. L., Reynolds, J. R., Eds.; Marcel Dekker: New York, **1998**.
19. He, G. S.; Yuan, L.; Cheng, N.; Bhawalkar, J. D.; Prasad, P. N.; Brott, L. L.; Clarson, S. J.; Reinhardt, B. A. *J. Opt. Soc. Am. B* **1997**, *14*, 1079.
20. Ehrlich, J. B.; Wu, X. L.; Lee, I.-Y. S.; Hu, Z.-Y.; Rockel, H.; Marder, S. R.; Perry, J. W. *Opt. Lett.* **1997**, *22*, 1843.
21. He, G. S.; Gvishi, R.; Prasad, P. N.; Reinhardt, B. A. *Opt. Comm*un. **1995**, *117*, 133.
22. (a) Kim, O. K.; Lee, K. W.; Woo, H. Y.; Kim, K. S.; He, G. S.; Swiatkiewicz, J.; Prasad, P. N. *Chem. Mater*. **2000**, *12*, 284. (b) Kannan, R.; Chung, S.; Lin, T.; Prasad, P.N.; Vaia, R. A.; Tan, L.; *Chem. Mater.* **2004**, *16,* 185.
23. Reinhardt, B. A.; Brott, L. L.; Clarson, S. J.; Dillard, A. G.; Bhatt, J. C.; Kannan, R.; Yuan, L.; He, G. S.; Prasad, P. N. *Chem. Mater.* **1998**, *10,* 1863.
24. Strehmel, B.; Sarker, A. M.; Detert, H. *ChemPhysChem*, **2003**, *4*, 249.
25. Xu, C.; Zipfel, W.; Shear, J. B.; Williams, R. M.; Webb, W. W. *Proc. Natl. Acad. Sci. U. S. A.* **1996**, *93*, 10763.
26. He, G. S.; Lin, T.-C.; Prasad, P. N.; Kannan, R.; Vaia, R. A.; Tan, L.-S.; *J. Phys. Chem. B.* **2002**, *106,* 11081.
27. Rumi, M.; Ehrlich, J. E.; Heikal, A. A.; Perry, J. W.; Barlow, S.; Hu, Z. Y.; McCord-Maughon, D.; Parker, T. C.; Rockel, H.; Thayumanavan, S.; Marder, S. R.; Beljonne, D.; Bredas, J. L. *J. Am. Chem. Soc.* **2000**, *122*, 9500.
28. Pond, S. J. K.; Rumi, M.; Levin, M. D.; Parker, T. C.; Beljonne, D.; Day, M. W.; Bredas, J. L.; Marder, S. R.; Perry, J. W. *J. Phys. Chem. A* **2002**, *106*, 11470.
29. Beljonne, D.; Wenseleers, W.; Zojer, E.; Shuai, Z.; Vogel, H.; Pond, S. J. K.; Perry, J. W.; Marder, S. R.; Bredas, J.-L. *Adv. Funct. Mater.* **2002**, *12*, 631.
30. Chung, S.-J.; Kim, K.-S.; Lin, T.-C.; He, G. S.; Swiatkiewicz, J.; Prasad, P. N. *J. Phys. Chem. B* **1999**, *103*, 10741.
31. Katan, C.; Terenziani, F.; Mongin, O.; Werts, M. H. V.; Porre´s, L.; Pons, T.; Mertz, J.; Tretiak, S.; Blanchard-Desce, M. *J. Phys. Chem. A* **2005**, *109*, 3024.

32. (a) Mongin, O.; Porres, L.; Katan, C.; Pons, T.; Mertz, J.; Blanchard- Desce, M. *Tetrahedron Lett.* **2003**, *44*, 8121. (b) Venleton, L.; Moreaus, L.; Mertz, J.; Blanchard-Desce, M. *Chem. Commun.* **1999**, 2055.
33. Lee, H. J.; Sohn, J.; Hwang, J.; Park, S. Y.; Choi, H.; Cha, M. *Chem. Mater.* **2004**, *16*, 456.
34. Kogej, T.; Beljonne, D.; Meyers, F.; Perry, J.W.; Marder, S.R.; Bredas, J.L. *Chem. Phys. Lett.* **1998,** *298,* 1.
35. Drobizhev, M.; Karotki, A.; Dzenis, Y.; Rebane, A.; Suo, Z.; Spangler, C. W. *J. Phys. Chem. B* **2003**, *107*, 7540.
36. Jeong, H. C.; Piao, M. J.; Lee, S. H.; Jeong, M.-Y.; Kang, K. M.; Park, G.; Jeon, S.-J.; Cho, B. R. *Adv. Funct. Mater.* **2004**, *14*, 64.
37. Varnavski, O. P.; Ostrowski, J. C.; Sukhomlinova, L.; Twieg, R. J.; Bazan, G., C.; Goodson, T., III *J. Am. Chem. Soc.* **2002**, *124*, 1736.
38. Katan, C.; Terenziani, F.; Mongin, O.; Werts, M. H. V.; Porre´s, L.; Pons, T.; Mertz, J.; Tretiak, S.; Blanchard-Desce, M. *J. Phys. Chem. A* **2005**, *109*, 3024.
39. Goodson, T., III. *Acc. Chem. Res.* **2005**, *38*, 99.
40. Lahankar, A. S.; West, R.; Varnavski, O.; Xie, X.; Goodson, T., III; Sukhomlinova, L.; Twieg, R. *J. Chem. Phys.* **2004**, *120*, 337.
41. Varnavski, O.; Samuel, I. D. W.; Palsson, L.-O.; Beavington, R.; Burn, P. L.; Goodson, T., III. *J. Chem. Phys.* **2002**, *116*, 8893.
42. Wang, Y.; Ranasinghe, M. I.; Goodson, T., III. *J. Am. Chem. Soc.* **2003**, *125*, 9562.
43. Varnavski, O.; Goodson, T., III; Sukhomlinova, L.; Twieg, R. *J. Phys. Chem. B* **2004**, *108*, 10484.
44. Wang, Y.; He, G. S.; Prasad, P. N.; Goodson, T. III *J. Am. Chem. Soc.* **2005**, *127*, 10128.
45. Li, B.; Tong, R.; Zhu, R.; Meng, F.; Tian, H.; Qian, S. *J. Phys. Chem. B.* **2005**, *109*, 10705.
46. Goodson, T., III. *Annu. Rev. Phys. Chem.* **2005**. *56*, 581.
47. Zhou, X.; Feng, J.; Ren, A. *Chem. Phys. Lett.* **2005**, *403*, 7.
48. Drobizhev, M.; Rebane, A.; Suo, Z., Spangler, C. W. *J. Lumin.* **2005,** *111*, 291.
49. Macak, P.; Luo, Y.; Norman, H.; Ågren, H. *J. Chem. Phys.* **2000**, *113*, 7055.

50. Cho, B. R.; Son, K. H.; Lee, S. H.; Song, Y.-S.; Lee, Y.-K.; Jeon, S.-J.; Choi, J. H.; Lee, H.; Cho, M. *J. Am. Chem. Soc.*, **2001**, *123*, 10039.
51. Delgado, M. C. R.; Hernandez, V.; Casado, J.; Navarrete, J. T. L.; Raimudo, J.-M.; Blanchard, P.; Roncali, J. *Chem. Eur. J.* **2003**, *9*, 3670.
52. Charlot, M.; Izard, N.; Mongin, O.; Riehl, D.; Blanchard-Desce, M.; *Chem. Phys. Lett.* **2006**, *417*, 297.
53. Mongin, O.; Charlot, M.; Katan, C.; Porre;, L.; Parat, M.; Pions, T.; Mertz, J.; Blanchard-Desce, M. *Proc. SPIE Int. Soc. Opt. Eng.* **2004**, *9*, 5516.
54. Cho, B. R.; Lee, S. J.; Lee, S. H.; Son, K. H.; Kim, Y. H.; Doo, J.-Y.; Lee, G. J.; Kang, T. I.; Lee, Y. K.; Cho, M.; Jeon, S.-J. *Chem. Mater.* **2001**, *13*, 1438.
55. Cho, B. R.; Ratner, M. A.; Mark, T. J. *Chem Rev.* **1994**, *94*, 195.
56. McIlroy, S. P.; Clo, E.; Nikolajsen, L.; Federiksen, P. K.; Nielsen, C. B.; Mikkelsen, K. V.; Gothelf, K. V.; Ogilby, P. R. *J. Org. Chem.* **2005**, *70*, 1134.
57. (a) Martin, R. E.; Diederich, F. *Angew. Chem. Int. Ed.* **1999**, *38*, 1350. (b)Lee, J. Y.; Kim, K. S.; Mhin, B. J. *J. Chem. Phys.* **2001**, *115*, 9484.
58. Maciejewski, A.; Steer, R. P. *J. Photochem.* **1986**, *35*, 59.
59. Xu, C.; Webb, W. W. *J. Opt. Soc. Am. B.* **1996**, *13*, 481.
60. Negres, R. A.; Hales, J. M.; Kobyakov, A.; Hagan, D. J.; Van Stryland, E. W. *IEEE J. Quant. Elec.* **2002**, *38*, 1205.
61. Hales, J. M.; Hagan, D. J.; Van Stryland, E. W.; Schafer, K. J.; Morales, A. R.; Belfield, K. D.; Pacher, P.; Kwon, O.; Zojer, E.; Bredas, J. L. *J. Chem. Phys.*, **2004**, *121*, 3152.
62. O'Connor, D. V.; and Phillips, D. *Time Correlated Single Photon Counting*, Academic Press, New York, **1984**.
63. Demas, J. N. *Excited State Life Time Measurements* Academic Press, New York, **1983.**
64. Bevington, P. R. *Date Reduction and Error Analysis for the Physical Sciences*, McGraw Hill, New York, **1969**.
65. Marquardt, D. W. *Journal of the Society for Industrial and Applied Mathematics*, **1963**, *11*, 431.
66. Dewar, M. J. S. *J. Am. Chem. Soc.* **1952**, *72*,1345.

67. Cheng, L.; Tam, W.; Marder, S. R.; Stiegman, A. E.; Rikken, G.; Spangler, C. W. *J. Phys. Chem.* **1991**, *95*, 10643.
68. Strickler, S. J.; Berg, R. A. *J. Chem. Phys.* **1962**, *37*, 814.
69. Rubio-Pions, O.; Luo, Y.; Agren, H. *J. Chem. Phys.* **2006**, *124*, 094310.
70. Ray, P. C.; Leszcczynski, J. *J. Phys. Chem. A* **2005**, *109*, 6689.
71. Hansch, C.; Leo, A.; Taft, R. W. *Chem. Rev.* **1991**, *91*, 165.
72. Ramakrishna, G.; Goodson, T. G. III., *J. Phys. Cham. A* **2007**, *111*, 993.
73. Premvardhan, L.; Papagiannakis, E.; Hiller, R. G.; van Gorndelle, R. *J. Phys. Chem. B.* **2005**, *109*, 15589.
74. Ahlheim, M.; Barzoukas, M.; Bedworth, P. V.; Blanchard-Desce, M.; Fort, A.; Hu, Z.-Y.; Marder, S. R.; Perry, J. W.; Runser, C.; Statehelin, M.; Zysset, B. *Science*, **1996**, *271*, 335.
75. Lee, W.-H.; Lee. H.; Kim, J.-A.; Choi, J.-H.; Cho, M.; Jeon, S.-J.; Cho, B. R. *J. Am. Chem. Soc.* **2001**, *123*, 10658.
76. Wang, C.-K.; Macak, P.; Luo, Y.; Agren, H. *J. Chem. Phys.* **2001**, *114*, 9813.
    33. Norman, P.; Luo, Y.; Agren, H. *Chem. Phys. Lett.* **1998**, *296*, 8.
77. Poliakov, E. Y.; Chernyak, V.; Tretiak, S.; Mukamel, S. *J. Chem. Phys.* **1999**, *110*, 8161.
78. Latterini, L.; De Belder, G.; Schweitzer, G.; Van der Auweraer, M.; De Schryver, F. C. *Chem. Phys. Lett.* **1998**, *295*, 11.
79. Verbouwe, W.; Van der Auweraer, M.; De Schryver, F. C.; Piet, J. J.; Warman, J. M. *J. Am. Chem. Soc.* **1998**, *120*, 1319.
80. Bangal, P. R.; Lam, D. M. K.; Peteanu, L. A.; Van der Auwerear, M. *J. Phys. Chem. B.* **2004**, *108*, 16834.
81. Rogers, J. E.; Slagle, J. E.; McLean, D. G.; Sutherland, R. L.; Sankaran, B.; Kannan, R.; Tan, L.-S.; Fleitz, P. A. *J. Phys. Chem. A* **2004**, *108*, 5514.
82. Thompson, W. H.; Blanchard-Desce, M.; Hynes, J. T. *J. Phys. Chem. A.*, **2003**, *107*, 6032.
83. Birks, J. B. *Photophysics of Aromatic Molecules*, Wiley-Interscience, New York, **1986**.
84. Lewis, J. E.; Marocelli, M. *Chem. Phys. Lett.* **1998**, *282*, 197.

85. Larsen, D. S.; Ohta, K.; Fleming, G. R. *J. Chem. Phys.* **1999**, *111*, 8970.

86. Elsaesser, T.; Kaiser, W. *Ann. Rev. Phys. Chem.* **1991**, *42*, 83.

87. Owrutsky, J. C.; Rattery, D.; Hochstrasser, R. M. *Ann. Rev. Phys. Chem.* **1994**, *45,* 519.

88. Horng, M. L.; Dahl, K.; Jones, G. II.; Maroncelli, M. *Chem. Phys. Lett.* **1999**, *315*, 363.

89. Halls, J. J. M.; Friend, R. H. In *Clean Electricity from Photovoltaics*; Archer, M. D., Hill, R., Eds.; Series on Photoconversion of Energy; Imperial College Press: River Edge, NJ, 2001; Vol 1, 377.

90. Granstrom, M.; Petrisch, K.; Arias, A. C.; Lux, A.; Andersson, M. R.; Friend, R. H. *Nature* **1998**, *395*, 257.

91. Padinger, F.; Rittberger, R. S.; Sacriftci, N. S. *Adv. Funct. Mater.* **2003**, *13*, 85. (b) Jinag, D. –L.; Aida, T. *Nature*, **1997**, *388*, 454.

92. Jinag, D. –L.; Aida, T. *Nature*, **1997**, *388*, 454.

93. Morisue, M.; Yamatsu, S.; Haruta, N.; Kobuke, Y. *Chem. Eur. J.* **2005**, *11*, 5563.

94. Forrest, S. R. *Nature* **2004**, *428*, 911.

95. Kopleman, R.; Shortreed, M.; Shi, Z.-Y.; Tan, W.; Xu, Z.; Moore, J. S.; Bar-Haim, A.; Klafter, J. *Phys. Rev. Lett.* **1997**, *78*, 1239.

96. Bari-Haim, A.; Klafter, J.; Kopleman, R. *J. Am. Chem. Soc.* **1997**, *119*, 6197.

97. Bari-Haim, A.; Klafter, J. *J. Phys. Chem. B* **1998**, *102*, 1662.

98. Moore, J. S. *Acc. Chem. Res.* **1997**, *30*, 402.

99. Devadoss, C.; Bharathi, P.; Moore, J. S. *J. Am. Chem. Soc.* **1996**, *118*, 9635-9644.

100. Adronov, A.; Frechet, J. M. *J. Chem. Soc., Chem. Commun.* **2000**, *18*, 1701.

101. Kawa, M.; Frechet, J. M. J. *Chem. Mater.* **1998**, *10*, 286.

102. Gilat, S. L.; Adronov, A.; Frechet, J. M. J. *Angew. Chem. Int. Ed.* **1999**, *38*, 1422.

103. Wang, P. W.; Liu, Y. J.; Deavadoss, C.; Bharathi, P.; Moore, J. S. *Adv. Mater.* **1996**, *8*, 237

104. Glebler, C.; Antoniadis, H.; Bradley, D. D. C.; Shirota, Y. *Appl. Phys. Lett.* **1998**, *72*, 2448.

105. Halim, M. Samuel, I. D. W; D.; Pilow, J. N. D.; Monkman, A. P.; Burn, P. L. *Synth. Met.* **1999**, *102*, 1571.

106. Markham, J. P. J.; Lo, S. –C.; Magennis, S. W.; Burn, P. L.; Samuel, I. D. W. *Appl. Phys. Lett.* **2002**, *80*, 2645.

107. Goodson, T., III. *Ann. Rev. Phys. Chem.* **2005**, *56*, 581.

108. Chuang, S.-J.; Liu, T.-C.; Kim, K. S.; He, G. S.; Swiatkiewicz, J. et al *Chem. Mater.* **2001**, *13*, 4071.

109. Varnavski, O.; Leanov, A.; Lih, L.; Takacks, J.; Goodson, T. III *J. Phys. Chem. B* **2000**, *104*, 179.

110. Ranasinghe, M. I.; Varnavaski, O. P.; Pawlas, J.; Hauck, S. I.; Lowie, J et al *J. Am. Chem. Soc.* **2002**, *124*, 6520.

111. Varnavski, O.; Yan, X.; Mongin, O.; Blanchard-Desce, M.; Goodson, T. III. *J. Phys. Chem. C* **2007**, *111*, 149.

112. McCullough, R. D. *Adv. Mater.* **1998**, *10*, 93.

113. Bauerle, P. in *Electronic materials: The oligomer approach*; Mullen, K.; Wegner, G. Eds.; Wiley-VCH: New York 1998.

114. Fichou, D. Ed *Handbook of Ologo- and Polythiophenes*, Wiley-VCH: Weinheim 1999.

115. Roncali, J. *Chem. Rev.* **1997**, 97, 173.

116. Fichou, D. *J. Mater. Chem.* **2000**, *10*, 571.

117. Braun, D.; Gustaffson, G.; McBranch, D.; Heeger, A. J. *J. App. Phys.* **1992**, *72*, 564.

118. Mitschke, V.; Bauerle, P. *J. Chem. Soc. Perkin Trans.* **2001**, 740.

119. Vatterlin, C.; Neureiter, H.; Gebauer, W.; Ziegler, B.; Sokolowski, M.; Bauerle, P.; Umbach, E. *J. Appl. Phys.* **1997**, *82*, 3003.

120. Dodabalapur, A.; Torsi, L.; Katz, H. E. *Science* **1995**, *270*, 26.

121. Katz, H. E.; Bao, N.; Gilat, S. L. *Acc. Chem. Res.* **2001**, *34*, 359.

122. Chen, T .-A.; Rieke, R. D. *J. Am. Chem. Soc.* **1992**, *114*, 10087.

123. McCullough, R. D.; Lowe, R. D.; Jayaraman, M.; Anderson, D. L. *J. Org. Chem.* **1993**, *58*, 904.

124. Granstrom, M.; Petritsch, K.; Arias, A. C.; Lux, A.; Andersson, M. R.; Friend, R. H. *Nature* **1998**, *395*, 257.

125. Brabec, C. J.; Sacrittel, N. S.; Hummelen, J. C. *Adv. Funct. Mater.* **2001**, *11*, 85.

126. Noma, N.; Tsuzuki, T.; Shirota, Y. *Adv. Mater.* **1995**, *7*, 647.

127. Reyes-Reyes, M.; Kim, K.; Caroll, D. J. *Appl. Phys. Lett.* **2005**, *87*, 083506.

128. Kromer, J.; Rios-Carreras, I.; Fuhrmann, G.; Musch, C.; Wunderlin, M.; Debaerdemaeker, T.; Mena-Osteritz, E.; Bauerle, P. *Angew. Chem. Int. Ed.* **2000**, *39*, 3481.

129. Mena-Osteritz, E.; Bauerle, P. *Adv.Mater.* **2001**, *13*, 243.

130. Fuhrmann, G.; Bauerle, P. *Chem.Commun.* **2003**, 926.

131. Bauerle, P.; Fishcer, T.; Bidlingmeier, B.; Stabel, A.; Rabe, J. P. *Angew. Chem. Int. Ed. Engl.* **1995**, *34*, 303.

132. Nicolas, Y.; Blanchard, P.; Levillain, E.; Allain, M.; Mercier, N.; Roncali, J. *Org. Lett.* **2004**, *6*, 6433.

133. Mitchell, W. I.; Kopidakis, N.; Rumbles, G.; Ginley, D. S.; Shaheen, S. E. *J. Mater. Chem.* **2005**, *15*, 4518.

134. Xia, C.; Fan, X.; Locklin, J.; Advincula, R. C. *Org. Lett.* **2002**, *4*, 2067.

135. Xia, C.; Fan, X.; Locklin, J.; Advincula, R. C.; Gies, A.; Nonidez, W. *J. Am. Chem. Soc.* **2004**, *126*, 8735.

136. Locklin, J.; Patton, D.; Deng, S.; Baba, A.; Millan, M.; Advincula, R. C. *Chem. Mater.* **2004**, *16*, 5187.

137. Deng, S.; Locklin, J.; Patton, D.; Baba, A.; Advincula, R. C. *J. Am. Chem. Soc.* **2005**, *127*, 1744.

138. Ma, C.-Q.; Mena-Osteritz, E.; Debaerdemaeker, T.; Wienk, M. M.; Janssen, R. A. J.; Bauerle, P. *Angew. Chem. Int. Ed.* **2007**, *46*, 1679.

139. Zhao, M.-T.; Singh, B. P.; Prasad, P. N. *J. Chem. Phys.* **1988**, *89*, 5535.

140. Marder, S. R.; Kippelen, B.; Jen, A. K.; Peyghambarian, N. *Nature* **1997**, *388*, 845.

141. Lanzani, G.; Nisoli, M.; De Silvestri, S.; Tubino, R. *Syn. Met.* **1996**, *76*, 39.

142. Lanzani, G.; Nisoli, M.; De Silvestri, S.; Tubino, R. *Chem. Phys. Lett.* **1996**, *251*, 339.

143. Lanzani, G.; Cerullo, G.; Stagoara, S.; De Silvestri, S. *J. Photochem. Photobiol. A* **2001**, *144*, 13.

144. van Hal, P. A.; Janssen, R. A. J.; Lanzani, G.; Cerullo, G.; Zaveleni-Rossi, M.; De Silvestri, S. *Chem. Phys. Lett.* **2001**, *345*, 33.

145. Cerullo, G.; Lanzani, G.; Muccini, M.; Taliani, C.; De Silvestri, S. *Syn. Met.* **1999**, *101*, 614.

146. Grebner, D.; Helbig, M.; Rentsch, S. *J. Phys. Chem.* **1995**, *99*, 16991.

147. Paa, W.; Yang, J.-P.; Rentsch, S *Appl. Phys. B.* **2000**, *71*, 443.

148. Yang, J.-P.; Paa, W.; Rentsch, S. *Syn. Met.* **1999**, *101*, 624.

149. Paa, W.; Yang, J.-P.; Rentsch, S. *Syn. Met.* **2001**, *119*, 525.

150. Kodara, T.; Watanabe, A.; Ito, O.; Watanabe, M.; Saito, H.; Koishi, M. *J. Phys. Chem.* **1996**, *100*, 15309.

151. Frolov, S. V.; Kloe, Ch.; Berg, S.; Thomas, G. A.; Batlogg, B.; Tubino, R. *Phys. Rev. B.* **1996**, *53*, 4453.

152. Klein, G. *Chem. Phys. Lett.* **2000**, *320*, 65.

153. Grage, M. M.-L; Zaushitsyun, Y.; Yartsev, A.; Chachivilis, M; Sundstrom, V.; Pullerits, T. *Phys. Rev. B.* **2003**, *67*, 205207.

154. Westenhoff, S.; Beenkem, W. J. D.; Friend, R. H.; Greenham, N. C.; Yartsev, A.; Sundstrom, V. *Phys. Rev. Lett.* **2006**, *97*, 166804.

155. Cheng, X.; Ichimura, K.; Fichou, P.; Kobayashi, T. *Chem. Phys. Lett.* **1991**, *185*, 286.

156. Yang, A.; Kuroda, M.; Shiraishi, Y.; Kobayashi, T. *J. Phys. Chem. B* **1998**, *102*, 3706.

157. Bosman, A. W.; Janssen, H. M.; Meijer, E. W. *Chem. Rev.* **1999**, *99*, 1665.

Chapter 5

Investigation of Enhancement of Two-Photon Absorption Cross Section in Macrocyclic Thiophenes

5.1. Introduction

The search for new optical devices has inspired the creation of novel materials with tailored structure-property relationships. Multi-chromophore and self-assembly approaches have been applied towards the creation of superior light harvesting, light emitting and nonlinear optical materials. This has included organic polymers, dendrimers and rotaxanes.[1-3]. An important characteristic that is common to many of these materials is the multi-chromophore architecture that possesses collective excitations where several chromophores in the architecture contribute to the optical response. For applications involving nonlinear optical (NLO) processes, this collective behavior is utilized and it results, in some cases, enhanced properties beyond what is expected for the isolated or localized set of individual chromophores. Previous reports in regards to organic branched structures have categorized the excitations in such systems as either incoherent (hopping regime) or coherent (strongly coupled) [4-5]. It was found that for cases of coherent interactions in multi-chromophore systems, strong enhancement of the two-photon absorption (TPA) effects was possible[6]. The investigation of this effect in several dendrimer systems has inspired possible applications in two-photon imaging and photodynamic therapy[7-8].

A large number of reports have been published, elaborating the structure-property relationships such as conjugation length[9-10], nature of substituents[11-12], dimensionality (dipoles, quadrupoles, and octupoles) [13-16] and intramolecular interactions[6] among others. Majority of the reports have concentrated on linear and branched architectures. In terms of particular structures, various organic chromophores have been studied for their nonlinear optical (NLO) behavior. Oligo and polythiophenes are some of the primary candidates for organic electronics[17-23]. They are used as hole transport materials in Organic Light Emitting Diodes (OLEDs) [24-26], Field Effect Transistors (FETs) [26-27], photovoltaic cells [28-29] and light modulators [30-31]. Thiophenes are more amenable to synthetic modifications by virtue of enhanced reactivity at α and β positions of the thiophene ring. This enables the synthesis of a wide variety of molecules with systematic variations in structure[32]. Donor-acceptor substituted thiophene derivatives have been investigated for their TPA behavior[33-34]. However, these investigations involved linear dipolar and quadrupolar molecules. To our knowledge, the nonlinear optical properties of thiophenes in geometries other than linear have not been explored in detail. For example, thiophenes in cyclic architectures have not been explored for their TPA properties or their collective excitations. Electronic structure calculations of thiophene-based systems resembling annulenes have been investigated previously[35] Marsella et al have proposed that they can be used as molecular muscles[36]. Also, applications in biological areas have been proposed[37-39]. Other applications in opto-electronics and photonics have also been determined[40].

In this section, the optical properties of two series of conjugated macrocyclic thiophenes, both having circular geometry are presented. The first series consists of macrocycles comprising of terthiophene and diacetylene building blocks (3T_DA). The second series consists of building blocks composed of segments containing alternating thiophene and alkyne linkages. Such segments are then interconnected via double bonds to produce the macrocycles. The advantage that circular chromophores have over linear systems is that there are no “end-effects”, which particularly in shorter oligomers influence the conjugation length and consequently the electronic and optical properties [35, 41-42]. Hence, theoretically, such macrocycles can be regarded as infinitely conjugated molecular wires, which render them attractive for a variety of applications. Furthermore, cyclic systems also mimic natural light harvesting systems[43-45]. Hence, a detailed study on NLO properties of macromolecules possessing cyclic geometry could uncover intriguing optical properties.

5.2. Two-Photon Absorption Behavior of Macrocycles Containing Short Thiophene and Alkyne Segments.

5.2.1. Background

The NLO properties of two cyclo(terthiophene-diacetylenes), namely the cyclodimer C[3T-DA]$_2$ and the cyclopentamer C[3T-DA]$_5$ (structures shown in Figure 5.1), with different ring sizes, have been investigated. The macrocycles can be regarded as nanometer sized cavities, which renders them attractive for several potential applications. Their TPA cross section (δ) spectra were measured using Two-photon excited fluorescence (TPEF) method. We have also investigated the fluorescence dynamics and the excited state dynamics in these chromophores. Because the number of [3T-DA] repeating units differ in the molecule, the chromophore density in cyclopentamer C[3T-DA]$_5$ is 2.5 times higher than in the cyclodimer C[3T-DA]$_2$. This enables tuning of the size of the nanometer-sized cavities by simply changing the number of building blocks. An interesting question is the synergistic enhancement in TPA cross section as a result of increase in chromophore density. The extent of enhancement might elucidate the extent of conjugation in cyclic systems.

These macrocyclic systems are equally interesting from a theoretical standpoint as well. It has been found in previous theoretical studies that the main differences in the absorption spectra of cyclothiophenes in comparison to the corresponding linear oligothiophenes are caused by different selection rules as a consequence of their different geometries. The cyclothiophenes have transition dipole moments mainly arranged in the ring plane with a very small perpendicular component, which results in a forbidden S_0-S_1 transition, but allowed S_0-S_2 transition. Furthermore, the coupling between S_2 and S_1 is proposed to become more efficient with increasing ring size.Theoretical reports on the relation between conformations of a series of cyclothiophenes (C6T-C30T) on their electronic properties, e.g., their HOMO-LUMO energy levels and gaps have been published recently.[35, 46]

Hence, in addition to investigating the nonlinear optical (NLO) properties of these cyclic thiophenes, evidence has been obtained for the abovementioned theoretical calculations, which suggest the presence of two different electronic energy levels in these conjugated macrocycles experimentally. The proposed theoretical framework regarding the location and coupling between excited states is presented in Scheme 5.1.

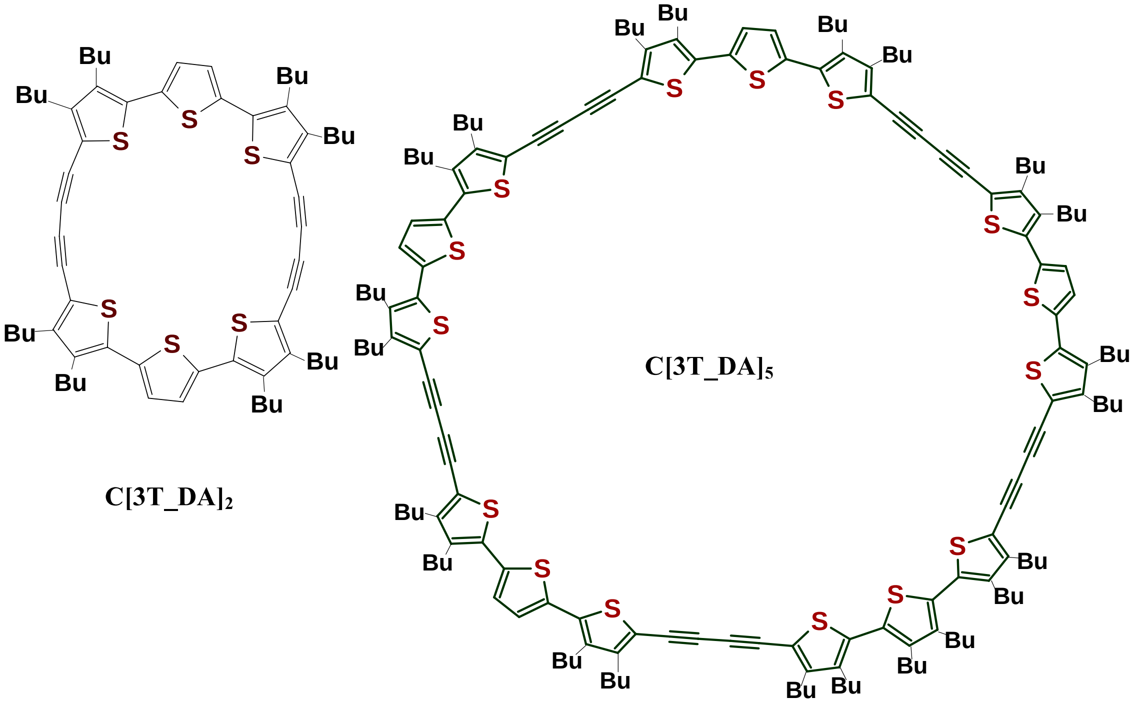

C[3T_DA]$_2$

C[3T_DA]$_5$

Figure 5.1. Structures of the macrocyclic terthiophene-diacetylenes studied in this section.

Scheme 5.1. Theoretical considerations for excited states of thiophene macrocycles.

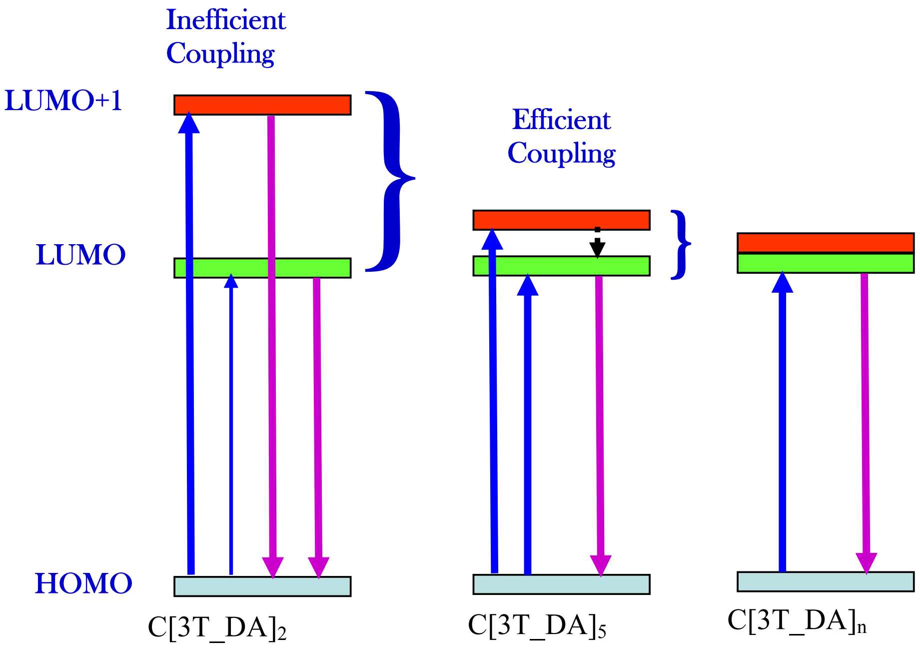

These thiophene macrocylcles are also capable of exhibiting interesting self-assembly and ordering[47]. Scanning Tunneling Microscope image obtained for a similar thiophene macrocycle at a 1, 2, 4-trichlorobenzene/HOPG interface is presented in Figure 5.2. A highly stable, two-dimensional crystalline monolayer with hexagonal 6mm symmetry was observed. The lattice constants were found to be a=2.46, b=2.52 and c=2.53 respectively.

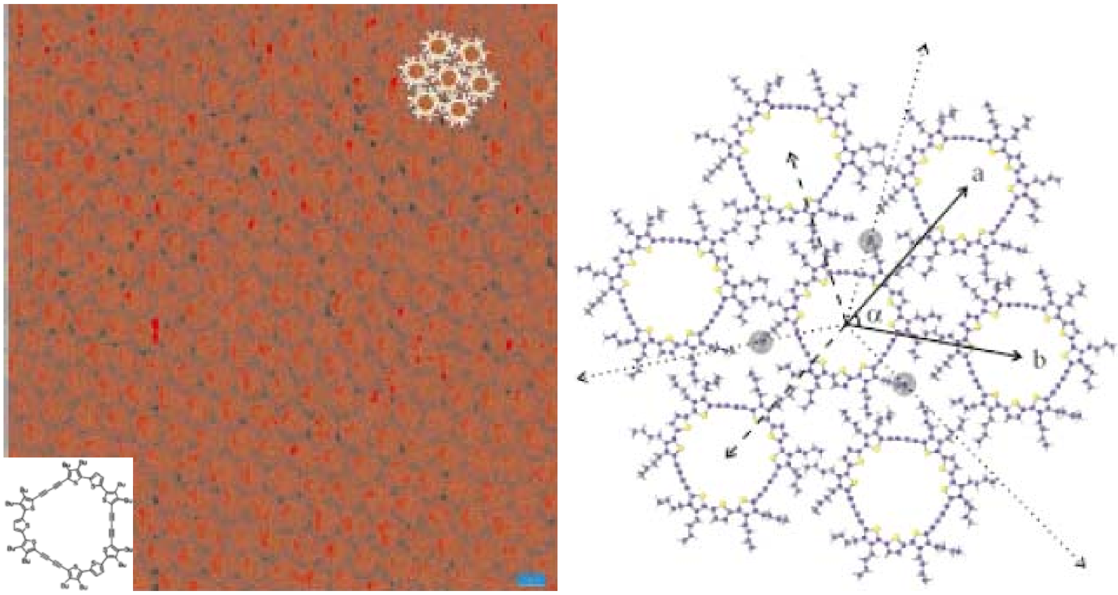

Figure 5.2. Long range ordering in thiophene macrocycles. The lattice parameters for the corresponding periodic structure are also shown. Inset shows the structure of the macrocycle investigated[47].

Figure 5.3 shows short range ordering of the same macrocycle. Island-like patterns were observed. Such islands could serve as hosts for potential guest species. Such ordering behavior opens new avenues for potential applications. The macrocycle also showed reversible conformational change upon variation in STM voltage. When the voltage was varied from -603 mV to -621 mV, a slight deformation of the cyclic units occurred, resulting in slightly triangular morphologies. When the negative bias was further raised to -640 mV, circular shape was recovered. This was ascribed to rearrangement of molecular orbitals in response to tunneling current. Thus, such reversible changes in conformations present the possibility of utilization of such materials as molecular switches. It is of interest to correlate the electronic properties of such macrocycles with their optical properties.

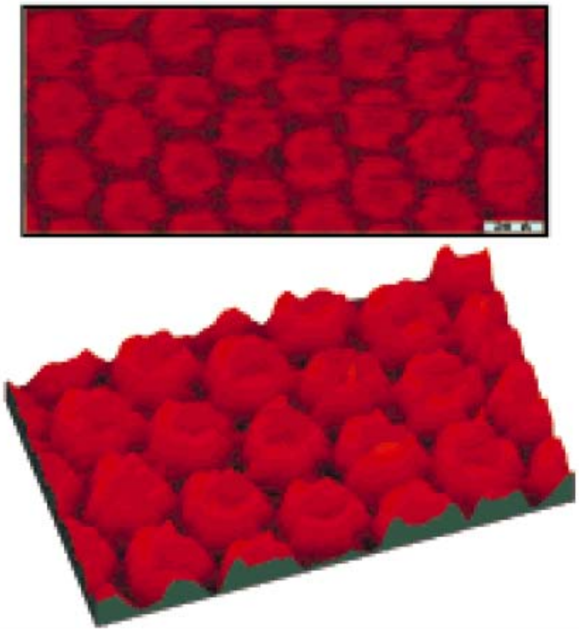

Figure 5.3. Short range ordering of thiophene macrocycles[47].

5.2.2. Experimental Details

5.2.2.1. Synthesis and Structural Characterization

The synthesis of the two macrocyles studied in this report has been previously reported by Professor Peter Bauerle[47]. Structural characterization using X-ray measurements[47] of single crystals have shown a nearly perfect circular shape for C[3T-DA]$_2$ and the diameter of the circular cavity was estimated to be 1.1 nm.

5.2.2.2. Steady state measurements

Unless stated otherwise, all the experiments were performed in toluene. The absorption spectra of the molecules were recorded using an Agilent (Model # 8341) spectrophotometer. The emission spectra were acquired using a Jobin Yvon Spex Fluoromax-2 spectrofluorimeter. The quantum yields of the molecules were measured using a known procedure[48]. Coumarin 307 in methanol was used as the standard.

5.2.2.3. Two-Photon Excited Fluorescence Measurements

In order to measure the two-photon absorption cross-sections (δ), the two photon excited fluorescence (TPEF) method[49] was followed. A 10^{-4} M Coumarin 307 solution in methanol was used as the reference over a wavelength range of 700-800nm. Fluorescein (pH=11) was used as a standard over 800nm-900 nm range. In order to measure the TPA cross-sections for wavelengths less than 700nm, bis-MSB dissolved in cyclohexane was used as the reference[50]. A mode-locked Ti: Sapphire laser (Kapteyn Murnane (KM)) was used for determining the δ over 760-820nm. For the remaining wavelengths (630-760 nm and 820-900 nm), an Optical Parametric Amplifier (OPA-800C, Spectraphysics) was employed. The seed used was a mode locked Ti:Sapphire laser (Tsunami, Spectra Physics). This was amplified using a regenerative amplifier (Spitfire, Spectra Physics) which in turn was pumped by a Nd:YLF laser (Empower, Spectra Physics). The amplified pulses were obtained at 1 KHz, 800 nm and ~100 fs. This was used for pumping the OPA.

5.2.2.4. Fluorescence Lifetime Measurements

Time Correlated Single Photon Counting (TCSPC) was used to determine the fluorescence lifetimes of the macrocycles used in this study. The laser used was the KM system dmentioned earlier. The second harmonic from the 800 nm output was used for these measurements. Brief theoretical description and detailed description of the experimental set-up is provided in Chapter 2.

5.2.2.5. Fluorescence Upconversion

Time-resolved polarized fluorescence of $C[3T\_DA]_5$ and $C[3T\_DA]_2$ was studied using femtosecond up-conversion spectroscopy. The sample solution was excited with a frequency-doubled light from a mode-locked Ti-sapphire laser (Tsunami, Spectra Physics). This produced pulses of approximately 100fs duration in the wavelength range of 380-430nm. The polarization of the excitation beam for the anisotropy measurements was controlled with a Berek compensator. The circular sample cell used had an optical path length of 1mm and it was held in a rotating holder to avoid possible photo-degradation and other accumulative effects. The horizontally polarized fluorescence component emitted from the sample was up-converted in a nonlinear crystal of β-barium borate using a pump beam at about 800nm that was first passed through a variable delay line. This system acted as an optical gate and enabled the fluorescence to be resolved temporally with a time resolution of about 200fs (pump-excitation 400/800nm cross correlation function had a FWHM of 230 fs). Spectral resolution was achieved by dispersing the up-converted light in a monochromator and detecting it by using a photomultiplier tube (Hamamatsu R1527P). The excitation average power was kept below 3 milliwatts. This corresponded to excitation pulse energy well below 0.1 nJ. In this excitation intensity regime the fluorescence dynamics was found to be independent of the excitation intensity for all investigated samples.

5.2.2.6. Excited State Measurements

Transient absorption was used to investigate the excited state dynamics of the cyclic thiophenes. The pump beam was produced by the optical parametric amplifier described above. The pump beams used in the present investigation were obtained from the fourth harmonic of signal and idler beams and were focused onto the sample cuvette. The probe beam was delayed with a computer controlled motion controller and then focused into a 2 mm sapphire plate to generate white light continuum. The white light was then overlapped with the pump beam in a 2 mm quartz cuvette containing the sample and the change in absorbance for the signal was collected by a CCD detector (Ocean optics). Data acquisition was controlled by the software from Ultrafast systems inc. Typical power of probe beam was < 0.1 μJ while the pump beam was around ~0.5 to 1 μJ per pulse. Magic angle polarization was maintained between the pump and probe using a wave plate. The pulse duration was obtained by fitting the solvent response, which was ~130 fs. The sample was stirred with a rotating magnetic stirrer.

5.2.3. Results and Discussion

The linear and nonlinear optical properties of the cyclothiophenes are summarized in Table 5.1. Results obtained from individual measurements are discussed below.

5.2.3.1. Optical absorption and Steady State Fluorescence Measurements

The absorption and emission spectra of the cyclothiophenes are presented in Figure 5.4. It is interesting to note that the molecules have different absorption maxima but the same emission maximum. A shoulder in the range of 440 to 500 nm is observed in C[3T-DA]$_2$. The absorption maximum at 400 nm is assigned to the S_0-S_2 transition according to the selection rules. The shoulder is therefore assigned to the S_0-S_1 transition. This shoulder is not seen in the absorption spectrum of C[3T-DA]$_5$. There is only one distinct absorption maximum at 433 nm. Hence, the S_0-S_2 transition shows a bathochromic shift attributed to increase in conjugation and it is suggested that single peak results due to the close proximity between S_2 and S_1 states, which would now be separated by a smaller energy gap. This conclusion is further corroborated by the parameter “full width at half maximum” (FWHM) which is 4000 cm^{-1} for cyclodimer C[3T-DA]$_2$ and much larger for the cyclopentamer (5526 cm^{-1}).

Table 5.1. Summary of linear and nonlinear optical properties of cyclothiophenes.

Molecule	**λ_{abs} (nm)**	**λ_{em} (nm)**	**Φ*****	**δ_{max} (GM)**	**τ_{FL} (ns)**	**τ_R (ns)****
C[3T-DA]$_2$	400	540	0.04	105 (52.5)*	0.395	9.9
C[3T-DA]$_5$	433	541	0.12	1470 (294)*	0.408	3.4

*Figures in parentheses indicate value per [3T-DA] repeating unit.

**For this single excited state model, calculated by dividing lifetime by quantum yield.

***Quantum yields were measured at 430 nm.

The excitation spectra of the molecules are presented Figure 5.5. The absorption spectra are also provided for reference. It is seen that the excitation spectrum for C[3T-DA]$_2$ shows a bathochromic shift with respect to its absorption spectrum. This indicates that the emitting state is different from the absorbing state. On the other hand, no such red-shift is observed for C[3T-DA]$_5$. Based on these results, it is suggested that the absorbing state in both molecules is the S_2 state, whereas the emitting state is the S_1. This supports the suggestion regarding the proximity of the higher excited states in C[3T-DA]$_5$. The present excitation spectrum for C[3T-DA]$_2$, along with its absorption spectrum, also suggests that there is no emissive pathway from S_2 to ground state and that S_2 and S_1 states are not efficiently coupled.

5.2.3.2. Fluorescence Quantum Yield and Lifetime Measurements

The fluorescence quantum yields for the cyclothiophenes were measured at two excitation wavelengths, namely 400 nm and 430 nm. These corresponded to S_1 and S_2 states respectively. Toluene was used as the solvent. The fluorescence quantum yields were found to be 0.01 and 0.04 respectively for C[3T_DA]$_2$, whereas C[3T_DA]$_5$ showed a constant value of 0.12 at both excitation wavelengths. This suggests that in the case of C[3T_DA]$_2$, there is a nonradiative pathway from S_2 state. The low quantum yields for these cyclothiophenes in general suggest that there is an efficient non-radiative decay from S_1 state. Figure 5.6 shows the results obtained from TCSPC. The decay profiles for both macrocycles seem to virtually overlap each other. The fluorescence lifetimes for C[3T-DA]$_2$ and C[3T-DA]$_5$ were obtained by fitting the decay profiles using the software after deconvolution with respect to the instrument response function. Their fluorescence lifetimes were found to be 395 ps and 408 ps, respectively. The similarity in fluorescence lifetimes indicates that the emitting states are similar for both molecules. The radiative lifetimes (fluorescence lifetime divided by quantum yield) for C[3T-DA]$_2$ and C[3T-DA]$_5$ were found to be 9.9 ns and 3.4 ns respectively.

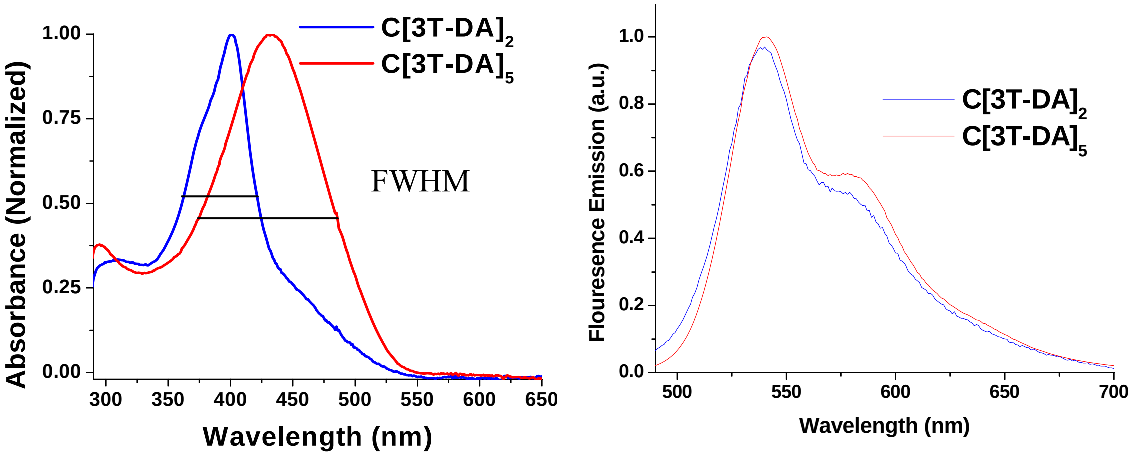

Figure 5.4. Absorption and emission spectra of C[3T-DA]$_2$ and C[3T-DA]$_5$.

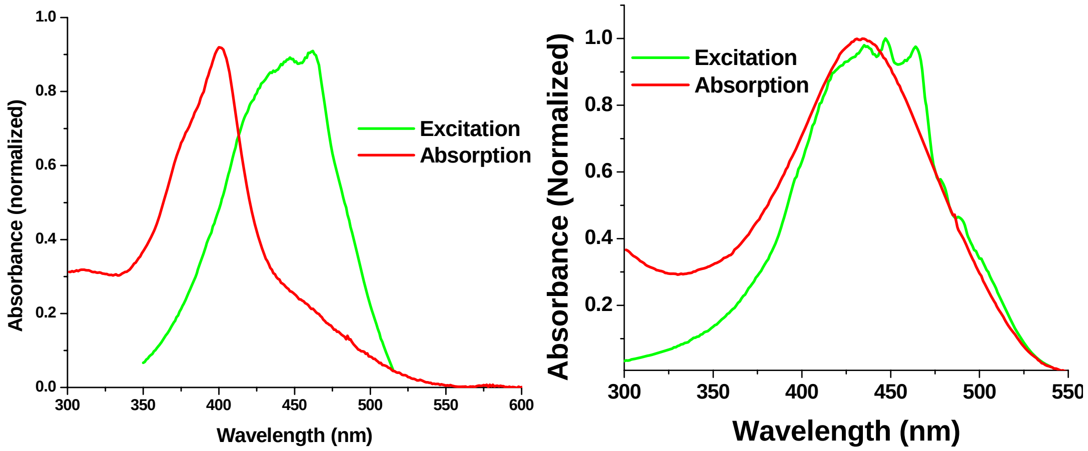

Figure 5.5. Excitation spectra (green curves) of C[3T-DA]$_2$ and C[3T-DA]$_5$ respectively. Absortion spectra (red) are also provided for comparison.

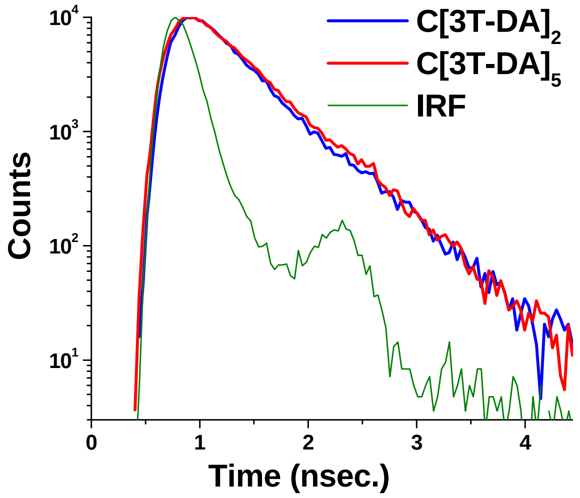

Figure 5.6. TCSPC results for C[3T-DA]$_2$ and C[3T-DA]$_5$. Also shown is IRF, the instrument response function.

5.2.3.3. TPA cross section measurements

The TPA cross section (δ) spectra for both rings are shown in Figure 5.7. It can be observed that both rings show a maximum around 760 nm, suggesting that the first TPA state has similar energetic location for both macrocyles. However, the bigger ring C[3T-DA]$_5$ shows a δ_{max} of 1470 GM which is about 14 times the δ_{max} of C[3T-DA]$_2$ (105 GM), suggesting more than an order of magnitude increase in δ. Considering that there are two [3T_DA] units in C[3T-DA]$_2$, the δ per [3T_DA] unit is 52.5 GM. The same for

C[3T-DA]$_5$ is 294 GM. Hence, it is seen that an increase in chromophore density by a factor of 2.5 results in 5.6 times enhancement of TPA cross-section per building block.

Higher TPA cross-section for larger ring suggests that the conjugation is extended over significant fraction of the ring, if not over the entire ring. It is to be accentuated that these systems do not possess any charge transfer character. Considering the same, we believe that the δ values obtained for our cyclothiophene systems are quite large and even comparable with some of the quadrupolar derivatives reported in the literature[51]. Hence, we also suggest that by adding strong donor acceptor groups to our cyclic systems, it is possible to engineer novel molecules with even higher TPA cross sections

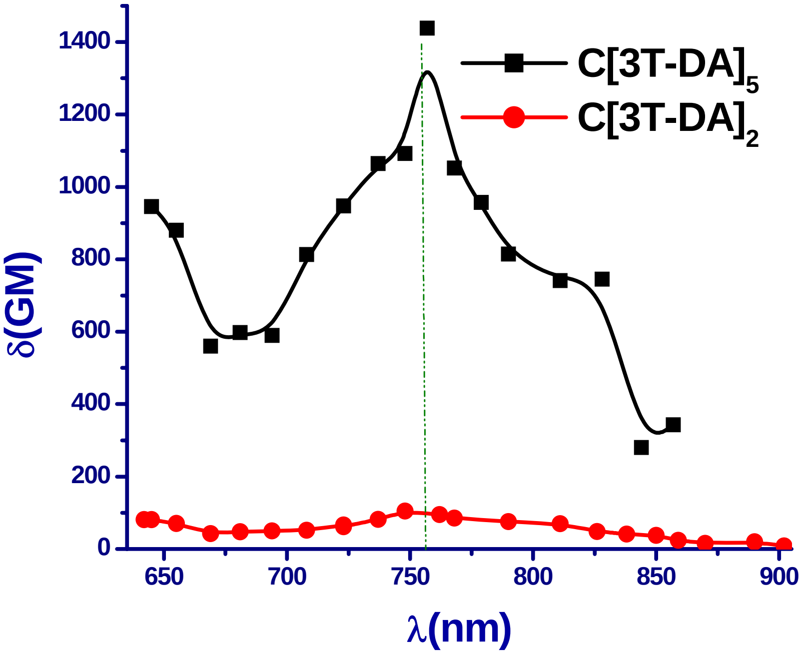

Figure 5.7. TPA cross sections of C[3T-DA]$_2$ and C[3T-DA]$_5$ at different wavelengths.

5.2.3.4. Transient Absorption Measurements

In order to understand the excited state dynamics of the cyclo-thiophenes, ultrafast transient absorption measurements have been carried out. Figure 5.8a shows the transient absorption spectra at different time delays from 6 ps to 800 ps for C[3T-DA]$_2$ in toluene after excitation at 420 nm. At a time delay of 6 ps, excited state absorption (ESA) with a maximum at 690 nm has been observed and has been ascribed to singlet-singlet excited state absorption (ESA). As time delay increases from 6 ps to 800 ps, the singlet-

singlet ESA decays with a concomitant growth in the region of 450 to 600 nm with a maximum at 500 nm. Clear isobestic point at 540 nm suggests that the singlet state decays to form a new transient which is long lived. Figure 5.8b shows the kinetic decay traces at 700 nm and 500 nm. It can be clearly seen that there is a growth of transient at 500 nm and it is long lived (> 1 ns, time limit of instrument). As this ESA is long lived, it has been ascribed to triplet-triplet absorption.

However, interesting transient absorption features are observed when the transients are followed at shorter time delays. Figure 5.9a shows the transient absorption spectra of C[3T-DA]$_2$ in toluene from 150 fs to 6 ps. Broad transient absorption from 450 nm to 750 nm has been observed at a time delay of 150 fs. As the time delay is increased, this broad ESA decays to give rise to ESA with a maximum at 690 nm with a time constant of 350 fs. This broad ESA can be attributed to S$_2$ state's ESA. The ESA with a maximum at 690 nm has already been ascribed to singlet state excited state absorption. Kinetic traces at 490 nm and 690 nm at very short time scale show that the initial ESA (S$_2$ state) decays to give rise to S$_1$ state.

Figure 5.9b shows the kinetic decay trace at 520 nm and the growth of transient at 720 nm observed for C[3T-DA]$_2$. The dynamics of growth (~350 fs) and decay clearly match, suggesting that there is an internal conversion from S$_2$ (Franck-Condon) to S$_1$ state. However, as the excitation spectrum did not match with the absorption spectrum, it can be concluded that there is an efficient non-radiative pathway (with a lifetime of ~300 fs) from S$_2$ state to some other non-radiative state. If the entire population of S$_2$ state were transferred to S$_1$ state, a clear isobestic point at the initial time delays should have been observed. Since it found to be absent, this suggests that there is a cascade relaxation of population to another non-radiative state. However, as seen above, an efficient population transfer from S$_1$ to triplet is observed (inter system crossing, ISC) (Figure 5.9b) with a clear isosbestic point at 540 nm and with a time constant of ~350 ps. As ISC process is radiationless, this explains the low fluorescence quantum yield observed for the molecule.

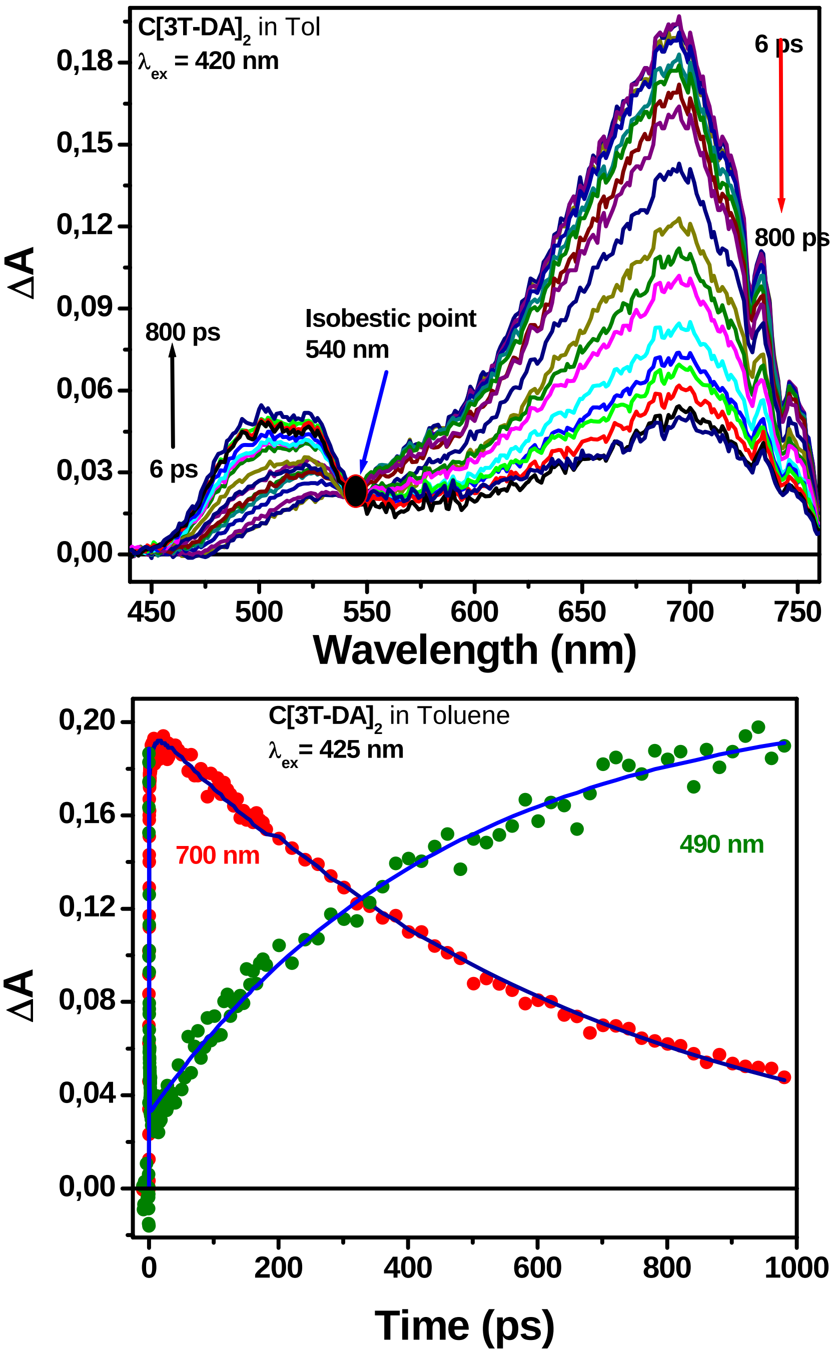

Figure 5.8. (a) Transient absorption of C[3T-DA]$_2$ in Toluene at different time delays from 6 ps to 800 ps. (b) Kinetic traces at 700 nm and 480 nm of C[3T-DA]$_2$ in Toluene after excitation at 420 nm.

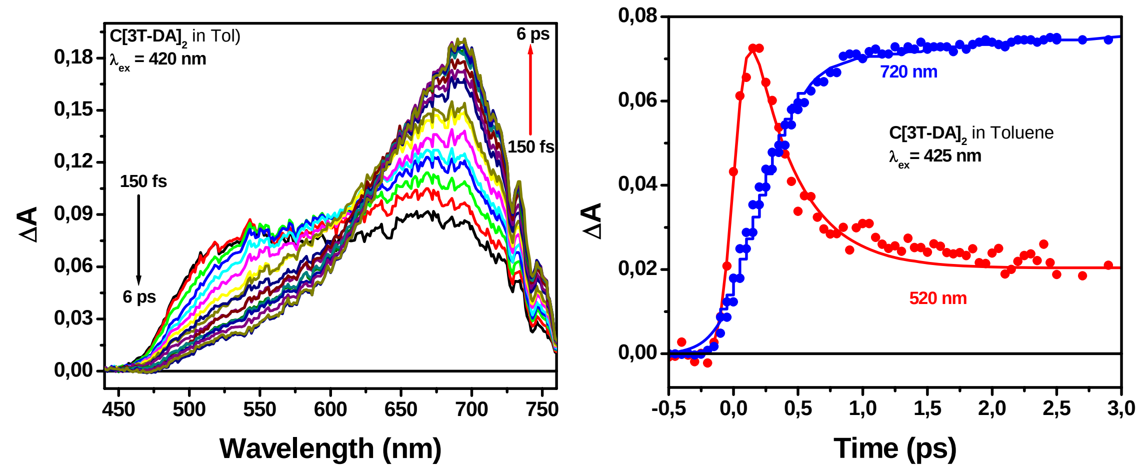

Figure 5.9. (a) Transient absorption of C[3T-DA]$_2$ in toluene at different time delays from 150 fs to 6 ps. (b) Kinetic traces at 700 nm and 480 nm of C[3T-DA]$_2$ in toluene after excitation at 420 nm.

It has been proposed that the coupling between excited states would increase with ring size. Also, the energetic separation initial and final excited states should reduce as well. In an effort to clarify this, we have carried out transient absorption measurements on C[3T-DA]$_5$ dissolved in toluene and respective excited state absorption features and kinetics are shown in Figure 5.10. It can be observed that the ESA spectral features are different from C[3T-DA]$_2$. Figure 5.10a shows the transient absorption spectra from 6 ps to 800 ps. The transient absorption spectrum at 6 ps consists of bleach in the region of 450 to 650 nm with characteristic bleach maxima around 490, 545 and 585 nm and a positive absorption with a maximum around 690 nm. The bleach with maxima at 545 and 585 nm can be ascribed to stimulated emission from the S$_1$ state. However, the bleach with a maximum at 490 nm is due to the disappearance of ground state. As the time delay is increased, the bleach decays to give rise to a positive transient. The transient absorption spectrum at 800 ps had shown a positive absorption spectrum in the entire visible region from 450 to 750 nm with maxima around 520 nm and 690 nm. It has been observed from fluorescence measurements that the lifetime of the S$_1$ state of the molecule is around 400 ps and thus the transient present at 800 ps can be attributed to triplet-triplet absorption.

It can be observed from the kinetic trace shown in Figure 5.10b that the stimulated emission recovers back to give rise to positive ESA corresponding to triplet state absorption. The growth of this triplet is found to be around 300 ps, which is comparable to the observed fluorescence lifetime. However, Figure 5.10b shows no decay to form a triplet state. This might be due to overlapping absorptions of singlet and triplet states. It can be observed from the kinetics shown in Figure 5.10b and Figure 5.10c that there exist interesting excited state dynamics at early time scales. Shown in Figure 5.11a is the transient absorption spectrum of [C-3TDA]$_5$ in shorter time window (from 150 fs to 5 ps). Immediately after the photoexcitation, a negative absorption with a maximum at 480 nm and positive absorptions with maxim around 540 nm and 700 nm are observed. The negative absorption at 480 nm is due to the bleach of ground state absorption. The positive absorption bands at 480 nm and 700 nm can be ascribed to the ESA of S_2 state. The fact that the S_2 state's ESA is decaying to S_1 state's emission unambiguously suggests that S_2 and S_1 states are intimately connected.

Kinetic decay trace corresponding to bleach of ground state absorption is provided in Figure 5.11b. The fact that there is no recovery of bleach suggests that there is no ultrafast pathway from S_2 state back to ground state and the S_2 state is decaying to give the stimulated emission from S_1 state. This information is further established by the kinetic decay trace at 520 nm shown in Figure 5.11c. Global fit analysis has shown that the decay time from S_2 state to S_1 state is around 460 fs. Presence of another non-radiative state in C[3T-DA]$_2$ observed from the transient measurements explains the lower quantum yield in C[3T-DA]$_2$ than C[3T-DA]$_5$. The results further suggest the proximity between S_2 and S_1 states and efficient coupling between the same in C[3T-DA]$_5$. Hence, the present transient measurements confirm the existence of S_2 and S_1 states, which have been theoretically predicted for cyclo-thiophenes, compare and elucidate the efficiency of coupling between the two states and also explain the differences in observed fluorescence quantum yields.

Scheme 5.2. Energy level diagrams for C[3T-DA]$_2$ and C[3T-DA]$_5$. The energies for the S$_0$ ground states are taken from cyclic voltammetry whereas other energy levels are taken from optical investigations.

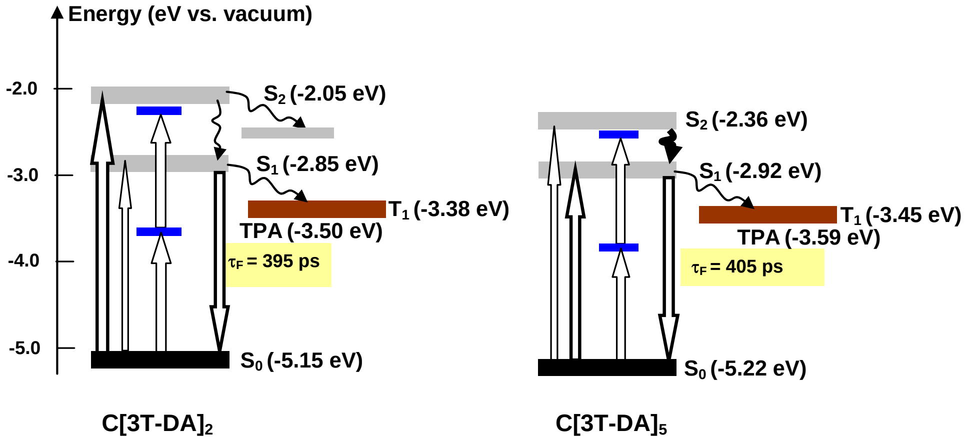

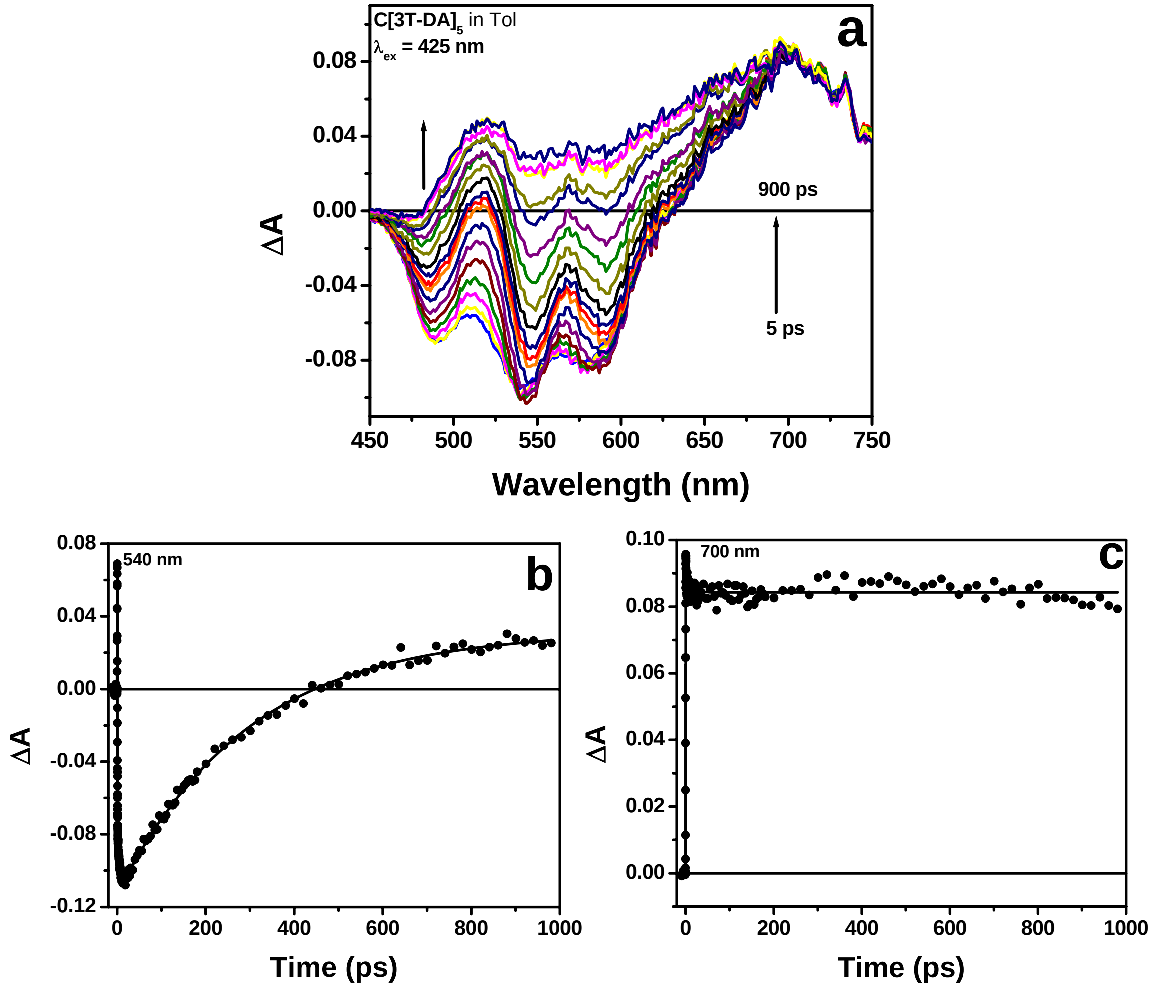

Figure 5.10. (a) Transient absorption spectra at different time delay from 6 ps to 800 ps of [C-3TDA]$_5$ in toluene. (b) Kinetic trace at 540 nm (c) Kinetic decay trace at 700 nm.

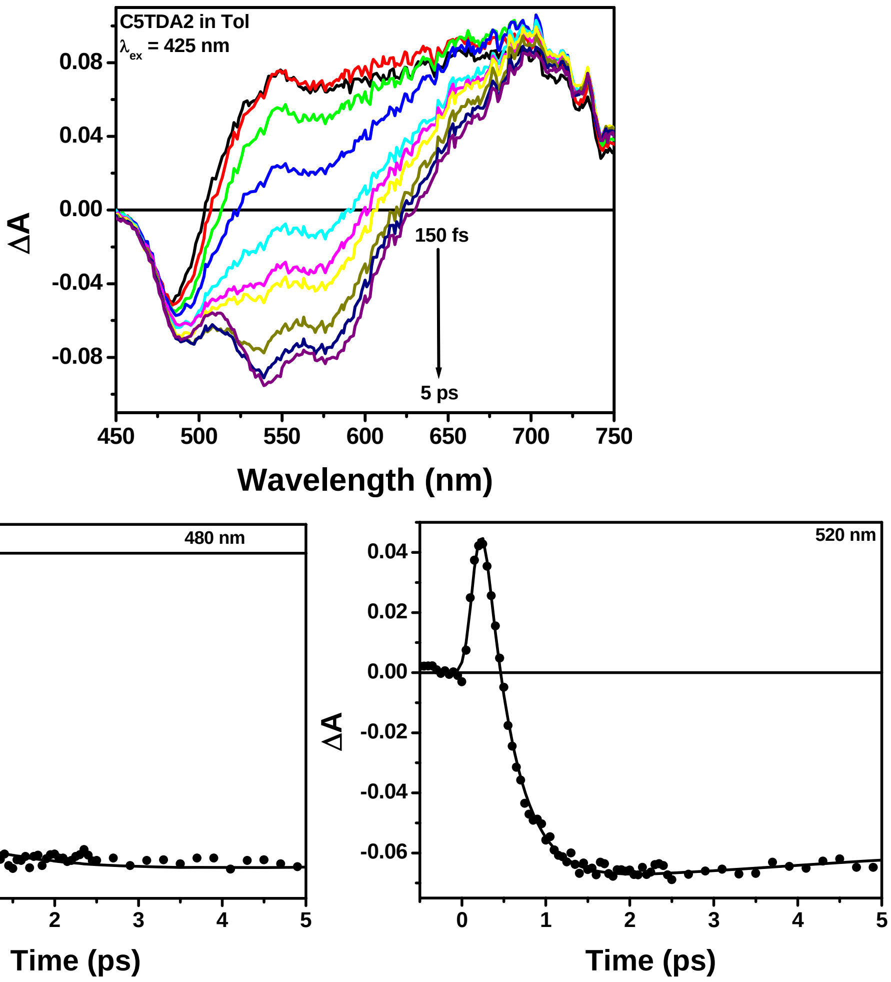

Figure 5.11. (a) Transient absorption spectra at of [C-3TDA]$_5$ in toluene from 150 fs to 5 ps. (b) Kinetic trace at 480 nm (c) Kinetic decay trace at 520 nm.

5.2.3.5. Fluorescence Upconversion

In order to examine the possibility of complete conjugation, is is important to investigate the dynamics of energy migration after photoexcitation. Hence, fluorescence upconversion measurements were used to obtain time resolved fluorescence data on the two macrocyclic systems C[3T-DA]$_2$ and C[3T-DA]$_5$. After obtaining parallel and perpendicular polarized fluorescence measurements, equation 5.1 was used to determine the fluorescence anisotropy[52].

$$\Gamma = \frac{I_{par} - I_{per}}{I_{par} + 2I_{per}} \tag{5.1}$$

Depolarization of fluorescence emission can be caused by a number of phenomena. For these molecules only two depolarization times were observed, one was very fast (less than 100 fs) the other was very slow (over one nanosecond). The first depolarization is a fast process due to migration of the exciton to other chromophores in the ring; the second depolarization time is due to rotational diffusion. After deconvoluting the data from the instrument response function (Figure 5.12), it was found that the initial anisotropy decay in C[3T-DA]$_5$ was 27 ± 10 fs. This supports a coherent movement of the exciton. A Förster hopping mechanism would be excluded with these results because Förster hopping occurs on the order of picoseconds. In the presenta case, Förster energy transfer mechanism can not be applied with physically reasonable parameters when energy transfer is so fast. Similarly, the system C[3T-DA]$_2$ has an initial anisotropy decay of 20 ± 10 fs. Thus, our data supports a coherent energy migration in both systems. This is possible only when conjugation extends over the entire chromophore.

Hence, it has been observed that in spite of increasing the number of 3T_DA building blocks, complete conjugation is still preserved. This, from Sum-Over-States formalism, increases the ground state transition moment, and hence, enhances the TPA cross section. We can compare these systems to the natural photosystem LH2 of the purple bacteria Rhodobacter sphaeroides which has nine chromophores and experiences a combination of Förster and wavelike energy migration. The natural system LH2 presents two anisotropy decay times of 100 fs and 300-500 fs. 100 fs is too fast for Förster type energy migration, but the presence of the 300-500 fs decay supports the theory of an LH2 photosystem where the energy is delocalized over four chromophores and hops to the remaining chromophores[53].

When chromophore transition moments are oriented randomly in a plane, the residual anisotropy value[47] is 0.1. After the initial anisotropy decay, the steady state anisotropy value of C[3T_DA]$_5$ was calculated to be 0.081 ± .01 with little observed anisotropy decay up to 200 ps. The rotational diffusion time of C[3T-DA]$_5$ was crudely calculated using the Debye-Stokes-Einstein (DSE) equation to be longer than one nanosecond, a timescale considerably longer than the time scales we observed which explains why a significant drop in anisotropy up to 200 ps due to rotational diffusion was not observed.[47] The smaller ring system C[3T-DA]$_2$ had a anisotropy residual value of 0.11 ± .01 and a decrease in anisotropy due to rotational diffusion was apparent and by fitting the data to an exponential decay the rotational diffusion was calculated to be 850 ps. Terthiophene, an oligomer with three thiophene rings, has a rotational diffusion time of 175 ps.

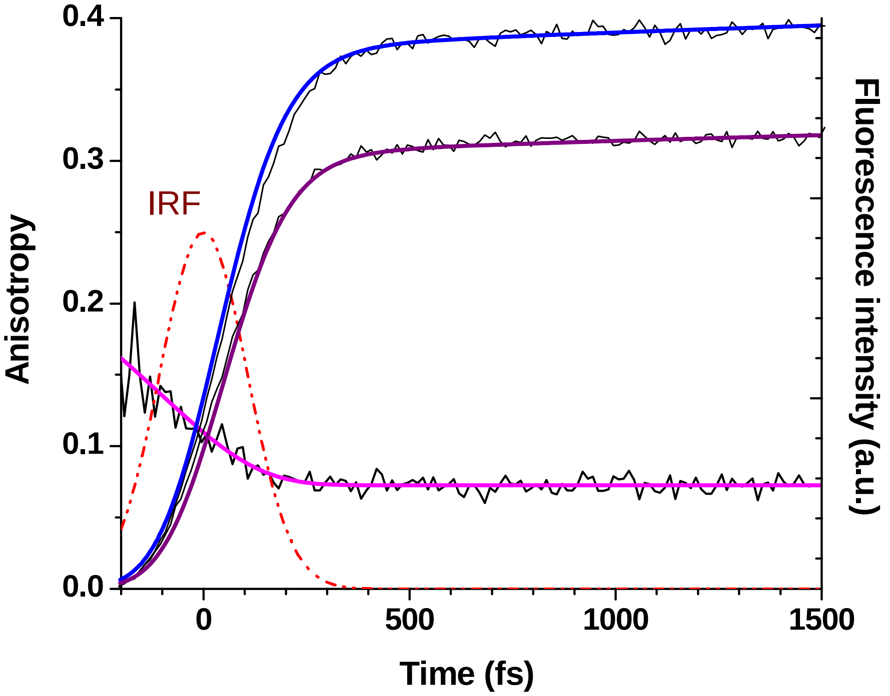

Figure 5.12. Raw data shown in the parallel and perpendicular measurements above is convoluted with the instrument response function. A mathematical procedure removes the instrument response function leaving the experimental decay, shown in the anisotropy curve.

We postulate that there are two ways by which we can account for the residual anisotropy of C[3T-DA]$_5$ being 0.081 ± .01 while the theoretical anisotropy for a planar system is 0.1. Either some fraction of the rings is deformed from planarity, or the chromophores are twisted with respect to the plane of the molecule. Demidov and Andrews discussed the effect of chromophore orientation with respect to the plane of the ring on the residual anisotropy and obtained the following formula[54].

$$R = 0.1\left(9Cos^4(\theta) - 6Cos^2(\theta) + 1\right) \tag{5.2}$$

Using this formula we can calculate that if the anisotropy of our system is 0.081 and if a planar system is expected to have anisotropy of 0.1, then the difference could be explained if the chromophores average inclination with respect to perpendicular is 7.9 ± 1 degrees. This value is a maximum, as we do not discount the possibility that the deviation from the ideal planar anisotropy may be due in some part to a concentration of deformed, damaged or broken rings mixed in.

The average value for the anisotropy decay time was found to be 27 fs. Combining this with spectroscopic information can give us an idea of the type of energy transfer (exciton or hopping dynamics) [52-55]. A large homogeneous line width would indicate strong interaction between the environment and the chromophores, lending to a hopping type energy transfer, while fast anisotropy decay times would indicate strong interaction between chromophores and lend to wavelike energy transfer[52-54]. This is a relatively simple approach which neglects inhomogeneous line broadening and can be quantified by an equation developed by Leegwater[52]. Equation 5.3 s a general expression for the anisotropy decay rate k_{dep} in a ring molecular system at high temperature.

$$k_{dep} = \Gamma\left(1 - \frac{1}{N}\sum_{k=1}^{N} \frac{\Gamma^2}{\Gamma^2 + 16J^2 \sin^2\left(\frac{2\pi}{N}\right)\sin^2\left(\frac{2\pi k}{N}\right)}\right) \tag{5.3}$$

In this equation Γ is the homogeneous line width and N the number of chromophores. For a system of 5 chromophores the expression becomes equation 5.4.

$$k_{dep} = \frac{7.236\Gamma\left(\Gamma^2 + 7.236J^2\right)J^2}{\left(\Gamma^2 + 5J^2\right)\left(\Gamma^2 + 13.09J^2\right)} \tag{5.4}$$

A plot of decay time vs interaction strength is shown in Figure 5.12. Each curve respresents a different value of gamma in equation 4 and 27 fs, the anisotropy decay time for this system, is shown as a red dot. Figure 5.12 can be used to get a sense of the types of excitation transport present in the thiophene system. For the region to the left in the graph where homogeneous linewidth is much larger than the electronic coupling, interaction (J) between chromophores, we can model energy transfer as a type of hopping of excitations (Förster type energy transfer). In the region to the right where interchromophore interaction is much larger than homogeneous linewidth, we can model energy transfer as a coherent (wavelike) transport. Our time-resolved depolarization data places the anisotropy decay time at 27 fs, which according to the Leegwater's theory would mean that excitation transfer in this system can not be accounted for by pure Förster hopping mechanism and the excitation delocalization over substantial part of the ring should be considered.

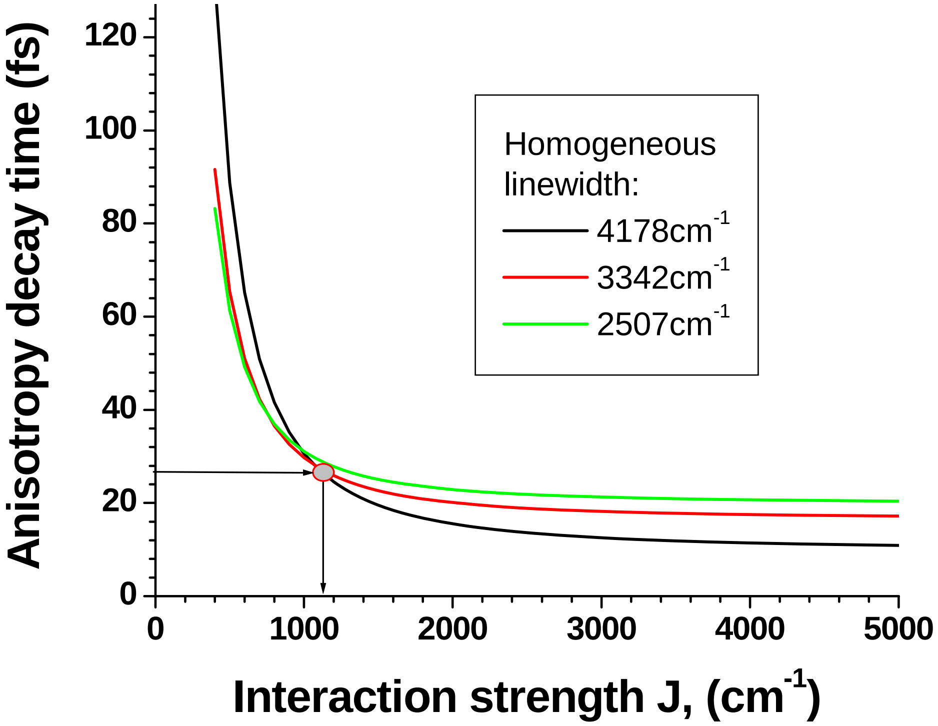

Figure 5.13. Anisotropy decay time vs. interaction strength. The plot indicates energy transfer is predominately wavelike, but does not exclude hopping type energy transfer.

From all these measurements we can deduce the model that these cyclothiophenes have two different electronic energy levels (Figure 5.13). According to the energy diagram shown in Figure 5.13, as the ring size increases, the coupling between the higher excited state (S_2) and the first excited state (S_1) becomes more efficient. Also, in case of the smallest ring, C[3T-DA]$_2$, the S_0-S_2 transition is proposed to have the largest oscillator strength. As the ring size increases, since S_1 and S_2 seemingly become coupled and the emitting state is the lowest S_1-state.

5.3. TPA Enhancement in Thiophene Macrocycles Consisting of Alternating Thiophene and Alkyne Segments

5.3.1. Background

This section discusses thiophene based macrocycles consisting of a different building block than those studied in the previous section. In this case, the building block can be considered as a linear segment. This segment has alternating thiophene rings and triple bonds. Thus each segment consists of six thiophene units and five triple bonds. Each segment is connected by an alkene linkage to form macrocycles. Hence, 12mer has two such building blocks, 18mer has three building blocks, 24mer has four building blocks and 30mer has five building blocks. The structures of the macrocycles studied in this section are presented in Figure 5.14 . These thiophenes can also be regarded as nanometer sized cavities, the size of which can be tuned by simply varying the number of building blocks.

Interestingly, these macrocycles were not found to yield single crystals like the previous macrocycles, but supramolecular assemblies[56]. This is shown for four similar macrocycles in Figure 5.15. As the ring size was increased, the supramolecular assembly changed from fibrous to nanoparticles. Hence, by changing the characteristics of the building block, macrocycles with different morphological features can be obtained.

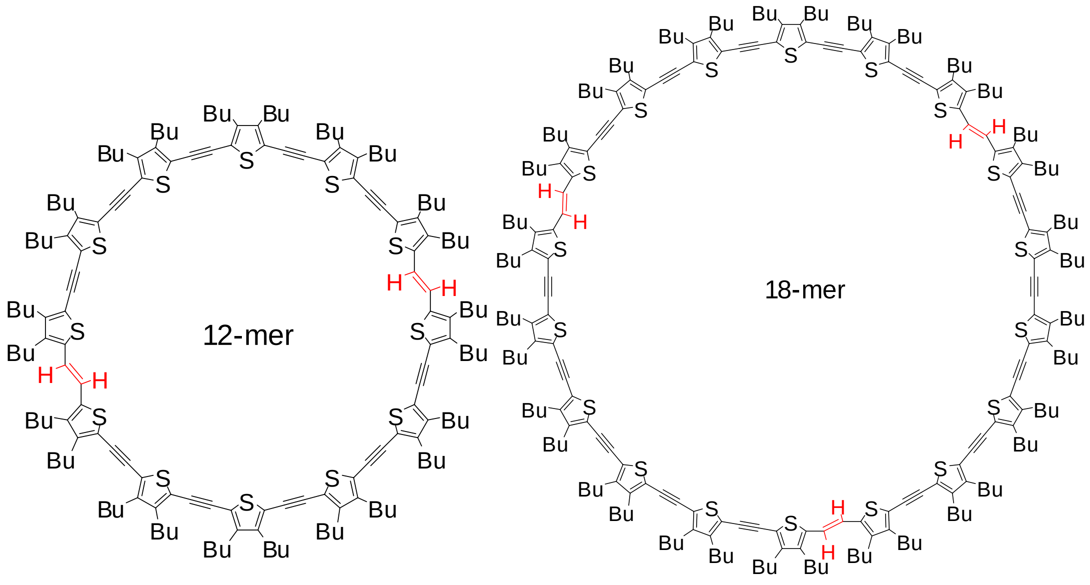

$C_{168}H_{220}S_{12}$
Mol. Wt.: 2624.32

$C_{252}H_{330}S_{18}$
Mol. Wt.: 3936.49

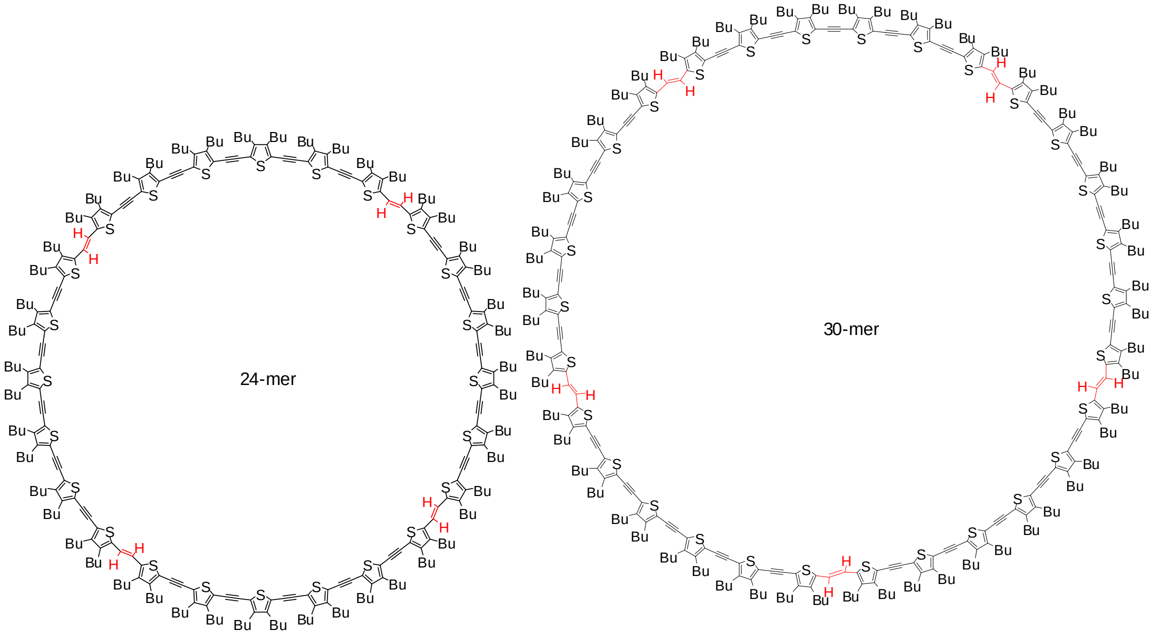

$C_{336}H_{440}S_{24}$
Mol. Wt.: 5248.65

$C_{420}H_{550}S_{30}$
Mol. Wt.: 6560.81

Figure 5.14. Macrocyclic thiophenes investigated in this section.

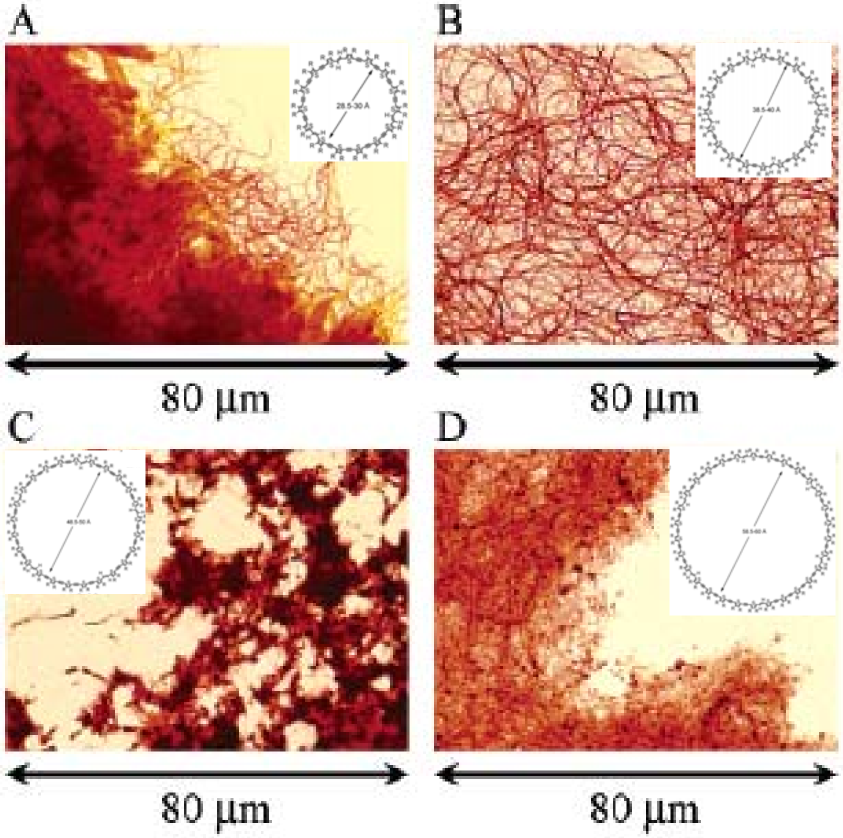

Figure 5.15. Supramolecular assemblies obtained from thiophene macrocycles[56].

5.3.2. Experimental Details

5.3.2.1. Synthesis and Structural Characterization

The thiophene macrocycles were obtained as a generous gift from Professor Masahiko Iyoda at the Tokyo Metropolitan University, who has also reported their synthetic methodology[56]. Structural characterization using X-Ray measurements[56] have shown that individual rings in the presence of alkanes adopt a chair-like conformation and serve as hosts for guest alkane molecules.

5.3.2.2. Steady State Measurements

Unless stated otherwise, all the experiments were performed in THF. The absorption spectra of the molecules were recorded using an Agilent (Model # 8341) spectrophotometer. 10^{-7} to 10^{-6}M solutions were used for determining their molar extinction coefficients. The emission spectra were acquired using a Jobin Yvon Spex Fluoromax-2 spectrofluorimeter. The quantum yields of the molecules were measured using a known procedure[43]. Coumarin 307 in methanol was used as the standard. An excitation wavelength of 400 nm was used to determine their quantum yields.

5.3.2.3. Two-Photon Excited Fluorescence Measurements

In order to measure the two-photon absorption cross-sections (δ), we followed the two photon excited fluorescence (TPEF) method[44]. A 10^{-4} M Coumarin 307 solution in methanol was used as the reference. A mode-locked Ti: Sapphire laser (Kapteyn Murnane) was used for determining δ over 760-820nm.

5.3.2.4. Fluorescence Upconversion

Time-resolved polarized fluorescence of 12mer and 30mer using one and two-photon excited modes were studied using the femtosecond up-conversion spectroscopy technique.

5.3.3. Results and Discussion

5.3.3.1. Steady State Properties

The absorption and emission spectra of the macrocycles measured in THF are shown in Figure 5.16 . 12mer shows a band between 350nm and 550nm with a maximum at 450nm. 18mer shows a broader feature between 350nm and 550nm with a maximum at 470nm. The 20nm bathochromic shift is an indication of extension of conjugation, which can be expected as a result of increase in the number of conjugated chromophore units. On the other hand, 24mer and 30mer show little red-shifts in their absorption maxima. This suggests that there might not be siginficant extension of conjugation as a result of increase in chromophore density beyond 18mer.

The absorption behavior observed is significantly different from the thiophene macrocycles investigated in the previous section. There is no significant inhomogeneous line broadening observed for any of the present macrocycles. Coupled with changes in morphological characteristics, this corroborates the importance of the design of building block on the optical properties of the resulting macrocycles. Molar extinction coefficients (ε) of the macrocycles were measured in THF and the results are presented in Figure 5.17. There is a systematic increase in ε with increasing number of building blocks, suggesting stronger ground state transition dipole moments. Inspection of emission spectra shown in Figure 5.18 suggests identical emitting states. 12mer shows a peak at 550nm and a shoulder at 592nm. 24mer shows identical features but each is red-shifted by 3 nm. The shoulder can be attributed to vibrational structure. Similarly, 30mer shows a peak at 550 nm and a shoulder at 590 nm. The general shape of the emission spectra resembles to those observed previously in section 4.2. Hence, it appears that the final emitting state in these macrocycles is also S_1.

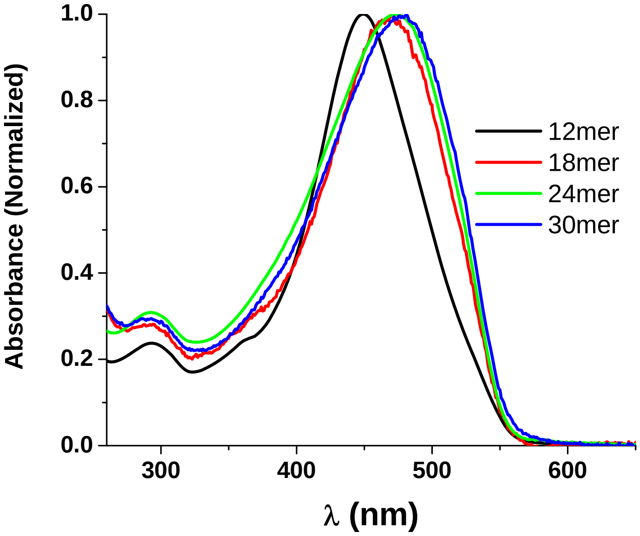

Figure 5.16. Normalized absorption spectra of the thiophene macrocycles.

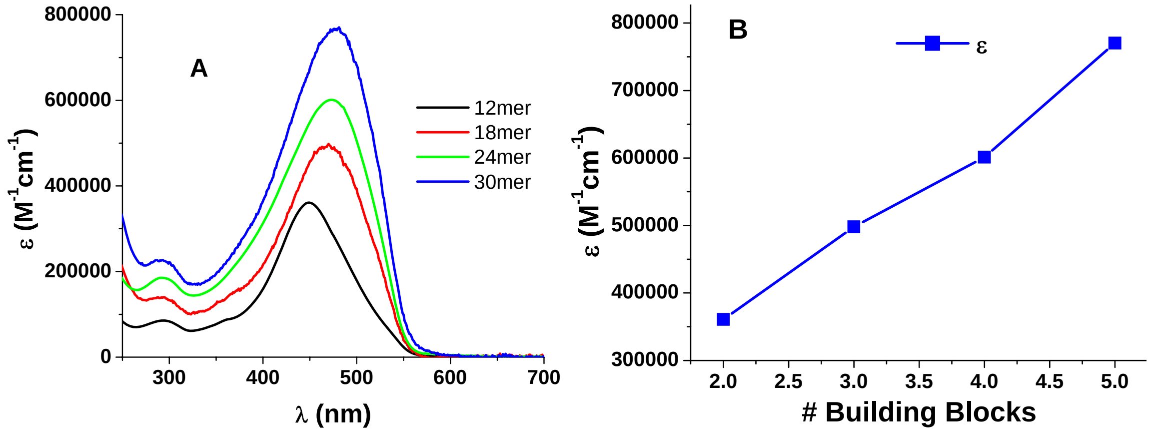

Figure 5.17. A) Molar extinction coefficients of the thiophene macrocycles. B) Molar extinction coefficient as a function of number of building blocks.

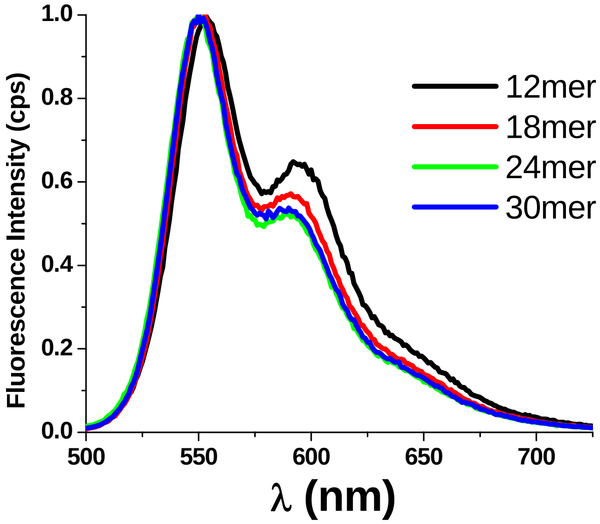

Figure 5.18. Normalized emission spectra of macrocyclic thiophenes studied in this section.

5.3.3.2. Two-Photon Absorption Measurements

TPA cross section spectra for the macrocycles from 770nm to 820 nm are presented in Figure 5.19. A systematic increase in TPA cross section (δ) is observed with increasing ring size. In order to accentuate the enhancement of δ, it is necessary to consider δ per building block. In order to achieve this, we divide the maximum value of δ by the number of building blocks. The values of δ per building block as a function of number of building blocks is shown in Figure 5.20. If there is no enhancement, then a flat line parallel to x-axis should be observed. However, that is not the case. A nearly linear trend is observed from Figure 5.20. This suggests that there is enhancement of δ. 30mer shows 75% enhancement over 12mer. It is worthwhile mentioning at this point that these values could change since these values are based on measurements over a limited wavelength range. Entire TPA cross section spectrum of these macrocycles is necessary in order to make a better comparison. Enhancement of TPA cross section indicates coupling and strong electronic communication between the building blocks. In order to examine the possibility of complete conjugation, fluorescence upconversion measurements are needed and the results from the same are discussed next.

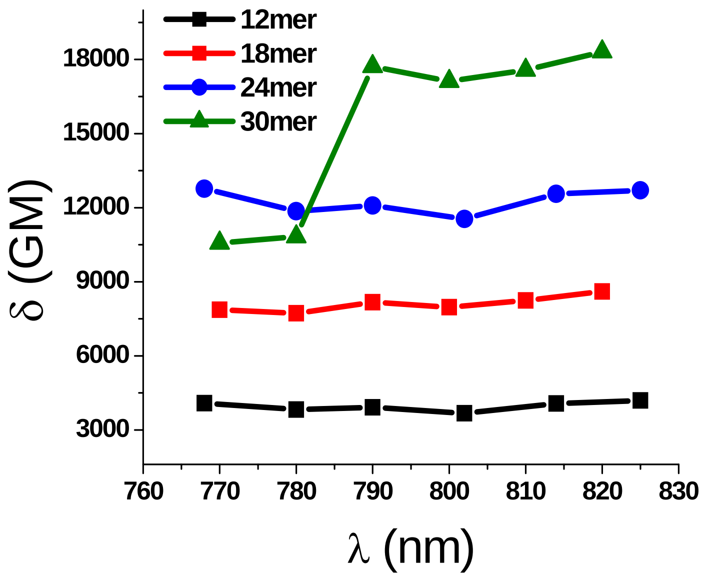

Figure 5.19. TPA cross section spectra for thiophene macrocycles studied in this section.

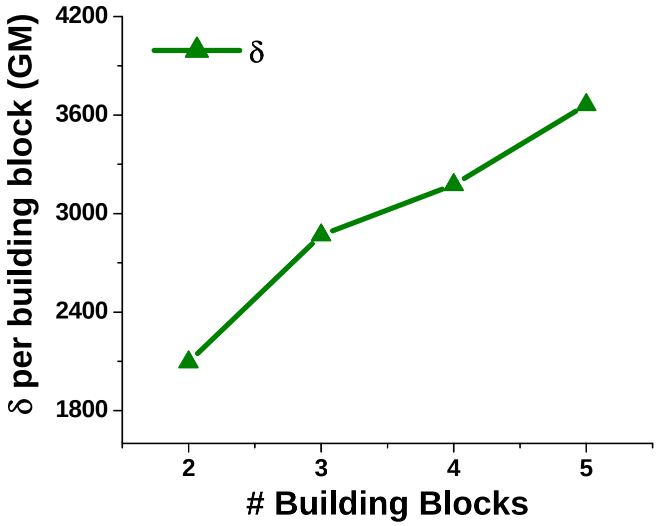

Figure 5.20. TPA cross section per building block as a function of number of building blocks.

5.3.3.3. Fluorescence Upconversion Measurements

Fluorescence upconversion measurements were performed at 400nm and 800nm, corresponding to one and two-photon excitation modes respectively. The emission was collected at 550nm for both cases. The fluorescence profiles under parallel and perpendicular excitation modes obtained from one-photon excited upconversion (OPEU) are presented in Figure 5.21. The behavior observed for 12 and 30mer was similar. Using these results, the fluorescence anisotropy decay can be calculated and the anisotropy decay profiles with respect to time for 12 and 30mer are shown in Figure 5.22. Two important features can be observed from the figure. Firstly, there is a fast component which suggests delocalization of excitation over entire chromophore. This is the primary reason for enhancement of TPA cross section observed in 30mer. Secondly, the residual anisotropy values for both macrocycles is ~0.05 which suggests some deviation from planarity.

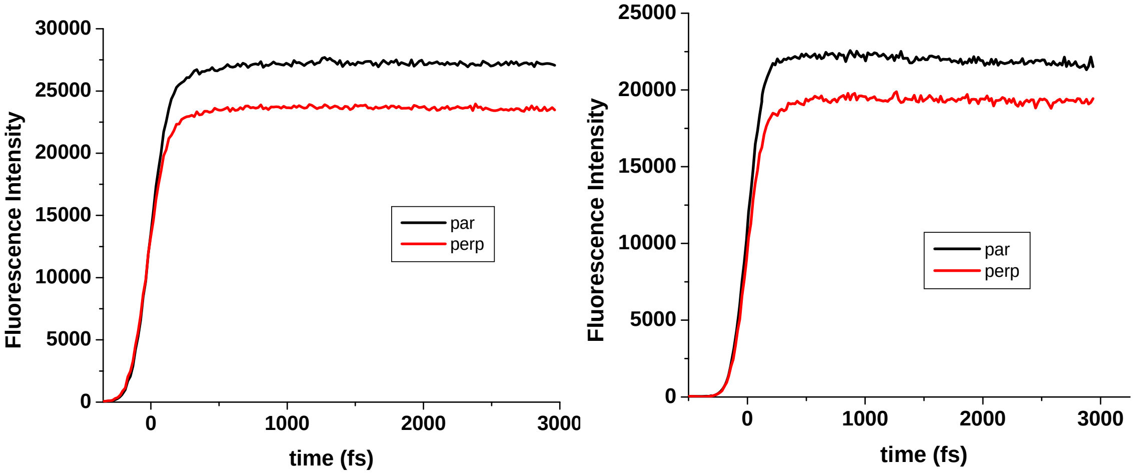

Figure 5.21. Short timescale fluorescence profiles for 12 and 30mer at 400nm excitation and 550nm emission.

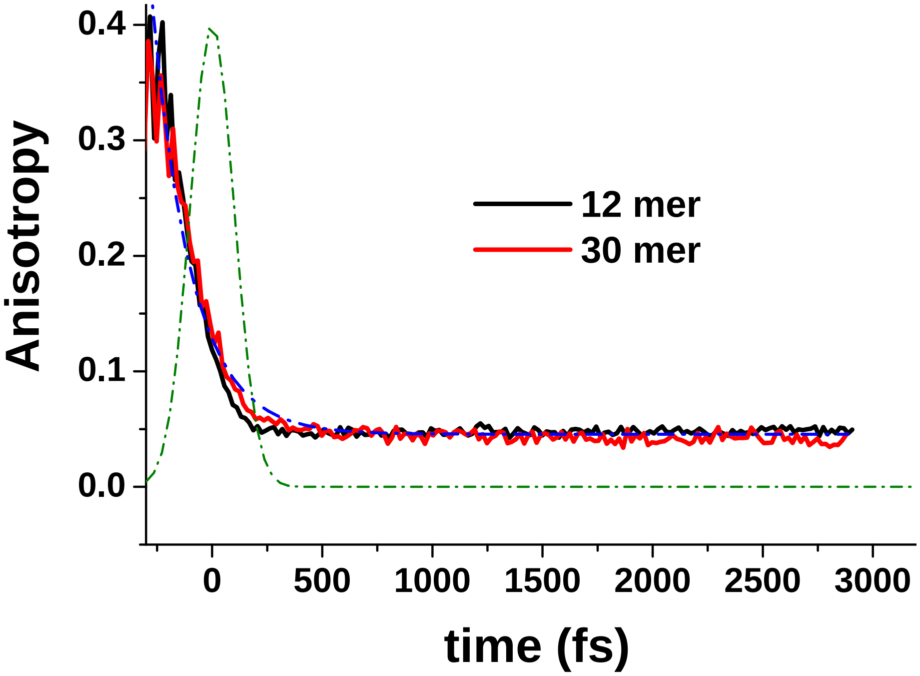

Figure 5.22. Fluorescence anisotropy decay results for 12 and 30mer at 400nm excitation and 550nm emission. The blue curve is a single exponential fit for the observed

anisotropy decay. Instrument response function (dotted green line) is also shown for convenience.

The short timescale fluorescence profiles obtained from two-photon excited upconversion (TPEU) at 800nm for both 12 and 30mer are shown in Figure 5.23. Slight differences between 12 mer and 30mer are observed from the figure. In order to further investigate this, anisotropy decay curves were plotted. The decay profiles are shown in Figure 5.24. A rapid decay within instrument response function (green dotted line) is observed for 12mer. However, a longer decay component is observed for 30mer. This could possibly imply that the excitation might not be delocalized over the entire chromophore instantaneously and that some hopping might occur. This is in accord with the TPA cross section measurements for the thiophenes studied in section 4.2. C[3T_DA]$_5$ showed 550% enhancement in TPA cross section per building block upon increase in chromophore density by a factor of 2.5. However, in this case, upon increasing the building block density by a factor of 2.5 from 12mer to 30mer, only 75% enhancement in δ is observed. One photon upconversion is unable to explain this observation. Therefore, we suggest that for certain materials, two-photon excited fluorescence upconversion could provide more sensitive information that one-photon excited upconversion measurements might overlook. Thus, two-photon excited upconversion might be used as a more sensitive probe for investigating excitation delocalization in certain nonlinear optical materials.

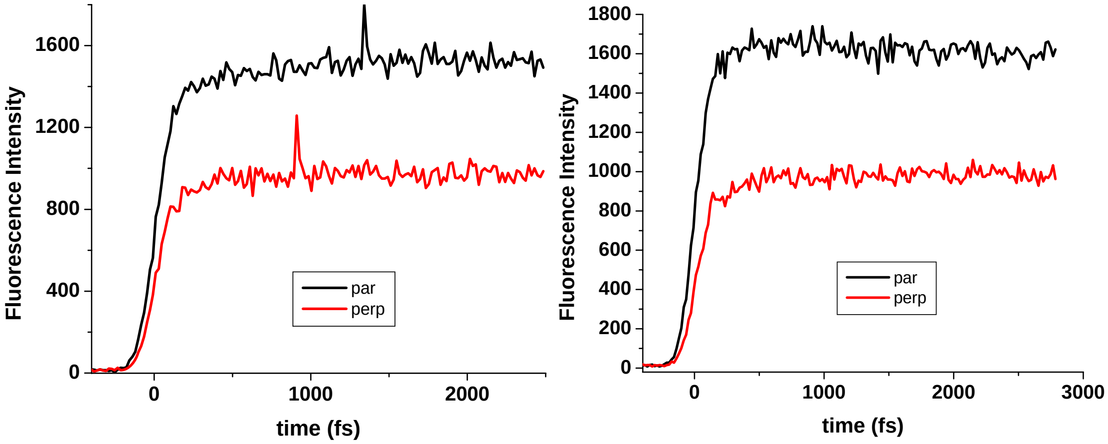

Figure 5.23. Short timescale fluorescence profiles for 12 and 30 mer at 800nm excitation and 550nm emission.

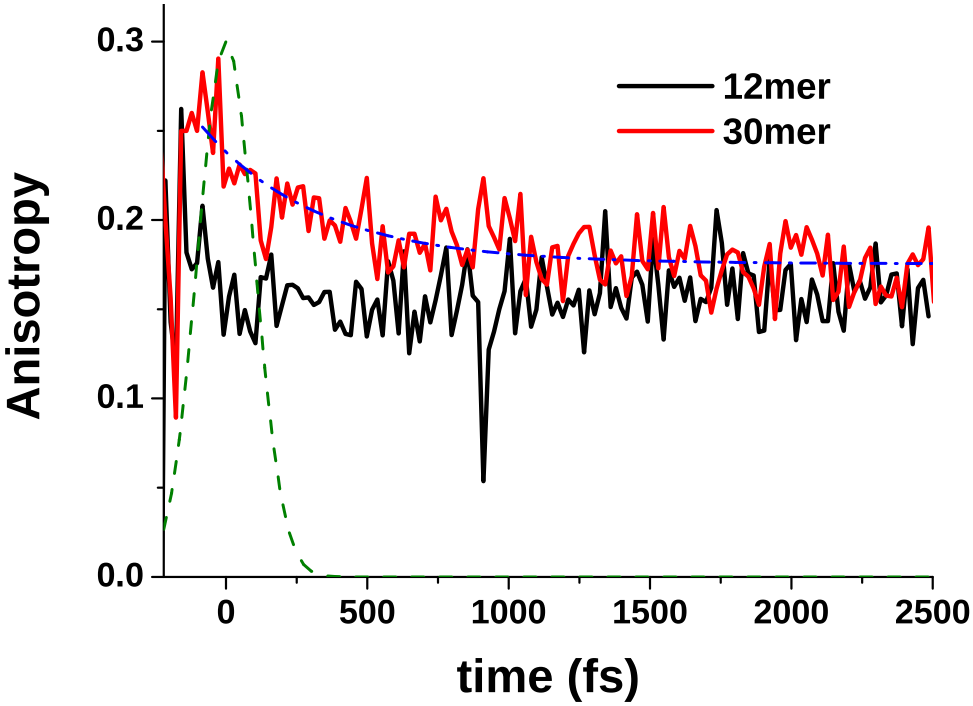

Figure 5.24. Two photon excited fluorescence anisotropy decay profiles for 12 and 30mer. The blue curve is a single exponential fit for the observed anisotropy decay for 30mer.

5.4. Conclusions

In this chapter, cyclic nano-cavities composed of thiophenes, alkene and alkyne π-bridges have been investigated for their nonlinear optical properties. Some of these materials are capable of exhibiting interesting self-assembly behavior into nanofibers and nanoparticles. The optical properties, electronic structure and location of excited states and the coupling between them are highly influenced by the chemical structure of the building block. For the first set of cyclic thiophenes, 550% enhancement in TPA cross section was observed. Ultrafast fluorescence measurements provided the mechanism for this enhancement in the form of extended conjugation. In the second set of thiophene macrocycles, the observed enhancement was not as pronounced as the first case. One photon excited upconversion measurements were not able to elucidate this observation. Two-photon excited upconversion measurements were able to shed some light on this behavior. The presence of a slower component in 30mer is an indication of some hopping. However, further experiments are required to confirm this. However, it is proposed that two-photon excited fluorescence upconversion could serve as a more sensitive probe for investigating excitation migration dymanics, particularly for molecules possessing cyclic architecture. The cyclic character of these materials renders them hosts for various guest motifs. Extended conjugated in these materials could find possible applications in organic electronics and photonics.

Summary

- Novel, cyclic architecture was investigated for two-photon absorption behavior.
- Using ultrafast upconversion, extended delocalization in thiophene macrocycles was proved and determined to be the reason behind enhanced two-photon absorption (TPA) behavior.
- Using transient measurements, coupling between excited states was examined as a function of size of macrocycle. Increased coupling was found with increasing ring size, thereby corroborating proposed theoretical framework.
- By changing the nature of building block, significant changes in morphology as well as TPA behavior was observed.
- It is proposed that two-photon excited fluorescence upconversion measurements could serve as a more sensitive probe for investigating materials with potentially extended conjugation.

5.5. References

1. McQuade, D. T.; Hegedus, A. H.; Swager, T. M. *J. Am. Chem. Soc.* **2000**, *122*, 12389-12390.
2. Franco, C.; Wilson, J. S.; Jasper, M. J.; Clement, D.; Silva, C.; Friend, R. H.; Severin, N.; Samori, P.; Rabe, J. P.; O'Connell, M. J.; Taylor, P. N.; Anderson, H. L. *Nat. Mater.* **2002**, *1*, 160.
3. Burley, G. A.; Avent, A. G.; Boltalina, O. V.; Gol'dt, I. V.; Guldi, D. M.; Marcaccio, M.; Francesco, P.; Demis, P.; Taylor, R. *Chem. Comm.* **2003**, *1*, 148.
4. Goodson, T. III. *Acc. Chem. Res.*, **2005**, *38*, 99.
5. Varnavski, O. P.; Ostrowski, J. C.; Sukhomlinova, L.; Twieg, R. J.; Bazan, G., C.; Goodson, T., III *J. Am. Chem. Soc.* **2002**, *124*, 1736.
6. Wang, Y.; He, G. S.; Prasad, P. N.; Goodson, T. III *J. Am. Chem. Soc.* **2005**, *127*, 10128.
7. Mascher-Brust, I.; Webb, W. W. *Biophys. J.* **1998,** *75*, 1669.
8. Oh, D. H.; Stanley, R. J.; Lin, M.; Hoeffler, W. K.; Bozer, S. G.; Berns, M. W.; Bauer, E. A. *Photochem. Photobiol.* **1997**, *65*, 91.
9. Albota, M. *et al.* *Science* **1998**, *281*, 1653.
10. Reinhardt, B. A.; Brott, L. L.; Clarson, S. J.; Dillard, A. G.; Bhatt, J. C.; Kannan, R.; Yuan, L.; He, G. S.; Prasad, P. N. *Chem. Mater.* **1998**, *10,* 1863.
11. Mongin, O.; Porres, L.; Moreaux, L.; Mertz, J.; Blanchard-Desce, M. *Org. Lett.*, **2002**, *4*, 719.
12. Brunel, J.; Mongin, O.; Jutand, A.; Ledoux, I.; Zyss, J.; Blanchard-Desce, M. *Chem. Mater.*, **2003**, 15, 4139.
13. Beljonne, D.; Wenseleers, W.; Zojer, E.; Shuai, Z.; Vogel, H.; Pond, S. J. K.; Perry, J. W.; Marder, S. R.; Bredas, J.-L. *Adv. Funct. Mater.* **2002**, *12*, 631.
14. Wang, Y.; Ranasinghe, M. I.; Goodson, T., III. *J. Am. Chem. Soc.* **2003**, *125*, 9562.

15. Varnavski, O. P.; Ostrowski, J. C.; Sukhomlinova, L.; Twieg, R. J.; Bazan, G., C.; Goodson, T., III *J. Am. Chem. Soc.* **2002**, *124*, 1736.
16. Katan, C.; Terenziani, F.; Mongin, O.; Werts, M. H. V.; Porre´s, L.; Pons, T.; Mertz, J.; Tretiak, S.; Blanchard-Desce, M. *J. Phys. Chem. A* **2005**, *109*, 3024.
17. Martin, R. E.; Diederich, F. *Angew. Chem. Intl. Ed.* **1999**, *38*, 1350.
18. Meier, H. *Angew. Chem.* **1992**, *104*,1425.
19. Kraft, A. ; Grimsdale, A. C.; Holmes, B. C. *Angew. Chem.* **1998**, *110*, 416.
20. Loutfy, R. O.; Hor, A. M..; Hsiao, C. K.; Baranyi, G.; Kazmaier, P. *Pure. Appl. Chem.* **1988**, *60*, 1047.
21. Feringa, L.; Jager, W. F.; de Lange, B. *Tetrahedron* **1993**, *49*, 8267.
22. Marsella, M. J.; Yoon, K.; Tham, F. S. *Org. Lett.* **2001**, *3*, 2129.
23. Dürr, H. *Angew. Chem.* **1989**, *101*, 427.
24. Kraft, A. ; Grimsdale, A. C.; Holmes, B. C. *Angew. Chem.* **1998**, *37*, 403.
25. Thompson, J.; Blyth, R. I. R.; Mazzeo, M. *Appl. Phys. Lett.* **2001**, *79*, 560.
26. Katz, H. E.; Laquindanum, J. G.; Lovinger, A. J. *Chem. Mater.* **1998**, *10*, 633.
27. Horowitz, G. Adv. Mater. **1998**, *10*, 365.
28. Noma, N.; Tsuzuki, T.; Shirota, Y. *Adv. Mater.* **1995**, *7*, 647.
29. Noda, T.; Imae, I.; Noma, N.; Shirota, Y. *Adv. Mater.* **1997**, *9*, 239.
30. D. Fichou, D.; Nunzi, J. M.; Charra, F.; Pfeffer, N. *Adv. Mater.* **1994**, *6*, 64.
31. McCullough, R. D.; *Adv. Mater.* **1998**, *10*, 93.
32. *Handbook of Oligo- and Polythiophenes*, D. Fichou, Ed., Wiley-VCh, Weinheim, **1999;** P. Bäuerle in *Electronic Materials: The Oligomer Approach*, K. Müllen, G. Wegner, Eds., Wiley-VCh, Weinheim, **1998**, pp. 105-197.Lightowler, S.; Hird, M. *Chem. Mater.* **2005**, *17*, 5538.
33. Zhao, M. –T.; Singh, B. P.; Prasad, P. N.; *J. Chem. Phys.* **1988**, *89*, 5535.
34. Marder, S. R.; Kippelen, B.; Jen, A. K.; Peyghambarian, N. *Nature* **1997**, *388*, 845.
35. Bednarz, M.; Reineker, P.; Mena-Osteritz, E.; Baeuerle, P. *J. Lumin.,* **2004**, *110*, 225.
36. Marsella, M. J.; *Acc. Chem. Res.* **2002**, *35*, 944.

37. Brault, L.; Miginau, E.; Neguesque, A.; Battaglia, E.; Bagrel, D.; Kirsch, G. *Eur. J. Med. Chem.* **2005**, *40*, 757.
38. Sarkar, A.; Haley, M. M. *Chem. Comm.* **2000**, *18*, 1733.
39. Yamada, T.; Azumi, R.; Hiroaki, S.; Hideki, A.; Abe, M.; Baeuerle, P.; Matsumoto, M. *Chem. Lett.* **2001**, 10, 1022.
40. Kroemer, J.; Carreras, I. R.; Fuhrmann, G.; Musch, C.; Wunderlin, M.; Debaerdemaker, T.; Mena-Osteritz, E.; Baeuerle, P. *Angew. Chem. Intl. Ed.*, **2000**, *39*, 3481.
41. Chung, S.-J.; Kim, K.-S.; Lin, T.-C.; He, G. S.; Swiatkiewicz, J.; Prasad, P. N. *J. Phys. Chem. B* **1999**, *103*, 10741.
42. Drobizhev, M.; Rebane, A.; Suo, Z.; Spangler, C. W. *J. Lumin.* **2005**, *111*, 291.
43. You, C.-C.; Hippius, C.; Gruene, M.; Wuerthner, F. *Chem. Eur. J.* **2006**, *12*, 7510.
44. Ambroise, A.; Li, J.; Yu, L.; Jonathan, S. *Org. Lett.* **200**, *2*, 2563.
45. Wu, H.-M.; Ratsep, M.; Jankowiak, R.; Cogdell, R. J.; Small, G. J. *J. Phys. B* **1997**, *101*, 7641.
46. Baeuerle, P. *Adv. Mater.*, **1992**, *4,* 102.
47. Fuhrmann, G.; Debaerdemaker, T.; Baurerle, P. *Chem. Comm.* **2003**, *8*, 949.
48. Maciejewski, A.; Steer;, R. P. *J. Photochem.* **1986**, 35, 59.
49. Xu, C.; Webb, W. W.; *J. Opt. Soc. Am. B.* **1996**, 13, 481.
50. Beljonne, D.; Wenseleers, W.; Zojer, E.; Shuai, Z.; Vogel, H.; Pond, S. J. K.; Perry, J. W.; Marder, S. R.; Bredas, J.-L. *Adv. Funct. Mater.* **2002**, *12*, 631.
51. Zhao, M. –T.; Singh, B. P.; Prasad, P. N.; *J. Chem. Phys.* **1988**, *89*, 5535.
52. J. A. Leegwater. *J. Phys. Chem.* **1996**, 100, 14402.
53. S. E. Bradforth; R. Jimenez; F. VanMourik; R. van Grondelle; G. Fleming. *J. Phys. Chem.* **1995**, 99, 16179.
54. Demidov, A; Andrews, D. *Photochem. Pphotobiol.* **1996**, 63(1), 39-52.
55. R. Kumble; S. Palese; R. Visschers; P. Dutton; R. Hochstrasser. *Chem. Phys. Lett.* **1996**, 261, 396.
56. Nakao, K.; Nishimura, M.; Tamachi, T.; Kuwatani, Y.; Miyasaka, H.; Nishinaga, T.; Iyoda, M. *J. Am. Chem. Soc.* **2006**, *128*, 16740.

Chapter 6

Nonlinear Optical Properties of Giant Porphyrin Macrocycles

6.1. Introduction

In this chapter, giant macrocycles consisting of porphyrin dimers as building blocks are investigated for their nonlinear optical (NLO) behavior. Porphyrins are a class of aromatic heterocycles, typically consisting of pyrrole units. The pyrrole units are connected by methine bridges. Several porphyrins have metallic centers and they are called metalloporphyrins. The structure of a porphyrin and a metalloporphyrin are shown in Figure 6.1.

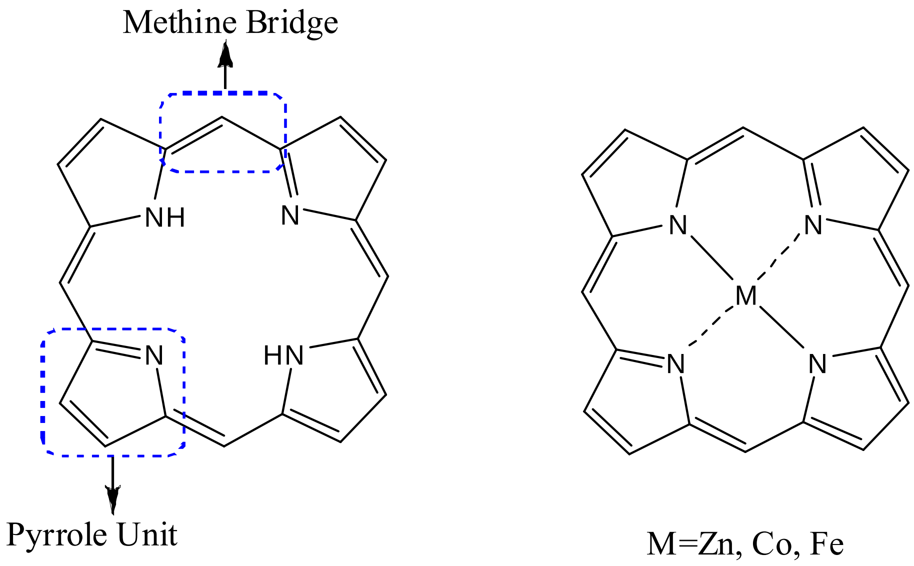

Figure 6.1. Chemical structures of porphyrins and metalloporphyrins.

Porphyrins are not new materials. Porphyrin occurs naturally in several forms. One of them is chlorophyll, which has been studied since as early as 1878[1]. Chlorophyll, the pigment commonly found in leaves responsible for their green color, is an example of Magnesium porphyrin. One of the first spectroscopic studies on chlorophyll was carried out by Russell and Lapraik in 1882[2]. They observed the four characteristic absorption features and the influence of acids and bases on the absorption behavior of chlorophyll.

Griffiths[3] discovered that a fairly large proportion of soluble iron in the soil is favorable to the growth of plants by developing a large amount of chlorophyll, especially in the leaf of the plant[3]. He considered iron to be closely related to the production of chlorophyll and the increased production of soluble carbohydrates, woody fiber and fat in certain cases was a direct consequence of increase in chlorophyll. With the use of modern tools of spectroscopy and chemical analysis, the role of chlorophyll in plant and bacterial photosynthesis has been examined in detail[4-10]. These investigations have also involved ultrafast spectroscopy[11-17].

Another naturally occurring porphyrin is heme, which is the pigment found in hemoglobin. Heme is an example of iron porphyrin and has also been the subject of detailed study[18-21]. As a final example, vitamin B12 or cyanocobalamine is a cobalt porphyrin. It has also been the subject of recent spectroscopic investigations[22, 23] as well as several mechanistic studies[24-26]. One of them has even linked it to Parkinson's disease[27].

Chlorophyll has been known to play a pivotal role in photosynthesis due to its light harvesting ability. Along with carotenoids, plants are able to absorb the entire visible spectrum of light and several energy and electron transfer reactions later, CO_2 and water is converted into oxygen and carbohydrates. This has stimulated significant research into the mechanisms governing energy transfer and other spectroscopic characteristics of photosynthesis[27-42]. Many of these studies have employed the tools of ultrafast spectroscopy in order to elucidate key aspects of spectroscopic behavior of chlorophyll. For example, Croce et al used femtosecond transient absorption measurements to investigate chlorophyll b to chlorophyll a energy transfer processes in antenna complex CP29. They observed three lifetimes for chlorophyll b 652 nm to chlorophyll a energy transfer process and attributed the presence of the third lifetime to mixed chlorophyll binding sites[28]. Similar investigation was carried out using three pulse photon echo and transient grating measurements by Salverda et al[29]. They investigated energy transfer in both CP29 and Light Harvesting Complex II (LHCII) in spinach. They concluded that mixed states must be present in native LHCII and suggested that a pair of chlorophyll b units must be present on A_3 and B_3 sites for chlorophyll b↔chlorophyll b and chlorophyll b↔chlorophyll a energy transfer. Holt et al used femtosecond upconversion measurements for probing the energy transfer from β-carotene to chlorophyll in the photosystem I (PSI) and PSII core complexes[30]. Based on chlorophyll rise time kinetics and S_2 state kinetics of β-carotene, they concluded that the S_1 state of β-carotene was not significant in energy transfer processes in PSII. They also concluded that energy transfer from S_2 state of β-carotene to PSII was nearly two times more efficient than that to PSI. Some of these studies have laid the foundation for designing artificial light harvesting systems using porphyrins as building blocks[43-52]. For this purpose, porphyrins have been assembled in several architectures such as polymers[53-57], dendrimers[58-66] and ladders[67, 68].

While these architectures have yielded some interesting electronic and optical behavior, natural light harvesting systems such as LHCII arrange porphyrins in the form of macrocycles[69]. A schematic representation of LHCII is shown in Figure 6.2. The red and yellow chromophores represent porphyrins arranged in cyclic fashion.

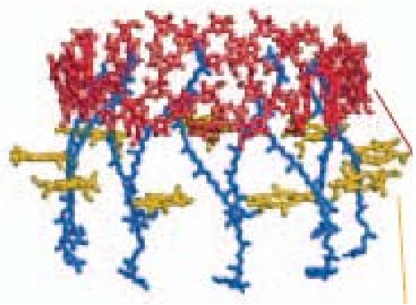

Figure 6.2. Structure of light harvesting system LHCII[69].

As a result, significant research has been expended over the years to synthesize and understand energy transfer processes in macrocyclic porphyrins[70-73]. The cyclic and conjugated nature of porphyrins also renders them attractive from nonlinear optical (NLO) properties standpoint. The absorption spectrum of tetratphenylporphyrin, with chemical structure is shown in Figure 6.3. There are two characteristic regions, named Soret band and Q-band. These features arise from S_2 and S_1 states respectively. It can be observed that porphyrins show absorption into the longer wavelengths (500nm-700nm). Hence, by developing novel materials using porphyrins as building blocks, it is possible to explore materials that would exhibit TPA behavior at telecommunication wavelengths (1200nm onwards). Such materials find applications in optical pulse suppression[70], development of photorefractive composites[74, 75], and all optical beam stabilization[76]. Even though porphyrins are capable of exhibiting large NLO responses in the IR region, their scope for application in multiphoton imaging seems to be limited due to their low fluorescence quantum yields. In this chapter, the linear and nonlinear optical properties of giant macrocyclic porphyrins have been investigated. However, the linkage between individual building blocks is non-conjugated. Hence, the objective is objective to investigate the NLO behavior of such non conjugated porphyrin macrocycles and to correlate the same to energy migration dynamics observed in these systems. It is an interesting possibility to explore communication between building blocks that are connected by nonconjugated bridges.

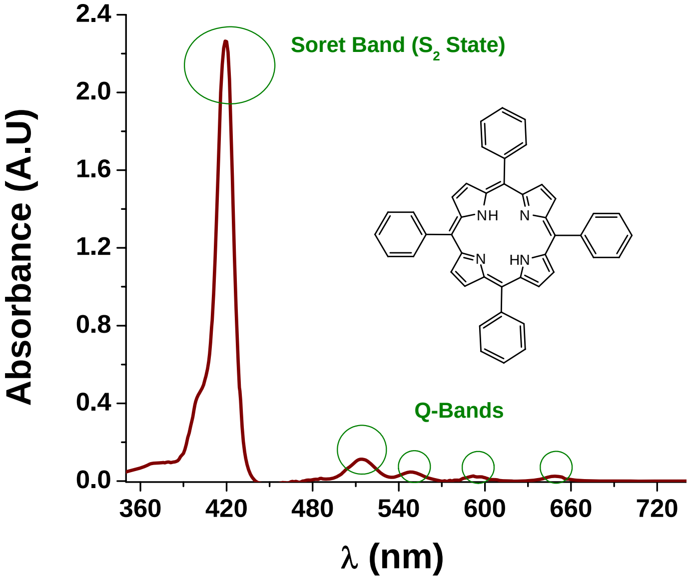

Figure 6.3. Absorption spectrum of tetraphenylporphyrin.

6.2. Experimental Section

6.2.1. Materials

Professor Kazuya Ogawa at Nara Institute of Technology has synthesized the porphyrin macrocycles investigated in this study. The structure of the building block is shown in Figure 6.4. It consists of three parts. A fluorene unit sandwiched between two ethynyl linkages that provides the π-conjugating bridge, two zinc-porphyrin units at each end and a methyl imidazole end group on each porphyrin ring. The structures of the giant macrocycles are presented in Figure 6.5. Due to the complexity of the structure, only a general form is presented. The macrocycles investigated in this chapter had n values of 4, 6, and 10. These molecules are named N4, N6 and N10 respectively. A value of n= 4 corresponds to a macrocycle containing 11 dimer units and hence 22 porphyrin rings. It can be clearly observed from Figure 6.5 that the linkage connecting individual building blocks (dimer units) is non-conjugated. The linkage consists of two vinyl groups with two long alkoxy segments. The general synthetic strategies for preparing porphyrin macrocycles similar to those studied in this chapter have been documented in the literature by Professor Ogawa and coworkers[77, 78]. The solvent used for the present studies was a mixture consisting of 8 parts of dimethyl formamide (DMF) and 2 parts of pyridine.

6.2.2. Steady State Measurements

The absorption spectra of the molecules were measured using an Agilent (Model # 8341) spectrophotometer. Their emission spectra were acquired using a Jobin Yvon Spex Fluoromax-2 spectrophotometer. The results presented in Figure 6.6. The quantum yields of the molecules were measured using a known procedure[79]. Tetraphenylporphyrin dissolved in toluene was used as the standard. The following relation was used to measure quantum yields:

$$\phi_F = (\phi_F)_S \frac{\int J(\bar{\nu})d\bar{\nu}}{\int J_S(\bar{\nu})d\bar{\nu}} \frac{(J_a)_S}{J_a} \frac{n^2}{n_s^2} \qquad (6.1)$$

These measurements may have some error due to sensitivity of the fluorescence spectrophotometer and other environmental conditions.

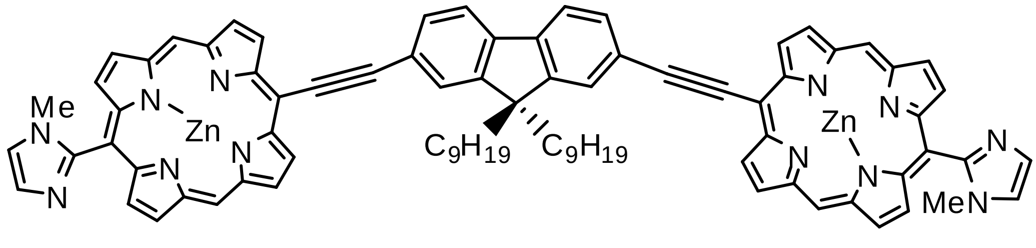

Figure 6.4. Structure of the building block used in porphyrin macrocycles.

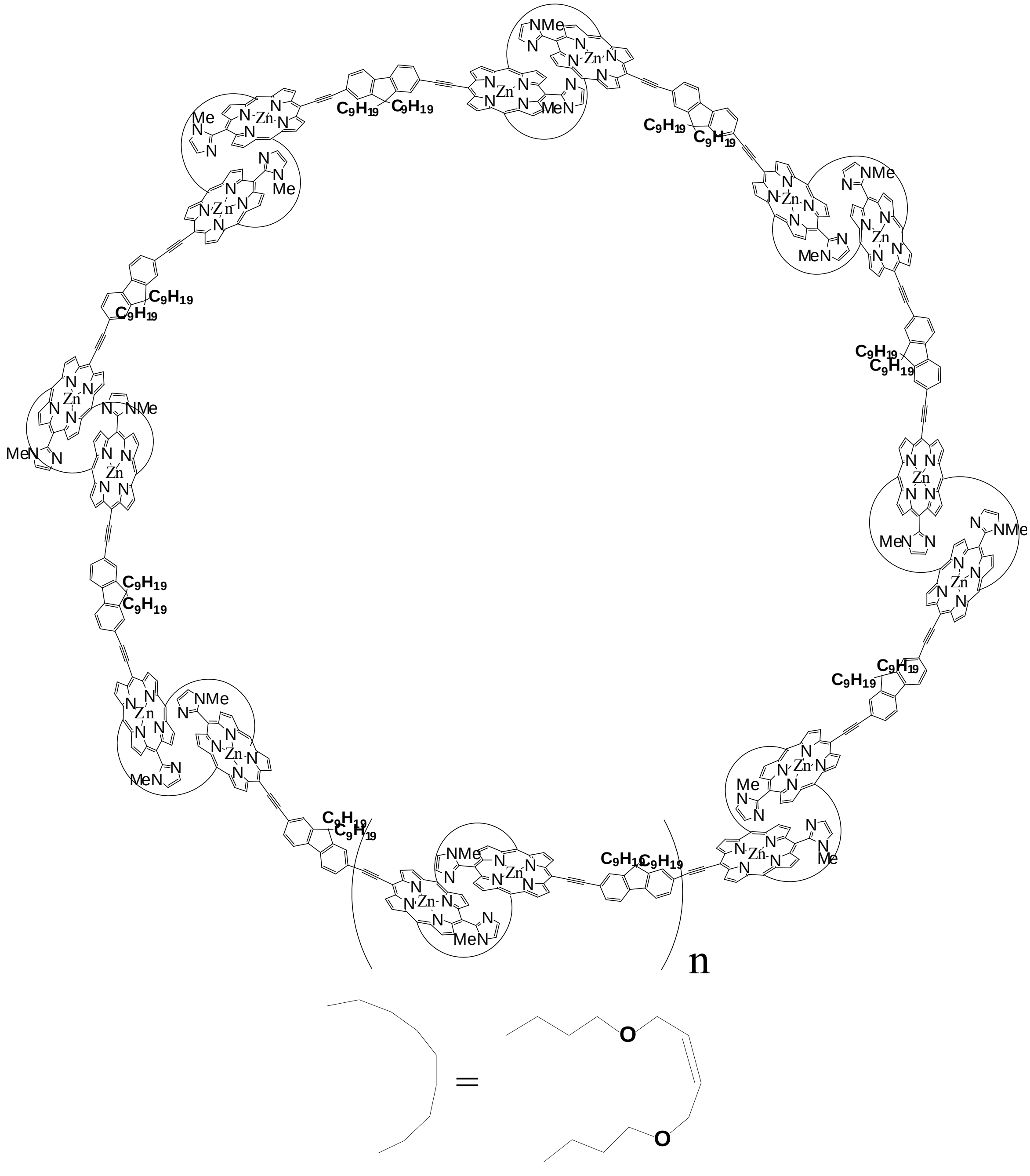

Figure 6.5. General structure of the porphyrin macrocycles investigated in this chapter.

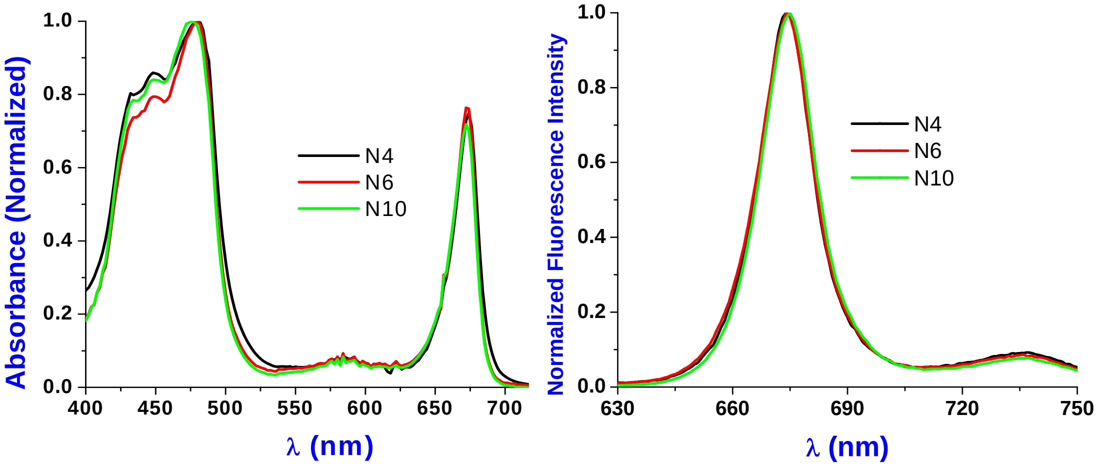

Figure 6.6. Absorption and emission spectra of giant porphyrin macrocycles.

6.2.3. Two-Photon Absorption Measurements

In order to measure the two photon absorption cross sections, we followed the two photon excited fluorescence (TPEF) method[80]. A 10^{-4} M Coumarin 307 solution in methanol was used as the reference between 790nm-840nm. For wavelengths over 840nm, Fluorescein at pH 11.3 was used as standard. The laser used for the study was a tunable, mode-locked Ti:Sapphire laser (Mai Tai HP from Spectra-Physics). This system could be tuned from 690nm-1020nm. Typical pulse width was 100fs. However, the pulse had a sech^2 intensity distribution. The repetition rate was 80MHz.The input power from the laser was varied by using a neutral density filter. An iris was placed prior to the polarizer in order to ensure a circular beam. The beam from the polarizer was focused on the sample cell (quartz cuvette, 0.5cm path length) using a lens with a focal length of 11.5 cm. The fluorescence was collected in a direction perpendicular to the incident beam. A 1″ focal length planoconvex lens was used to direct the collected fluorescence into a monochromator (Cornerstone 130, Oriel Instruments). The output from the monochromator was coupled to a PMT (R7518P, Hamamatsu). The photons were converted into counts by a photon counting unit. A logarithmic plot between collected fluorescence photons and input intensity gave a slope of two, ensuring a quadratic dependence between the same. The intercept enabled us to calculate the two photon absorption cross sections.

6.2.4. Ultrafast Transient Absorption Measurements

Femtosecond transient absorption investigations have been carried out using ultrafast pump-probe spectrometer detecting in the visible region. Briefly, 1 mJ, 100 fs pulses at 800 nm with a repetition rate of 1 KHz were obtained from Nd:YLF(Empower) pumped Ti:Sapphire regenerative amplifier (Spitfire, Spectra physics) with the seed pulses from Millennia pumped Ti:Sapphire oscillator (Tsunami, Spectra physics). The output of laser beam was split to generate pump and probe beam pulses with a beam splitter (85% and 15%). The pump beam was produced by optical parametric amplifier (OPA-800C, Spectra Physics). The pump beam used in the present investigation, i.e., 415 nm, was obtained from the fourth harmonic of the idler beam and was focused onto the sample cuvette. The probe beam was delayed with a computer controlled motion controller and then focused into a 2 mm sapphire plate to generate white light continuum. The white light was then overlapped with the pump beam in a 2 mm quartz cuvette containing the sample and the change in absorbance for the signal was collected by a CCD detector (Ocean optics). Data acquisition was controlled by the software from Ultrafast systems inc. Typical power of probe beam was < 0.1 μJ while that of the pump beam was ~0.5 to 1 μJ per pulse. Magic angle polarization was maintained between the pump and probe using a wave plate. The pulse duration was obtained from fitting of the solvent response, which is ~130 fs. The sample was stirred by a rotating magnetic stirrer.

6.3. Results and Discussion

6.3.1. Steady State Measurements

The molar extinction coefficients (ε values) for the macrocycles were calculated by multiplying the number of dimer units in the macrocycle with the ε values obtained for the dimer (Figure 6.7). Table 6.1 summarizes the results from steady state measurements. The absorption spectra of the porphyrins presented in Figure 6.6 shows a Soret band with a maximum at 480nm with shoulders at 454 and 430nm. The Q-band features are observed at 585nm and 654nm. There is no significant bathochromic shift observed with increase in the size of macrocycle which could be a consequence if noncunjugated linkage between individual building blocks. Inspection of emission spectra presented in Figure 6.6 also shows virtually identical spectra for all the macrocycles. The emission spectra for all the macrocycles contain two distinct features; very narrow emission band and very small Stokes' shift with respect to Q-band maximum. Small Stokes' shift is a typical feature observed in zinc porphyrin based systems[81-83].

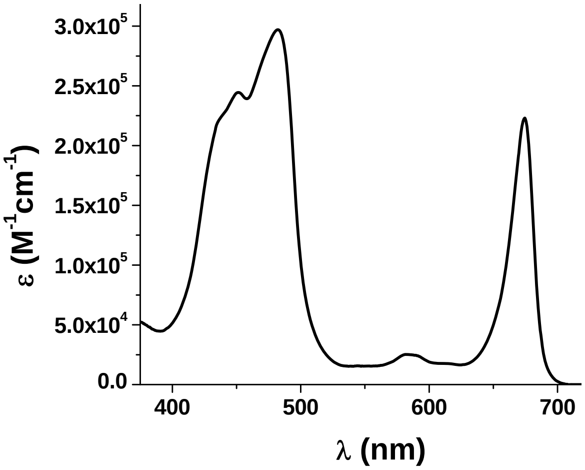

Figure 6.7. Molar extinction coefficient of dimer.

The porphyrin macrocycles have low quantum yields as shown in Table 6.1. This is also observed commonly for metalloporphyrins due to preferential excited state pathways from excited states to triplet states due to presence of a metal atom amidst the porphyrin ring. That is why porphyrins are used as efficient singlet oxygen generators[81, 82]. Hence, with increase in ring size, the steady state properties do not seem to be affected significantly with the exception of molar extinction coefficient. It will be interesting to investigate the influence of increase in ring size on nonlinear optical properties of these macrocycles and the results from TPA measurements are discussed next.

Table 6.1. Steady state properties of giant porphyrin macrocycles.

Sample	ε_{soret} **($M^{-1}cm^{-1}$)**	ε_Q **($M^{-1}cm^{-1}$)**	**η**
N4	3266805	2452873	0.026
N6	3860770	2898850	0.034
N10	5048699	3790804	0.044

6.3.2. Two Photon Absorption Measurements

The TPA cross section values for N4, N6 and N10 from 800nm-875 nm are presented in Figure 6.8. A maximum at 830nm is observed for all the macrocycles, which corresponds to 415nm in terms of excited state's transition wavelength. Thus, a state lying close to the Soret band is the two-photon excited state for these macrocycles. The TPA cross section shows a marginal increase with increasing ring size, suggesting that there might be saturation behavior observed due to large size of the macrocycles. Further, the smallest macrocycle N4 contains 11 building blocks, which translates into 22 Zn-porphyrin units. Thus, N10 has 17 building blocks, corresponding to 34 Zn-porphyrin rings. 11 dimer units itself might be large enough to yield saturation of TPA behavior. However, in order to confirm this assessment, experiments are needed to be carried out on the dimer and smaller macrocycles.The TPA cross section maximum over the wavelength range investigated for N4 is 143720 GM. Dividing this value by the number of building blocks (11), we obtain a value of 13065 GM. This value is much larger than similar porphyrin dimer systems reported in literature[84-87]. Theoretical considerations suggest that coupling between ground state and the first excited state via transition dipole moment is a vital factor influencing the net TPA behavior of these materials[84].

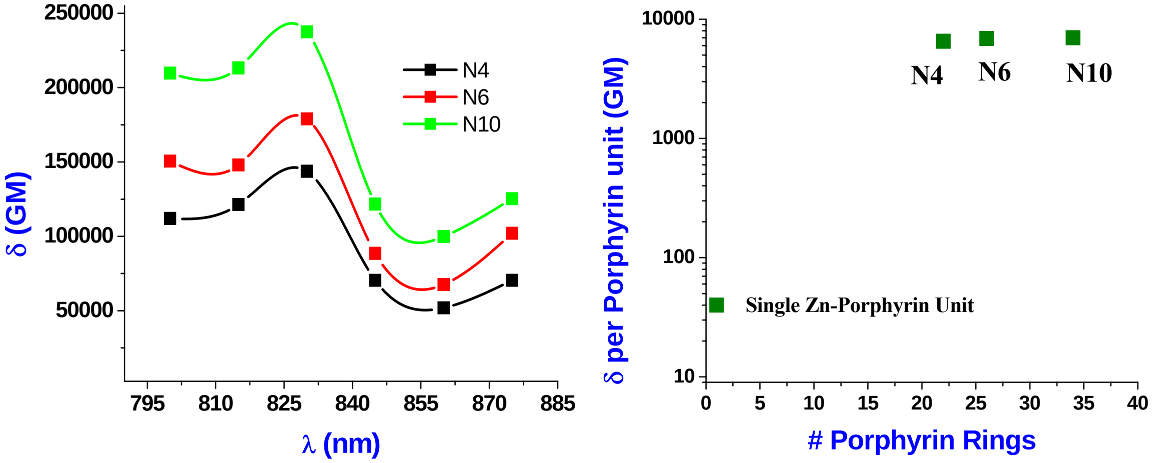

Figure 6.8. TPA cross sections of the porphyrin macrocycles studied in this chapter. Also shown are maximum TPA cross section values as a function of number of dimer units.

However, it is known that a single Zn-porphyrin unit has a TPA cross section of ca. 20 GM[88]. Taking this into consideration, we realize that since TPA cross section per dimer for N4 is 13065 GM, the TPA cross section per porphyrin unit is ~650 GM. Thus, there is significant improvement in TPA cross section per Zn-porphyrin unit. However, further investigations are needed to be conducted on the dimer itself in order to draw better comparisons between the TPA behavior of the dimer and the macrocycles studied in this chapter.

6.3.3. Ultrafast Transient Absorption

Transient absortion measurements were performed on N4 and N10 in an attempt to investigate any differences in their excited state dynamics as a result of increase in size of macrocycle. Such changes could provide some insight into differences in light and energy harvesting capabilities of these materials. Figure 6.9 shows the variation of excited state absorption (ESA) spectra with time for N4 between 100fs and 1ps. There are three distinct features. The negative absorption feature at 480nm which grows instantaneously is assigned to bleach recovery of S_2 state. The broad feature between 515 nm and 625 nm that decays concomitantly is assigned to S_2 state decay. These two features represent decrease in population of S_2 state. The third feature, which is another negative absorption feature, occurs at 675nm. This negative absorption grows with time. This is ascribed to S_1 state growth. Hence, population transfer from S_2 to S_1 state is observed over a very fast time scale. Longer timescale ESA behavior for N4 between 1ps and 750ps is shown in Figure 6.9. The bleach recovery and S_2 state decay are still observed, but now, the population of S_1 state also shows decay. This suggests recovery of ground state population. This is surprising because such dynamics are observed over few picoseconds, whereas it is well known that the lifetime of S_1 state for a Zn-porphyrin unit is ~2ns[89]. Thus, the species responding to excitation in transient absorption measurements seem to possess different characteristics than a single Zn-Porphyrin unit. However, whether or not the behavior observed for N4 is different from its building block (dimer) cannot be ascertained at this point due to unavailability of dimer material. Resonant kinetics corresponding to these processes for N4 are presented in Figure 6.10. N10 also showed similar trends in its transient absorption behavior. Figure 6.11 shows the short and long timescale ESA behavior for N10 with similar S_2 bleach recovery and S_1 state growth. Longer timescale transients presented in Figure 6.11 show similar S_1 state decays. The resonant kinetics presented in Figure 6.12 shows similar trends at different wavelengths when compared to N4. The growth profiles at 480 nm and 670nm observed for N4 and N10 are quite similar.

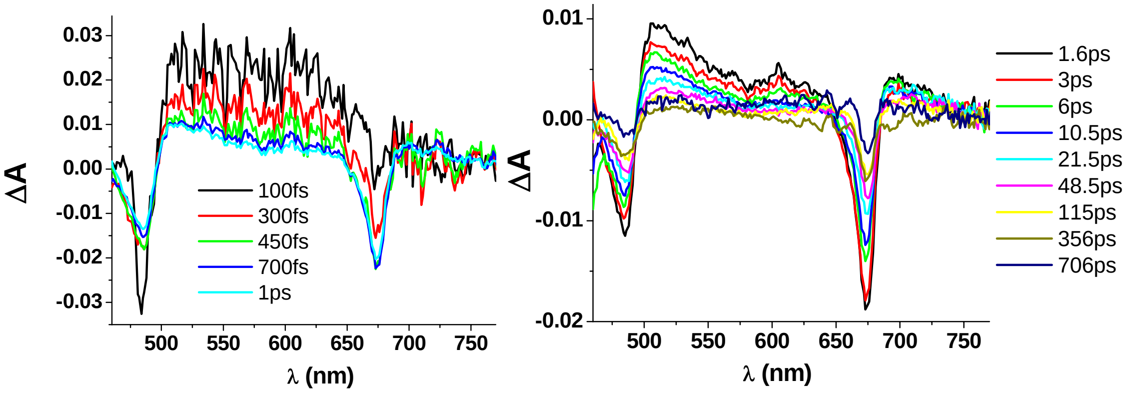

Figure 6.9. Short and long timescale transients for N4.

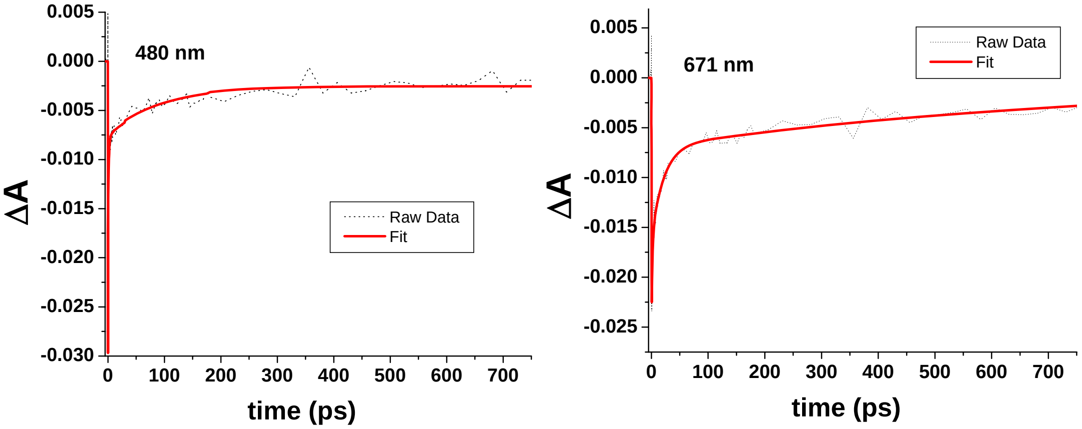

Figure 6.10. Resonant kinetics for N4.

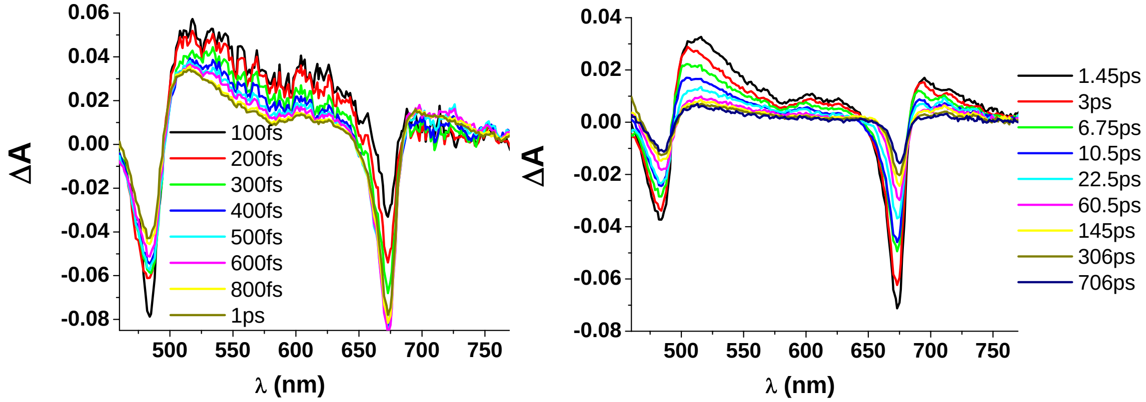

Figure 6.11. Short and timescale transients for N10.

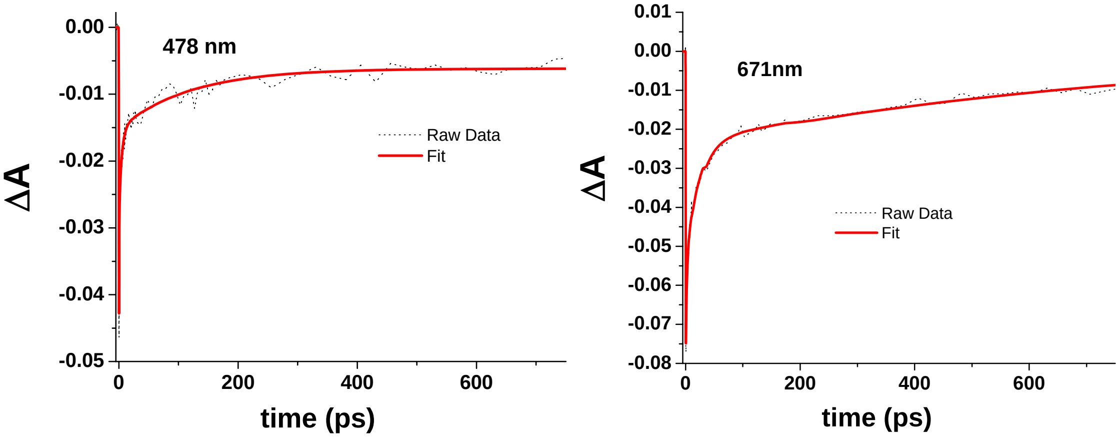

Figure 6.12. Resonant kinetics for N10.

6.4. Conclusions

TPA cross sections of giant porphyrin macrocycles were investigated in this chapter. These macrocycles could be potentially considered for light harvesting applications. The macrocycles were composed of building blocks that were connected by non-conjugated linkages. Steady state measurements showed some of the common features observed for zinc porphyrin based systems and very large molar extinction coefficients. TPA measurements showed that the macrocycles exhibited significant improvement in TPA cross section over single Zn-porphyrin unit. Transient absorption measurements showed different dynamics for S_1 state than a regular Zn-porphyrin unit. However, further experiments must be carried out on the building block (dimer) in order to further assess the enhancement as well as excited state dynamics.

Summary

- Giant macrocycles consisting of zinc-porphyrins as building blocks were investigated for two-photon absorption (TPA) behavior.
- The unique feature of these macrocycles was that the linkage between individual building blocks was non conjugated in nature.
- TPA cross section measurements have shown enhanced behavior over single zinc-porphyrin unit.
- Transient absorption investigations have indicated dynamics before the lifetime of singlet state of individual zinc-porphyrin units, indicating possible communication between building blocks.

6.5. Reference

1) Vines, S. H. *J. Chem. Soc.* **1878**, *33*, 375.
2) Russell, W. J.; Lapraik, W. *J. Am. Chem. Soc.* **1882**, *4*, 257.
3) Griffiths, A. B. *J. Chem. Soc.* **1885**, *47*, 46.
4) Fajer, J.; Davis, M. S.; Forman, A.; Klimov, V. V.; Dolan, E.; Ke, B. *J. Am. Chem. Soc.* **1980**, *102*, 7143.
5) Melis, A.; Brown, J. S. *Proc. Natl. Acad. Sci.* **1980,** *77*, 4712.
6) Dougherty, R. C.; Dreifuss, P. A.; Sphon, J.; Katz, J. J. *J. Am. Chem. Soc.* **1980**, *102*, 416.
7) Blakehship, R.; McGuire, A.; Sauer, K. *Proc. Natl. Acad. Sci.* **1975,** *72*, 4943.
8) Van Best, J. A.; Duysens, L. N.; *Biochim. Biophys. Acta* **1975**, *408*, 154.
9) Uphaus, R. A.; Norris, J. R.; Katz, J. J. *Biochem. Biophys. Res. Commun.* **1974**, *61*, 1057.
10) Arnon, D. I. *Proc. Natl. Acad. Sci.* **1971**, *68*, 2883.
11) Lokstein, H.; Leupold, D.; Voigt, B.; Nowak, F.; Ehlert, J.; Hoffmann, P.; Garab, G. *Biophys. J.* **1995**, *59*, 1536.
12) Melkozernov, A. N.; Blakenship, R. E. *J. Phys. Chem. B.* **2000**, *104*, 1651.
13) Pellegrino, F. *Opt. Engg.* **1983**, *22*, 508.
14) Wasielewski, M. R.; Liddell, P. A.; Barrett, D.; More, T. A.; Gust, D. *Nature* **1986**, *322*, 570.
15) Yoshihara, K.; Kumazaki, S. *J. Photochem. Photobiol. C* **2000**, *1*, 22.
16) Zuo, P., Li, B.-X.; Zhao, X.-H.; Wu, Y.-S.; Ai, X.-C.; Zhang, J.-P.; Li, L.-B.; Kuang, T.-Y. Biophys. J. 2006, 90, 4145.
17) Ilagan, R. P.; Koscielecki, J. F.; Hiller, R. G.; Sharples, F. P.; Gibson, G. N.; Birge, R.; R.; Frank, H. A. *Biochemistry* **2006**, *45*, 14052.
18) Zhuang, J.; Amoroso, J. H.; Kinloch, R.; Dawson, J. H.; Baldwin, M. J.; Gibney, B. R. *Inorg. Chem.* **2006**, *45*, 4685.
19) Adams, K. L.; Tsoi, S.; Yan, J.; Durbin, S. M.; Ramdas, A. K.; Cramer, W. A.; Sturhahn, W. Alp, E. E.; Schulz, C. *J. Phys. Chem.* **2006**, *110*, 530.

20) Garcia-Rubio, I.; Martinez, J. I.; Picorel, R.; Yruela, I.; Alonso, P. J. *J. Am. Chem. Soc.* **2003**, *125*, 15846.

21) Owens, J. W.; O'Connor, C. *J. Coord. Chem. Rev.* **1988**, *84*, 1.

22) He, M.; Dowd, P. *J. Am. Chem. Soc.* **1998**, *120*, 1133.

23) Shiang, J. J.; Cole, A. G.; Sension, R. J.; Hang, K.; Weng, Y.; Trommel, J. S.; Marzilli, L. G.; Lian, T. *J. Am. Chem. Soc.* **2006**, *128*, 801.

24) Franke, A.; Roncaroli, F.; van Eldik, R.; *Eur. J. Inorg. Chem.* **2007**, *6*, 773.

25) Ealick, S. E.; Begley, T. P.' Nature, **2007**, *446*, 387.

26) Kandt, C.; Xu, Z.; Tieleman, D. P. *Biochemistry*, **2006**, *45*, 13284.

27) Polivka, T.; Van Stokkum, I. H. M.; Zigmantas, D.; Van Grondelle, R.; Sundstroem, V.; Hiller, R. G. Biochmistry, **2006**, *45*, 8516.

28) Croce, R.; Muller, M. G.; Caffarri, S.; Bassi, R.; Holzwarth, A. R. *Biophys. J.* **2003**, *84*, 2517.

29) Das, S. K.; Frank, H. A. *Biochemistry* **2002**, *41*, 13087.

30) Holt, N. E.; Kennis, J. T. M.; Dall'Osto, L.; Bassi, R.; Fleming, G. R. Chem. Phys. Lett. **2003**, *379*, 305.

31) Mathis, P. *Photochem. Photobiol.* **1969**, *9*, 55.

32) Connelly, J. P.; Muller, M. G.; Bassi, R.; Croce, R.; Holzwarth, A. R. Biochemistry, **1997**, *36*, 281.

33) Dutton, H. J.; Manning, W. M.; Duggar, B. M., J. Phys. Chem 191943, 47, 308.

34) Tomita, Giiti, Rabinowitch, E. *Biophys. J.* **1962**, *2*, 483.

35) Bauer, R. K.; Szalay, L.; Tombacz, E. Biophys. J. **1972**, *12*, 731.

36) Binnie, N. E.; Haley, L. V.; Koningstein, J. A. Chem. Phys. Lett. **1985**, *120*, 564.

37) Shreve, A. P.; Trautman, J. K.; Owens, T. G.; Albrecht, A. C. Chem. Phys. **1991**, *154*, 171.

38) Paalsson, L, O.; Spangfort, M. D.; Gulbinas, V.; Gilbro T. *FEBS Lett.* **1994**, *339*, 134.

39) Akimoto, S.; Takaichi, S.; Ogata, T.; Nishimura, Y.; Yamazaki, I.; Mimuro, M. *Chem. Phys. Lett.* **1996**, *260*, 147.

40) van Amerongen, H.; van Grondelle, R. *J. Phys. Chem. B.* **2001**, *105*, 604.

41) Horn, R.; Paulsen, H. *J. Mol. Biol.* **2002**, *318*, 547.

42) de Weerd, F. L.; Dekker, J. P.; van Grondelle, R. J. Phys. Chem. B. **2003**, *107*, 6214.

43) Ren, D.; Guo, Z.; Du, F.; Zheng, J.; Chen, Y. *J. Nanosci. Nanotechnol.* **2007**, *7*, 1539.

44) Valentini, L.; Trentini, M.; Mengoni, F.; Alongi, J.; Armentano, I.; Ricco, L.; Mariani, A.; Kenny, J. M. Diamond Rel. Mater. **2007**, *16*, 658.

45) Hasselman, G. M.; Watson, D. F.; Stromberg, J. R.; Bochian, D. F.; Holten, D.; Lindsey, J. S.; Meyer, G. L. *J. Phys. Chem. B* **2006**, *110*, 25340.

46) Huijser, A.; Savenije, T. J.; Kotlewski, A.; Picken, S. J.; Siebbeles, L. D. A. *Adv. Mater.* **2006**, *18*, 2234.

47) Wang, Q.; Campbell, W. M.; Bonfatani, E. E.; Jolley, K. W.; Officer, D. L.; Walsh, P. J.; Gordon, K.; Humphry-Baker, R.; Nazeeruddin, M. K.; Graetzel, M. *J. Phys. Chem. B* **2005**, *109*, 15397.

48) Hauschild, R.; Riedel, G.; Zeller, J.; Balaban, T. S.; Prokhorenko, V. I.; Kalt, H.; Berova, N.; Huang, X.; Pescitelli, R.; Nakanishi, K. *J. Lumin.* **2005**, *112*, 454.

49) Li, J.; Lindsey, J. S. *J. Org. Chem.* **1999**, *64*, 9101.

50) Seth, J.; Palaniappan, V.; Johnson, T. E.; Prathapan, S.; Lindsey, J. S.; Bochian, D. F. *J. Am. Chem. Soc.* **1994**, *116*, 10578.

51) Prathapan, S.; Johnson, T. E.; Lindsey, J. S. *J. Am. Chem. Soc.* **1993**, *115*, 7519.

52) Davila, J.; Harriman, A.; Milgrom, L. R. Chem. Phys. Lett. **1987**, *136*, 5.

53) Ogawa, T.; Ozawa, H.; Kawao, M.; Tanaka, H. *J. Mater. Sci.* **2007**, *18*, 939.

54) Ozawa, H.; Kawao, M.; Tanaka, H. Ogawa, T. *Langmuir*, **2007**, *23*, 6365.

55) Chen, F.; Adronov, A. *Chem. Eur. J.* **2006**, *12*, 5053.

56) Sarno, D. M.; Matienzo, L. J.; Jones, W. E. *Inorg. Chem.* **2001**, *40*, 6308.

57) Ikeda, A.; Hatano, T.; Shinkai, S.; Akiyama, T.; Yamada, S. *J. Am. Chem. Soc.* **2001**, *123*, 4855.

58) Lee, D.-I.; Goodson, T. III J. Phys. Chem. B **2006**, *110*, 25582.

59) Cho, S.; Li, W.-S.; Yoon, M.-C.; Ahn, T. K.; Jiang, D.-L.; Kim, J.; Aida, T.; Kim, D. *Chem. Eur. J.* **2006**, *12*, 7576.

60) Li, Y,; Rizzo, A.; Aurora, S. M.; Marco, M.; Huo, C.; Wang, Y.; Li, K.; Cingolani, R.; Gigli, G. Appl. Phys. Lett. **2006**, *89*, 061125/1.

61) Oar, M. A.; Serin, J. M.; Dichtel, W. R.; Frechet, J. M. J.; Ohulchanskyy, T. Y.; Prasad, P. N. Chem. Mater. **2005**, *17*, 2267.

62) Hasobe, T.; Kamat, P. V.; Absalom, M. A.; Kashiwagi, Y.; Sly, J.; Crossley, M. J.; Hosomizu, K.; Imahori, H.; Fukuzumi, . *J. Phys. Chem. B* **2004**, *108*, 12865.

63) Paulo, P. M. R.; Gronheid, R.; De Schryver, F. C.; Costa, S. M. B. *Macromolecules*, **2003**, *36*, 9135.

64) Frampton, M. J.; Magennis, S. W.; Pilow, J. N. G.; Burn, P. L.; Samuel, I. D. W. J. Mater. Chem. **2003**, *13*, 235.

65) Imaoka, T.; Horiguchi, H.; Yamamoto, K.; J. Am. Chem. Soc. 2003, 125, 340.

66) Uyemura, M.; Aida, T. *J. Am. Chem. Soc.* **2002**, *124*, 11392.

67) Drobizhev, M.; Stepanenko, Y.; Rebane, A.; Wilson, C. J.; Screen, T. E. O.; Anderson, H. L. *J. Am. Chem. Soc.* **2006**, *128*, 12432.

68) Taylor, P. N.; Anderson, H. L. *J. Am. Chem. Soc.* **1999**, *121*, 11538.

69) Scholes, G. D.; Rumbles, G. *Nat. Mater.* **2006**, *5*, 683.

70) Kadish, K. M.; Wenbo, E.; Zhan, R.; Khoury, T.; Govenlock, L. J.; Prashar, J. K.; Sintic, P. J.; Ohkubo, K.; Fukuzumi, S.; Crossley, M. J. J. Am. Chem. Soc. 2007, 129, 6576.

71) Sessler, J. L.; Tomat, E.; Lynch, V. M. *Chem. Comm.* **2006**, *43*, 4486.

72) Ballester, P.; Costa, A.; Deya, P. M.; Frontera, A.; Gomila, R. M.; Oliva, A. I.; Sanders, J. K. M.; Hunter, C. A. J. Org. Chem. **2005**, *70*, 6616.

73) Shoji, O.; Tanaka, H.; Kawai, T.; Kobuke, Y. *J. Am. Chem. Soc.* **2005**, *127*, 8598.

74) Lin, T.-C.; He, G. S.; Zheng, Q.; Prasad, P. N. *J. Mater. Chem.* **2006**, *16*, 2490.

75) Tay, S.; Thomas, J.; Eralp, M.; Li, G.; Norwood, R. A.; Schulzgen, A.; Yamamoto, M.; Barlow, S.; Walker, G. A.; Marder, S. R.; Peyghambarian, N. *Appl. Phys. Lett.* **2005**, *87*, 171105/1.

76) Tay, S.; Thomas, J.; Eralp, M.; Li, G.; Kippelen, B.; Marder, S. R.; Meredith, G.; Schulzgen, A.; Peyghambarian, N. *Appl. Phys. Lett.* **2004**, *85*, 4561.

77) Ogawa, K.; Kobuke, Y. *J. Photochem. Photobiol C* **2006**, *7*, 1.

78) Dy, J. T.; Ogawa, K.; Akiharu, S.; Atsushi, I.; Kobuke, Y. *Chem. Eur. J.* **2007**, *13*, 3491.

79) Maciejewski, A.; Steer, R. P. *J. Photochem.* **1986**, *35*, 59.

80) Xu, C.; Webb, W. W. *J. Opt. Soc. Am. B.* **1996**, *13*, 481.

81) Ishi-i, T.; Taguri, Y.; Kato, S.; Shigeiwa, M.; Gorohmaru, H.; Maeda, S.; Mataka, S. *J. Mater. Chem.* **2007**, *17*, 3341.

82) Chen, C.-Y.; Tian, Y.; Cheng, Y.-J.; Young, A. C.; Ka, J.-W.; Jen, A. K.-Y. *J. Am. Chem. Soc.* **2007**, *129*, 7220.

83) Zhou, X.; Ren, A.-M.; Feng, J.-K.; Liu, X.-J.; Zhang, Y.-D. *Chem. Phys. Chem.* **2003**, *4*, 991.

84) Frampton, M. J.; Akdas, H.; Cowley, A. R.; Rogers, J. E.; Slagle, J. E.; Fleitz, P. A.; Drobozhiev, M.; Rebane, A.; Anderson, H. L. *Org. Lett.* **2005**, *7*, 5365.

85) Drobozhiev, M.; Stepanenko, Y.; Rebane, A.; Wilson, C. J.; Screen, T. E. O.; Anderson, H. L. *J. Am. Chem. Soc.* **2006**, *128*, 12432.

86) Drobozhiev, M.; Stepanenko, Y.; Yuliya, D.; Karotki, A.; Rebane, A.; Taylor, P. N.; Anderson, H. L. *J. Am. Chem. Soc.* **2004**, *126*, 15352.

87) Zhang, X.-B.; Feng, J.-K.; Ren, A.-M.; Sun, C.-C. *J. Mol. Str. Theochem* **2007**, *804*, 21.

88) Karotki, A.; Drobozhiev, M.;Kruk, M.; Spangler, C.; Nickel, E.; Mamardashvili, N.; Rebane, A. *J. Opt. Soc. Am. B* **2003**, *20*, 321.

89) Yu, H.-Z.; Baskin, S.; Zewail, A. H. *J. Phys. Chem. A* **2002**, *106*, 9845.

Chapter 7

Zinc Ion Sensing via Enhancement of Two-Photon Excited Fluorescence

7.1. Introduction

Two-Photon Absorption (TPA) is an example of a third order nonlinear optical process. It offers distinct advantages over one-photon processes such as quadratic dependence of TPEF intensity on input intensity, increased penetration depth and reduced scattering among many others, which renders TPA attractive for several applications [1-2]. One such emerging application lies in multiphoton metal ion sensing using near infra-red excitation wavelengths[3].

In this chapter, a chromophore, which shows enhancement in Two-Photon excited fluorescence (TPEF) upon formation of complex with zinc ions, is discussed. Several studies have focused on combining the unique features of two-photon excitation and interaction of organic chromophores with metal ions. One of the first studies involving metal ions and organic molecules was published by DeArmond et al in 1971[4]. They investigated the sensitized photolysis of alcohol glass using Rhodium Phenanthroline chelates. The authors elaborated a reaction pathway based on generation of solvent radicals involving two-photon absorption by the chelate and subsequent attack by the solvent radical upon relaxation of the chelate to its ground state. Kapinus and Dilung demonstrated reversible oxidation and reduction of metal porphyrins via two-photon absorption mechanism[5]. There are reports on systems involving zinc ions with interesting TPA behavior. Righetto et al investigated branched chromophores with pyridine groups and reported a decrease in TPA cross section upon coordination with zinc ions[6]. The authors explained this observation on the basis of a two-state model, suggesting that coordination with zinc resulted in species with ground state closer to the “cyanine” form, which in turn would cause a decrease in TPA cross section. Fabbrini et al have reported a chromophore that showed increase in TPA cross section upon binding with zinc ions using nanosecond pulsed nonlinear absorption method. However, no information on fluorescence behavior was reported[7]. Bozio et al have developed a zinc chemosensor based on a sharp decrease in TPEF response as zinc ions were added[8]. The authors attributed this to a change in tetramethylcyclen moiety present in their sensor from a donor to an acceptor upon coordination with zinc ions. Ahn et al have also observed a similar trend where addition of zinc ions resulted in decrease of TPA cross section[9]. Das et al have reported a Schiff's base type ligand which showed enhancement in TPA cross section as it coordinated with zinc [10]. Liu et al performed a theoretical study on multi-pyridyl ligand chromophores and predicted an increase in TPA cross section upon coordination with zinc due to spiroconjugation effect[11]. However, little information was provided regarding TPEF behavior. To the best of our knowledge, a system which shows substantial increases in both TPEF signal and TPA cross section upon coordination with zinc ions has not been reported.

In this study, we report a molecule that can detect zinc at the ppm level. It forms a complex with Zn^{2+} and subsequently shows more than one order of magnitude increase in the net TPEF signal ($\eta\delta$) in the near IR excitation region, in spite of a decrease in fluorescence quantum yield. It is highly sensitive and selective towards zinc ions. Our sensor does not yield a positive TPEF response to Cd^{2+}, which has been a challenge in the selective detection of zinc ions. We also investigate the effect of branch length on TPEF behavior and provide the mechanism of selectivity and sensitivity of the chromophore towards Zn^{2+}. The present work therefore, provides a guideline along which fluorescent materials for multiphoton excited metal sensing as well as TP imaging could be designed and developed.

7.2. Experimental

7.2.1. Synthesis of Chromophores

The synthesis of the main chromophore under investigation, Tris[p-(4-pyridylethynyl)phenyl]amine (addressed as TPPA from here onwards), T161, T233 and T119 was performed by Professor Robert Twieg at Kent State University (Chapter IV). The synthesis of other similar branched chromophores, used for comparison has also been reported previously (Chapter IV). Their structures are shown in Figure 7.1.

7.2.2. Steady state measurements

All compounds were used as received without any further purification. Unless otherwise stated, all measurements were carried out in THF. The absorption spectra of the molecules were measured using an Agilent (Model # 8341) spectrophotometer. Their emission spectra were acquired using a Shimadzu RF-1501spectrofluorimeter. Quantum yields were determined using Coumarin-307 in methanol as reference.

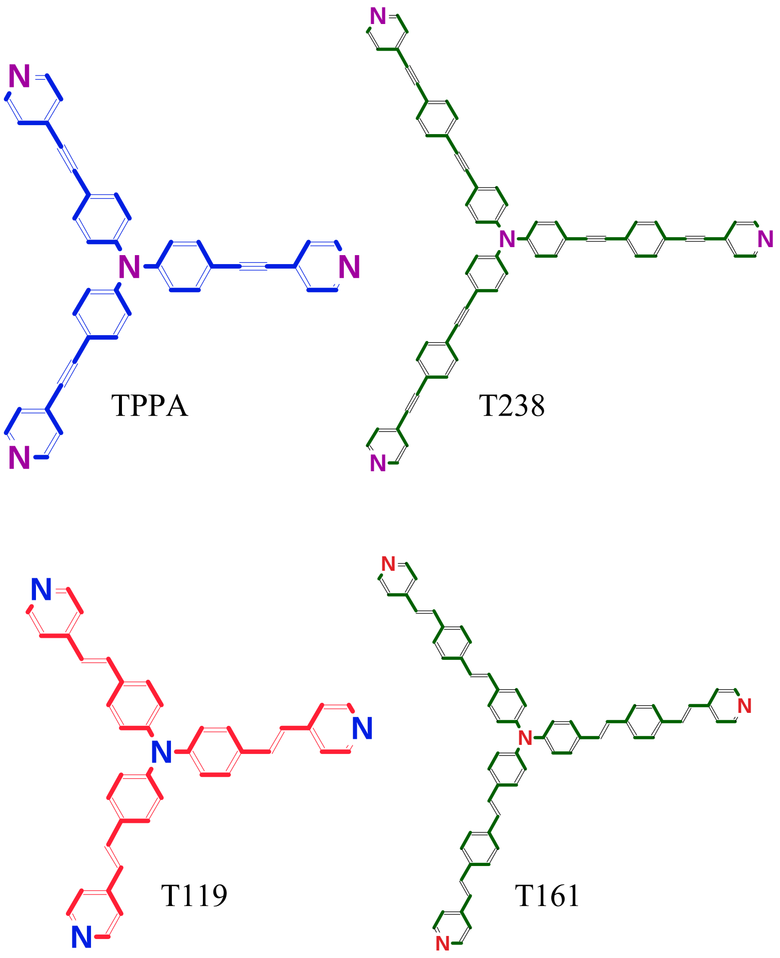

Figure 7.1. Structures of branched chromophores studied.

7.2.3. Two-Photon Absorption Cross Section measurements

In order to measure TPA cross sections, we followed the two photon excited fluorescence (TPEF) method[12]. The details of the lasers and optical set-up have been previously described (Chapters II and III). A 10^{-4} M Coumarin 307 solution in methanol was used as the reference over 700-830 nm range. Bis-MSB was used as the reference over 550-695 nm range[13]. Quadratic dependence of fluorescence intensity on input intensity was ensured at every wavelength.

7.2.4. Ultrafast Transient Absorption Measurements

Femtosecond transient absorption investigations have been carried out using an ultrafast pump-probe spectrometer detecting in the visible region. The details of this set-up have been discussed previously (Chapters II and III). The pump beams used in the present investigation were 375nm and 430nm.

7.3. Results and Discussion

7.3.1. Steady Stateand TPA measurements

The optical absorption and fluorescence results were obtained by adding $ZnCl_2$ in THF in a stepwise fashion (25μL per step) to 800 μL of 7.05 X 10^{-7} M TPPA. Different concentrations of $ZnCl_2$ were used, ranging from 0.5 mM-25 mM. The TPPA solution turned from colorless to green upon addition of $ZnCl_2$ solution. The initial absorption spectrum of the dye prior to addition of Zn^{2+} and the final absorption spectrum after addition of Zn^{2+} are shown in Figure 7.2. The final emission spectra taken from the exact same solutions are presented in Figure 7.3. The "final" spectrum in this case corresponded to an amount of Zn^{2+} where contribution from dye's emission was not significant. The detailed absorption and emission spectra obtained for every step as a result of addition of zinc chloride solution are presented in Figure 7.4 and Figure 7.5 respectively. As a control, identical volumes of pure THF were added in a separate sample cell. No change in absorption or emission behavior was observed except for decrease in peak intensity values. However, upon coordination with Zn^{2+}, bathochromic shifts in both absorption and emission spectra were observed, as indicated in Figure 7.2. The broadening and red shift of absorption spectrum for TPPA-Zn^{2+} suggests the formation of a partial charge transfer complex (between pyridine end group and Zn^{2+}).

The quantum yield of the complex was determined to be 0.27 while it was 0.58 for TPPA alone.

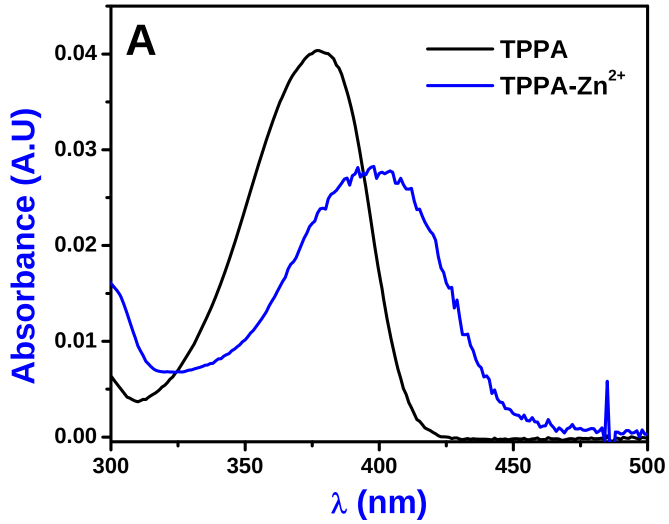

Figure 7.2. Absorption spectra of TPPA and TPPA-Zn^{2+}.

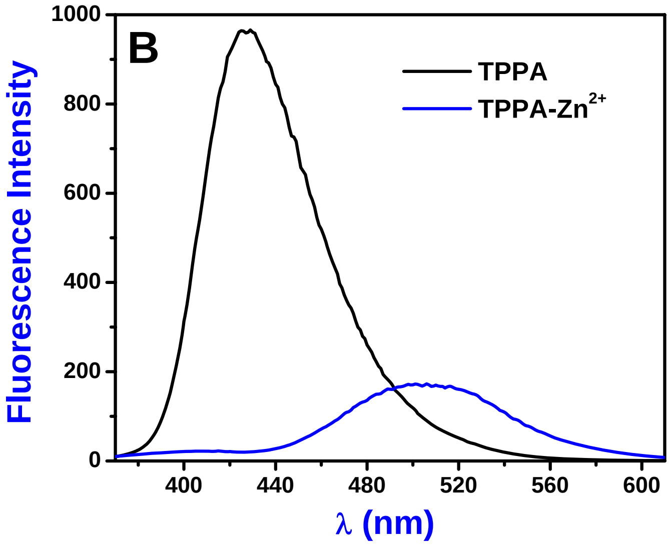

Figure 7.3. Emission spectra of TPPA and TPPA-Zn^{2+}.

Figure 7.6 shows images of TPPA (left) and TPPA-Zn^{2+} (right) solutions obtained using a digital camera. It is clearly seen that TPPA has intense blue emission. Upon addition of Zn^{2+} (right), the emission shifts to green. Also, the emission is not as intense since the bottom of the vial can be observed as a result of increased transparency of the solution. The concentration of TPPA in both vials was identical so the decrease in quantum yield is evident. In order to determine the nature of the complex (1:1 versus 1:2

and so on) between TPPA and Zn^{2+}, we followed a known procedure[14]. The change in optical density at a particular absorption wavelength as a function of metal ion concentration is an indication of binding dynamics. By fitting the data obtained to 1:1 and 1:2 complexation kinetics, the nature of complexation process can be investigated. The equation for 1:1 kinetics is:

$$\frac{\Delta A}{L} = \frac{D_t[K_1]\Delta\varepsilon_{11}M}{1+[K_1]M} \tag{7.1}$$

Where,

ΔA = difference in absorbance values of between pure dye and dye-metal ion complex at a particular wavelength.

D_t = Total dye concentration.

M = concentration of free metal.

$\Delta\varepsilon_{11}$ = change in extinction coefficient at the measurement wavelength between dye and dye-metal ion complex.

L = path length.

K_1 = binding constant.

An assumption made during the derivation is that the concentration of the metal ion is not significantly altered as a result of binding to the dye molecule. Rearranging equation 7.1, we have,

$$\frac{D_t}{\Delta A} = \frac{1}{[K_1]L\Delta\varepsilon_{11}M} + \frac{1}{L\Delta\varepsilon_{11}} \tag{7.2}$$

Hence, a plot with $D_t/\Delta A$ as abscissa and 1/M as ordinate should be a straight line with a slope of $1/[K_1]L\Delta\varepsilon_{11}$ and an intercept of $1/ L\Delta\varepsilon_{11}$. In other words, the slope equals $1/(\text{intercept}\times K_1)$. Hence, the binding constant can be calculated easily. In order to obtain more accurate results, we choose three different wavelengths, namely 410, 420 and 430nm. The results obtained for each wavelength are shown in Figure 7.7. The average value for K_1 was found to be 7200 M^{-1}. Similar procedure was employed to evaluate 2:1

and 3:1 complexes. However, the fits obtained were extremely poor. Hence, a 1:1 complex is assumed.

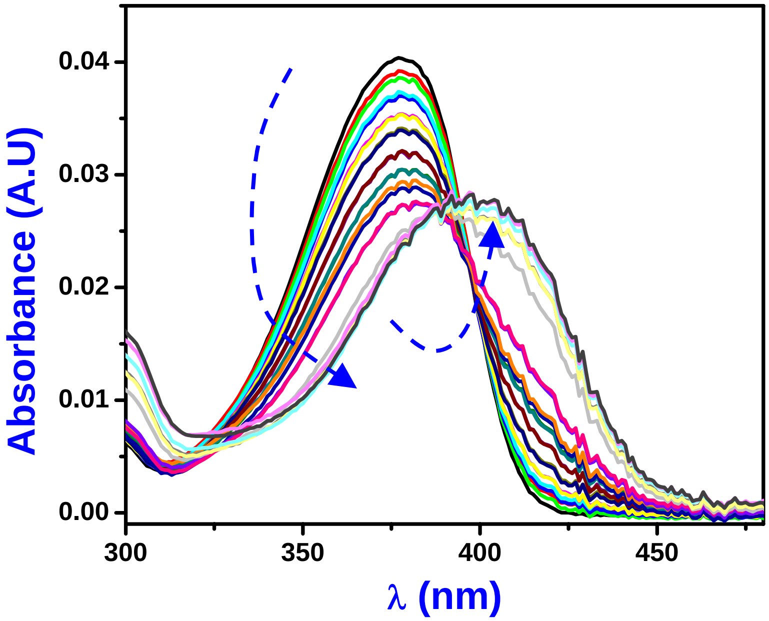

Figure 7.4. Change in absorption spectrum of TPPA upon addition of Zn^{2+}.

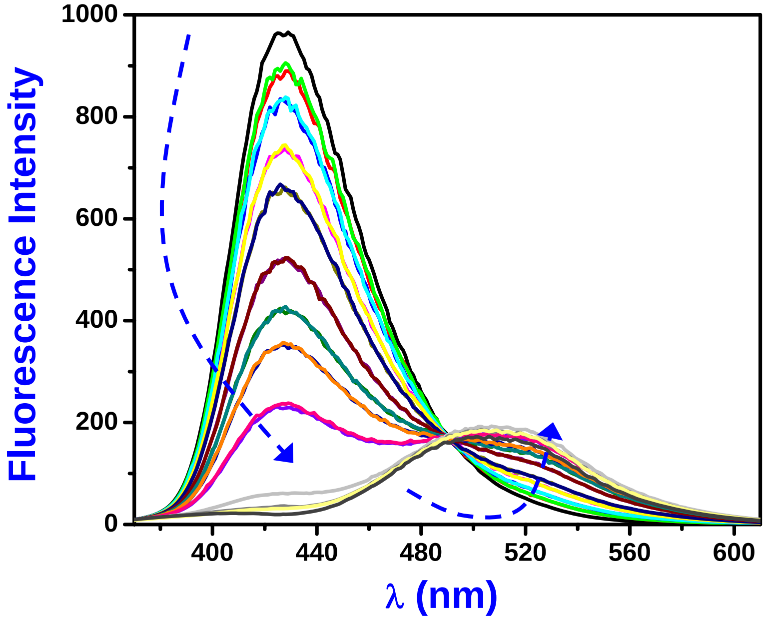

Figure 7.5. Change in emission behavior of TPPA upon addition of zinc ions.

Figure 7.6. Digital images of TPPA and TPPA-Zn^{2+} solutions. The solutions were irradiated with a UV lamp.

The value of K_1 obtained is comparable to some of the previously reported molecules in the literature [14, 15]. Besides $ZnCl_2$, other zinc salts such as zinc acetate, zinc nitrate and zinc cyanide were added to TPPA and the formation of complex was still observed, thereby precluding any spurious effects due to anions. We also added $ZnCl_2$ in THF to a previously reported chromophore N(DSB $)_3$[16], which has the same tri-branched nitrogen core as TPPA, but with alkene π-bridges and a tert-butyl phenyl end group. We did not observe any change in the absorption or emission characteristics. The results are shown in Figure 7.8 and Figure 7.9 respectively. This affirms that coordination occurs between Zn^{2+} and the pyridine end groups and that the core nitrogen atom does not participate in the complexation process. The use of pyridine group to coordinate with zinc ions has been reported in the literature[17-22]. However, most reports concentrate on ligands in bipyridyl or multi-pyridyl configurations. In the present study, the TPPA chromophore has pyridine units where the separation between the nitrogen atoms is larger than the commonly reported multi-pyridyl chromophores used for coordination with zinc ions in the literature[6-9]. Several other studies have reported porphyrins for zinc complexation[23, 24]. We have also carried out measurements with branched chromophores with structures similar to that of TPPA. These other chromophores had longer branch lengths or alkene π-linkages instead of alkyne linkages (as with TPPA) or both.

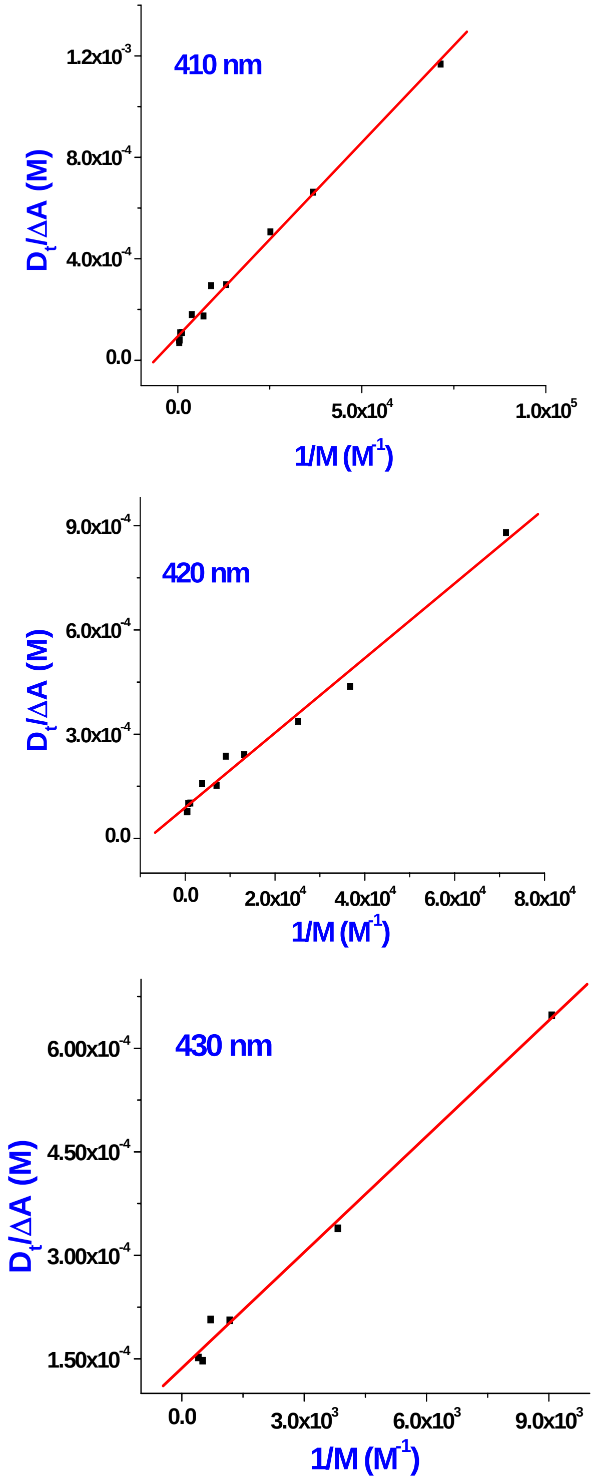

Figure 7.7. 1:1 complexation kinetics fitting of TPPA-Zn^{2+} coordination.

The results obtained for the other chromophores will be discussed in the next section along with TPEF measurements in order to obtain a comparison between one and two-photon excited processes. However, we saw a similar bathochromic shifts in both absorption and emission spectra for all the chromophores. However, as shall be seen from TPEF measurements, only TPPA proved to be the best sensor for Zn^{2+}.

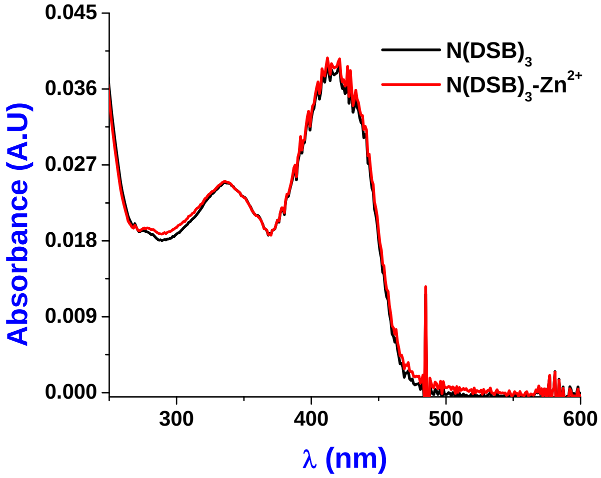

Figure 7.8. Absorption spectra for $N(DSB)_3$ and $N(DSB)_3$-Zn^{2+} .

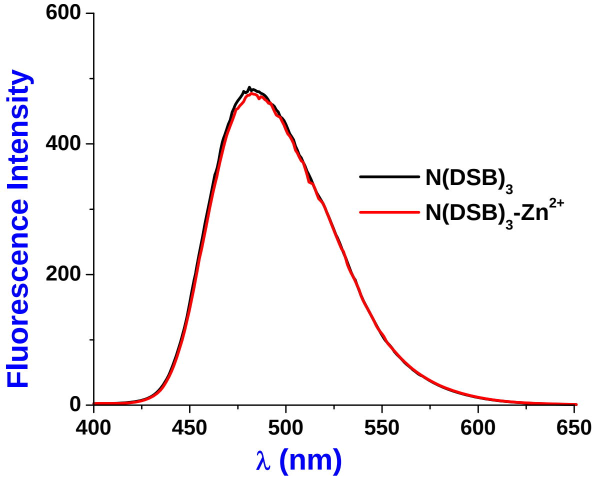

Figure 7.9. Emission spectra for $N(DSB)_3$ and $N(DSB)_3$-Zn^{2+} .

TPEF and TPA cross section measurements were carried out using the same solutions that were used for the determination of binding constants and quantum yields. The one and two photon excited fluorescence spectra for TPPA and TPPA-Zn^{2+} are shown in Figure 7.10. The TPEF spectra were measured at identical incident photon flux. Since the dye concentration was identical in both TPPA and TPPA- Zn^{2+}, it can be concluded that TPPA- Zn^{2+} shows ~11.5 fold increase in the TPEF signal over TPPA at their respective emission maxima. However, if we monitor the TPEF at 550nm, we observe two orders of magnitude enhancement in the TPEF intensity. This is in contrast to the steady state fluorescence results where coordination with zinc results in decrease in fluorescence intensity at the emission maximum. Hence, coordination with zinc not only results in a significant enhancement of TPA cross-section, but it also increases the net TPEF signal. Further, the enhancement of fluorescence intensity is observed only with TP excitation. Figure 7.11 shows the results obtained from identical experiments with another tri-branched chromophore T233 which has an additional phenylethynyl unit, but the same pyridine termini. T233 shows a net decrease in both one and TPEF peak intensities when coordinated with Zn^{2+}. T161, which has alkene linkages, shows similar trends in one and TPEF intensities upon coordination with Zn ions (Figure 7.12). We also investigated T119, a tri-branched chromophore similar to T161, but with one fewer phenylvinyl unit. T119 showed some improvement (Figure 7.13) under two-photon excitation, but the effect was not as pronounced as TPPA. The values of the TPEF signal $\eta\delta$ are plotted against the excitation wavelength. T119 shows approximately 1.5 to twofold improvement in $\eta\delta$ at virtually any excitation wavelength upon complexation with zinc ions. The TPEF results for TPPA and TPPA-Zn^{2+} at similar excitation wavelengths are presented in Figure 7.14. It can be observed that enhancement in TPEF signal is more than four times, especially at longer wavelengths. Since 550nm is chosen as the detection wavelength, the TPEF results over a wide range of wavelengths are shown in Figure 7.15. It is evident that several wavelengths in the near IR regime show two orders of magnitude or greater enhancement in TPEF signal upon coordination with Zn^{2+}.

In order to measure the sensitivity of TPPA towards Zn^{2+}, we added small volumes of $ZnCl_2$ stock solutions to 1 mL of 4.23×10^{-7} M TPPA. The results are shown in Figure 7.16. The TPEF enhancement factor refers to the ratio of TPEF signal at 550nm obtained after addition of zinc ions to TPEF signal obtained for parent dye at 550nm. From the linear fit shown in Figure 7.16, it is evident that in order to increase the TPEF signal by three-fold, the amount of Zn^{2+} required is 12.8 μM. This translates into a detection limit of 0.8 mg/L or 0.8 parts per million (ppm). These estimations do not take into account that the concentration of the TPPA dye is decreasing progressively with each step of addition of zinc chloride solution. So clearly, this is an underestimation of the sensitivity and we believe that this limit could be pushed further easily by a factor of 2. However, the present sensitivity is comparable with some of the zinc sensors reported in the literature[25, 26]. Sensors that claim to detect Zn^{2+} in the nanomolar and femtomolar regime based have been reported[27, 28]. However, the authors have not addressed the selectivity of those sensors towards zinc. In order to demonstrate the selectivity of our sensor, several other metal ions were investigated for their TPEF response. It was observed that alkali and alkali metal ions such as Na^+, K^+, Mg^{2+}, Ca^{2+} did not cause any change in steady state or TPEF behavior.

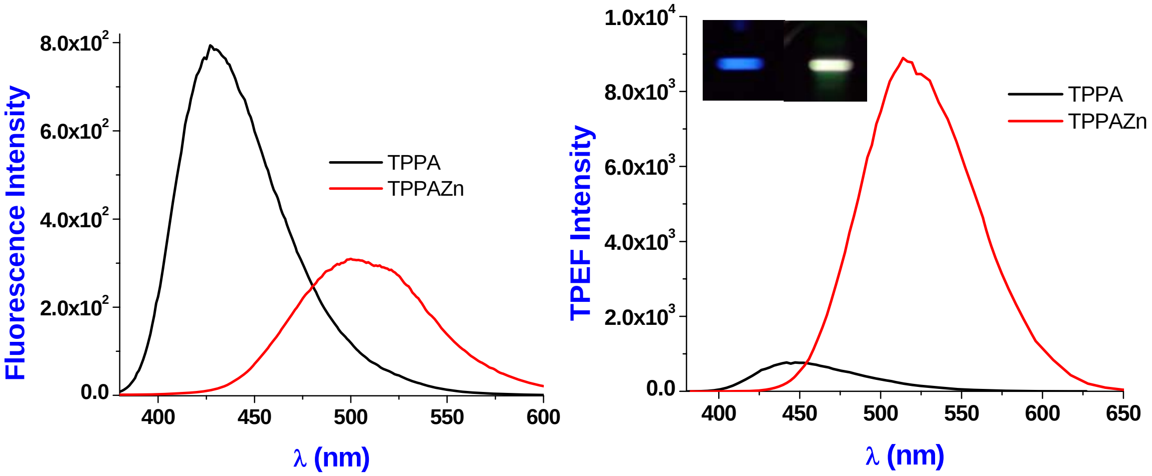

Figure 7.10. One and TPEF spectra for TPPA and TPPA-Zn^{2+}. Digital images from TPPA (blue) and TPPA-Zn^{2+} (green) are also shown.

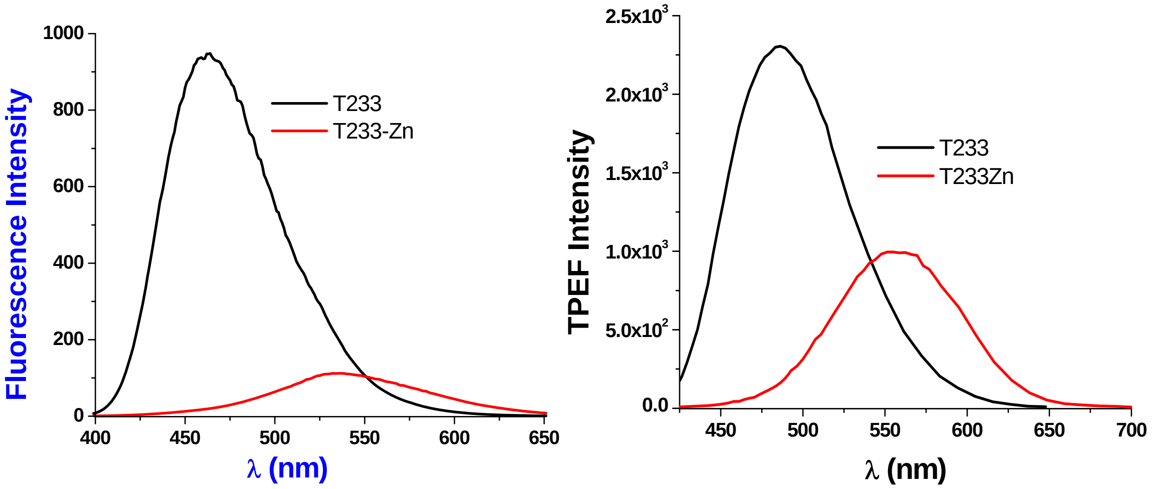

Figure 7.11. One and TPEF spectra for T233 and T233-Zn^{2+}.

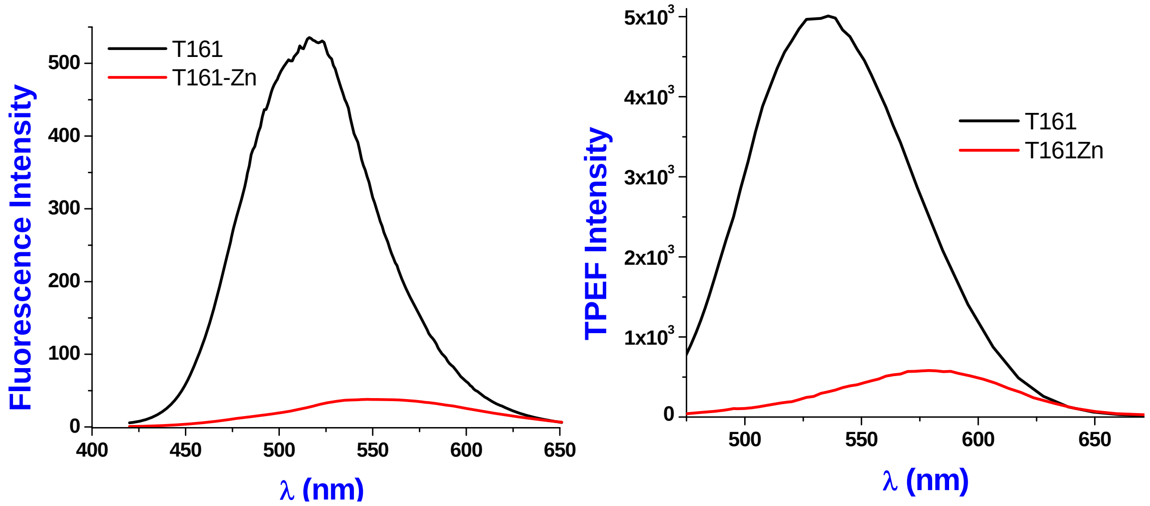

Figure 7.12. One and TPEF spectra for T161 and T161-Zn^{2+}.

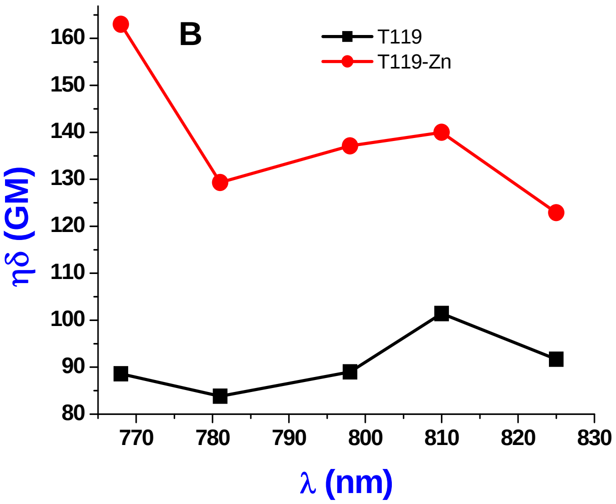

Figure 7.13. TPEF enhancement observed in T119 upon coordination with Zn^{2+}.

The selectivity of TPPA towards Zn^{2+} over Cd^{2+} is one of the challenges encountered while designing zinc sensors [11, 29-31]. As shown in Figure 7.17 , Cd^{2+} causes a bathochromic shift in absorption maximum, a feature observed similar to Zn^{2+}. This confirms a similar charge transfer complexation process. The emission spectra presented in Figure 7.18 shows quenched emission from the complex in both steady state and TPEF modes. Other metal ions such as Au (I and III), Fe (II and III), Cu (I and II), were also investigated. All of them exhibited turn off behavior in both one and TPEF modes. Selected results for Au (I and III) are presented in Figure 7.19 . Table 7.1 and Table 7.2 summarize the linear and NLO properties of the various metal ions that were studied or complexation with TPPA. Figure 7.20 further demonstrates the selectivity in a graphical fashion. It should be noted that Cd^{2+} studies were performed in acetone since $CdCl_2$ was not soluble in THF. Hence, TPPA serves as a highly sensitive and selective two-photon "turn-on" sensor for zinc ions.

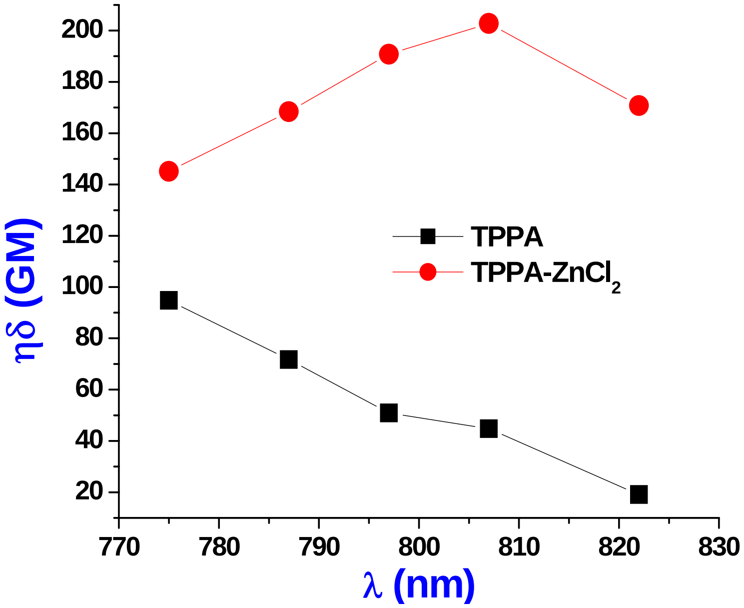

Figure 7.14. TPEF values for TPPA and TPPA-Zn^{2+} at several wavelengths.

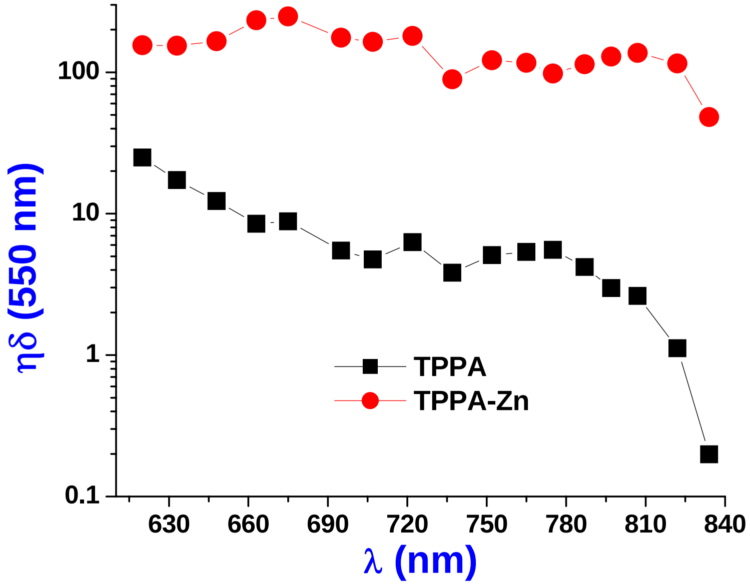

Figure 7.15. TPEF cross-section spectra for TPPA and TPPA-Zn^{2+} at 550 nm collection.

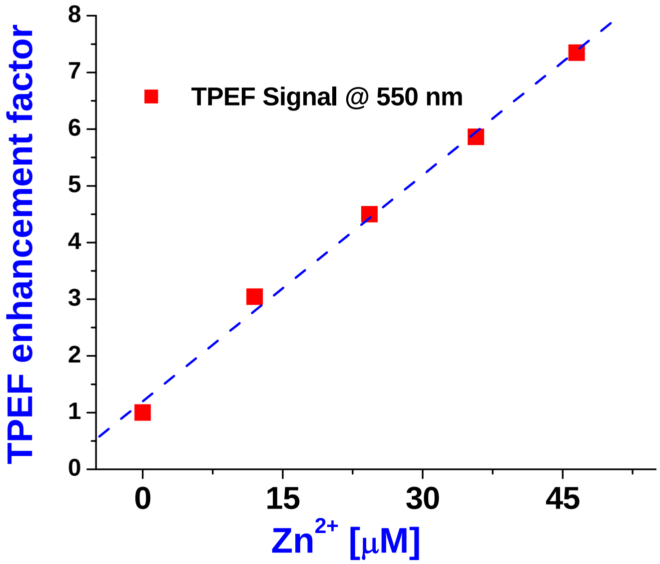

Figure 7.16. Determining the sensitivity of TPPA towards zinc ions.

The effect of zinc ion coordination on the absolute TPA cross sections shows some intriguing trends. The results for TPPA, T233 and T119 are presented in Figure 7.21, Figure 7.22, and Figure 7.23 respectively. T161 showed almost no change in TPA cross section at 810nm upon addition of zinc ions. The cross section changed from 1037 GM to 1065 GM, which is not significant considering the fact that TPA cross section measurements are within 20% error. From these results, it is evident that addition of zinc ions to all chromophores increases the acceptor strength of pyridine end group, thereby increasing the charge transfer character of the pyridine end group.

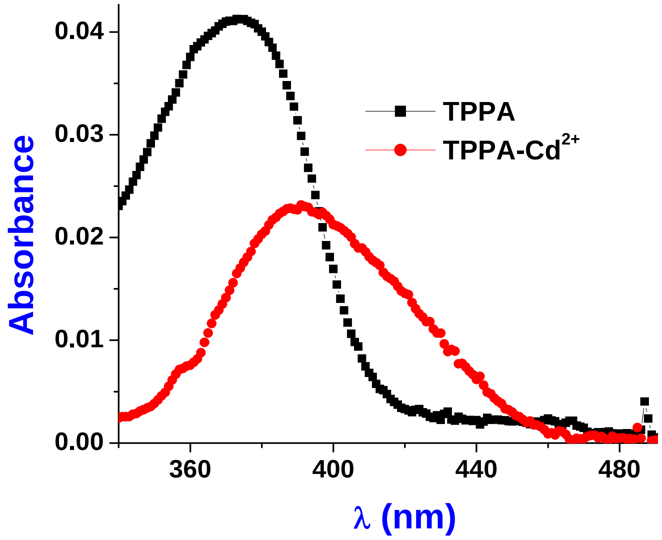

Figure 7.17. Absorption spectrum of TPPA and TPPA-Cd^{2+}.

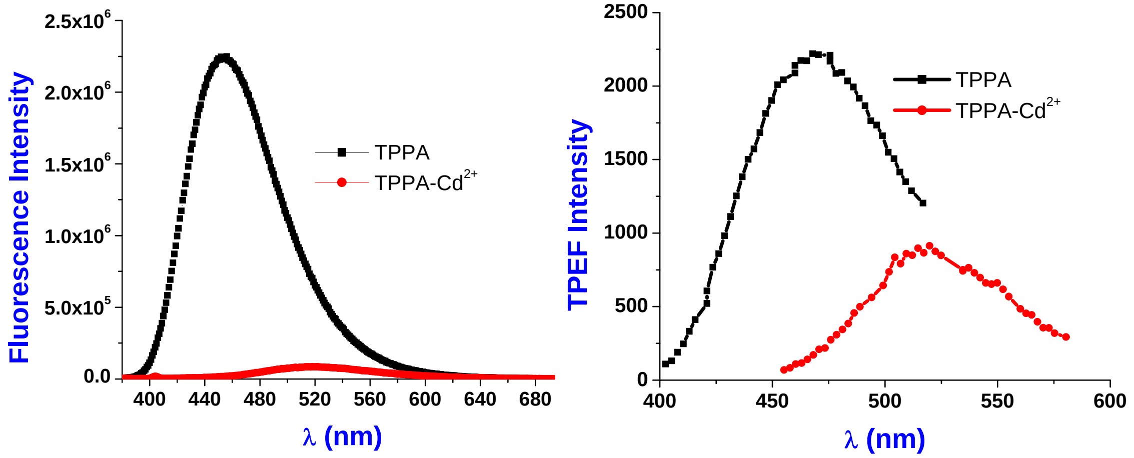

Figure 7.18. One and TPEF spectra of TPPA and TPPA-Cd^{2+}.

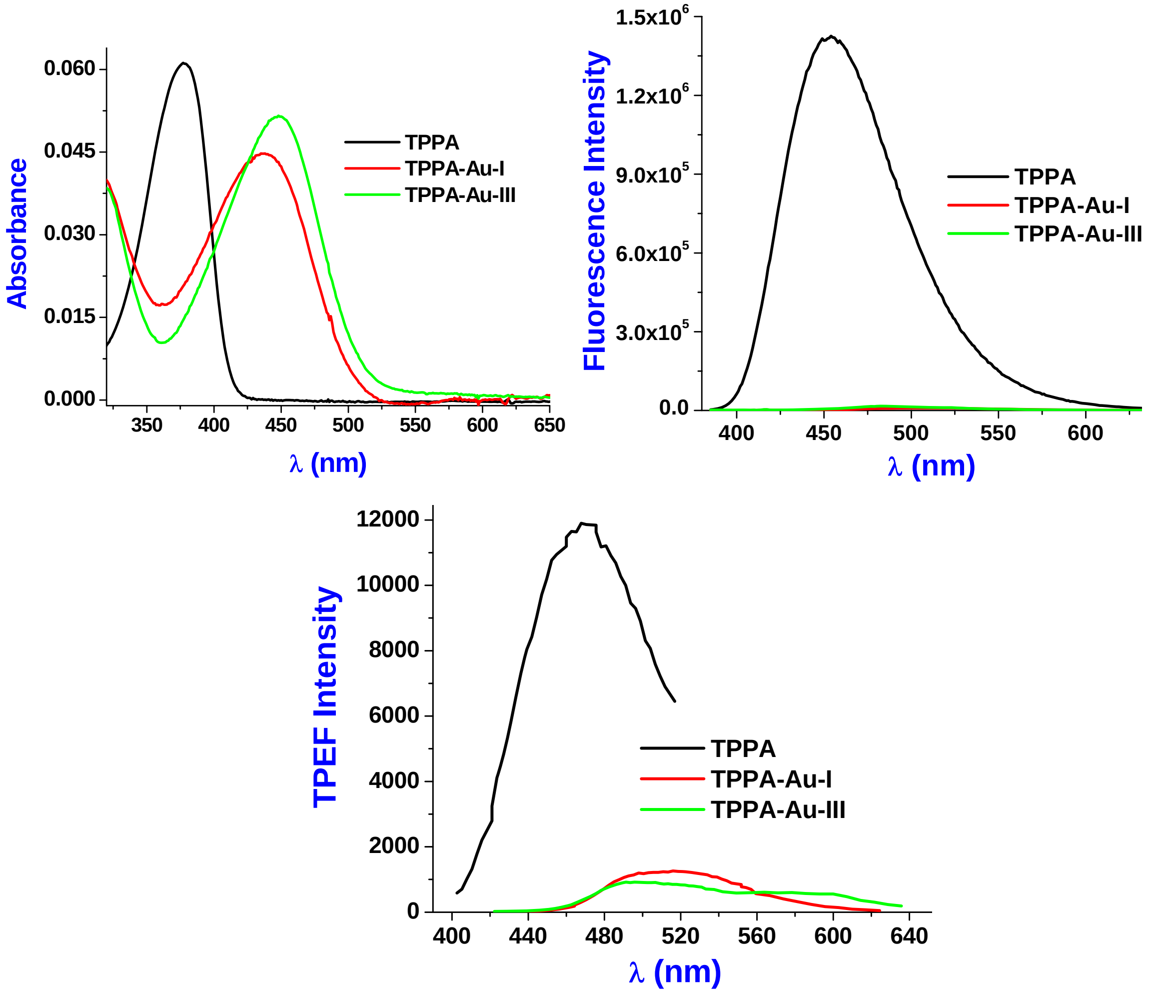

Figure 7.19. Absorption, one and TPEF results for TPPA, TPPA-Au(I) and TPPA-Au(III).

Table 7.1. Linear and nonlinear optical properties of TPPA, TPPA-Zn^{2+} and TPPA-Cd^{2+}.

Molecule	$\lambda_{abs\ max}$ **(nm)**	$\lambda_{em\ max}$ **(nm)**	**Stokes Shift (cm^{-1})**	η	$\eta\delta$ **(GM)**	δ **(GM)**
TPPA(THF)	378	427	3036	0.58	61.6	96.7
TPPA-Zn^{II}	398	500	5126	0.27	192.9	618.1
TPPA(Acetone)	375	448	4345	0.38	30.8	81
TPPA-Cd^{II} (Acetone)	392	508	5825	0.033	9.7	298.3

However, from earlier TPA measurements on native dyes (Chapter IV), it was shown that pyridine served as the strongest acceptor in T161 and weakest acceptor in TPPA. This is a possible reason why the effect of increase in acceptor strength on both TPEF and TPA cross section is more pronounced in TPPA than any other chromophore. Hence, the mere presence of pyridine groups does not explain the observed trends in TPEF or TPA cross section enhancement observed with the branched chromophores studied in this chapter. A more detailed insight into the steady state and excited state properties is required in order to elucidate the observed TPEF trends. Since the proposed mechanism involves increase in the charge transfer character of the complex, it is important to understand the excited state behavior of the complex since change in dipole moment due to solvent stabilization could be critical in determining the TPEF response. Hence, in an attempt to elucidate the mechanism of enhancement, transient absorption measurements were employed, which are discussed next.

Table 7.2. TPEF signal at 800nm for different metal ions upon complexation with TPPA.

Metal (Oxidation Number)	Zn (+2)	Cd (+2)	Au (+1)	Au (+3)	Cu (+2)	Ni (+2)	Fe (+3)	Fe (+2)
$\eta\delta$ **at 800 nm (GM)**	193	9.7	7.3	5.3	0.1	0.3	0.8	0.5

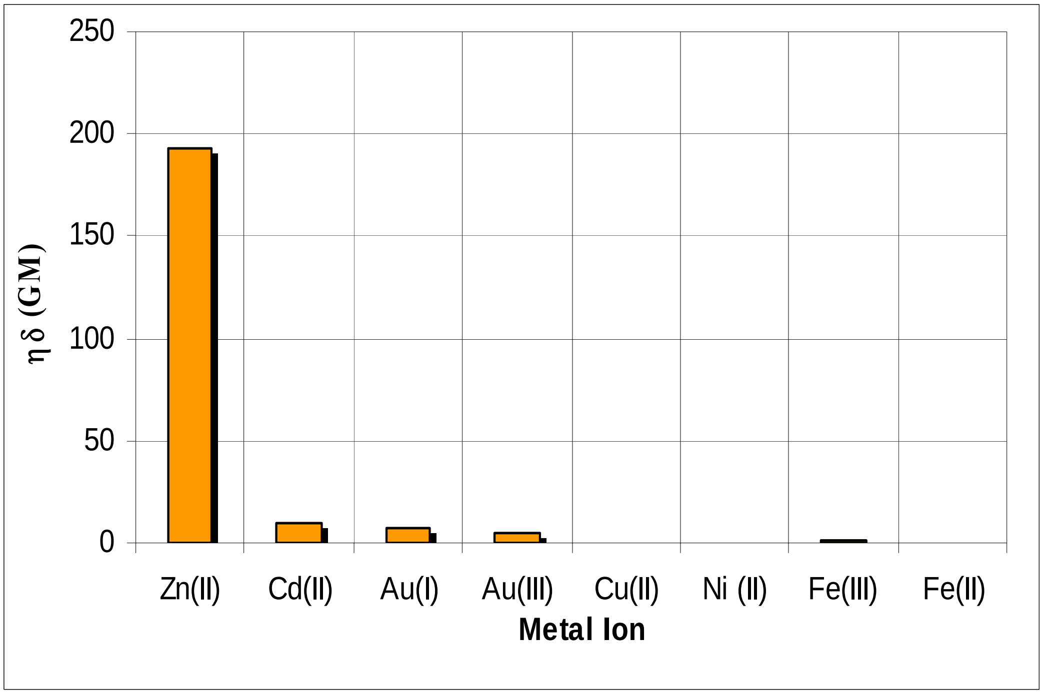

Figure 7.20. Selectivity of TPPA chromophore towards Zn^{2+}.

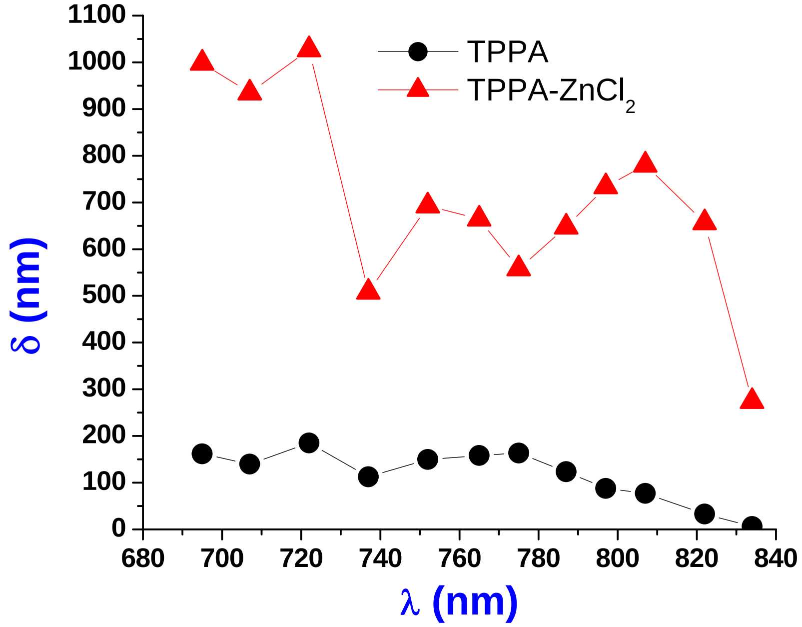

Figure 7.21. TPA cross section spectrum for TPPA and TPPA-Zn^{2+}.

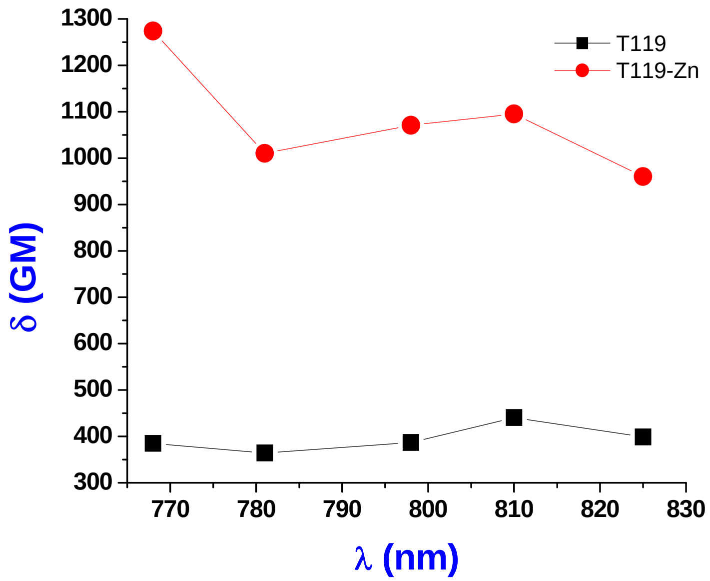

Figure 7.22. TPA cross section spectrum for T119 and T119-Zn^{2+}.

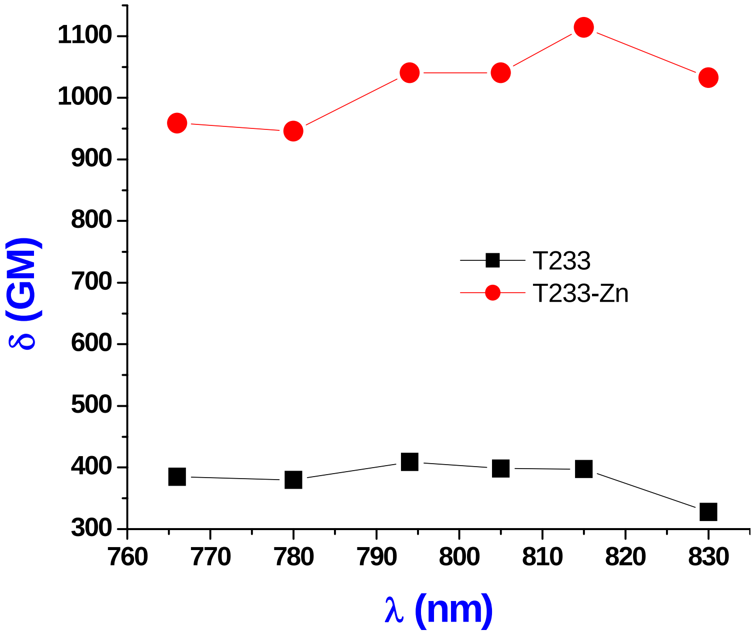

Figure 7.23. TPA cross section spectrum for T233 and T233-Zn^{2+}.

7.3.2. Transient Absorption Measurements

TPA cross-section and TPEF results have shown that TPPA is very good turn-on sensor for Zn^{2+} and turn-off towards other metal ions. Structurally similar dye molecules (T-233, T119 and T-161) with pyridine end groups have not shown such enhancement in

TPEF signal in presence of Zn^{2+} as TPPA. To understand the mechanism behind these observations, we have investigated the excited state dynamics of dye with and without metal ions using ultrafast pump-probe spectroscopy.

Figure 7.24 shows the excited state absorption (ESA) spectra of the Franck-Condon (FC) states at 100 fs whereas Figure 7.25 shows the ESA of final emitting states at 20 ps for TPPA in THF and TPPA in THF with Zn^{2+}. It can be observed that the FC state's ESA spectrum is unchanged upon complexation with Zn^{2+}. However the steady-state results show that the acceptor strength of pyridine is increased with metal ion complexation. This result suggests that there is a either significant elongation or even possible breaking of the Zn^{2+}-pyridine bond upon photo-excitation. This should cause a large change in conformations between ground and excited state, leading to a large change in dipole moment ($\Delta\mu_{ge}$). To relate this to enhancement of TPA cross section, we utilized a Sum-Over-States (SOS) expression for calculating the TPA cross-sections for non-centrosymmetric molecules[35], which is shown in equation 7.3. We concentrate on the lower energy absorption peak of the TPPA chromophore. In this case, there is no contribution from the excited state transition dipole moment ($M_{ee'}$). There is some bathochromic shift of the absorption spectrum upon addition of Zn^{2+} but this doesn't explain the order of magnitude enhancement of TPEF as we have observed. Steady state measurements with Zn^{2+} suggest that there is not a significant change in the ground state transition dipole moment (M_{ge}). The bathochromic shift in both absorption and emission maxima suggest a ground state complex between TPPA and Zn^{2+}. The present transient absorption measurements suggest that the excited state behavior results in a large increase in $\Delta\mu_{ge}$, thereby enhancing the TPA cross section.

$$\delta_{g\rightarrow e}\alpha\frac{{M_{ge}}^{2}\Delta\mu_{ge}^{2}}{(\frac{E_{ge}^{2}}{4})} \qquad (7.3)$$

Similar breaking of a weak bond under photo-excitation is observed for hydrogen bonded Coumarin-amine system[31]. However, the FC state immediately reforms the bond with Zn^{2+} with a time constant of 400 fs to give TPPA-Zn^{2+} which is followed by solvation to give an ESA maximum at 540 nm with a shoulder at 500 nm and stimulated emission around 610 nm (Figure 7.25 B). These transient features are ascribed to that of singlet-singlet absorption of TPPA—Zn^{2+} intramolecular charge transfer (ICT) state. Complete transient spectra are presented in Figure 7.26 .

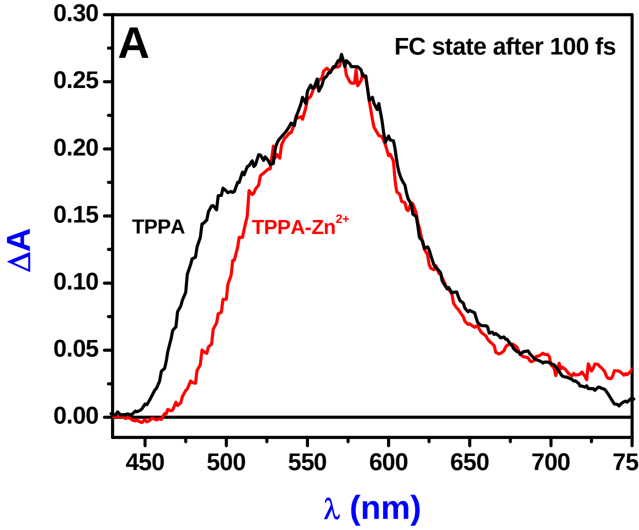

Figure 7.24. Excited state absorption spectra of FC states of TPPA and TPPA-Zn^{2+}.

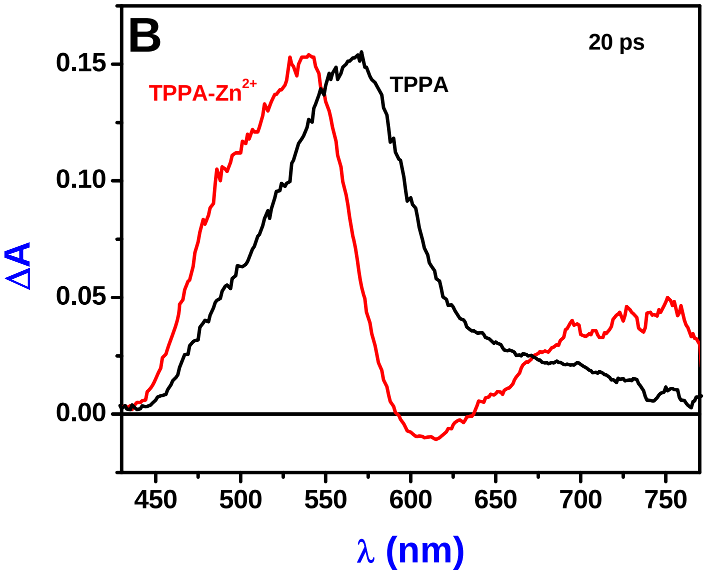

Figure 7.25. Excited state absorption spectra of final emitting states at 20 ps for TPPA and TPPA—Zn^{2+}.

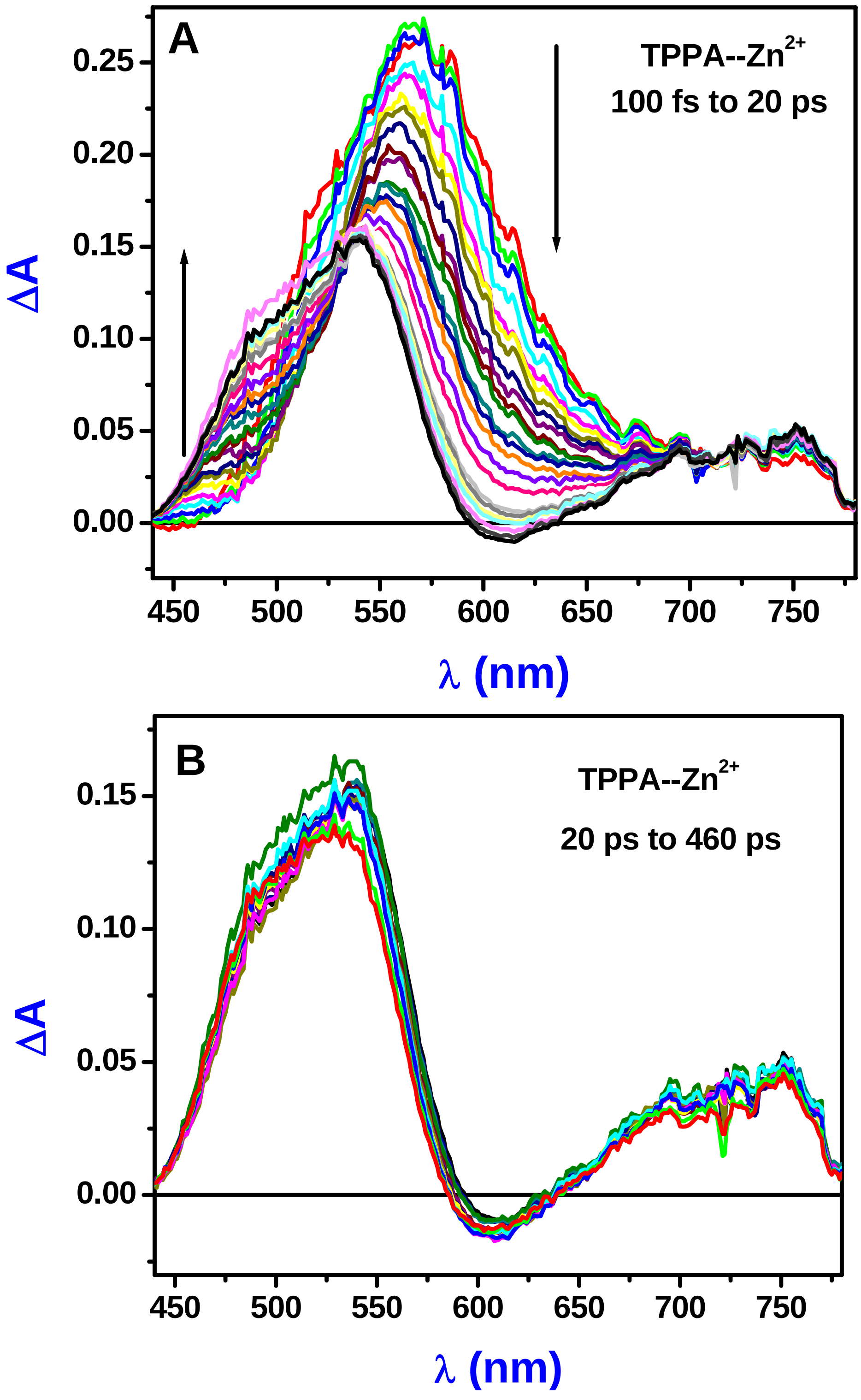

Figure 7.26. (A) Excited state absorption spectra at different time delay from 100 fs to 20 ps of TPPA with $ZnCl_2$ and (B) 20 ps to 460 ps.

The question that needs to be addressed here is why is the fluorescence quantum yield of TPPA with Zn^{2+} higher compared to the results with other metal ions? The answer comes from the analysis of the kinetic traces of TPPA with Zn^{2+} and Au^{3+} which are shown in Figure 7.27. The decay traces show that the emitting state of TPPA—Zn^{2+} has a lifetime greater than 2 ns while that of TPPA—Au^{3+} is only 20 ps. The fall in radiative lifetimes is the main reason behind low quantum yield and thereby lower TPEF signal observed for TPPA in presence of the other metals. Thus, it acts as a turn-off sensor for other metal ions while it is a turn-on TPEF sensor for Zn^{2+}.

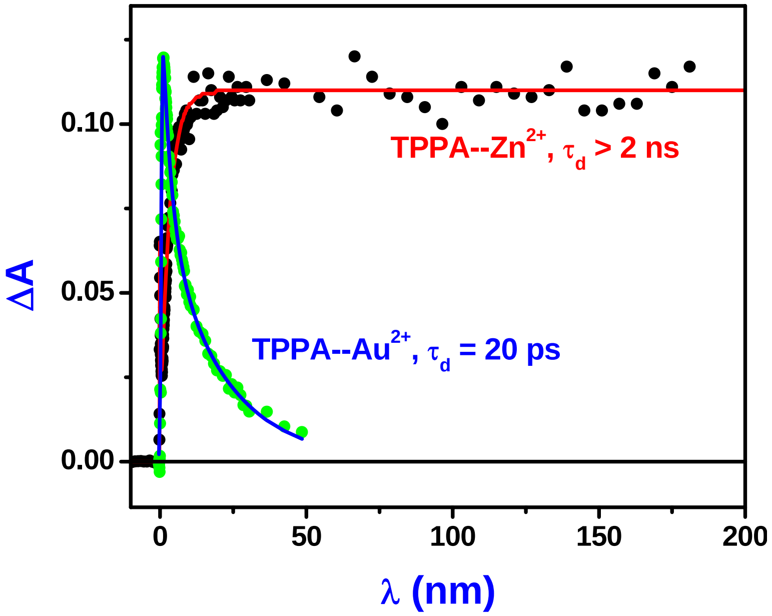

Figure 7.27. Kinetic decay profiles for TPPA—Zn^{2+} and TPPA—Au^{3+} at 490 nm after femtosecond laser excitation. Traces are fitted with exponential growth and decay functions.

In order to further resolve the origin of final ESA of TPPA-Zn^{2+}, comparisons of the transient absorption spectra were made with that of protonated form of TPPA. Figure 7.28a, b and c show the transient absorption spectra at different time delay for TPPA in THF in presence of TFA (1%) (TPPA-H^{+}). Immediately after photo-excitation, ESA with a maximum around 560 nm was observed which decayed rapidly with a time constant of 340 fs to give rise to another ESA centered at 500 nm and a stimulated emission at 590 nm. As the time delay was increased, ESA at 500 nm shifted towards blue wavelength and the stimulated emission shifted to longer wavelengths to 650 nm with a time constant of 3.1 ps. This is the characteristic of solvation of the excited state. Final state thus formed decayed with a lifetime of 260 ps. The results suggest that the emitting state of TPPA-Zn^{2+} has a close resemblance to that of 238-H^{+}.

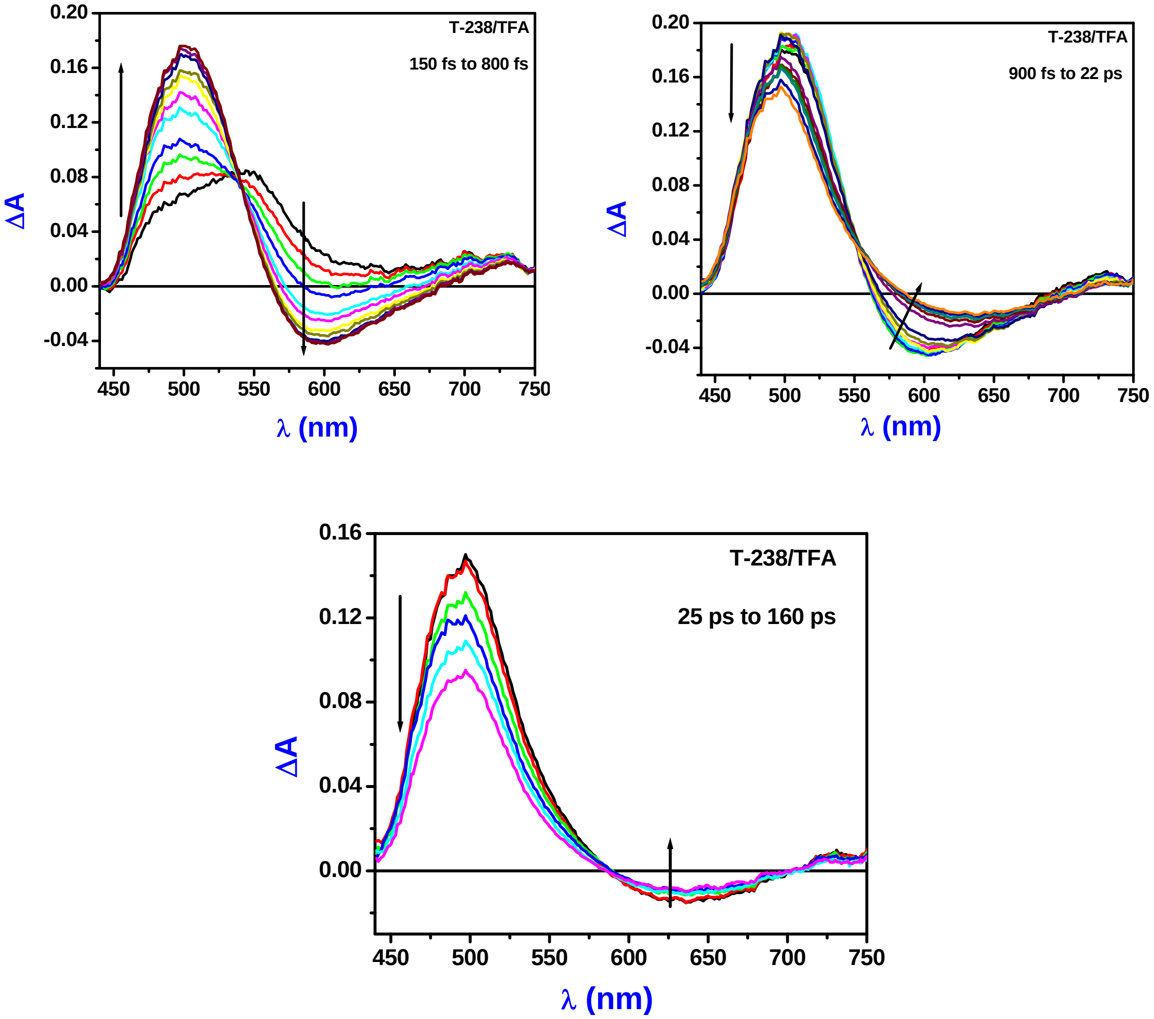

Figure 7.28. Transient absorption spectra of 238-H+ (T-238 in THF with TFA) at different time delays from a) 150 fs to 800 fs b) 900 fs to 22 ps, and c) 25 ps to 160 ps.

It has also been observed from two photon measurements that the enhancement of TPEF signal is only observed with TPPA while there is a decrease in net TPEF signal for similar branched dye molecules (T-233, T119 and T-161) with pyridine end groups. Transient absorption measurements were carried out for all the other chromophores with and without zinc ions. The transient absorption spectra at different time delays for T233 are presented in Figure 7.29, showing the presence of additional state which has been ascribed to solvent and conformationally relaxed intramolecular charge transfer state (ICT').

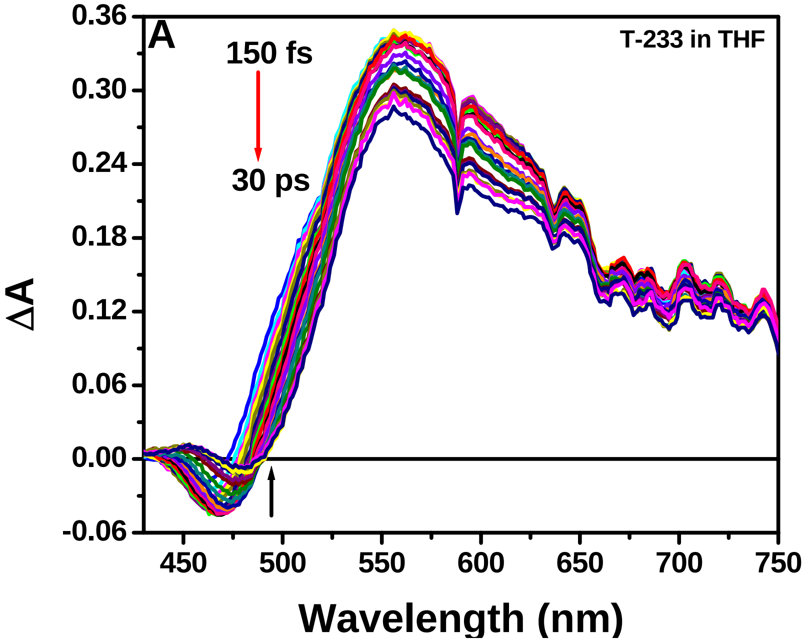

Figure 7.29. Excited state absorption spectra at different time delay from 150 fs to 30 ps for T-233 in THF.

Figure 7.30 A and B show the ESA at different time delays for T-233—Zn^{2+}. In contrast to the results obtained for TPPA-Zn^{2+}, immediate excited state of T-233—Zn^{2+} is red-shifted by ~10 nm in comparison to the first excited state of T-233 in THF suggesting the elongation of pyridine—Zn^{2+} bond. However, there is a reformation of complete pyridine—Zn^{2+} bond with a lifetime of 440 fs followed by solvation to form the non-emissive state. There is a large population of non-emissive ICT' state for T-233—Zn^{2+}, probably making it to possess lower quantum yield in comparison to TPPA—Zn^{2+}. Similar ESA features are observed for T-161 and T-119. The ESA spectra for T161 are shown in Figure 7.31 whereas the transient results for T119 are presented in Figure 7.32.

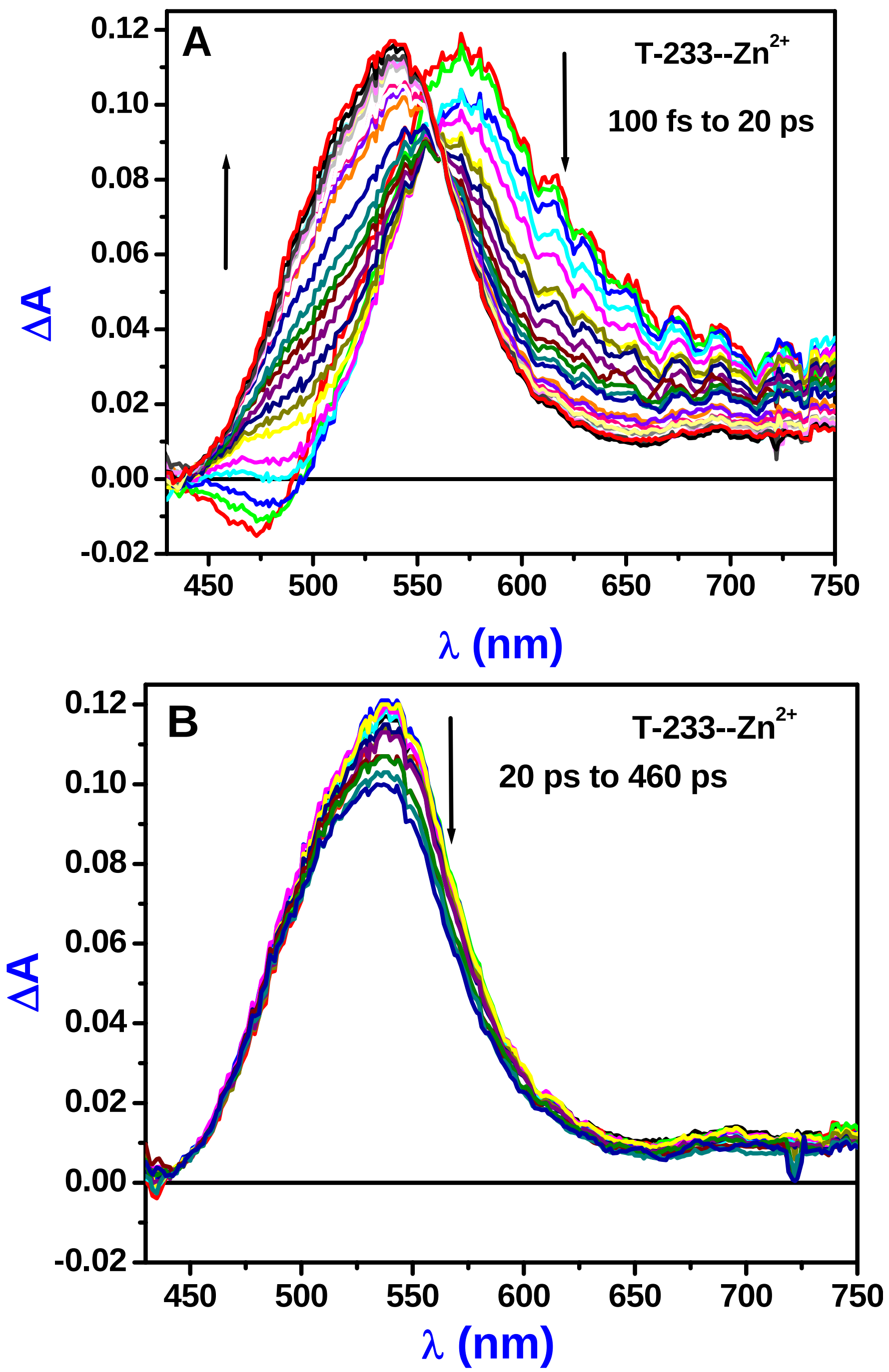

Figure 7.30. (A) Excited state absorption spectra at different time delay from 100 fs to 20 ps of T-233 with $ZnCl_2$ and (B) 20 ps to 460 ps.

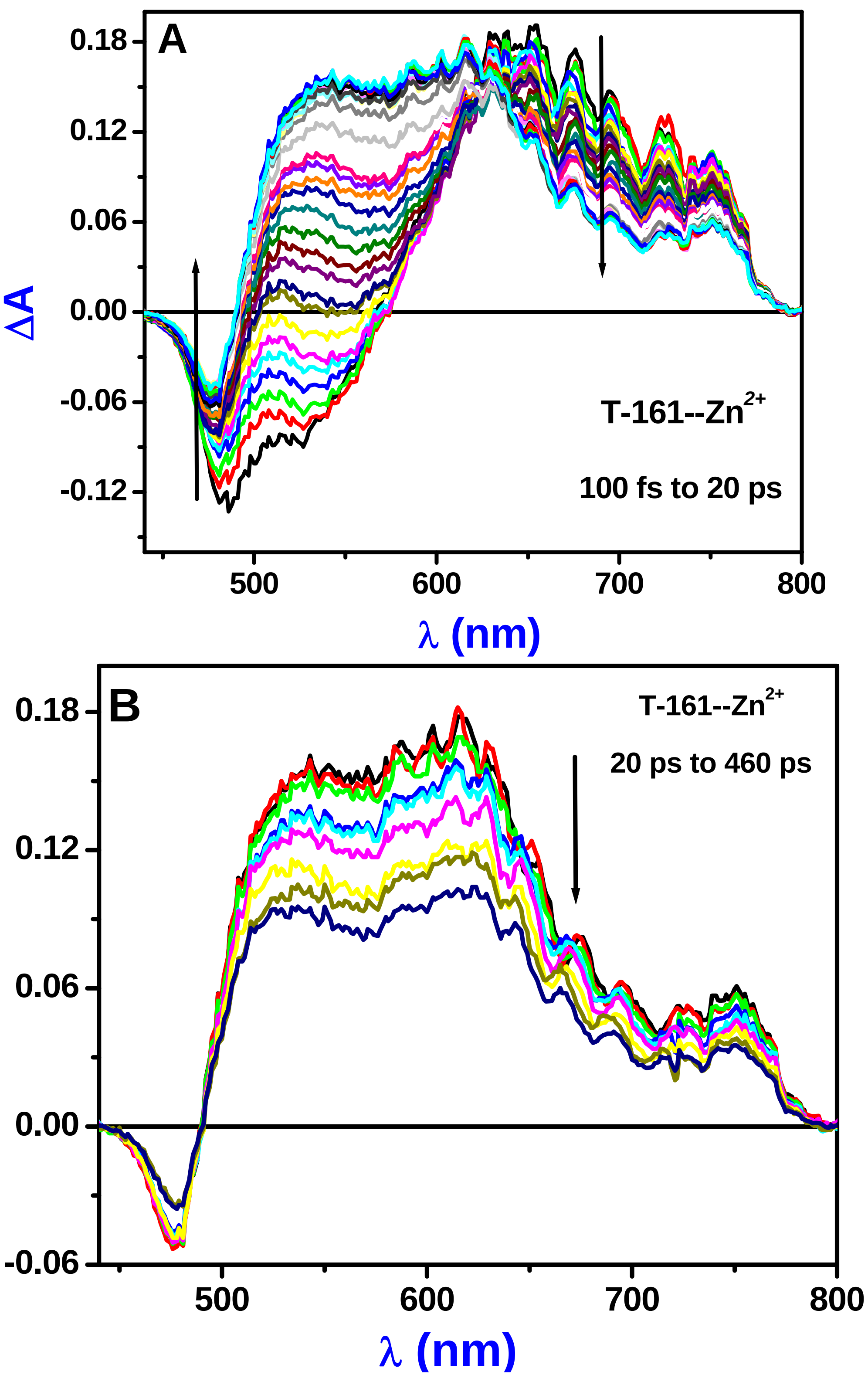

Figure 7.31. (A) Excited state absorption spectra at different time delay from 100 fs to 20 ps of T-233 with ZnCl2 and (B) 20 ps to 460 ps.

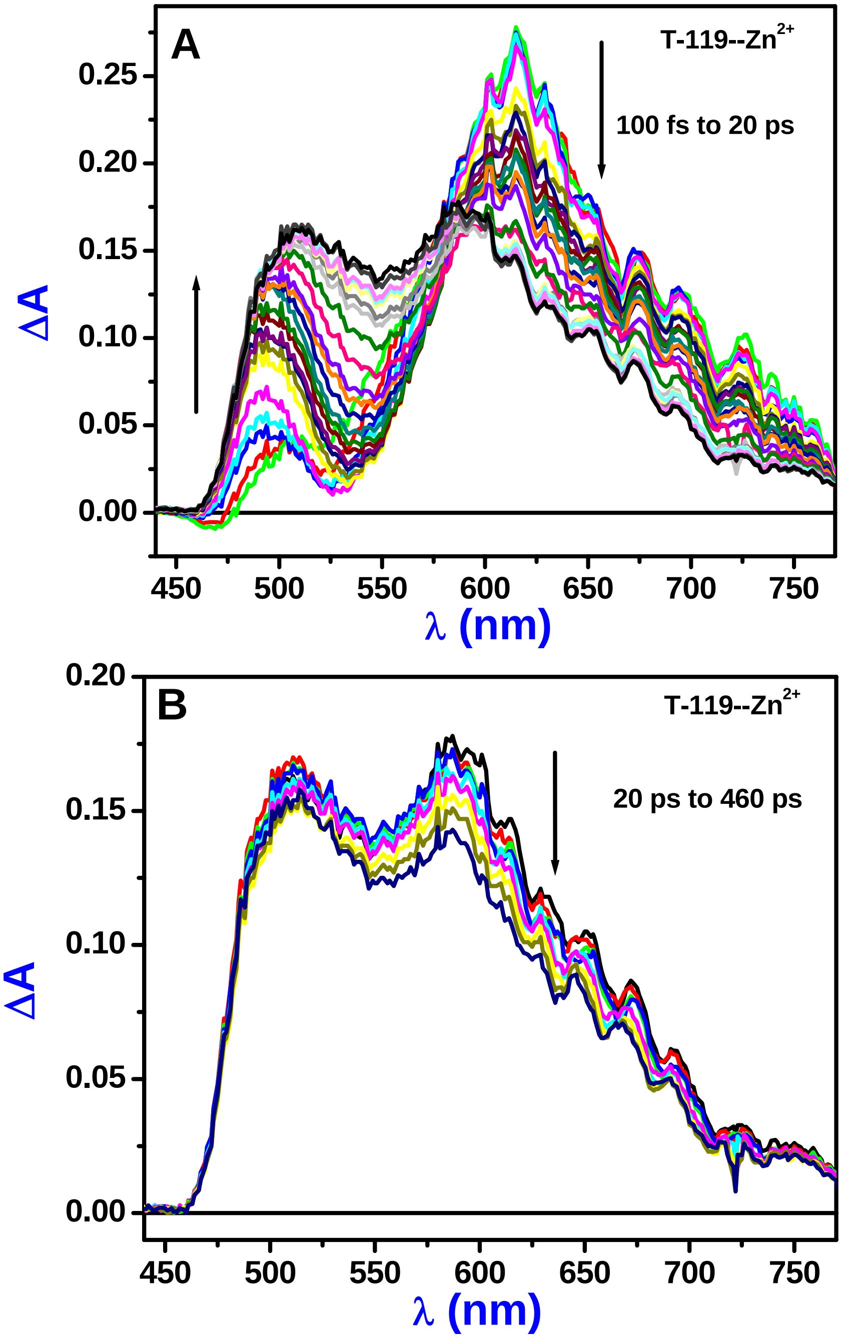

Figure 7.32. (A) Excited state absorption spectra at different time delay from 100 fs to 20 ps of T-233 with ZnCl2 and (B) 20 ps to 460 ps.

ESA spectra of FC state and at final emitting state at 20 ps are shown for all the dye molecules in presence of Zn^{2+} in Figure 7.33 A and Figure 7.33 B respectively for clearer comparison. As stated earlier, ESA spectrum of FC state of TPPA—Zn^{2+} is similar to that of TPPA in THF while the ESA spectrum of T-233—Zn^{2+} is red-shifted by around 10 nm when compared to the FC state's ESA spectrum of free T-233 in THF. Similar results were observed for T-161. These results suggest that the FC state of T-233 and T-161 are affected by the presence of Zn^{2+} unlike TPPA though very slightly. It appears as if the Zn^{2+}-pyridine bond is possibly elongated upon photo-excitation in these molecules, but not completely broken.

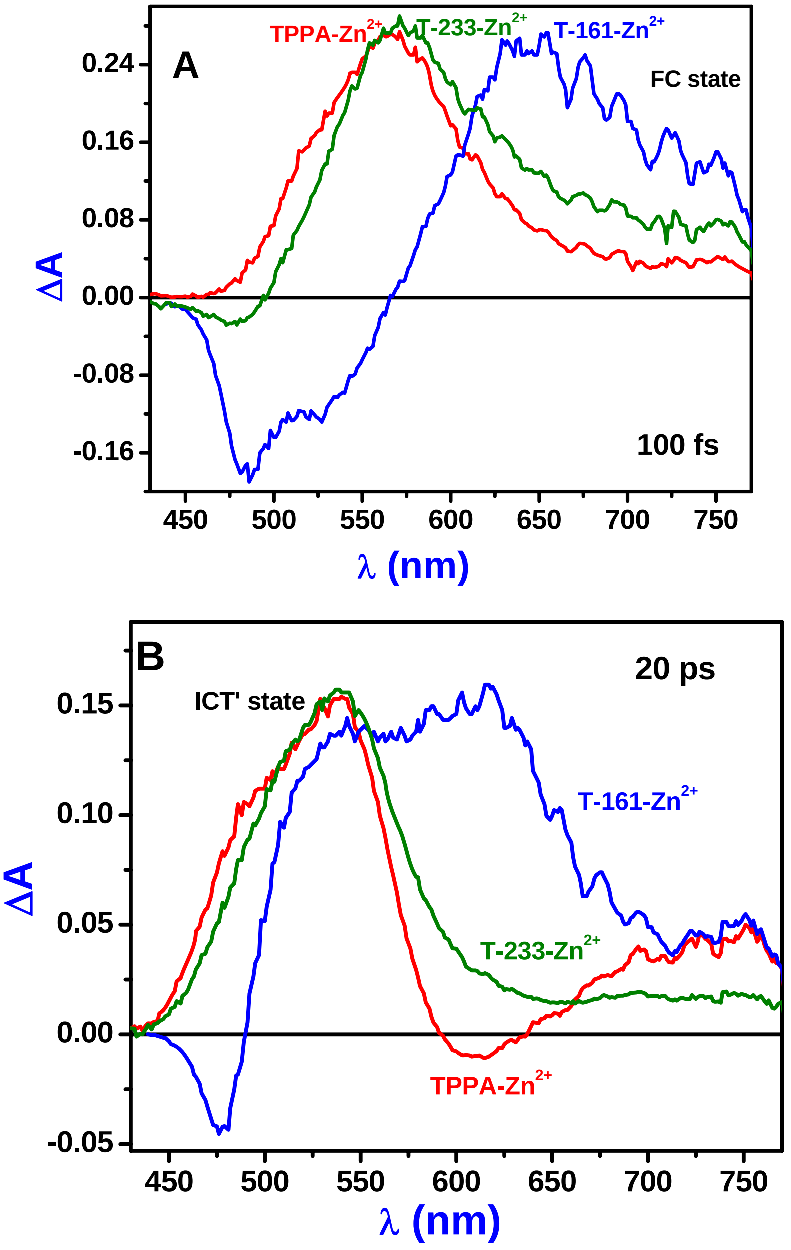

Figure 7.33. Excited state absorption spectra of (A) FC state of TPPA—Zn^{2+}, T-233—Zn^{2+} and T-161—Zn^{2+} and (B) at 20 ps of TPPA—Zn^{2+}, T-233—Zn^{2+} and T—161-Zn^{2+}.

Interestingly, reformation of Dye—Zn^{2+} does take place for T-233 and T-161 with a time constant of 400 fs to give rise to ICT state. Similar to what is observed earlier for the native dyes in THF (Chapter IV), there is an additional formation of conformationally relaxed intramolecular charge transfer state (ICT′) at 540 nm which is non-emissive. It can be observed from Figure 7.33B that for T-161—Zn^{2+}, the population of ICT′ state (570nm) is similar to the ICT state (at 630 nm). On the other hand, the population of ICT′ state (at 540 nm) is higher than ICT for T-233—Zn^{2+} whose ICT state is merged in the peak of ICT′ state. But the ICT′ state for smaller branched TPPA—Zn^{2+} occurs at 505 nm, which appears as a shoulder to the main ICT state at 540 nm. This suggests a smaller population of ICT′ state for TPPA in presence of Zn^{2+}. Larger population ratios of non-emissive ICT′ state to ICT state (2.5 for T-233—Zn^{2+}, 0.85 for T-161—Zn^{2+} and only 0.3 for TPPA—Zn^{2+}) is responsible for the lowering of fluorescence quantum yields in case of T-233 and T-161 in presence of Zn^{2+} and subsequently , a decrease in TPEF signal in comparison with TPPA—Zn^{2+}. This is the reason why TPPA alone is showing significant enhancement in TPEF signal with Zn^{2+} and not all other molecules with pyridine end group. Complete mechanism excited state dynamics of the dye molecules are depicted in Scheme1 shown below.

Scheme 7.1. Mechanistic scheme for excited state dynamics of dye molecules in presence of Zn^{2+}. Here, FC represents Franck-Condon state, ICT represent intramolecular charge transfer state, ICT state is the solvent and conformationally relaxed ICT state, τ_f.

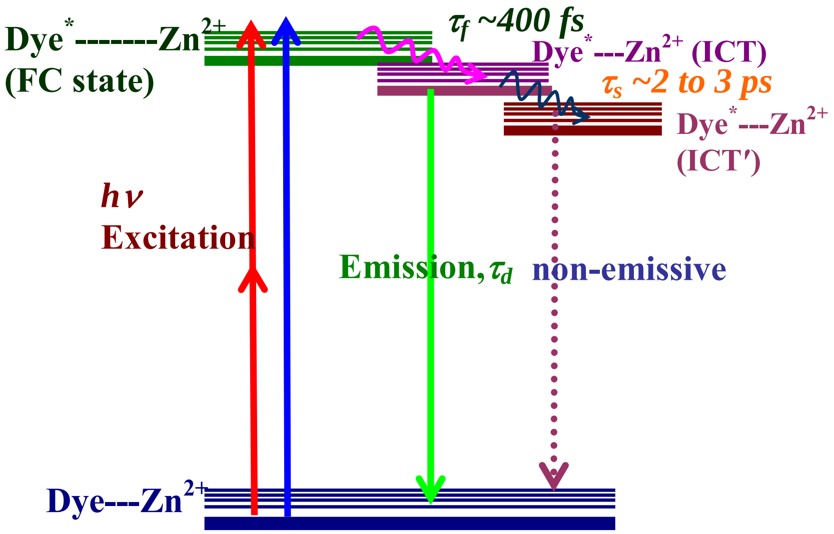

Upon photo-excitation of dye—Zn^{2+} complex, there is a considerable elongation of Zn^{2+}-pyridine bond, even leading to possible cleavage of the bond in case of TPPA—Zn^{2+}. However this bond reforms in the excited state with a time constant of 400 fs to give rise to the intramolecular charge transfer state of that particular dye-Zn^{2+} complex. There is additional formation of non-emissive intramolecular charge transfer state (with a lifetime of 2-3 ps) which is a solvent conformationally relaxed state. This state is attributed to be non-emissive from our previous results[37, 38] wherein its increase in population is manifested via a decrease in fluorescence quantum yield. Present transient results were able to provide the mechanism for the enhancement of TPA cross-section of TPPA in presence of Zn^{2+}. Lifetime of the final excited states in presence of different metals was successful in explaining its selectivity and sensitivity for Zn^{2+} alone and not for other metal ions. Higher population of non-emissive ICT′ state for T-233—Zn^{2+} and T-161—Zn^{2+} are the suggested reasons behind their lower TPEF signals observed in comparison with TPPA—Zn^{2+}.

Table 7.3 summarizes complete transient lifetimes obtained for the investigated dye molecules with and without Zn^{2+}. In the presence of Zn^{2+}, all the dye molecules possessed lifetime for reformation of pyridine—Zn^{2+} bond with a lifetime of ~400-500 fs and all had a lifetime associated with the formation of non-emissive ICT' state which is solvation controlled. However, the singlet lifetime of TPPA—Zn^{2+} is actually higher than al the other dye molecules with Zn^{2+}. This result also explains the higher fluorescence quantum yield of TPPA—Zn^{2+} in comparison to other dye molecules.

Table 7.3. Lifetimes of transients of dye molecules in THF and in presence of $ZnCl_2$.

Sample	**Lifetimes in THF**	**Lifetimes in THF with $ZnCl_2$**
TPPA	2.9 ps (Vib. cooling), 1.9 ns (decay)	490 fs, 2 ps (gr), > 2 ns (decay)
T-233	2.05 ps (solvn and gr of ICT') and 1 ns (decay)	440 fs, 1.7 (solvn and gr) and > 2 ns(decay)
T-161	2.85 ps (solvn and gr of ICT') and 1.85 ns (decay)	330 fs, 1.9 ps (solvn and gr) and 990 ps (decay)
T-119	1.94 ps (solvn and gr of ICT') and 2 ns (decay)	450 fs, 2.5 (solvn and gr) and 880 ps (decay)

7.4. Conclusions

A TPEF turn-on sensor for selective and sensitive detection of Zn^{2+} has been developed. Significant enhancement in both TPEF signal as well as TPA cross section was observed over a wide range of wavelengths. Increase in the acceptor strength and larger change in dipole moment are the suggested reasons behind the enhancement of TPA cross-section upon addition of Zn^{2+}. Enhancement of TPEF signal with Zn^{2+} is observed for only TPPA and not for other structurally similar branched molecules with pyridine end groups. Presence of non-emissive state in the excited state dynamics is suggested as the mechanism behind the lower TPEF signal for other chromophores. TPPA-Zn shows the least population of this state, it serves as a turn-on sensor.

The selectivity of TPPA was also confirmed by testing its TPEF response against several other metal ions. None of them showed TPEF enhancement. Since the TPEF signal of TPPA can be enhanced only by Zn^{2+}, it could serve as a guideline for developing sensors for sensing zinc in biological systems such as amyloids and Prion peptides. Their interaction with zinc and possible role in neurological disorders has been a subject of significant investigation[22-23] which can be well studied with the present TPPA and can be imaged using two-photon excitation. PrP106-126 is known to have seven orders of magnitude larger affinity for Cu than Zn[24]. With the present approach, one could design a chromophore that shows TPEF enhancement specifically upon coordinating with Zn in order to gain further insight into the role of zinc in Alzheimer's disease.

Summary

- The first ever two-photon excited turn-on zinc ion sensor was reported.
- The chromophore investigated is highly sensitive (1ppm) and highly selective towards Zn^{2+}.
- More than one order of magnitude enhancement in two-photon excited fluorescence (TPEF) signal was observed upon binding with zinc ions, in spite of decrease in fluorescence quantum yield.
- Transient absorption measurements revealed the mechanism behind sensing action. By investigating the Franck-Condon state immediately after photoexcitation, it was observed that the bond between the chromophore and zinc ion could be considerably elongated or even cleaved.
- This should result in large change in dipole moment and hence, enhancement of TPEF behavior.
- This study could serve as a guideline along which sensors for multiphoton biological imaging of metal ions could be designed and developed.

7.5. Reference

1) Cumpston, B. H.; et al. *Nature* **1999**, *398*, 51.
2) Kawata, S.; Sun, H.-B.; Tanaka, T.; Takada, K. *Nature* **2001**, *412*, 697.
3) Huang, F.; Tian, Y.; Ching-Yi, C.; Young, C. A.; Jen, A. K. *J. Phys. Chem. C*, **2007**, *111*, 10673.
4) DeArmand, K.; Halper, W. *J. Phys. Chem.* **1971**, *75*, 3230.
5) Kapinus, E. I.; Dilung, I. I. *Khimiya Vysokikh Energii*, **1975**, *9*, 353.
6) Righetto S.; Rondena, S.; Locatelli, D.; Roberto, D.; Tessore, F.; Ugo, R.; Quici, S.; Korystov, D.; Srdanov, V. I. *J. Mater. Chem.* **2006,** *16*, 1439.
7) Fabbrni, G.; Riccó, R.; Menna, E.; Maggini, M.; Amendola, V.; Garbin, M.; Villano, M.; Meneghetti, M. *Phys. Chem. Chem. Phys.* **2007**, *9*, 616.
8) Bozio, R.; Cecchetto, E.; Fabbrini, G.; Ferrante, C.; Maggini, M.; Menna, E.; Pedron, D.; Riccò, R.; Signorini, R.; Zerbetto, M. *J. Phys. Chem. A* **2006**, *110*, 6459.
9) Ahn, H. C.; Yang, S. K.; Kim, H. M.; Li, S.; jeon, S.-J.; Cho, B. R. *Chem. Phys. Lett.* **2005**, *410*, 312
10) Das, S.; Nag, A.; Goswami, D.; Bharadwaj, P. K. *J. Am. Chem. Soc.* **2006,** *128*, 402.
11) Liu, X.; Feng, J.; Ren, A.; Cheng, H.; Zhou, A. *J. Chem. Phys.* **2004**, , *120,* 11493.
12) Xu, C.; Webb, W. W. *J. Opt. Soc. Am. B.* **1996**, *13*, 481.
13) Beljonne, D.; Wensellers, W.; Zojer, E.; Shuai, Z.; Vogel, H.; Pond, S. J.; Perry, J. W.; Bredas, J.-L. *Adv. Funct. Mater.* **2002**, *12*, 631.
14) Pond, S. J.; Tsutsumi, O.; Rumi, M.; Kwon, O.; Zojer, E.; Bredas, J.-L.; Marder, S. R.; Perry, J. W. *J. Am. Chem. Soc.* **2004**, *126*, 9291.
15) Marcotte, R.; Plaza, P.; Lavabre, D.; Fery-Forgues, S.; Martin, M. M. *J. Phys. Chem. A* **2003**, *107*, 2394.
16) Wang, Y.; Ranasinghe, M. I.; Goodson, T. III *J. Am. Chem. Soc.* **2003**, *125*, 9562.
17) Chen, C.-Y.; Cheng, P.-Y.; Wu, H.-H.; Lee, H. M. *Inorg. Chem.* **2007**, *46*, 5691.

18) Maeda, C.; Shinokubo, H.; Osuka, A. *Org. Lett.* **2007**, *9*, 2493.

19) Hartmann, U.; Vahrenkamp, H. *Inorg. Chem. Acta* **1995**, *239*,13.

20) Noro, S.; Kitagawa, S.; Susumu, Y.; Yamashita, M.; Wada, T. *Chem. Comm.* **2002**, *3*, 222.

21) Ma, C. T. L.; MacLachlan, M. J. *Angew. Chem. Intl. Ed.* **2005**, *44*, 4178.

22) Wen, L.-L.; Dang, D.-B.; Duan, C.-Y.; Li, Y.-Z.; Tian, Z.-F.; Meng, Q.-J. *Inorg. Chem.* **2005**, *44*, 7161.

23) Screen, T. O.; Thorne, R. G.; Denning, R. G.; Bucknall, D. G.; Anderson, H. L. *J. Am. Chem. Soc.* **2002**, *124*, 9712.

24) Ogawa, K.; Ohashi, A.; Kobuke, Y.; Kamada, K.; Ohta, K. *J. Phys. Chem. B* **2005**, *109*, 22003.

25) Chang, C. J.; Nolan, E. M.; Jaworski, J.; Okamoto, K.-I.; Hayashi, Y.; Sheng, M.; Lippard, S. J. *Inorg. Chem.* **2004**, *43*, 6774.

26) Nolan, E. M.; Burdette, S. C.; Harvey, J. H.; hilderbrand, S. A.; Lippard, S. J. *Inorg. Chem.* **2004**, *43*, 2624.

27) Bontidean, I.; Berggren, C.; Johansson, C.; Csöregi, E.; Mattiasson, B.; Lloyd, J. R.; Jakeman, K. J.; Brown, N. L *Anal. Chem.* **1998**, *70*, 4162.

28) McCarroll, M. E.; Shi, Y.; Harris, S.; Puli, S.; Kimaru, I.; Xu, R.; Wang, L.; Dyer, D. J *J. Phys. Chem. B* **2006**, *110*, 22991.

29) Wang, J.; Xiao, Y.; Zhang, Z.; Qian, X.; Yang, Y.; Xu, Q. *J. Mater. Chem.* ***2005***, 15, 2836.

30) Burdette, S. C.; Frederickson, C. J.; Bu, W.; Lippard, S. J. *J. Am. Chem. Soc.* **2003**, *125*, 1778.

31) Van Dongen, E. M. W. M.; Dekkers, L., M.; Spijker, S.; Meijer, E, W.; Klomp, L. W. J.; Merkx, M *J. Am. Chem. Soc.* **2006**, *128*, 10754.

Chapter 8

Overall Summary and Outlook

8.1. Summary

In this section, key results from each chapter are summarized and suggestions for future research are made wherever applicable. The dissertation began (Chapter I) with an introductory chapter. The purpose of this chapter was to familiarize the readers with the field of nonlinear optical (NLO) materials and the scientific and industrial importance of such materials. It was emphasized that organic materials would form the focus of this dissertation. Various classes of organic materials and the present strategies for development of novel NLO materials were outlined. The purpose of this was to demonstrate that present methodologies are ultimately limited by organic synthesis. This formed the basis for my proposed strategy for development of novel NLO materials by utilizing a building block approach which would take advantage of self assembly and aggregation behavior in conjugated organic materials. In addition, the building block approach would also be conducive towards enhancing the existing knowledge of structure-function relationships in NLO materials. Since there are several kinds of NLO properties, each with its own gamut of applications, it was important to narrow down on materials development for a certain type of NLO behavior. As a result, an introduction on Two-Photon Absorption (TPA), which is a third order optical nonlinearity, was provided. This was the NLO property of choice for my dissertation. Several applications for TPA in microfabrication, biology and optics were described in order to emphasize the practical aspects for development of novel materials for TPA. In order to achieve this, it is very important to understand the molecular parameters which influence the TPA behavior of conjugated organic materials. Hence, the reminder of the chapter concentrated on some theoretical treatment of TPA and structure-function relationships exemplifying the molecular parameters emphasized in theoretical treatment of TPA. The importance of excited state behavior and excitations in conjugated organic aggregates was also emphasized since this distinguishes NLO materials from other classes of organic materials and sets different criteria for development of novel materials for NLO applications.

In chapter II, the main experimental tools employed for quantifying the TPA behavior as well investigating the reasons and mechanisms behind observed trends in TPA behavior were outlined. The choice of method for measuring TPA cross sections in this dissertation is the Two-Photon Excited Fluorescence (TPEF) technique. Other tools of ultrafast spectroscopy include Time Correlated Single Photon Counting (TCSPC) which measures fluorescence lifetimes, Transient Absorption (TA) measurements which monitor the excited state dynamics and Fluorescence Upconversion which provides information on exciton/energy migration dynamics and geometry of emitting state. A section on laser radiation was also included in order to gain appreciation for the technology involved in generating very high intensity light sources. It is interesting to note that lasers are used for investigating NLO properties; however, in order to construct a laser, NLO crystals are required. Hence, lasers and nonlinear optics are highly interdependent and therefore, complement each other very well.

In subsequent chapters, the building block approach was demonstrated using various architectures. Thus, the common theme between different facets of my research has been the building block approach and the knowledge regarding structure-function relationships acquired by the application of this approach.

In chapter III, the building block approach was illustrated with the help of annulene networks. This chapter demonstrated another advantage of building block approach in its ability to investigate macrostructures that are synthetically inaccessible by breaking down the macrostructure into small substructures. They key findings from this chapter were:

i) Influence of synmmetry on TPA behavior.
ii) Large TPA cross sections without the addition of strong donor or acceptor groups
iii) It is possible to construct materials with large TPA cross sections from building blocks with small TPA cross sections

iv) Increase in TPA cross section is not merely due to increase in number of π-electrons. This was proved by measuring TPA cross section per π-electron.

v) The arrangement of building blocks plays a vital role in determining the TPA behavior by virtue of its influence on the excited state transition dipole moment.

vi) Steady state measurements were unable to explain the trends observed in NLO behavior in these materials. The tools of ultrafast spectroscopy enabled the investigation of excited state behavior and elucidated the TPA behavior observed in the annulenes.

vii) Symmetry breaking in the excited state could be a key parameter in enhancing TPA cross sections.

In chapter IV, branched architecture was investigated for TPA properties. The main results observed in this study were:

i) Alkene linkages provide larger TPA response than alkyne π-bridging units due to better stabilization of the intramolecular charge transfer state.

ii) Based on steady state results, it appeared that the chromophores containing alkyne π-units would provide the largest NLO response. However, TPA measurements, coupled with ultrafast time-resolved measurements suggested otherwise and also elucidated the mechanisms for observed trends in TPA behavior.

iii) The presence of an initially delocalized state in octupolar molecules was confirmed using transient absorption measurements. This state eventually decays to form an intramolecular charge transfer state where the excitation is localized over one arm of the octupole.

iv) The presence of the delocalized state results in cooperative enhancement of TPA cross section in the tri-branched with respect to its linear counterpart.

v) Three dimensional thiophene dendrons exhibit super-linear TPA behavior with increasing dendron generation.
vi) These dendrons serve as energy funneling systems since emission was observed from the longest α-conjugated segment of each dendron.

In chapter V, materials possessing cyclic architecture were considered for NLO applications. In this case, the building blocks consisted of thiophenes, alkene and alkyne segments. These materials were interesting from a theoretical standpoint in regards to coupling between excited states as a function of ring size as well. These materials were equally attractive from applications perspective since cyclic architecture presents us with the possibility of infinitely conjugated wires with no end effects. The main contributions from this study were:

i) Complete conjugation was observed and proved in some of the macrocycles.
ii) This resulted in enhancement of NLO properties
iii) Coupling between excited states became more efficient with increasing ring size. In this manner, I was able to provide experimental verification for a proposed theoretical model.
iv) The use of Two-Photon excited fluorescence anisotropy as a more sensitive probe for investigating dynamics of excitation migration was proposed by taking two macrocycles as examples.
v) By making small changes to the structure of building blocks, large changes in NLO properties were observed in spite of maintaining the same cyclic geometry.

In chapter VI, macrostructures composed of porphyrins as building blocks were investigated for their NLO behavior. The most intriguing aspect of this study was to examine the possibility of coupling between individual structural units even though the covalent link that connected them was non-conjugated. These systems are interesting from the standpoint of light harvesting and mimicking systems that occur in nature. It must be reiterated that due to unavailability of the building block (dimer), the results obtained are not very conclusive. Further studies must be conducted with the dimer in order to ascertain the findings. The key results from this study were:

i) Enhancement of TPA cross section per porphyrin unit upon assembly into macrocyclic structures.

ii) Possible communication between individual building blocks based on transient absorption investigations due to observation of dynamics at timescale less than fluorescence lifetime of individual porphyrin rings.

In chapter VII, a potential application based on the knowledge gained from structure-function relationships was applied in an attempt to develop a potential application in the form of a zinc ion sensor. For this purpose, a tri-branched chromophore with alkyne π-linkages and pyridine end group was considered. The highlights of this study were:

i) The first ever two-photon turn on sensor for highly selective and sensitive detection of zinc ions was reported.

ii) In spite of decrease in steady state quantum yield, an order of magnitude enhancement was observed upon two-photon excitation.

iii) The mere presence of pyridine group was insufficient to provide an explanation for the mechanism of sensing. Excited state investigations revealed that a balance between conformational relaxation of the excited state and conjugation length provided best sensing capabilities.

iv) The sensor did not respond to other biological metal ions such as Na^+, K^+, Mg^{2+} and Ca^{2+}. Hence, it serves as a guideline along which sensors for biological applications could be designed and developed.

8.2. Outlook

The main contribution of my research is the application of the building block as a methodology towards understanding, designing and developing novel materials for nonlinear optical applications. The idea is to extend the design principles beyond the limitations imposed by chemical synthesis. Taking advantage of aggregation and assembly of organic materials broadens their scope for further applications. It would be very interesting to perform spectroscopic studies on the organic materials studied in my research in solid state. The nature of symmetry breaking, interaction between neighboring molecules and possible alignment of some of the materials could give rise to NLO behavior that could be different than that observed in solution phase. It is well known that the thiophene macrocycles and the annulenes studied in this research are capable of forming self assembled nanostructures, as well as possessing liquid crystalline behavior. The combination of nonlinear optics, self assembly and liquid crystallinity could give rise to unique and possibly novel NLO effects that could open more avenues for applications.

Another equally significant contribution is selection of NLO materials for developing applications. The material that shows the best TPA properties need not be the molecule of choice for developing an application. A good example of this is the study on development of zinc ion sensor. Based on the structure-property investigations, I observed that the pyridine end group served as the strongest acceptor in the presence of alkene bridging units with largest conjugation length. Based on well documented interactions between zinc ions and pyridine group, I extrapolated that the positively charged zinc ions would attract the lone pair of electron from the pyridine end group, thereby rendering it a stronger acceptor. Thus, I could use such materials as sensors. However, sensor needs to provide a strong response upon introduction of the analyte. Hence, I chose the material in which pyridine served as the weakest acceptor. As a result, upon introduction of zinc ions, the change in acceptor would be the largest among all other chromophores. Hence, for this particular application, I chose the material with the lowest TPA cross section. Thus, the knowledge gained from the application of building block approach enabled me to understand the mechanism of change in acceptor strength upon changing the nature of π linkage in the branched system. Based on this knowledge, I was able to choose the right chromophore for developing a potential application.

The field of nonlinear optical materials has evolved from a spectroscopic tool into a variety of applications. Several instruments based on TPA such as confocal microscopes, imaging systems and microfabrication schemes have been commercialized. Hence, future research should focus on device design and developing novel applications. Sensing using TPA is a fairly new concept. Hence, TPA sensing on thin films, design of

TPA materials for sensing other elements such as copper and iron could combine the advantages of TPA, imaging along with sensing that could enable more accurate and convenient investigation of a variety of biological phenomena. TPA based detection of other important parameters such as pH could further enable the monitoring of biologically relevant reactions in a more efficient manner. Since some of the materials studied in this dissertation could find applications as actuators, actuators based on two-photon excitation as a stimulus could open new avenues for molecular machinery inside human body. Besides biological applications, TPA based materials could also be developed into waveguides, pulse shaping and signal processing components for electronics and telecommunications industry.

With the unique facets on nonlinear optical materials, a methodology to combine the benefits of chemical synthesis, aggregation and self assembly, powerful and sophisticated analytical tools, and highly interdisciplinary nature of modern day research, the possibilities seem endless. I would like to conclude by quoting George Bernard Shaw:

“**You see things and you say “Why?” I dream of things that never were; and I say “Why not?”** ”.